

ISOTHERMAL AND NONISOTHERMAL DIFFUSION
OF OXYGEN IN SINGLE CRYSTAL MgO

by

HAN-ILL YOO

B.S. Seoul National University
(1974)

M.S. Korea Advanced Institute of Science
(1976)

Submitted to the Department of
Materials Science and Engineering
in Partial Fulfillment of the
Requirements of the
Degree of

DOCTOR OF PHILOSOPHY

at the

MASSACHUSETTS INSTITUTE OF TECHNOLOGY

February 1984

© Massachusetts Institute of Technology 1984

Signature of Author _____

Department of Materials Science and Engineering
January 13, 1984

Certified by _____

B. J. Wuensch
Thesis Supervisor

Accepted by _____

Bernhardt J. Wuensch
Head Ph.D. Committee

Archives
MASSACHUSETTS INSTITUTE
OF TECHNOLOGY

MAR 21 1984

LIBRARIES

ISOTHERMAL AND NONISOTHERMAL DIFFUSION
OF OXYGEN IN SINGLE CRYSTAL MgO

by

HAN-ILL YOO

Submitted to the Department of
Materials Science and Engineering
on January 13, 1984 in partial fulfillment of the
requirements for the Degree of Doctor of Philosophy

ABSTRACT

Single crystal layers of ^{18}O -enriched MgO were epitaxially grown at rates of about 20 μm per hour at temperatures between 1000°C and 1100°C on substrates of normal MgO through chemical vapor transport with HCl. After deposition, exchange between ^{18}O in the epitaxial layer and ^{16}O present in air as well as isotopic interdiffusion between the epitaxial layer and the substrate were simultaneously produced by annealings in a temperature range of 1000°C to 1650°C. Diffusion coefficients were determined from concentration profiles established with the aid of secondary ion mass spectrometry. The diffusion coefficients extracted from the gas-exchange profiles and from the isotopic interdiffusion profiles were in good agreement. The effect of the gas-exchange rate on the overall kinetics was therefore not significant within the limits of experimental uncertainty. The temperature dependence of the oxygen tracer diffusivity, obtained from the gas-exchange profiles, is best represented, with a precision of a factor of 2 by a pre-exponential term D_0 of $1.8 \times 10^{-6} \text{ cm}^2/\text{sec}$ and an activation energy of $3.24 \pm 0.13 \text{ eV}$. The magnitude of the diffusivity is smaller than that obtained from the earlier gas-exchange measurements of other workers but agrees well with recent values obtained from gas-exchange profiles established through a proton activation analysis. The present activation energy is in the middle of the range reported in previous studies. Upon comparison with the theoretical estimates of defect-related energies for MgO, the experimental value seems too large to represent an enthalpy for anion vacancy migration (estimated as 2.4 eV), the activation energy to be expected when the concentration of anion vacancies is extrinsically fixed. It is far too small to represent the combination of the enthalpies for Schottky defect formation and the anion vacancy migration (estimated as 7.5 and 2.4 eV, respectively), the activation energy to be expected if either the system remains intrinsic or, as presently believed, the defect structure of MgO is governed by cation impurities of higher valences.

Nonisothermal interdiffusion of the oxygen isotopes in a

system of $\text{Mg}({}^{16}\text{O}_{1-x}{}^{18}\text{O}_x)$ was analyzed in the light of irreversible thermodynamics. For comparison, non-isothermal diffusion of interstitial solutes was also analyzed. It has been analytically possible, for both cases, to obtain approximate but highly accurate and explicit time-dependent solutions to the transport equation for semi-infinite, thin-film and finite source boundary conditions. Contrary to an initial intuitive expectation, the interdiffusion of the anion isotopes in MgO-like ionic solids is not affected by the influence of anion thermomigration but only by the temperature dependence of the anion self-diffusivity in the applied temperature gradient. This is attributed to the fact that the local crystalline lattice in an MgO-like ionic solid, which is stoichiometric and where diffusion proceeds via a Schottky vacancy mechanism, is rendered mobile by a net flux of electrically-neutral quasi-molecular vacancies V_{MgO}^x induced by the temperature gradient in very much the same way as in an elemental crystal with a vacancy diffusion mechanism. The heat of transport of the anion is consequently not accessible from the intermixing profile of the anion isotopes which is developed in a temperature gradient. The analytical time-dependent solution was employed to numerically predict the velocity of the local crystalline lattice, which provides a direct measure of the molecular heat of transport in an MgO-like ionic solid. It is shown, however, that the time required to produce a measurable shift of a specific lattice plane may be unrealistically long for a system such as MgO in which the anion diffusion rates have been found to be extremely sluggish. The analytical time-dependent solutions for a nonisothermal distribution of an interstitial solute, in contrast, bears two perturbations: One arises from the temperature dependence of the solute diffusivity through its activation energy and the other from the effect of solute thermomigration through its heat of transport. This different behavior, relative to a vacancy mechanism, is due to the fact that the center-of-mass of the interstitial solute can be displaced relative to that of the solvent. The time-dependent solutions which were obtained in the present work have been employed to design promising experiments, through which the heat of transport of interstitial solutes may be determined by either measuring the change of concentration at a specific point in the solid as a function of time or by measuring the rate of shift of the position of a specific concentration of the solute. It is shown that such experiments provide a highly-accurate measure of the heat of transport in an experiment which requires an order of magnitude less time than the conventional technique which utilizes the Soret effect.

Thesis Supervisor: Bernhardt J. Wuensch

Title: Professor of Ceramics

TABLE OF CONTENTS

TITLE PAGE.1
ABSTRACT2
TABLE OF CONTENTS4
LIST OF FIGURES7
LIST OF TABLES.	10
ACKNOWLEDGEMENTS.	11
PROLOGUE	13
PART I: ISOTHERMAL ANION SELF-DIFFUSION IN MgO.	17
1. Introduction	18
2. Review of Literature	20
3. Experimental Procedure	30
3.1. Preparation of ¹⁸ O-Enriched MgO Powder.	30
3.2. Epitaxy of ¹⁸ O-Enriched MgO Single Crystal.	34
3.3. Diffusion Anneal	40
3.4. Measurement of ¹⁸ O Concentration Gradients.	42
4. Results	46
4.1. Gas-Exchange.	46
4.1.1. Expected Diffusion Profiles.	46
4.1.2. Experimental Depth Profiles.	50
4.1.3. Diffusion Coefficients	56
4.2. Isotopic Interdiffusion	60
4.2.1. Expected Diffusion Profiles.	60
4.2.2. Experimental Depth Profiles.	63

TABLE OF CONTENTS (Cont'd)

4.2.3. Comparison of Interdiffusion and Gas-Exchange Gradients	78
5. Discussion of Results	81
6. Summary	86
7. Suggestions of Future Work	89
Appendix 1. Assessment of Errors	92
1.1. Error Propagation and Linear Regression.	92
1.2. Error Evaluation	95
Appendix 2. Experimental Data	101
References.	137
Part II: NONISOTHERMAL ANION SELF-DIFFUSION IN MgO	141
1. Introduction	142
2. Irreversible Thermodynamics.	144
2.1. Entropy Production.	145
2.2. Phenomenological Laws and Onsager Theorem .150	150
2.3. Transformation of Fluxes and Forces	154
2.4. Heats of Transfer	158
2.5. Application to Crystalline Solids	163
3. Development of a Model for Thermomigration of Interstitials	173
3.1. Phenomenological Laws	176
3.2. Time-Dependent Solutions.	180
3.3. Determination of Heat of Transport.	191
4. Nonisothermal Anion Self-Diffusion in MgO.	198
4.1. Phenomenological Laws	199
4.2. Time-Dependent Solutions.	214

TABLE OF CONTENTS (Cont'd)

4.3. Measurement of Self-Thermomigration	
in MgO	221
5. Summary	231
6. Suggestions for Future Work	233
Appendix 1. Solution of the Differential	
Equation	236
1.1. Differential Equation	236
1.2. Solution for a Semi-Infinite Source	241
1.3. Solution for a Thin-Film Source	246
1.4. Solution for a Thick-Film Source.	249
1.5. Accuracy of the Solutions	251
Appendix 2. Self-Thermomigration with Local Defect	
Equilibrium Violated	255
2.1. Introduction.	255
2.2. Irreversible Thermodynamics	256
2.3. Formulation	262
References	271
BIOGRAPHICAL NOTE	277

LIST OF FIGURES

PART I

<u>Figure</u>	<u>Page</u>
1. Schematic of apparatus for oxidizing Mg-metal with $^{18}\text{O}_2$	31
2. Schematic of apparatus for Mg^{18}O chemical transport in HCl	37
3. Secondary-ion mass spectrum for the epitaxial layer of Mg^{18}O bombarded with oxygen at 11.5 KeV	39
4. Crater depth per unit primary ion current as a function of sputtering time for MgO irradiated by a 9.65 KV $^{40}\text{Ar}^+$ primary ion beam	45
5. Measured SIMS depth profile for ^{18}O , ^{16}O , ^{24}Mg , and ^{197}Au in a layer of isotopically enriched single-crystal MgO after gas exchange for 74.5 hr at 1300°C with $^{16}\text{O}_2$ in air. Primary beam: rastering $^{40}\text{Ar}^+$, 51 nA, 9.65 KV	51
6. Plot of the atomic fraction Mg^{18}O as a function of penetration, derived from Fig. 5	53
7. Plot as a function of penetration of the inverse error function of the ratio of atomic fraction Mg^{18}O less surface concentration to initial atomic fraction less surface concentration	54
8. Plot of the logarithm of the diffusion coefficients for ^{18}O in single-crystal MgO as a function of reciprocal temperature	58
9. Intensity ratio of oxygen isotopes, ^{18}O to ^{16}O , as a function of depth for the unannealed sample sputtered by a rastering $^{40}\text{Ar}^+$ beam of 506 nA, 14.7 KV.	68
10. Linear plot of the atomic % Mg^{18}O vs. channel as derived from Fig. 9.	69
11. Plot of the inverse error function for the broadening of the ^{18}O profile across the interface before the diffusion anneal	70

LIST OF FIGURES (Cont'd)

<u>Figure</u>	<u>Page</u>
12. Intensity ratio of ^{18}O to ^{16}O as a function of depth for the specimen annealed in air at 1200°C for 15 days and sputtered by a rastering $^{40}\text{Ar}^+$ beam of 306 nA, 9.65 KV.	72
13. Replot of Fig. 12 on a linear scale, atomic % Mg^{18}O as a function of depth.	73
14. Plot of the inverse error function corresponding to the profile in Fig. 13 for the gas-exchange (a) and for the isotopic interdiffusion (b)	74
15. Intensity ratio of ^{18}O to ^{16}O as a function of depth for the specimen annealed in air at 1100°C for 20 days and sputtered by a rastering $^{40}\text{Ar}^+$ beam of 206 nA, 9.65 KV	76
16. Plot of the inverse error function corresponding to the profile in Fig. 15 for the gas-exchange (a) and for the isotopic interdiffusion (b)	77
17. Comparison of the oxygen self-diffusion coefficients of the present work with previously reported values	82

LIST OF FIGURES (Cont'd)

PART II

<u>Figure</u>		<u>Page</u>
1.	The nonisothermal diffusion profile developed from a semi-infinite source is expected to be a combination, $(a) + \epsilon(b) + \epsilon(c)$187
2.	The nonisothermal diffusion profile developed from a thin-film source is expected to be a combination, $(a) + \epsilon(b) + \epsilon(c)$188
3.	The nonisothermal diffusion profile developed from a finite source of $2h$ thickness is expected to be a combination, $(a) + \epsilon(b) + \epsilon(c)$. ζ has been arbitrarily taken as 1 in Eq. 188 b189

LIST OF TABLES

PART I

<u>Table</u>	<u>Page</u>
1. Oxygen Self-Diffusion Data in MgO.	27
2. Calculated Defect Energies in MgO.	29
3. Spectrochemical Analysis of As-Pressed Isotopic MgO	33
4. Approximate Impurity Contents of Substrate Crystal.	35
5. Oxygen Self-Diffusion Coefficients in Single Crystal MgO.	57
6. Comparison of Diffusion Coefficients	78

PART II

<u>Table</u>	<u>Page</u>
1. Experimental Heats of Transfer for Interstitial Solutes.174

ACKNOWLEDGEMENTS

I thank my thesis supervisor, Prof. B. J. Wuensch from the bottom of my heart for his persistent guidance throughout the course of this work and for his inducement into an exciting discipline, the "Science of Becoming."

I am honestly grateful to Dr. R. S. Roth at N.B.S.. He fertilized my interest in materials science and stimulated me to pursue its advanced study.

I am very much indebted to Dr. K. S. Kim who now belongs to the other side of this secular world. He sowed the seed of my interest in this field. My brief encounter with him on this worldly stage will not be forgotten.

My warmest appreciation goes to Prof. W. T. Petuskey in the University of Arizona for his painstaking SIMS in-depth profiling which shines in the first part of this work.

Many thanks to W. H. Choe in the Plasma Fusion Center of M.I.T. for his kind assistance in giving birth to the time-dependent solution of the transport equation. My kind friends, H. T. Sawhill and M. W. Barsoum are also thanked for their valuable criticism and discussion along this long journey. My gratitude is expressed to my dear comrades, J. M. Mckittrick, P. K. Moon, S.-K. Fan, and T. A. Nguyen who have kept this delivery room comfortable, warm and joyful. Especially to P. K. Moon for his frequent correction of my usage of English.

Credit goes to my darlings, daughter A-Ram and son Seulki. Finally to my endearing and enduring mate, my wife, Kyu.

This work was funded under Contract DE-AC02-76ER02923 with the Office of Basic Energy Sciences of the U.S. Department of Energy. Their support is gratefully acknowledged.

PROLOGUE

This work was originally aimed at analysis and experimental measurement of oxygen thermomigration in MgO , a material selected for study as a model ceramic oxide. Moreover, as MgO is a highly stoichiometric material, a thermomigration experiment would be free from the competing effects of variation in diffusivity arising from local equilibration with atmosphere along the temperature gradient. It was envisioned that oxygen self-diffusion in a temperature gradient would be affected by two factors: the temperature dependence of the oxygen self-diffusion coefficient and the oxygen thermal-diffusion or thermomigration. The magnitude of the first influence will be governed by the activation energy for oxygen self-diffusion and the second by the heat of transport of oxygen in MgO . If one were to supply an oxygen isotope such as ^{18}O , either from a semi-infinite source or from an embedded thin film source in the form of $Mg^{18}O$, an intermixing profile of the isotopes, ^{18}O and ^{16}O , may bear those two influences in addition to ordinary self-diffusion. Depending on the sign of the heat of transport, the degree of intermixing would be anticipated to be either amplified or attenuated in given temperature and isotopic concentration gradients. One might thus expect an overall intermixing profile to be distorted or shifted compared with what would be developed from e.g. a thin film source in an isothermal condition, an effect which would

be analogous to the classic Chemla experiment of ionic diffusion in an electric potential gradient. Deconvoluting upon appropriate analytical or numerical analysis of the intermixing profile, one might hope to separate out the net effect of the thermomigration from which the heat of transport of oxygen can be extracted. For a meaningful deconvolution, the temperature dependence of the oxygen diffusivity or its activation energy must be known accurately and precisely for the specific material employed in the experiments. Several studies reported in literature show no general agreement on activation energies, and the magnitudes of the diffusivity range over several orders of magnitude. It was thus required that the isothermal oxygen self-diffusion coefficients be precisely determined over a wide range of temperature before the analysis of thermomigration data could be performed.

In parallel with this experimental study of oxygen self-diffusion, a rigorous theoretical analysis of thermomigration was undertaken. No general time-dependent solution had been given for the redistribution of solute during diffusion in a temperature gradient. It was anticipated that numerical methods, such as finite-difference methods would have to be employed. It was possible, however, to obtain an approximate but explicit analytical solution to the problem for semi-infinite, thin-film and thick-film source initial conditions. The formulation of the problem and nature of the result depends on the diffusion mechanism. It was shown that all information on thermomigration effects disappears from an aniso-

thermal diffusion profile for a vacancy diffusion mechanism. Oxygen thermomigration in MgO —a material which is stoichiometric, ionically bonded, and in which diffusion on both the cationic and anionic sublattices presumably proceeds via a Schottky vacancy mechanism—would thus not be a process amenable to study by means of the diffusion experiments originally contemplated in the present work. Moreover, the experimental measurements of isothermal oxygen self-diffusion revealed diffusion coefficients up to two orders of magnitude smaller than those reported in the literature—thus increasing proportionately the time necessary to produce measurable effects in the largest temperature gradient which might reasonably be produced under laboratory conditions. Uncertainty remains whether oxygen truly diffuses via a vacancy mechanism in MgO . But, even if this were not the case, the present diffusion data show that the annealing times necessary to produce measurable perturbations in a diffusion profile (which must be created under highly hostile experimental conditions) to be unrealistically long: ca. 4 years. It is thus concluded that MgO is decidedly not a suitable model material for self-thermomigration studies.

Therefore, the description of the results of the present work has been broken into two seemingly independent parts. The first part is devoted to the experimental measurement of isothermal oxygen self-diffusion in MgO . A unique type of specimen was developed in which a layer of single crystal $Mg^{18}O$ was grown epitaxially on a substrate of normal MgO .

The self-diffusion coefficient was determined therefrom with the help of analysis of concentration profiles through secondary ion mass spectrometry.. The second part is devoted to the irreversible thermodynamical analysis of the self-thermomigration in MgO -like ionic solids. For generality and in order to support the related subtle physics, the thermomigration of interstitial impurities in a non-ionic lattice is treated first. In this development for the first time an explicit analytic solution is obtained for the time-dependent flux equation, the form of which suggests a new procedure for the determination of the heat of transport from a nonisothermal diffusion gradient. The method promises to be more rapid and precise than conventional methods involving time-independent stationary states.

PART I:

ISOTHERMAL ANION SELF-DIFFUSION IN MgO

1. INTRODUCTION

Approximately a dozen studies of oxygen self-diffusion in single crystal MgO have been reported subsequent to the first gas exchange measurements¹ performed by Oishi and Kingery in 1960. Although recent advances in theory have provided reliable estimates of the enthalpies for defect formation, migration, and association in MgO ,^{2,3,4} the various activation energies for anion self-diffusion provided by experiment are not in especially good agreement with either theory or each other, while a concensus by and large seems to have been reached for cations. Moreover, the magnitudes of the diffusion coefficients which were obtained range over more than two orders of magnitude although the difference, of itself, would not be unexpected if extrinsic, impurity controlled transport were involved.

The difference between the activation energies of previous studies may be at least partly due to the small temperature range over which experiments have been conducted. Each data set extends over a temperature range of $450^{\circ}K$ at most. This attaches considerable uncertainty to the reported activation energy. The significance of the difference cannot be established at the moment since errors associated with the various measurements have not been assessed to provide a realistic uncertainty to the activation energy and the diffusion coefficient as well. Results may be especially mis-

leading if the measurements extend over a temperature range where a change in diffusion mechanism appears to occur. If insufficient data are available to resolve a change in slope in an Arrhenius plot of the diffusion coefficients, the apparent activation energy will be some value intermediate to those for the two different mechanisms.

In the present work, oxygen self-diffusion coefficients were measured over a wider temperature range, 1000°C to 1700°C. The predominant isotope in air, ^{16}O , was exchanged with ^{18}O in an isotopically-enriched layer of single crystal MgO which had been grown epitaxially on a substrate of normal MgO . Diffusion profiles were established with secondary-ion mass spectrometry (SIMS). Diffusion coefficients measured from the gas exchange at the free surface of the epitaxial layer were also compared with those measured from the isotopic interdiffusion at the interface between the epitaxial layer and the substrate in order to elucidate the possibility of the surface (phase boundary) exchange reaction being rate-controlling.

2. REVIEW OF LITERATURE

Oishi and Kingery¹ first measured the oxygen diffusion in MgO with the gas/solid ¹⁸O isotope exchange technique in which crushed particles of single crystal MgO were annealed in an atmosphere of 150 torr ¹⁸O₂. The particles were subsequently reduced by carbon to convert the oxygen to the gas phase. The gas was then analyzed by means of mass spectrometry to determine the total amount of ¹⁸O which had diffused into the solid, a measurement from which the diffusion coefficient was deduced. The gas exchange rate at the specimen surface (phase boundary) was assumed to be fast enough that the overall kinetics of the gas exchange was limited by solid-state diffusion. In such boundary conditions as *diffusion from a well-stirred solution of limited volume to a sphere*, extraction of a diffusion coefficient necessitates knowledge of the radius of the sphere or the radius of particles⁵. Oishi and Kingery¹ employed as an equivalent sphere radius the value corresponding to that which would provide the same surface-to-volume ratio as was estimated from a photomicrograph of the irregularly shaped particles. The diffusion coefficients obtained could be represented by $D = 2.5 \times 10^{-6} \exp(-2.71 \text{ eV}/kT) \text{ cm}^2/\text{sec}$ at temperatures of 1300° to 1750°C. An enormous error may have been produced by the estimation of the radius from the surface-to-volume ratio. Measurement of the surface area by macroscopic means is likely to lead to a

underestimation of the true area, where the gas exchange reaction has taken place, due to surface irregularities on the atomic scale. Recently, Oishi *et al.*⁶ have reported the influence of surface condition on the apparent oxygen self-diffusion coefficient. It was shown that the oxygen diffusion coefficient of a single crystal Al_2O_3 , once measured by Oishi and Kingery⁷ with exactly the same technique, was overestimated by as much as a factor of 34 due to the underestimation of the surface-to-volume ratio. In this view, the first oxygen diffusion data seem to have been overestimated also.

Quite recently, the oxygen diffusion coefficient in MgO has been remeasured by Oishi *et al.*⁸ with the same method as before. A rectangular plate of single crystal rather than crushed powders was used this time and the exposed surface of the plate was polished chemically to eliminate a possible underestimation of the surface-to-volume ratio due to surface microroughness. The annealing atmosphere was again 150 torr $^{18}O_2$. The results for Norton* crystals were interpreted as having a break at around 1500°C in an Arrhenius plot of $\ln D$ as a function of reciprocal temperature. The steeper portion was represented by $D = 6.76 \exp(-5.56 \text{ eV}/kT) \text{ cm}^2/\text{sec}$ between 1500°C and 1750°C and that at lower temperatures by $D = 2.2 \times 10^{-9} \exp(-2.21 \text{ eV}/kT) \text{ cm}^2/\text{sec}$ from 1300°C to 1500°C. The former was interpreted as an intrinsic diffusion

* Norton Co., Worcester, MA

based on the observation that the result was comparable with that obtained for ORNL* crystals which had a differing impurity concentration. The latter was interpreted as not impurity-sensitive but structure-sensitive, being dependent on the method of sample preparation such as as-cleaved, as-crushed, or as-chemically-polished. According to Oishi *et al.*'s comparison of impurity contents⁸, the Norton crystal contains as much as 150 ppm of Al, Fe, and P combined, while the ORNL crystal has 60 ppm of Al, Fe, P, and Si combined as the major aliovalent cationic impurities. The activation energy for the so-called intrinsic diffusion above 1500°C appears comparable to the theoretical estimate, 6 eV, which is the sum of the enthalpy for the anion vacancy migration and a half of the enthalpy for the Schottky defect formation (see Table 2). But, this interpretation is suspicious in view of the impurity content, which is still too large to allow for intrinsic transport to occur[†]. It is also suspicious in view of the limited number of data points on the Arrhenius plot. The break was judged on the basis of only two seemingly-high diffusion coefficients at temperatures below 1500°C. In other words, the two seem to have been excluded

* Oak Ridge National Laboratory, Oak Ridge, TN

† Based on the theoretical estimate of Schottky defect formation energy, 7.5 eV, the fractional concentration of anion vacancies is on the order of only 10^{-9} or 0.001 ppm at the temperature of 1800°C when the entropy-related pre-exponential term of the Schottky defect equilibrium equation is taken as unity.

almost arbitrarily for the sake of obtaining an activation energy close to the expected value, 6 eV.

Hashimoto *et al.*⁹ applied the same technique to measure the oxygen diffusion in polycrystalline MgO. A sintered tablet of 96% theoretical density was crushed into polycrystalline particles with a diameter of ~3 or ~5 times the approximate grain size. These powder samples were annealed in an environment of 40 torr ¹⁸O₂ enrichment. When the approximate grain size rather than the size of the polycrystalline particles was taken as the radius of sphere, the volume diffusion coefficient between 1050° and 1438°C was calculated as $D = 4.5 \times 10^{-7} \exp(-2.61 \text{ eV}/kT) \text{ cm}^2/\text{sec}$, which was claimed to agree well with the earlier measurement¹ of Oishi and Kingery. It seems likely that the uncertainty associated with taking an average grain size for the corresponding sphere radius is no smaller than the procedure for estimating sphere radius micrographically in the earlier work of Oishi and Kingery.

With the use of the same technique, Rovner¹⁰ arrived at diffusion coefficients, $D = 4.3 \times 10^{-5} \exp(-3.56 \text{ eV}/kT) \text{ cm}^2/\text{sec}$ at temperatures of 975°C to 1150°C and $D = 4.8 \times 10^{-14} \exp(-1.31 \text{ eV}/kT) \text{ cm}^2/\text{sec}$ at 750° to 975°C for crushed Norton crystals, and $D = 2.4 \times 10^{-5} \exp(-3.56 \text{ eV}/kT) \text{ cm}^2/\text{sec}$ at 975° to 1150°C for crushed Semi Elements* crystals. Both crystals were diffusion-annealed in an ¹⁸O₂ atmosphere of 1

* Semi Elements Inc., Saxonburg, PA

torr. According to Wuensch^{11,12} these measurements were complicated, however, by the necessity of making large corrections for exchange with the system, and by the fact that the exchange rate plots did not extrapolate to zero at zero time.

Reddy¹³ used the ^{18}O exchange technique followed by proton activation analysis to establish an ^{18}O concentration profile, from which the oxygen diffusion coefficient was best estimated to be $D = 1.9 \times 10^{-4} \exp(-3.84 \text{ eV}/kT) \text{ cm}^2/\text{sec}$ at temperatures 1310° to 1544°C for ORNL MgO single crystals which had been mechanically polished and annealed in 760 to 800 torr $^{18}\text{O}_2$. In a proton activation technique,¹⁴ ^{18}O is activated *in situ* by irradiation with monochromatic protons. An experimental in-depth profile is obtained from the variation of the intensity of the nuclear reaction product (α -particles in Reddy's work, produced via the $^{18}\text{O}(p,\alpha)^{15}\text{N}$ reaction) with its energy which is, in turn, converted to a penetration depth. In this technique, the major uncertainty comes into existence, obviously, during the conversion of an intensity-energy relation into a concentration-depth relation.

Some authors have measured the oxygen diffusion coefficients indirectly from the observation of dislocation-related phenomena in a thin MgO single crystal by means of the transmission electron microscopy. Moriyoshi *et al.*¹⁵ measured elapsed times for subgrain boundary formation at 1400° to 1750°C in a thin sheet of single crystal MgO which had been mechanically polished to introduce dislocations.

Assuming that the subgrain boundary is formed by dislocation polygonization via diffusion processes and taking a diffusion distance in an elapsed time as an average spacing between neighboring dislocations (a value which is estimated from the density of dislocation etch pits), they have obtained a diffusion coefficient, $D = 1.35 \times 10^{-5} \exp(-3.28 \text{ eV}/kT) \text{ cm}^2/\text{sec}$. Upon comparison with the earliest oxygen diffusion data¹ of Oishi and Kingery, control of the rate of polygonization has been attributed to oxygen diffusion since the activation energy is but "a little different" from the earliest value, 2.71 eV , and the magnitude of the diffusion coefficient itself is rather smaller by the order of magnitude 1.

Narayan and Washburn¹⁶ measured shrinkage rates of dislocation loops in an MgO foil. Being based on the kinetic model that the dislocation climb rate is controlled by the diffusion of oxygen vacancies between a loop and the surface of a foil, the diffusion coefficient of oxygen has been given as $D = 1.37 \times 10^{-2} \exp(-4.78 \text{ eV}/kT) \text{ cm}^2/\text{sec}$ at temperatures of 1100° to 1427°C . In these dislocation-related methods, the diffusion coefficient is obviously dependent on the kinetic model chosen for dislocation movements just as diffusion coefficients estimated from sintering or creep experiments.

The experimental observations of oxygen diffusion in MgO are summarized in Table 1.

On the other hand, the success of theoretical calculations of defect energies has recently seen a major advance for MgO and similar oxides?^{2,3,4,17} The enthalpy for Schottky

defect formation, h_s , is calculated to be 7.5 eV by Mackrodt and Stewart² and 7.72 eV by Sangster and Rowell³. The similarity of results in different calculations using different potentials suggests that these values are reliable. The activation energy for cation vacancy migration, h_{m+} , has been put at 2.16 eV² or 2.07 eV³. These results are in good agreement with the experimental cation migration enthalpies, 2.2 eV¹⁸ or 2.29 eV¹⁹ obtained from ionic electrical conductivity measurement with heavily-doped crystals, but somewhat smaller than that obtained from the cation self-diffusion measurement, 2.76 eV²⁰.

With respect to the anion vacancy, its migration enthalpy has been calculated as 2.38 eV² or 2.11 eV³. These have often been favorably compared with the activation energies obtained from anion self-diffusion measurements, 2.71 eV by Oishi and Kingery¹ or 2.61 eV by Hashimoto *et al.*⁹, but this is meaningless at present as this interpretation is inconsistent with the interpretation of cation diffusion in terms of a defect structure dominated by vacancies created by impurity cations (see Chapter 5).

Interaction energies among defects in MgO have been also calculated rather extensively^{2,4,21}. Among those, the enthalpy for cation-anion divacancy formation is estimated to be -2.55 eV.

The theoretical estimations are summarized in Table 2, which will be referred to later.

TABLE 1. OXYGEN SELF-DIFFUSION DATA IN MgO*

Ref	Authors	Technique	Annealing Atmosphere	Temperature range (°C)	D_O (cm ² /sec)	Activation Energy (eV)	Samples
1	Oishi & Kingery, 1960	gas/solid ¹⁸ O isotope exchange - mass spectrometry	¹⁸ O ₂ 150 Torr	1300-1750	2.5×10^{-6}	-2.71	Crushed single crystals
8	Oishi et al., 1972			1500-1750	6.76	-5.56	Chemically polished, Norton ⁺ single crystal plate
			1300-1500	2.2×10^{-9}	-2.21		
9	Hashimoto et al., 1972		¹⁸ O ₂ 40 Torr	1050-1438	4.5×10^{-7}	-2.61	Crushed polycrystals
10	Rovner, 1966		¹⁸ O ₂ 1 Torr	975-1150	4.3×10^{-5}	-3.56	Crushed Norton single crystals
				750-975	4.8×10^{-14}	-1.31±0.13	
		975-1150		2.4×10^{-5}	-3.56±0.13	Crushed Semi-Elements# single crystals	

(cont'd)

* The structure of this table is reproduced from Ref. 11.

+ Norton Co., Worcester, MA

Semi-Elements, Inc., Saxonburg, PA

Table 1. (cont'd)

Ref	Authors	Technique	Annealing Atmosphere	Temperature range (°C)	D_O (cm ² /sec)	Activation Energy (eV)	Samples
13	Reddy, 1979	gas/solid ¹⁸ O iso- tope exchange- proton acti- vation analysis	¹⁸ O ₂ 760-800 Torr	1310-1550	$(1.9^{+4.8}_{-1.4})$ $\times 10^{-4}$	-3.84±0.21	Mechanically polished ORNL* single crystals
15	Moriyoshi et al., 1979	Polygoni- zation of dis- locations	air	1400-1750	1.35×10^{-5}	-3.28	Mechanically polished Tateho+ single crystal sheets
16	Narayan & Washburn, 1973	disloca- tion loop shrinkage	air	1100-1427	(1.37 ± 0.26) $\times 10^{-2}$	-4.78±0.18	Muscle Shoals# single crystals

* Oak Ridge National Laboratory, TN.

+ Tateho Comp., Japan.

Muscle Shoals Electro-Chemical Corp., Tuscumbia, AL.

Table 2. Calculated Defect Energies in MgO

Processes	Enthalpy (eV)	
	Ref. 2	Ref. 3
Scottky defect formation, h_s	7.5	7.72
free cation vacancy migration, h_{m+}	2.16	2.07
free anion vacancy migration, h_{m-}	2.38	2.11
cation-anion divacancy formation, h_a	-2.55	

3. EXPERIMENTAL PROCEDURE

3.1. PREPARATION OF ^{18}O -ENRICHED MgO POWDER

^{18}O -enriched MgO powder was made by oxidizing magnesium metal in $^{18}\text{O}_2$ atmosphere. Magnesium metal ribbon* of 0.18 mm thick and 3.2 mm wide was cut into a piece of about 35 cm long, zig-zagged to about 0.5 cm wide and 3-4 cm long, and washed ultrasonically in reagent grade methanol. After being dried, it was placed on a fused-silica boat, which was in turn put into the oxidation furnace depicted in Fig. 1.

The system was then evacuated to 10^{-3} torr and purged with dry nitrogen gas of low oxygen content (less than 0.5 ppm). The process was repeated several times. The system was then baked at about 200°C at least for one hour while evacuating with a high speed mechanical pump⁺. After being cooled to the room temperature and evacuated to 10^{-3} torr again, the system was disconnected from the pump and filled with $^{18}\text{O}_2$ gas to a pressure of 40 or 50 torr. Oxygen-18 gas, purchased from Monsanto Research Corp.[#], was 99.5 mol % pure with the isotope, ^{18}O , being enriched to 95-99 atom %. The total pressure was monitored by a capsule vacuum gauge.[§]

* Mg-ribbon, MX0010, Matheson Coleman & Bell, Norwood, OH
+ Duo-Seal 1405B

Mound Laboratory, Monsanto Research Corp., Miamisburg, OH

§ Leybold-Heraeus 160 63-MB

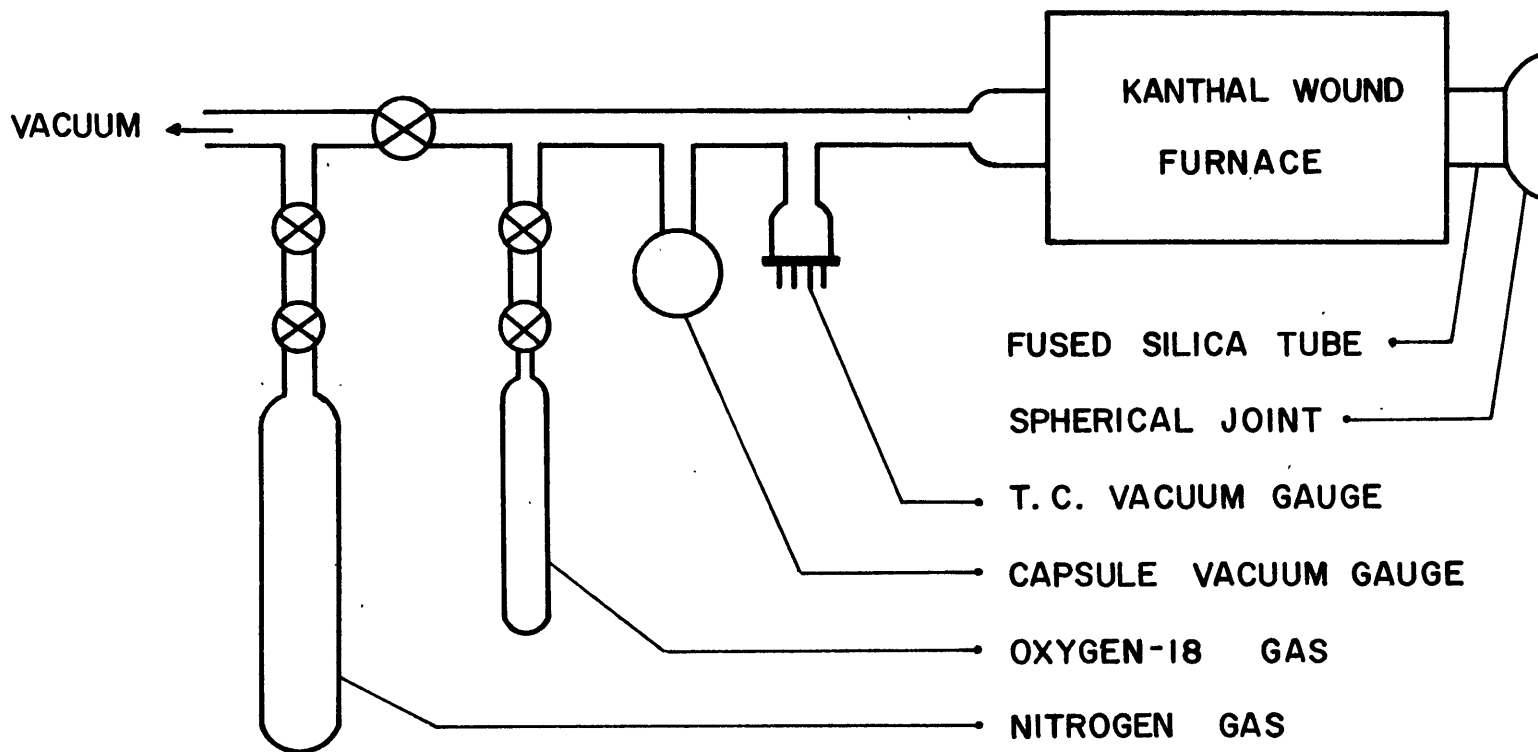


Fig. 1. Schematic of apparatus for oxidizing Mg-metal with $^{18}\text{O}_2$.

The system was then completely isolated.

Magnesium has been known to form a protective oxide film at lower temperatures while, at higher temperatures, a non-protective loose scale is formed.^{2,2-24} According to Gulbransen,^{2,2} the transition takes place at temperatures 450°C to 475°C. At 570°C or above, the metal undergoes ignition in the first few minutes.^{2,4} The oxidation was thus performed in the neighborhood of 550°C to enhance the oxidation rate while suppressing the explosive combustion. The oxidation was completed within an hour and the final pressure of the system was usually less than 1 torr. The system was open to the nitrogen gas first when the room temperature was restored.

The final product always maintained the shape of the zig-zagged metal ribbon. It was greyish-white in color. An X-ray powder diffraction pattern confirmed the presence of MgO but also indicated the presence of traces of magnesium metal in the as-oxidized product. The product was ground in an agate mortar and cold-pressed into 6.35 mm dia. × 2-3 mm pellets under a pressure of about 3000 psi for use as the source material in a closed system transport apparatus (a greyish-white pellet readily turned white on being baked out in the apparatus-see following). The pellet was subject to a semi-quantitative spectrochemical analysis. The result is given in Table 3. A large amount of silicon impurity was present which had originated probably from the tube and boat of fused silica in the oxidation furnace which was employed.

Table 3. Spectrochemical Analysis of As-PressedIsotopic MgO

Al	0.001% - 0.01%
Ca	0.001% - 0.01%
Cr	0.001% - 0.01%
Cu	<0.0001%
Fe	0.01% - 0.1%
Mg	>10.0%
Pt	0.01% - 0.1%
Si	1.0% - 10.0%
Ti	0.0001% - 0.001%

3.2. EPITAXY OF ^{18}O -ENRICHED MgO SINGLE CRYSTAL

An ^{18}O -enriched single crystal layer of MgO was grown epitaxially on a substrate of normal MgO single crystal by a chemical vapor transport method. Substrate crystals were obtained from Norton* as-cleaved on (100) to provide 17-18 mm \times 17-18 mm \times 2-3 mm plates. The purity of the crystal was reported by the vendor as in Table 4. As-received crystals were chemically polished in phosphoric acid at 150°-160°C to prepare surfaces on which the epitaxy was intended to occur. A layer of approximately 100 μm was removed from the as-cleaved surface to eliminate potential damages caused by cleaving. Substrate crystals were then washed in a dilute HCl solution and, subsequently, in distilled water to remove potential phosphates from the polished surface, and stored in reagent grade methyl alcohol.

Substrate surfaces with other surface preparations, i.e. as-cleaved and as-etched in a Stokes solution²⁵ (1 H_2SO_4 : 1 H_2O : 5 NH_4Cl saturated solution) were also utilized in other epitaxial growth experiments. It was, however, found that, in most cases, a polycrystalline material rather than a transparent epitaxial layer was deposited. Chemically-polished surfaces were thus exclusively employed in the present work.

The epitaxial growth was performed by following closely

* Norton Research Corp. (Canada) Ltd., Niagara Falls, Ontario, Canada

Table 4. Approximate Impurity Contents of Substrate Crystal*

<u>Impurities</u>	<u>Content in ppm</u>
SiO ₂	20 - 30
Fe O _{2 3}	110 - 140
TiO ₂	8 - 12
Al O _{2 3}	44 - 64
CaO	30
ZrO ₂	20
MnO ₂	3 - 25
NiO	<5
Cr O _{2 3}	2000 - 3000

* provided by Norton Co., Niagara Falls,
Ontario, Canada

a method developed by Gruber?⁶ The substrate crystal was supported over a pellet of source MgO or, in preparation of the final specimens, a cold-pressed powder pellet of ^{18}O -enriched MgO by a 15 mm diameter Pt ring. This assembly was placed in a 20 ml platinum crucible. The crucible was then closed with a snugly-fitting cover of platinum foil and suspended in a fused silica chamber as shown in Fig. 2. The chamber was then evacuated down to 10^{-5} torr and purged with dry nitrogen gas of low oxygen content (less than 0.5 ppm) several times. The contents of the crucible were baked out at the growth temperature, $1000^{\circ}C - 1100^{\circ}C$, for about 10 hours. After allowing the crucible to cool, anhydrous HCl was introduced into the chamber at 10^{-5} torr. An optimum range of HCl pressure at room temperature was found to be 20-30 torr. 40 torr seemed to be the upper limit to accomplish a successful epitaxy.

A small temperature gradient was established between the source pellet and substrate by heating the lower portion of the Pt crucible with an r.f. induction field. The temperature of the crucible bottom, as measured by an optical pyrometer, was kept almost constant at a temperature of $1000^{\circ}C$ to $1100^{\circ}C$. The rate of epitaxial growth on the substrate depends on temperature, temperature gradient, the partial pressure of HCl in the growth chamber, and the source-to-substrate separation. For certain conditions, growth rates of up to $100 \mu m/hr$ were once achieved, a rate equal to that reported by Gruber?⁶ By reducing the source-

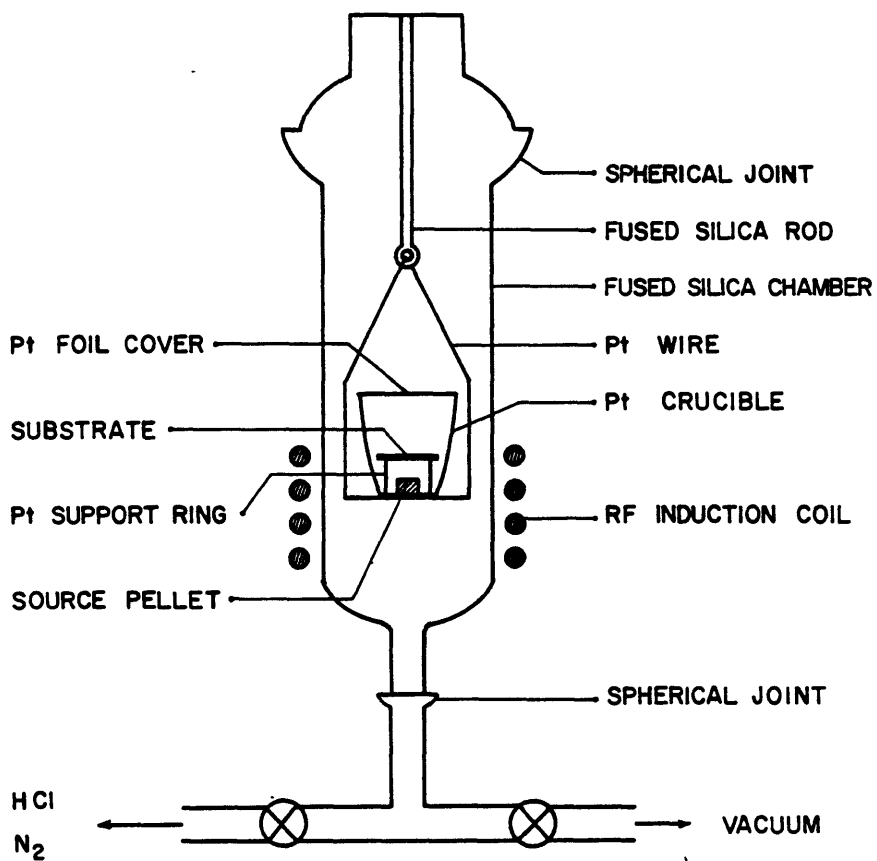


Fig. 2. Schematic of apparatus for Mg^{18}O chemical transport in HCl .

to-substrate distance to a few millimeters and by adjusting the position of the *Pt* crucible assembly in the induction coil, the epitaxial isotopic layers of the best quality were grown to a thickness of ~3 to ~50 μm in 10 minutes to 3 hours. The surfaces of these layers were observed to bear an irregular distribution of pits, but were used directly in the as-grown state for the exchange experiments in order to avoid mechanical damage or contamination by impurities.

Gruber²⁶ has shown that the chemical vapor transport is accompanied by a very high degree of perfection of the epitaxial layer in terms of dislocation densities and also leads to the purification with respect to most of the impurities in the source MgO . In particular, the reduced incorporation of Cl (less than 10 ppm) compared with that of the source (20 ppm) is noteworthy because the contamination by the transporting agent, HCl , had been feared. Si and Fe , however, have been shown to be preferentially transported. With this consideration, the as-grown layer of Mg^{18}O apparently contains the cationic impurities transported from the source pellet of Mg^{18}O powder (see Table 3). These impurities are enough to suppress the intrinsic transport behavior in the epitaxial layer. For a qualitative identification of the impurities in the layer, a secondary-ion mass spectrum was taken with help of SIMS* by sputtering the as-grown surface with a primary beam of oxygen negative ions. The result is shown in Fig. 3.

* CAMECA ims 3f ion microprobe, located at the Department of Earth and Planetary Science of M.I.T.

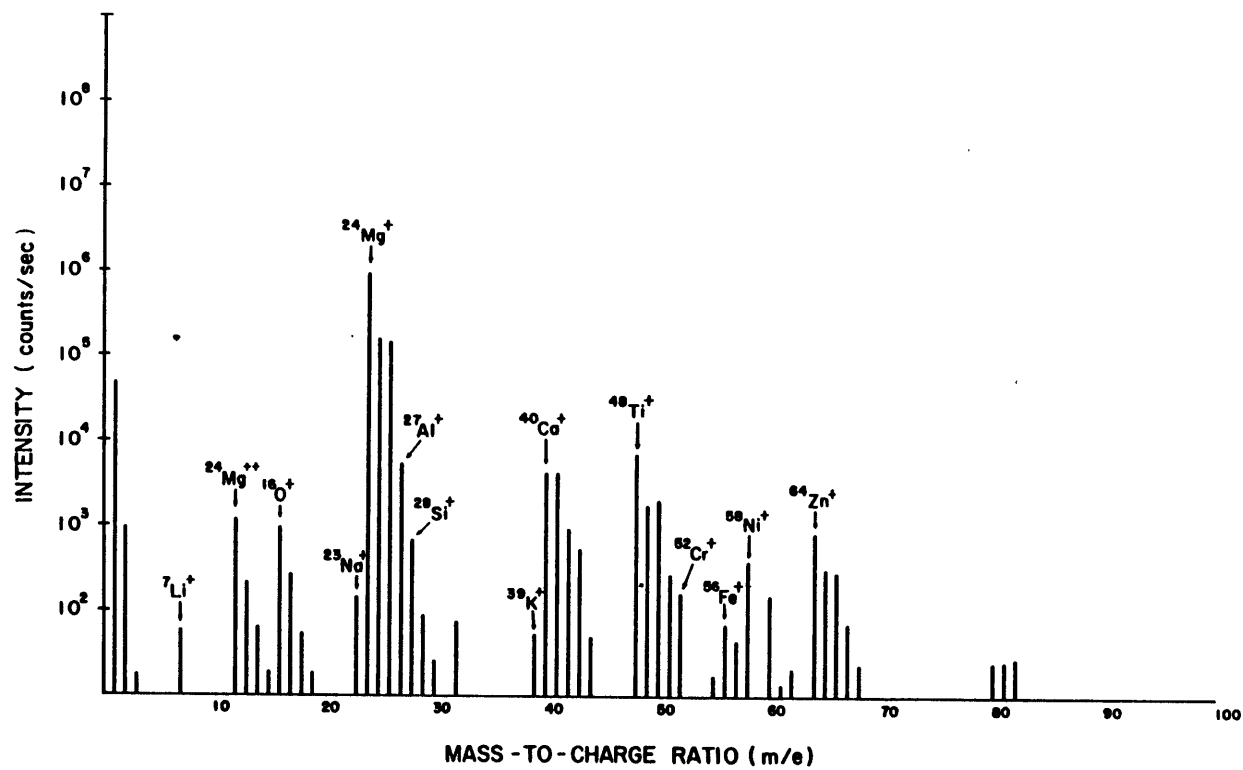


Fig. 3. Secondary-ion mass spectrum for the epitaxial layer of Mg^{18}O bombarded with oxygen at 11.5 KeV.

An absolute quantitative analysis of the impurity contents is not feasible from the intensities of secondary ions because the ionization yields from the common matrix MgO are not known for each kind of the impurities displayed in Fig. 3. From Fig. 3 and Table 3 in association with the enthalpy for the Schottky defect formation, 7.5 eV (see Chapter 2), however, it is safe to conclude that the epitaxially-grown crystal of $Mg^{18}O$ is infested mainly with the aliovalent cationic impurities of higher valence and that the crystal is apparently extrinsic in its defect structure.

Three different pieces of as-grown crystals, designated respectively as R27, R29 and R31, were cut by a low speed saw* along 100 planes normal to the growth front to provide diffusion samples carrying an epitaxial isotope deposit of about $4 \times 4 \text{ mm}$ area. 5 to 9 such diffusion samples could be made out of each piece. From SIMS in-depth profiling described in Chapter 4, the initial abundances of ^{18}O in atomic % $Mg^{18}O$ were found to be 7-10%, 8-14%, and 34-53%, respectively, for R27-, R29-, and R31- series diffusion samples (see for details Table 2.1. of Appendix 2).

3.3. DIFFUSION ANNEAL

Substrate crystals bearing the as-grown isotope deposit were annealed in an air atmosphere at temperatures in the range $1000^{\circ} - 1650^{\circ}C$. To minimize the possibility of contamination during the annealing, specimens were placed in a Pt

* Isomet[®] Low Speed Saw, VWR Scientific Inc.

envelope with an open end. Based on the earliest oxygen diffusion data¹ by Oishi and Kingery, the duration of the annealing was selected to produce a concentration gradient on the order of 1 μm in depth for subsequent in-depth profiling with SIMS.

Unlike the conventional gas/solid ^{18}O exchange technique, the minor isotope ^{18}O (0.2% natural abundance) diffused out of the sample to be replaced by the predominant ^{16}O isotope contained in air. The gas reservoir from which exchange occurs with the sample is thus essentially infinite and problems of change in isotopic composition of the atmosphere as exchange progresses are not encountered. In the conventional gas/solid ^{18}O exchange method used for the measurement of oxygen-diffusion in MgO , a gas reservoir of limited volume must be assumed to be infinite in its size and constant in its composition during diffusion annealing. Gas-exchange with components of the system must be assumed to be negligible if the amount of exchange is to be monitored by measurement of the composition of the atmosphere. As a concentration gradient in the sample is directly determined by SIMS analysis, rather than monitoring the isotopic composition of the atmosphere or the total amount of ^{18}O diffused into the specimen, the low exchange rate at reduced temperature is a less constraining influence. It is not necessary to contain a small volume of atmosphere at a fixed composition of special isotope. Long diffusion annealings may be employed without difficulty.

A unique aspect of the procedure is that two diffusion coefficients may be determined from each sample: one from the exchange gradient at the free surface of the isotopic layer (constant surface concentration boundary conditions) and the other from the gradient produced by interdiffusion between the isotopic epitaxial layer and substrate crystal (The times and temperatures are sufficiently low that negligible interdiffusion occurs during deposition of the epitaxial layer of isotopic material and semi-infinite source initial conditions apply. For a layer grown in 10 minutes at 1000-1100°C, the diffusion zone at the interface is about $8\sqrt{Dt}$ wide, or 30 Å at worst.). One can thus compare exchange diffusion coefficients and tracer interdiffusion coefficients for the same sample and thereby assess the possible influence of gas-exchange reaction rate, sample vaporization or surface flaws on diffusion coefficients measured by exchange.

3.4. MEASUREMENT OF ^{18}O CONCENTRATION GRADIENTS

The distribution of isotopes in the annealed specimens was determined by in-depth profiling sputtering with a CAMECA ims 3f ionmicroprobe*. The primary ion beam was $^{40}Ar^+$ accelerated to 9.65 ± 0.01 KeV for all of the surface exchange profiles with a few exceptions (see Table 2-2 in Appendix 2). The intensity of the positive secondary ions $^{16}O^+$, $^{18}O^+$, and

* A national facility located at the Center for Microanalysis of Materials in the Materials Research Laboratory at the University of Illinois.

$^{24}\text{Mg}^{2+}$ was measured. The primary beam was rastered over a $250 \times 250 \mu\text{m}$ area during irradiation, but a mechanical aperture was used to restrict the area which contributed to the measured intensity to a central area of $150 \mu\text{m}$ diameter in order to minimize artifacts arising from edge effects and redeposition of material.^{2,7-32} The problems caused by charging of an insulator surface under bombardment by the incident ion beam were almost completely eliminated in the present work by the deposition of a 300 \AA gold film on the sample surface and by flooding the sputtered area of the surface with an appropriate number of electrons. Determination of the proper electron flux and maintenance of the flux at the correct location was quite laborious. An interpretation of the charge neutralization process has been provided by several authors.³³⁻³⁶

An estimate of the sputtering rate was used to establish the time necessary to remove a layer of desired depth. This thickness (10 to 80 \AA) in turn was based on the total number of concentration measurements desired within the anticipated extent of the concentration gradient. The intensity accumulated during this time interval was stored in a multichannel analyzer. After completion of the analysis, the total depth, d_0 , of the sputtered crater was measured with a profilometer.* Most of the crater depths could be measured to within a 10% relative error at the 100% confidence level. A few measure-

* Sloan Dektak Surface Profile Measuring System

ments, however, were subject to an error as high as 50%. This was usually due to the inadvertent selection for analysis of a locally-rough area of the original specimen surface. As the sputtering rate for a homogeneous single-crystalline matrix remained constant within reasonable uncertainty for a prefixed primary accelerating voltage,^{2,8-30} an attempt was made to average the uncertainty in crater depth over the entire set of analyses. This was done by plotting for each sample the measured crater depth, d_0 , per primary ion beam current, I_p , as a function of sputtering time, t . Normalization by the total current rather than current density is justified as the irradiated sample area was kept constant in all analyses. Fig. 4 shows the relation to be linear and the results may be satisfactorily represented by the equation,

$$d/I_p = (1.3 \pm 0.2) \times 10^{-10} t + (3.2 \pm 0.7) \times 10^{-7} \text{ cm/nA.}$$

Eq. 1

Since the primary beam current, I_p , had been well stabilized and the sputtering time, t , had been subject to a negligible uncertainty, Eq. 1 rather than the measured value was used to evaluate a corrected total crater depth, d , for a given experiment. The thickness of each layer sputtered from the sample was thus provided by

$$\Delta x = d / N,$$

Eq. 2

where N is the total number of channels in each run.

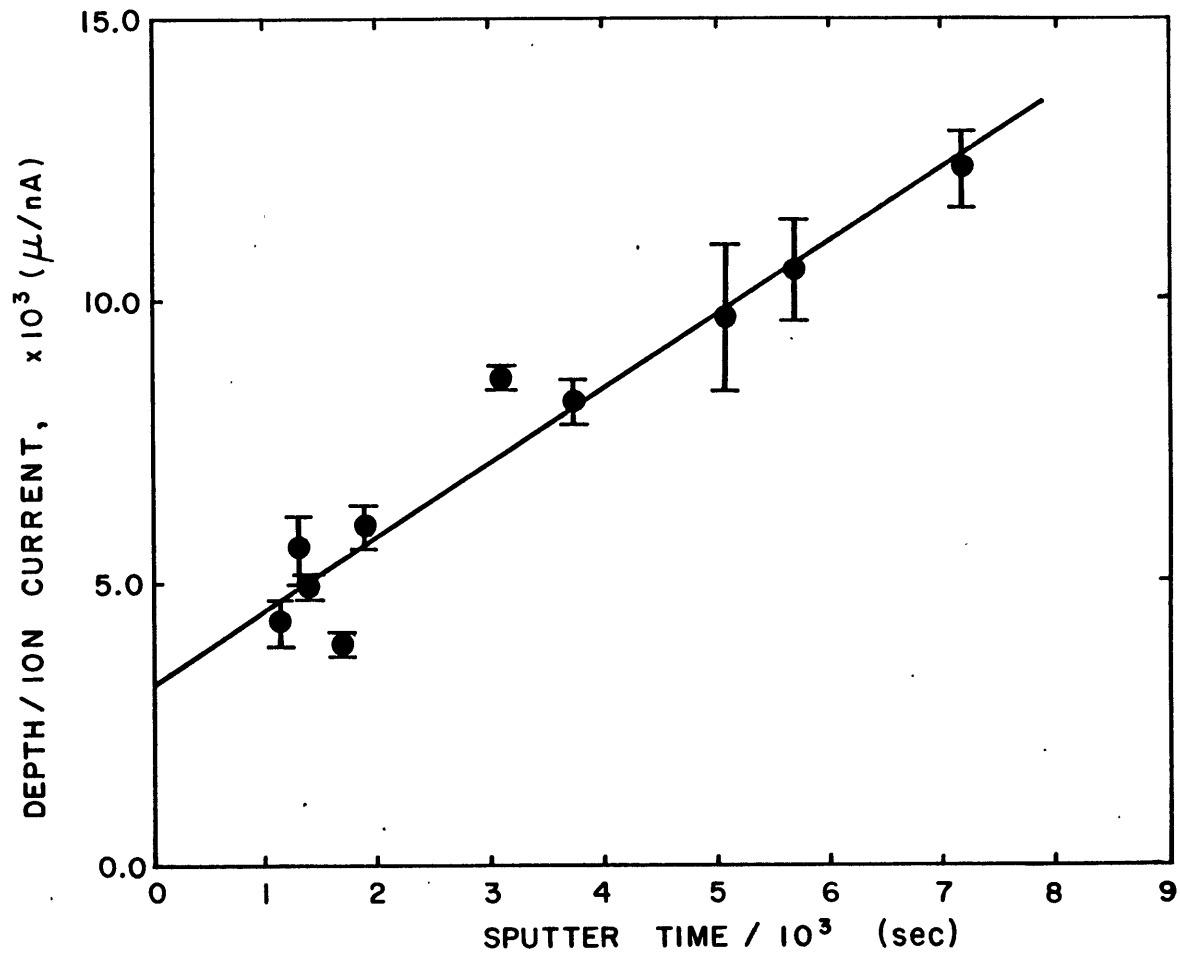


Fig. 4. Crater depth per unit primary ion current as a function of sputtering time for MgO irradiated by a 9.65 KV ⁴⁰Ar⁺ primary ion beam.

4. RESULTS

4.1. GAS-EXCHANGE

4.1.1. EXPECTED DIFFUSION PROFILES

For the gas/solid diffusion couple in question, namely $(^{16}\text{O}_{1-X_0} \ ^{18}\text{O}_{X_0})_2$ (in air, 0.21 atm) / $\text{Mg} (^{16}\text{O}_{1-X_\delta} \ ^{18}\text{O}_{X_\delta})$ where $X_0 = 0.002039$ is the natural abundance of ^{18}O and X_δ is the artificial enrichment of ^{18}O in the epitaxial layer, the ^{18}O exchange reaction rate at the surface or at the phase boundary must, in general, be brought under consideration since it can be a rate-controlling step of the overall gas exchange kinetics. The simplest reasonable assumption is that the rate of exchange is directly proportional to the difference between the actual concentration C' on the surface, where $x = 0$, at any time and the concentration C_0 which would be in equilibrium with the $^{18}\text{O}_2$ partial pressure in the atmosphere remote from the surface or a quasi-chemical exchange reaction of the first order at the phase boundary. Mathematically this means that the boundary condition at the surface⁵ is

$$-D \left. \frac{\partial C}{\partial x} \right|_{x=0} = k(C' - C_0), \quad \text{Eq. 3}$$

where k is the reaction constant, D is the oxygen diffusion coefficient, and C is the concentration of ^{18}O in the

isotope-enriched layer. If the concentration of ^{18}O in the semi-infinite medium is initially C_s throughout or

$$C(x > 0 ; t = 0) = C_s \quad \text{Eq. 4}$$

and the surface exchange is determined by Eq. 3, the ^{18}O concentration profile will be represented by⁵

$$\frac{C - C_0}{C_s - C_0} - \exp\left(\frac{k^2 t}{D} - \frac{kx}{D}\right) \operatorname{erfc}\left(\frac{x}{2\sqrt{Dt}} - k\sqrt{\frac{x}{D}}\right) = \operatorname{erfc}\left(\frac{x}{2\sqrt{Dt}}\right).$$

Eq. 5

In this expression, D is assumed to be independent of composition. The isotopic effect is not considered here and hence it is justified that D is independent of ^{18}O concentration. If the gas exchange reaction is very fast or the equilibrium is instantaneously established at the phase boundary so that the surface concentration of ^{18}O is kept at its natural abundance C_0 , then Eq. 5 may be rewritten as

$$\frac{C - C_0}{C_s - C_0} = \operatorname{erfc}\left(\frac{x}{2\sqrt{Dt}}\right). \quad \text{Eq. 6}$$

For the present system which is chemically and physically homogeneous, the concentration of ^{18}O , C , may be replaced by the corresponding mole fraction, X , since the molar volume does not change with ^{18}O concentration. If we neglect the isotope fractionization effect,^{37, 38} the mole fraction of ^{18}O

at a certain depth or the n th channel can be expressed in terms of ^{16}O and ^{18}O intensities measured at the same channel, $^{18}I(n)$ and $^{16}I(n)$, as

$$X(n) = \frac{^{18}I(n)}{^{16}I(n) + ^{18}I(n)} . \quad \text{Eq. 7}$$

The initial enrichment, X_{δ} , is similarly obtained from those intensities measured in the bulk, $^{16}I_{\delta}$ and $^{18}I_{\delta}$. As the equilibrated surface concentration, the natural abundance 0.0020 is taken. Thus in Eq. 5 and Eq. 6,

$$\frac{C(n) - C_0}{C_{\delta} - C_0} = \frac{[^{18}I(n) / \{^{16}I(n) + ^{18}I(n)\}] - 0.0020}{[^{18}I_{\delta} / \{^{16}I_{\delta} + ^{18}I_{\delta}\}] - 0.0020} . \quad \text{Eq. 8}$$

A diffusion depth, x , in Eq. 5 or Eq. 6 is converted into the sputtering time or number of channels, n , with the use of a unit channel thickness, Δx , determined by Eq. 2 or

$$x = n\Delta x. \quad \text{Eq. 9}$$

If a surface exchange reaction rate competes with the diffusion rate of ^{18}O and the second term on the left-hand-side of Eq. 5 is thus appreciable relative to the first term, a plot of $\exp^{-1}(C - C_0)/(C_{\delta} - C_0)$ as a function of x will not be linear but, rather, will display curvature. As will be shown later, however, all such plots obtained in the present

work are linear with higher correlation coefficients. This implies that the contribution of the exchange rate to the overall kinetics is negligible or at least not noticeable within the experimental error of the concentration measurement. This fact will be reconfirmed in Section 4.2. Eq. 6, combined with Eq.'s 8 and 9, thus provides as a good estimation of a sputtering profile,

$$\frac{[{}^{18}\text{I}(n)/\{{}^{16}\text{I}(n)+{}^{18}\text{I}(n)\}]-0.0020}{[{}^{18}\text{I}_\delta/\{{}^{16}\text{I}_\delta+{}^{18}\text{I}_\delta\}]-0.0020} = \text{erf}\left(\frac{\Delta x}{2\sqrt{D}\bar{x}} \cdot n\right).$$

Eq. 10

A diffusion coefficient may then be determined from the slope of a plot, the inverse error function of the left-hand-side of Eq. 10 as a function of the channel number, n . If we let A be the slope or

$$y = A \cdot n \quad \text{Eq. 11}$$

where

$$y \equiv \text{erf}^{-1} \frac{[{}^{18}\text{I}(n)/\{{}^{16}\text{I}(n)+{}^{18}\text{I}(n)\}]-0.0020}{[{}^{18}\text{I}_\delta/\{{}^{16}\text{I}_\delta+{}^{18}\text{I}_\delta\}]-0.0020},$$

then the diffusion coefficient will be provided by

$$D = \frac{1}{\bar{x}} \left(\frac{\Delta x}{2A} \right)^2 \quad \text{Eq. 12}$$

4.1.2. EXPERIMENTAL DEPTH PROFILES

An example of a measured in-depth profile is provided in Fig. 5. This specimen, designated as R31-1300-2, which had been diffusion-annealed at $1301 \pm 1^\circ\text{C}$ for 2.682×10^5 seconds with an uncertainty of less than 120 seconds, was sputtered by rastering an $^{40}\text{Ar}^+$ primary beam of 51.0 nA, 9.65KV. The secondary ions $^{24}\text{Mg}^{2+}$, $^{16}\text{O}^+$, $^{18}\text{O}^+$, and $^{197}\text{Au}^+$ were counted for 1 second each. The measured depth of the sputtered crater was $d_0 = 2.3 \pm 1.1 \text{ K\AA}$, which was corrected to $d = 2.5 \pm 0.7 \text{ K\AA}$ according to Eq. 1. A channel thickness is thus $\Delta x = (1.7 \pm 0.5) \times 10^{-7} \text{ cm/ch}$ since the total number of channel is $N = 150$ in Eq. 2. The variation of intensity with channel number, shown in Fig. 5, was converted to a plot of concentration as a function of penetration according to Eq. 7. The result is shown in Fig. 6. The initial enrichment or bulk concentration of ^{18}O was determined from the intensities measured beyond the diffusion zone or at channel numbers greater than 100 in this case, by means of either

$$X_{\delta} = \frac{\sum_{n=101}^{150} {}^{18}\text{I}(n)}{\sum_{n=101}^{150} \{ {}^{16}\text{I}(n) + {}^{18}\text{I}(n) \}} \quad \text{Eq. 13}$$

or

$$X_{\delta} = \frac{1}{150} \sum_{n=101}^{150} \frac{{}^{18}\text{I}(n)}{{}^{16}\text{I}(n) + {}^{18}\text{I}(n)} \quad \text{Eq. 14}$$

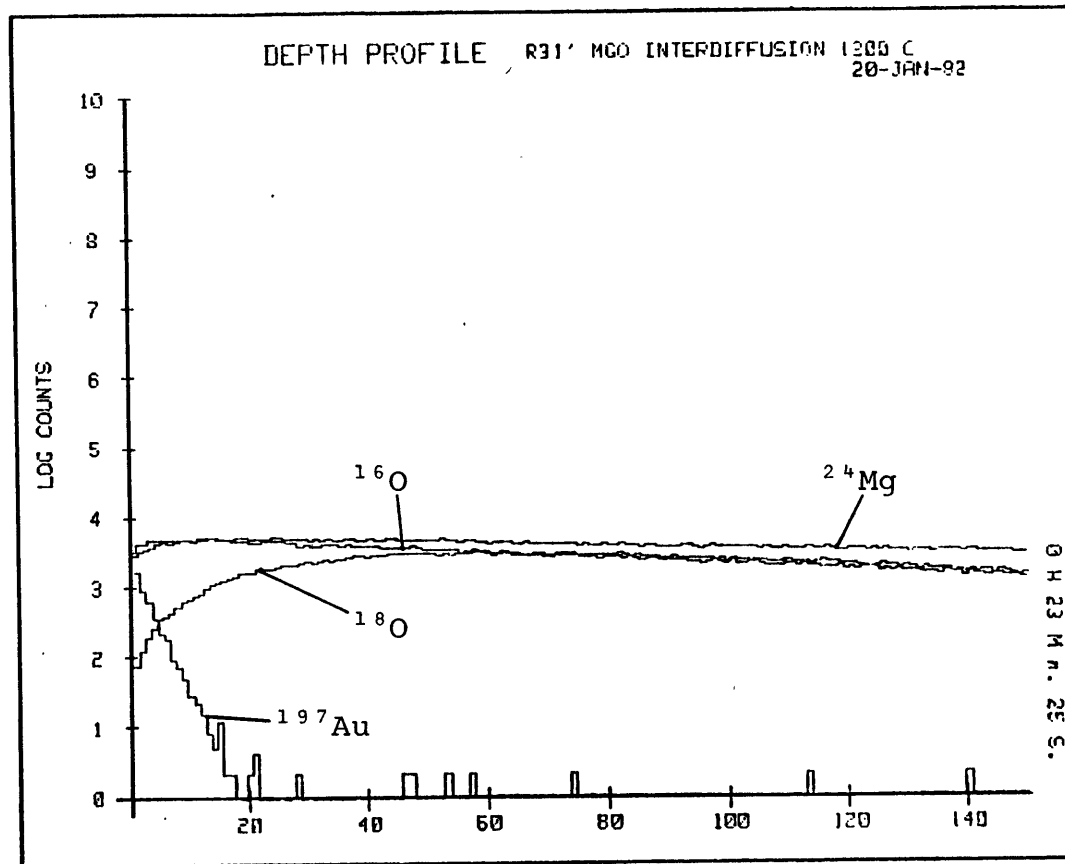


Fig. 5. Measured SIMS depth profile for ^{18}O , ^{16}O , ^{24}Mg , and ^{197}Au in a layer of isotopically enriched single-crystal MgO after gas exchange for 74.5 hr at 1300°C with $^{16}\text{O}_2$ in air. Primary beam: rastering $^{40}\text{Ar}^+$, 51 nA, 9.65 KV.

Equation 13 and Eq. 14 yield, of course, the same result within the experimental error which is estimated on the basis of counting statistics.^{39,40} The initial enrichment, X_s , was found to be 0.5253 (expressed as atomic fraction Mg^{180}) for the present specimen, R31-1300-2. The surface concentration, X_0 , was arbitrarily taken as the natural abundance, 0.0020, as already pointed out. The profile in Fig. 6 may then be represented by the equation,

$$\frac{X(n) - 0.0020}{0.5253 - 0.0020} = \operatorname{erf}\left(\frac{\Delta x}{2\sqrt{Dt}} \cdot n\right), \quad \text{Eq. 15}$$

where $X(n)$ is given by Eq. 7.

A plot of the inverse error function of Eq. 15 against the number of channels, n , is shown in Fig. 7. A slope of the plot, A , was obtained by a linear-squares method as

$$A = 0.0224 \pm 0.0003$$

and a linear correlation coefficient, r , was obtained as

$$r = 0.996,$$

for the set of data, $\{n, \operatorname{erf}^{-1}[(C - C_0)/(C_s - C_0)]\}$ where $1 \leq n \leq 50$. The high value of the correlation coefficient, as "an indicator of how well a set of data fits a straight line"⁴⁰ implies that ^{180}Mg exchange reaction at the surface is not

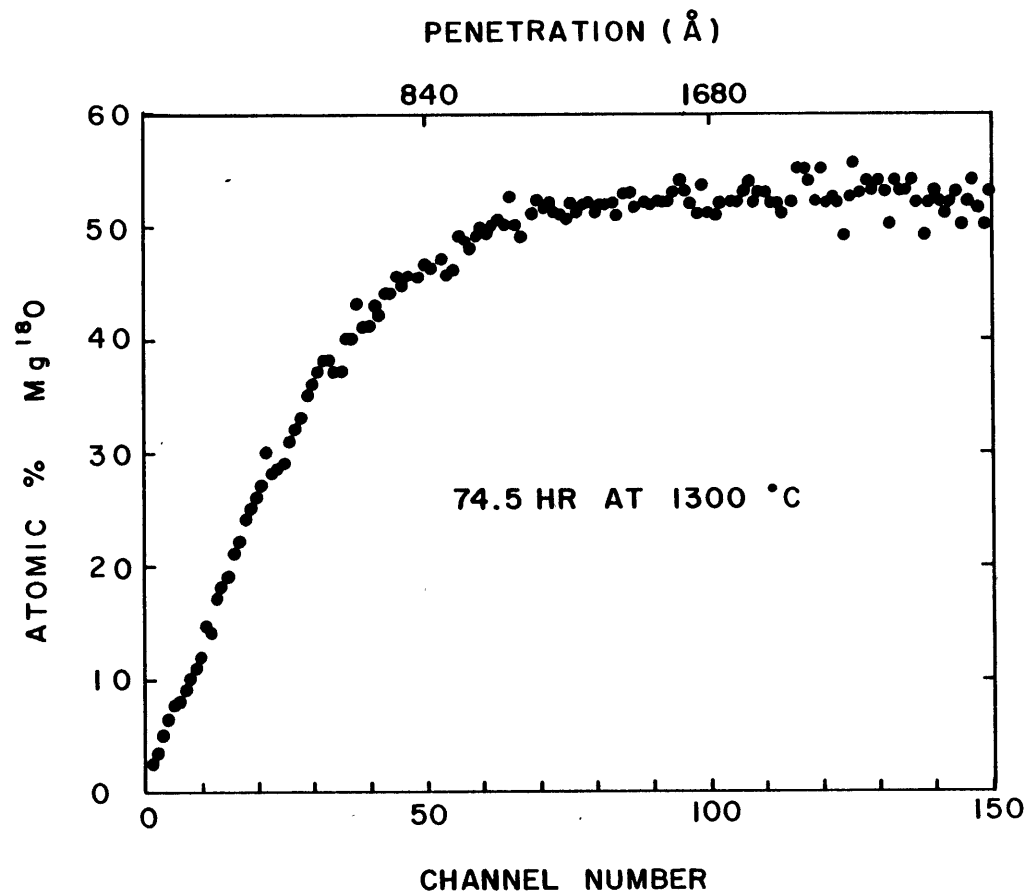


Fig. 6. Plot of the atomic fraction $Mg^{18}O$ as a function of penetration, derived from Fig. 5.

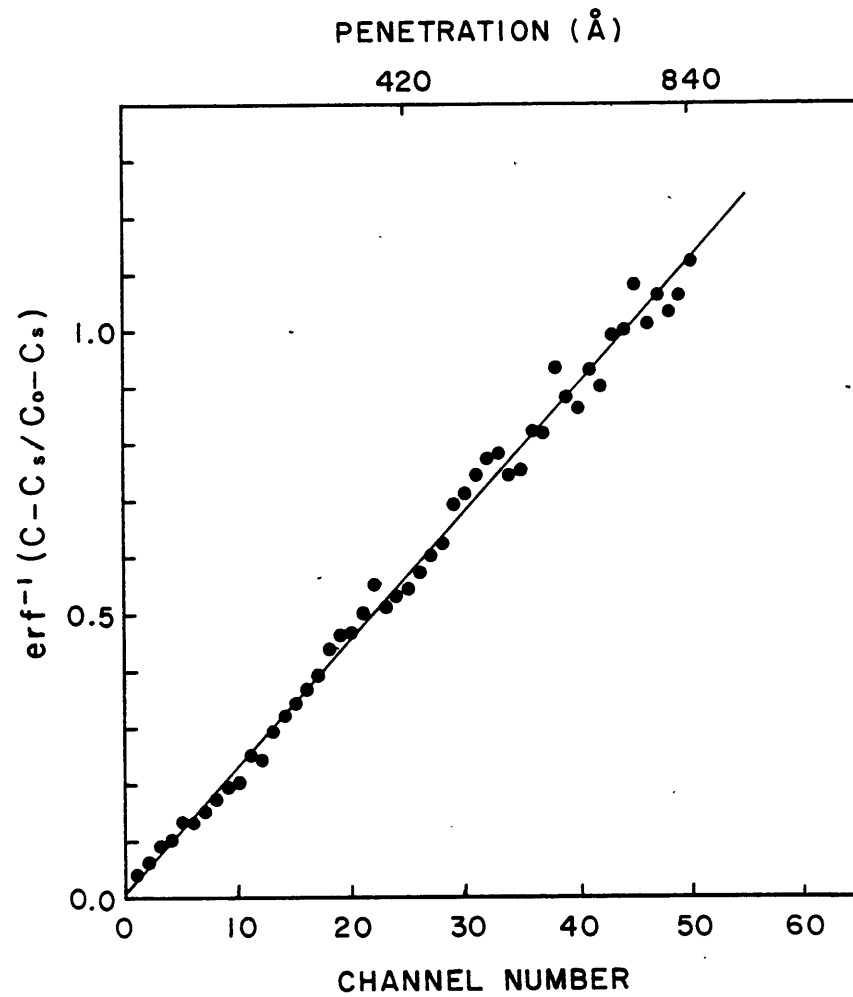


Fig. 7. Plot as a function of penetration of the inverse error function of the ratio of atomic fraction Mg^{18}O less surface concentration to initial atomic fraction less surface concentration.

rate-controlling at least within the present experimental error. If the surface reaction were competitive with the diffusion, a plot such as the one in Fig.7 would not be a straight line and accordingly the correlation coefficient would be far smaller. An experimental error associated with concentration measurement is, in turn, reflected in the standard deviation of the slope, $\sigma_A = 0.0003$. In the present work, the relative error of the slope is only on the order of 1 % for most cases. A diffusion coefficient is extracted from the slope, $A = 0.0224$, along with a channel thickness, $\Delta x = 1.7 \times 10^{-7}$ cm/ch, and diffusion annealing time, $t = 2.682 \times 10$ sec. Using Eq. 12, the diffusion coefficient, D , for the specimen, R31-1300-2, is calculated as

$$D = (5.2 \pm 2.9) \times 10^{-17} \text{ cm}^2/\text{sec.}$$

The uncertainty associated with a diffusion coefficient has been propagated from errors associated with a slope, A , annealing time, t , and a unit channel thickness, Δx . For the present work, it has been found that the major error source is the measurement of the final depth of the sputtered crater or, in other words, the value of a unit channel thickness. This uncertainty is attributed to the roughness of the as-grown surface. An analysis of the propagation estimated errors will be discussed in Appendix 1.

All the other specimens were analyzed similarly. All experimental profiles and their inverse error function plots

are collected in Appendix 2. The standard deviation of the slope was found to vary between 1 % and a maximum of 20 % but, as previously noted, with a correlation coefficient always no smaller than 0.98 (see Appendix 2).

4.1.3. DIFFUSION COEFFICIENTS

The average diffusion coefficient determined at each temperature in the present work is listed in Table 5 along with the representative conditions under which these values were obtained. When multiple analyses were performed on a given sample, the resulting diffusion coefficients have been combined into an average weighted according to the individual standard deviations as described in Appendix 2. A plot of the logarithm of the diffusion coefficient as a function of reciprocal temperature is presented in Fig. 8: the error bars, however uncosmetic, represent the standard deviations of Table 5, based on realistic assessment of error discussed in Appendix 1. As the uncertainty of the temperature measurements is considered negligible compared with the uncertainty in the diffusion coefficients, and because the relative standard deviations of D are comparable to each other in magnitude (the average relative standard deviation, $\overline{\sigma_D/D} = 0.4$), equal weights were assigned to each measurement in determining a least-squares fit⁴⁰ to the data of Fig. 8 and Table 5. The best estimate of D is expressed by

$$\ln D_{best} = -(13.22 \pm 0.96) - \frac{3.24 \pm 0.13 \text{ eV}}{kT},$$

Table 5. Oxygen Self-Diffusion Coefficients
in Single Crystal MgO

<u>T (°C)</u>	<u>Annealing Time (hr)</u>	<u>Extent of Gradient* (× 1000 Å)</u>	<u>D (cm²/sec)</u>	<u>σ_D/D</u>
1650	2.0	1.2	$(5.2 \pm 2.7) \times 10^{-15}$	0.52
1600	3.0	1.6	$(5.9 \pm 2.3) \times 10^{-15}$	0.39
1550	4.7	1.0	$(1.4 \pm 0.8) \times 10^{-15}$	0.57
1500	4.0	1.0	$(1.6 \pm 0.7) \times 10^{-15}$	0.44
1400	12.0	0.8	$(3.7 \pm 1.6) \times 10^{-16}$	0.43
1300	74.5	0.8	$(5.6 \pm 2.4) \times 10^{-17}$	0.43
1200	360.0	0.7	$(1.0 \pm 0.4) \times 10^{-17}$	0.40
1100	480.0	0.4	$(1.9 \pm 0.5) \times 10^{-18}$	0.26
1000	960.0	0.3	$(4.5 \pm 1.0) \times 10^{-19}$	0.22

* Approximate penetration to a value of erf^{-1} of ca. 1.0

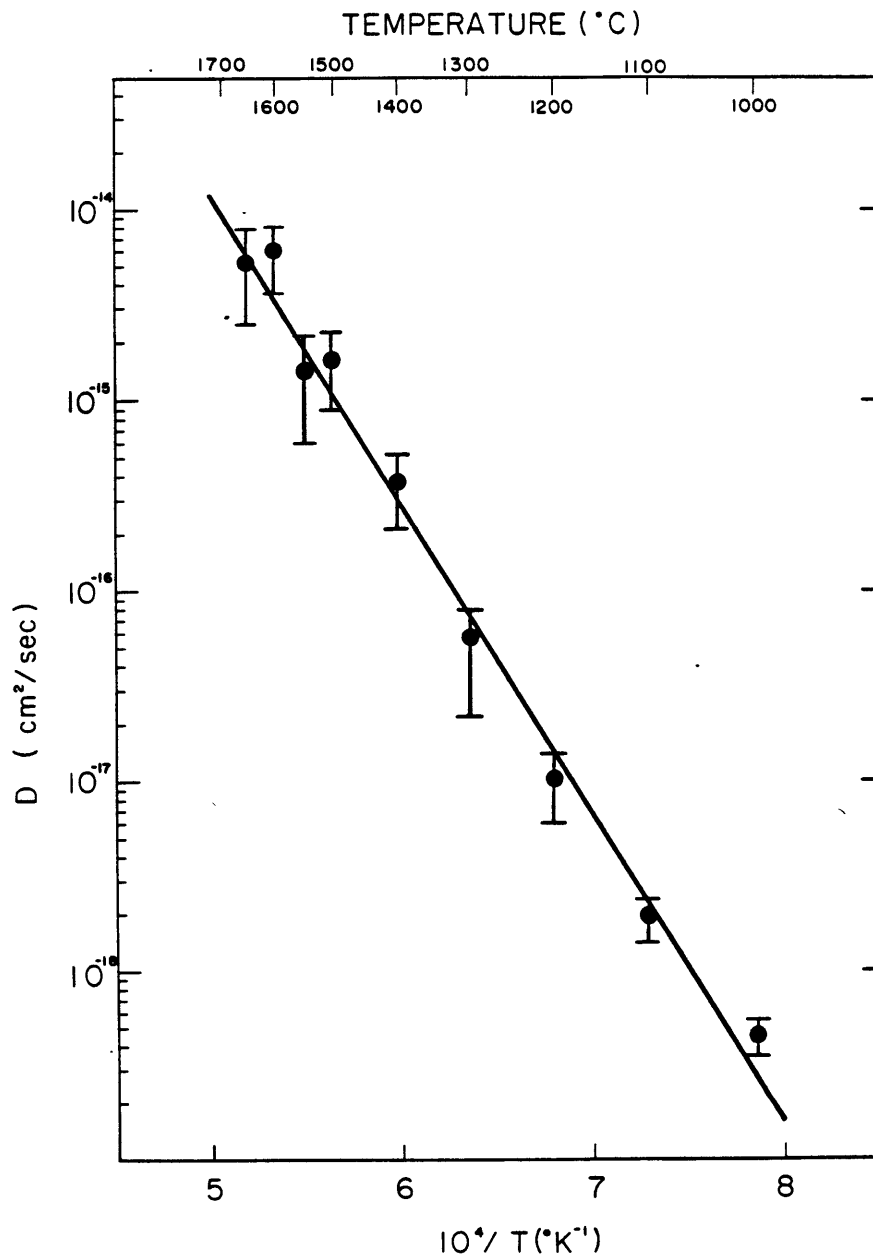


Fig. 8. Plot of the logarithm of the diffusion coefficients for ^{18}O in single crystal MgO as a function of reciprocal temperature.

or

$$D_{best} = (1.8_{-1.1}^{+2.9}) \times 10^{-6} \exp\left(-\frac{3.24 \pm 0.13 \text{ eV}}{kT}\right) \text{ cm}^2/\text{sec}$$

Eq. 16

over a temperature range, $1000^\circ\text{C} \leq T < 1700^\circ\text{C}$. The linear correlation coefficient of the set $\{1/T, \ln D\}$ is -0.989 . A diffusion coefficient specified by Eq. 16 is precise within a factor of approximately 2 (see Appendix 1). That is,

$$\frac{\sigma_D}{D_{best}} \sim 2.$$

Eq. 17

4.2. ISOTOPIC INTERDIFFUSION

4.2.1. EXPECTED DIFFUSION PROFILES

In our solid/solid isotope-intermixing system, $Mg(^{16}O_{1-X_\delta}^{18}O_{X_\delta})/Mg(^{16}O_{1-X_0}^{18}O_{X_0})$ where X_δ is again the artificial enrichment of ^{18}O in the epitaxial layer and X_0 the natural abundance, 0.002039, the two halves may be regarded as two semi-infinite media for annealings of an appropriately short time scale. If the initial distribution of ^{18}O satisfies the conditions,

$$\begin{aligned} X(x < 0 ; t = 0) &= X_\delta \quad (\text{in the epitaxial layer}) \\ X(x > 0 ; t = 0) &= X_0 \quad (\text{in the substrate}), \end{aligned} \quad \text{Eq. 18}$$

the intermixing profile will then be

$$\frac{X - X_0}{X_\delta - X_0} = \frac{1}{2} \operatorname{erfc}\left(\frac{x}{2\sqrt{Dt}}\right). \quad \text{Eq. 19}$$

Similar to the analysis provided for gas-exchange profile, diffusion depth, x , and the normalized concentration, i.e. the left-hand-side of Eq. 19, are replaced by Eq. 9 and Eq. 8, respectively, to yield a sputtering profile,

$$\frac{[^{18}I(n)/\{^{16}I(n)+^{18}I(n)\}] - 0.0020}{[^{18}I_\delta/\{^{16}I_\delta+^{18}I_\delta\}] - 0.0020} = \frac{1}{2} \operatorname{erfc}\left(\frac{\Delta x}{2\sqrt{Dt}} \cdot n\right). \quad \text{Eq. 20}$$

A diffusion coefficient, D , is then extracted from the slope, A , of $\operatorname{erfc}^{-1} 2(X-X_0)/(X_\delta-X_0)$ or $\operatorname{erfc}^{-1} [1-2(X-X_0)/(X_\delta-X_0)]$ as a function of n using the earlier expression of Eq. 12,

$$D = \frac{1}{t} \left(\frac{\Delta x}{2A} \right)^2.$$

For several possible reasons, however, an experimental measurement of the initial distribution of ^{18}O is likely to appear to have a finite spread rather than a well-defined step function, Eq. 18, across the interface between the isotope-enriched epitaxial layer and the substrate. Such a distribution could possibly arise from initial diffusion during the epitaxial deposition, interface roughness, and resolution limitations inherent to the profiling technique. In either of these cases, Eq. 19 generally ceases to represent a realistic description of the experimental sputtering profile. Even if a profile after diffusion anneal were to appear to be an erfc function, what one would obtain from the slope, A , is not the actual diffusion coefficient which is responsible for the spread during the diffusion anneal but an apparent diffusion coefficient representing the overall spread of the profile at the interface.

Hall and Morabito⁴¹ have developed a formalism for the deconvolution of the true diffusion profile from a measured distribution broadened by instrumental or experimental artifacts. The analysis is applicable to the extent to which the measured profiles before and after diffusion anneal can

be fitted by $erfc$ functions. The analysis is based on the fact that, when a gaussian diffusion process is observed with an instrument whose response function is also gaussian, the convoluted profile is also gaussian. Ho and Schuele⁴² have shown that the observed broadening in this case is given by the square root of the sum of the squares of the broadening due to diffusion and the broadening due to the resolution of the instrument, or

$$G_{obs}^{-2} = G_{diff}^{-2} + G_{resol}^{-2}$$

where G is the gradients of the normalized concentration profiles e.g. $\frac{d}{dx}(\frac{X-X_0}{X_s-X_0})$ in Eq. 19. According to Hall and Morabito,⁴¹ other broadening effects such as interface roughness will also add the same way provided the influence of these effects is also gaussian. If they are significantly non-gaussian, their convolution will be affected and the observed profiles will also not be gaussian. Thus to the extent to which the observed profiles are gaussian, we have

$$G_{obs}^{-2} = G_{diff}^{-2} + G_{init\ diff}^{-2} + G_{resol}^{-2} + G_{rough}^{-2} \quad \text{Eq. 21}$$

The deconvolution is then a simple subtraction,

$$G_{diff}^{-2} = [G_{obs}^{-2}]_{t=t} - [G_{obs}^{-2}]_{t=0} \quad \text{Eq. 22}$$

The deconvolution is valid for all concentration if all the functions are $erfc$ and it is valid for $(X-X_0)/(X_\delta-X_0) = 0.5$ in Eq. 19. Due to Eq. 19, the gradient at the interface ($x=0$) would be

$$G = - (4\pi Dt)^{-\frac{1}{2}}, \quad \text{Eq. 23}$$

if the concentration profile were an $erfc$ function extrapolated from the region where the $erfc$ fitted well. $[G_{obs}]_{t=t}$ is then equated to the diffusion coefficient which is obtained from the slope of the plot, $erfc^{-1} 2 \left(\frac{X-X_0}{X_\delta-X_0} \right)$ vs. n corresponding to the region where the measured profile after the diffusion anneal is fitted by the $erfc$ function, and $[G_{obs}]_{t=0}$ to the diffusion coefficient obtained from the corresponding region of the initial profile taken before the diffusion anneal. In view of Eq. 12 and Eq. 23, Eq. 22 will then be rewritten as

$$\frac{1}{(A/\Delta x)_{t=t}^2} - \frac{1}{(A/\Delta x)_{t=0}^2} = 4Dt, \quad \text{Eq. 24}$$

where Δx is unit channel thickness of a SIMS in-depth profile and A is the slope of the plot, $erfc^{-1} 2 \left(\frac{X-X_0}{X_\delta-X_0} \right)$ vs. n over the region of the in-depth profile where the $erfc^{-1}$ plot is found to have a good linearity.

4.2.2. EXPERIMENTAL DEPTH PROFILES

Intermixing profiles of oxygen isotopes have been obtained by the CAMECA ims 3f ionmicroprobe for five samples

of $Mg(^{16}O_{1-x_s}^{18}O_{x_s})/Mg(^{16}O_{1-x_o}^{18}O_{x_o})$ which had been diffusion-annealed at temperatures of 1000°, 1100°, 1200°, 1300°, and 1400°C, respectively. The profiles provided at only two temperatures, 1100°C and 1200°C could be completely analyzed since only for these samples could the corresponding initial profile be successfully obtained. An analysis of an unannealed portion of the deposit physically adjacent to each of the areas from which the remaining samples were taken was, in fact, performed. The results yielded features (i.e., an apparent spreading of the initial distribution or the height of an anomalous "lump" in concentration, to be discussed below) which did not correspond to the profile of the annealed specimen. The unannealed specimen was thus not truly characteristic of the portion which had been used in the diffusion specimen, a difference which is probably due to local variations in surface topology.

Fig. 9 presents the apparent initial distribution of ^{18}O isotope for the two specimens, which were diffusion-annealed at 1200°C and 1100°C and designated as R27-1200-5 and R27-1100-3, respectively. A portion of the same as-grown crystal from which the two specimens, R27-1200-5 and R27-1100-3, were prepared was sputtered for about 1.5 hr with a 506 nA, $^{40}Ar^+$ primary beam of 14.7 KeV to yield the initial profile before the diffusion anneal. The primary beam was rastered over an area of $250 \times 250 \mu m$ square and the extraction of the secondary ion beam was again restricted to a circular area of $150 \mu m$ in diameter centered within the sputtered square with

the help of the field aperture with which the CAMECA SIMS was equipped. The profile extends to $3.15 \pm 0.05 \mu\text{m}$ in depth and a unit channel thickness is thus 52.5 \AA or

$$\Delta x)_{t=0} = (5.25 \pm 0.08) \times 10^{-7} \text{ cm/ch.} \quad \text{Eq. 25}$$

The same data are replotted in the form of atomic percent Mg^{180} on an expanded scale of penetration for the region about the interface between the epitaxial layer and the substrate in Fig. 10. It is rather surprising that the initial spread is so wide, because it was expected to be a step function distribution. It is very likely an artifact that may be attributed to irregularities of the substrate crystal surface. As already described, the as-cleaved surface of the substrate crystal was heavily polished in a hot phosphoric acid. Chemical polishing usually induces a surface undulation, which is most severe for an as-cleaved surface especially when micro-cleavage-steps remain on it. Diffusional intermixing during the epitaxial deposition is a highly improbable reason for such a wide initial spread. Deposition of this epitaxial layer was accomplished within only 10 minutes at a temperature no greater than 1100°C . During this time a diffusion zone on the order of $8\sqrt{Dt}$ or 30 \AA in width would be expected at most. It is also unlikely that the resolution limitation of the SIMS in-depth profiling bears the whole responsibility for such a wide spread^{4,3}. If the original interface had been sharp, the profile would have

been an apparent $erfc$ as usual³² from which a depth resolution could be experimentally determined for the given sputtering condition. The interface at each microscopic element of area beneath the sputtered square may have been sharp and well-defined, but undulations on the order of the 0.5 μm observed for the spread in the distribution would not be surprising over a macroscopic area as large as 250 \times 250 μm . In this connection, it is also not ruled out that the undulation of the as-grown surface under the irradiation may be propagated deep into the epitaxial layer to yield an apparent initial broadening across even an ideal interface.

It remains puzzling, however, whether the concentration bump between the 200th and the 270th channel is a real local variation in isotope ratio or whether it is an instrument-related artifact. In view of the growth technique employed, it is difficult to understand a gradual change of 180 concentration within the 10 minutes of growth time in the growth chamber filled with the anhydrous HCl gas. The origin of this artifact remains unclear.

A plot of $erfc^{-1} 2(X-X_0)/(X_\delta-X_0)$ or $erfc^{-1} [1-2(X-X_0)/(X_\delta-X_0)]$ against the channel number, in Fig. 11, examined whether the initial spread across the interface was gaussian. The initial abundance, X_δ , was arbitrarily taken as 0.0935, an average over channel from 221 to 235, which corresponds to the maximum concentration in the profile of Fig. 10. It is noted that the portion of the plot above approximately the 305th channel has a good linearity. This implies that the

initial spread over the same range of channels is gaussian as is strongly suggested from the shape of the profile shown in Fig. 10. For 26 data points, the linear correlation coefficient was 0.99 and the slope was

$$A)_{t=0} = 0.075 \pm 0.002, \quad \text{Eq. 26}$$

where the subscript, $t=0$, denotes the *initial* or *pre-diffusion anneal*. Selection of an alternative choice for X_δ in a concentration range between 0.07 and 0.08 (concentrations in the epitaxial layer far from the interface, Fig. 10) does not change the slope of Fig. 11 sufficiently to exceed the experimental standard deviation of ca. 3 % in Eq. 26. Neither does it alter significantly the range of channel where the apparent initial spread is gaussian. For a relative variation of the initial abundance, $\delta X_\delta / X_\delta \sim 0.2$, i.e., when X_δ is chosen 0.07 instead of 0.0935, it can be shown* that the slope of Fig. 11 or Eq. 26 increases only by approximately 5 %.

The sputtering profile of the specimen R27-1200-5 is provided in Fig. 12. The specimen was sputtered by a 9.65 KeV, 306 nA, $^{40}\text{Ar}^+$ primary beam. The sputtered crater was measured to be $2.60 \pm 0.05 \mu\text{m}$ and hence a unit channel

* A variation in Y such that $Y = \text{erfc}^{-1}(2X/X_\delta)$, δY , is related to a variation, δX_δ as $\delta Y = (\sqrt{\pi}/2) \exp(Y^2) \text{erfc}(Y) \cdot (\delta X_\delta / X_\delta)$ for the given X . The slope of the plot, $Y + \delta Y$ vs. Y in $0 < Y < \sim 2$ is 1.052 from which the relative increase in the slope of Y vs. penetration depth turns out to be ca. 5 %

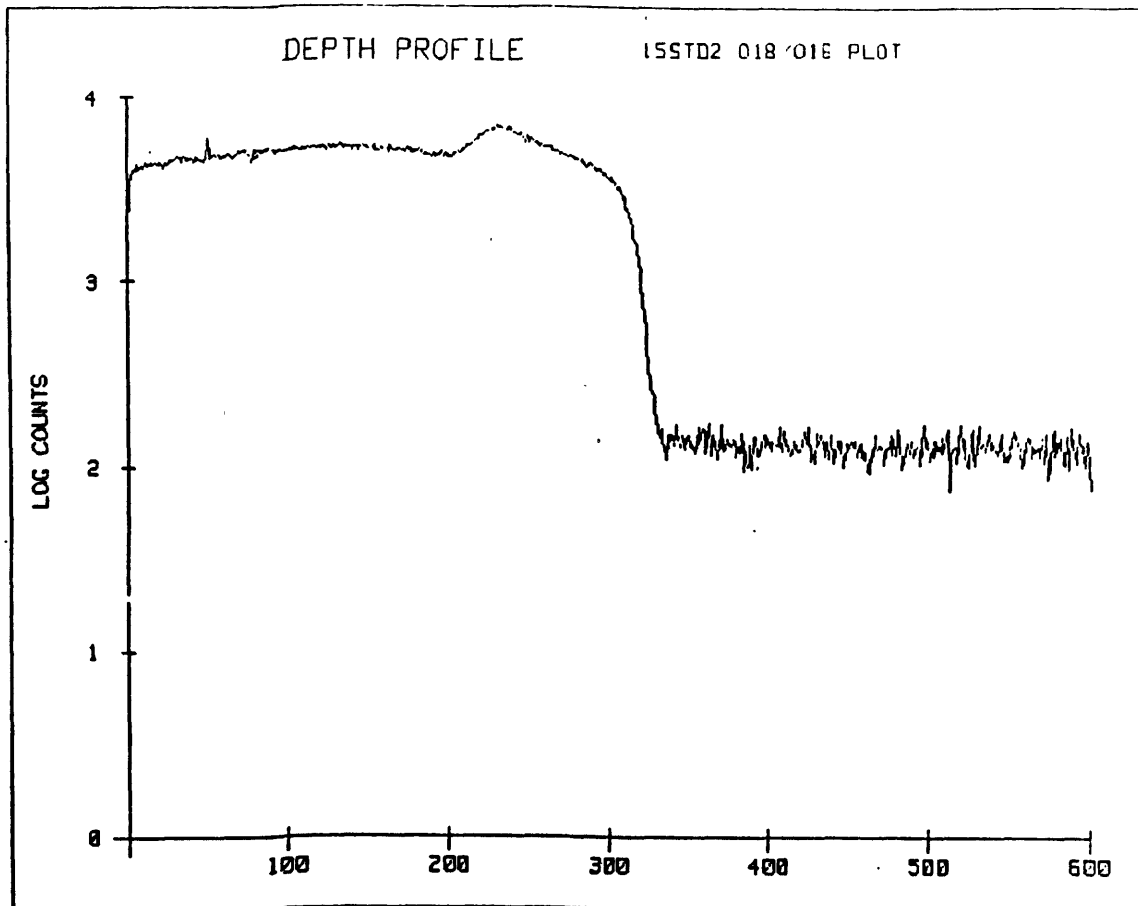


Fig. 9. Intensity ratio of oxygen isotopes, ^{18}O to ^{16}O , as a function of depth for the unannealed sample sputtered by a rastering $^{40}\text{Ar}^+$ beam of 506 nA, 14.7 KV.

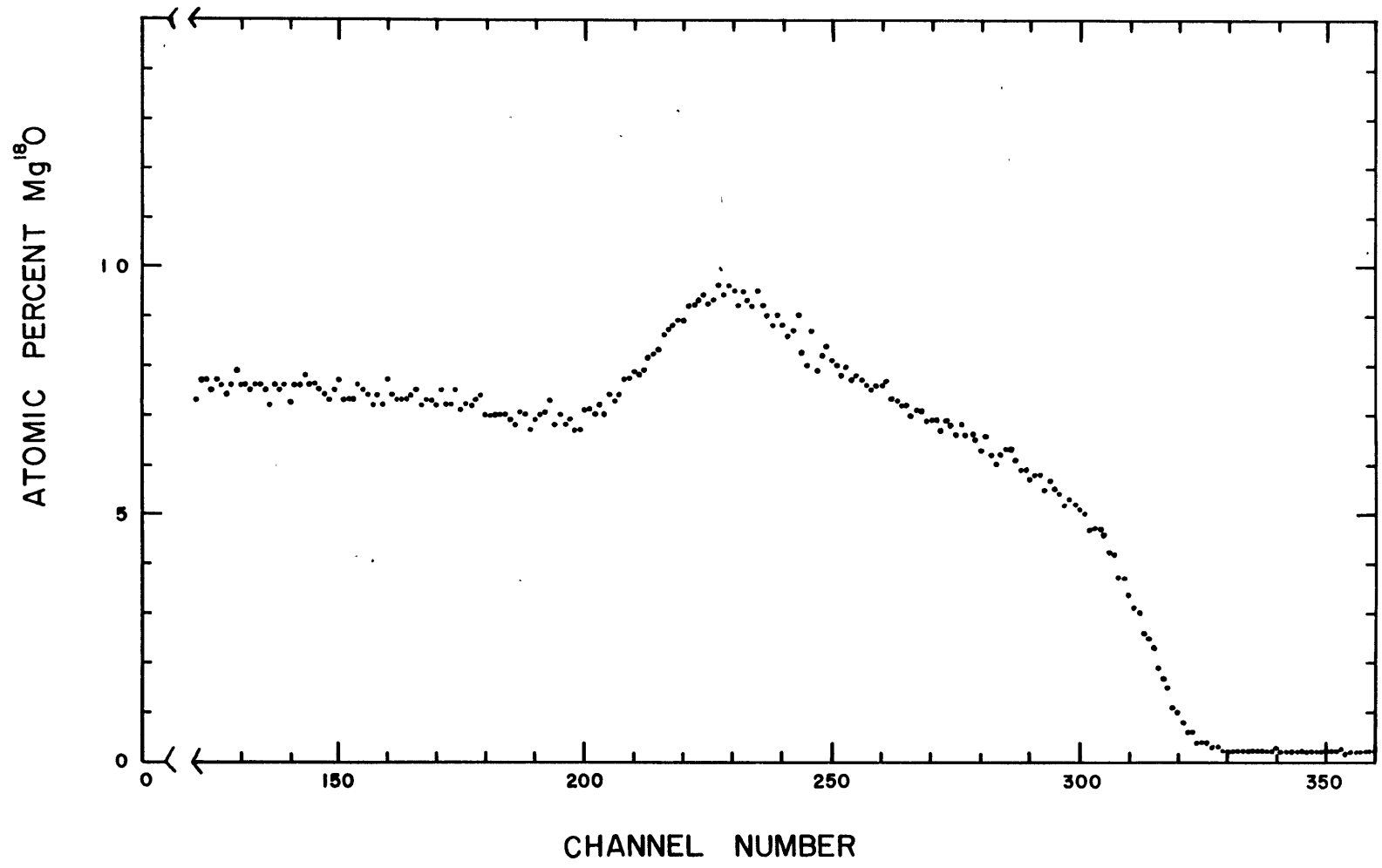


Fig. 10. Linear plot of the atomic % Mg¹⁸O vs. channel as derived from Fig. 9.

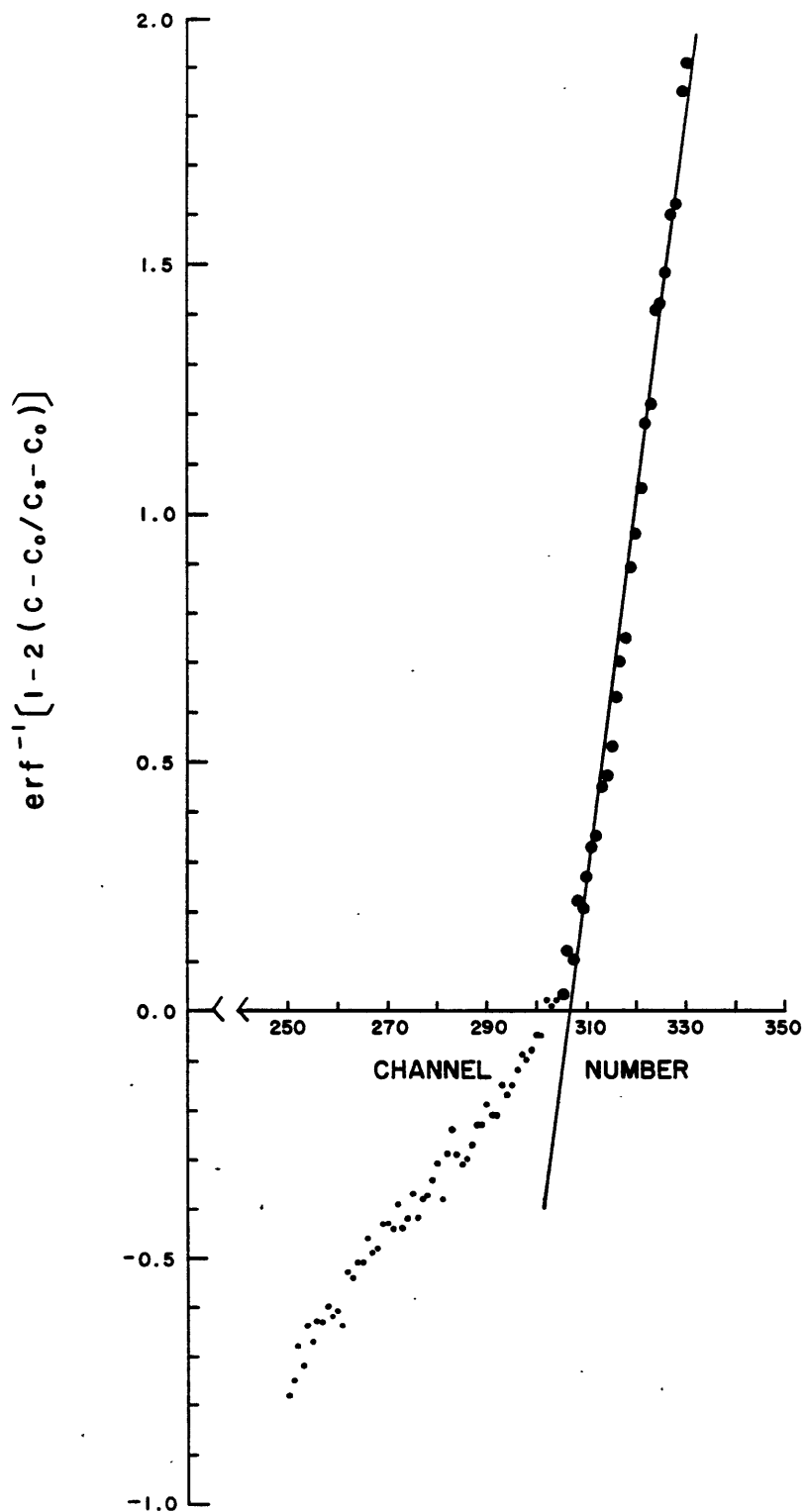


Fig. 11. Plot of the inverse error function for the broadening of the ^{18}O profile across the interface before the diffusion anneal.

thickness is 94 Å or

$$\Delta x = (9.4 \pm 0.2) \times 10^{-7} \text{ cm/ch.} \quad \text{Eq. 27}$$

The linearly-scaled plot of the concentration of $Mg^{18}O$ as a function of penetration is shown in Fig. 13 to emphasize its similarity to the initial profile of Fig. 10 in the neighborhood of the interface. One may readily identify in Fig. 12 or Fig. 13 the two diffusion profiles in the specimen: the first established by the gas exchange at the surface of the epitaxial layer and the second (of much greater apparent extent) by the isotope intermixing at the interface between the layer and the substrate. A plot of $\text{erfc}^{-1} 2(X-X_0)/(X_\delta-X_0)$ or $\text{erfc}^{-1} [1-2(X-X_0)/(X_\delta-X_0)]$ as a function of channel number for the intermixing profile is plotted in Fig. 14 (b), in which X_δ has been taken to be the maximum abundance or 0.0945 (an average over channels from 120 to 130). An excellent linearity is conspicuous. The linear correlation coefficient is 0.99 for 18 data entries and the slope is

$$A)_{t=t} = 0.094 \pm 0.003, \quad \text{Eq. 28}$$

where the subscript, $t=t$, denotes *after the diffusion anneal*. The diffusion coefficient is extracted from the interdiffusion profile by using the simple deconvolution provided by Eq. 24. From the slopes and the unit channel thicknesses, Eq.'s 25 and 26 and Eq.'s 27 and 28, the diffusion coefficient is obtained

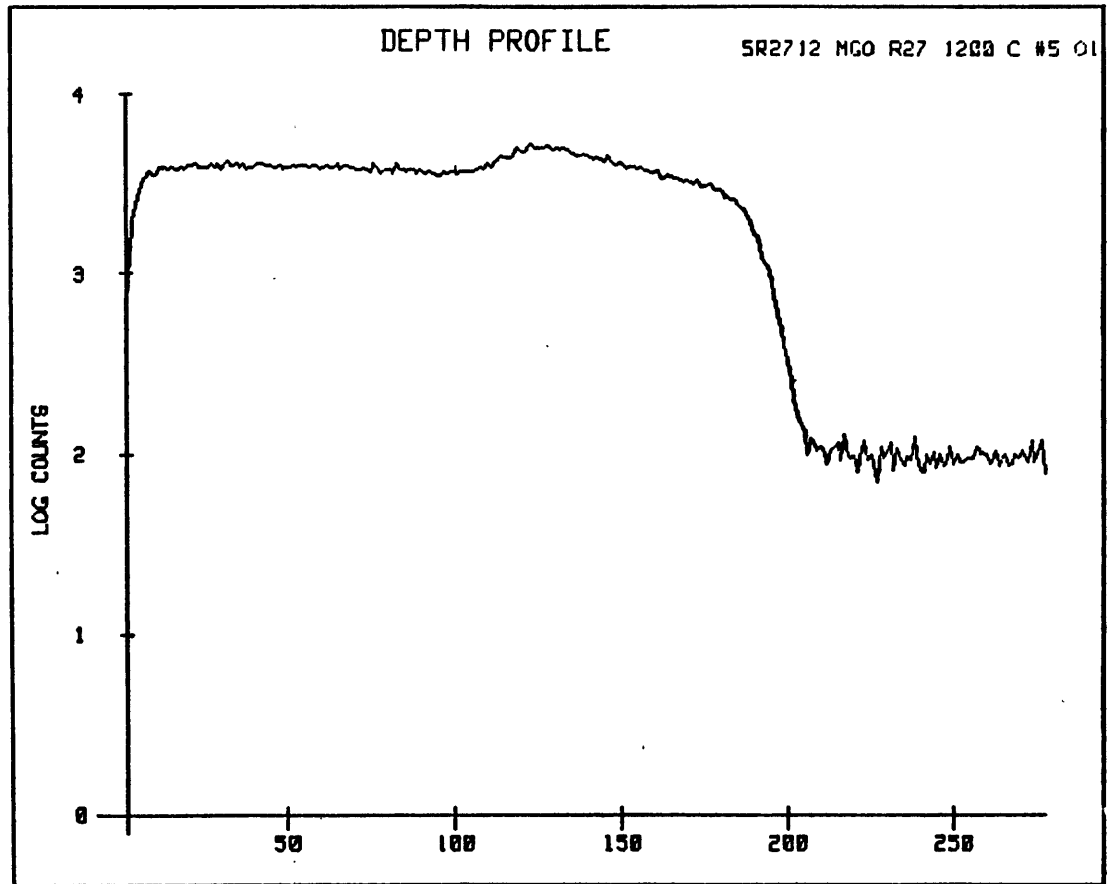


Fig. 12. Intensity ratio of ^{18}O to ^{16}O as a function of depth for the specimen annealed in air at 1200°C for 15 days and sputtered by a rastering $^{40}\text{Ar}^{+}$ beam of 306 nA, 9.65 KV.

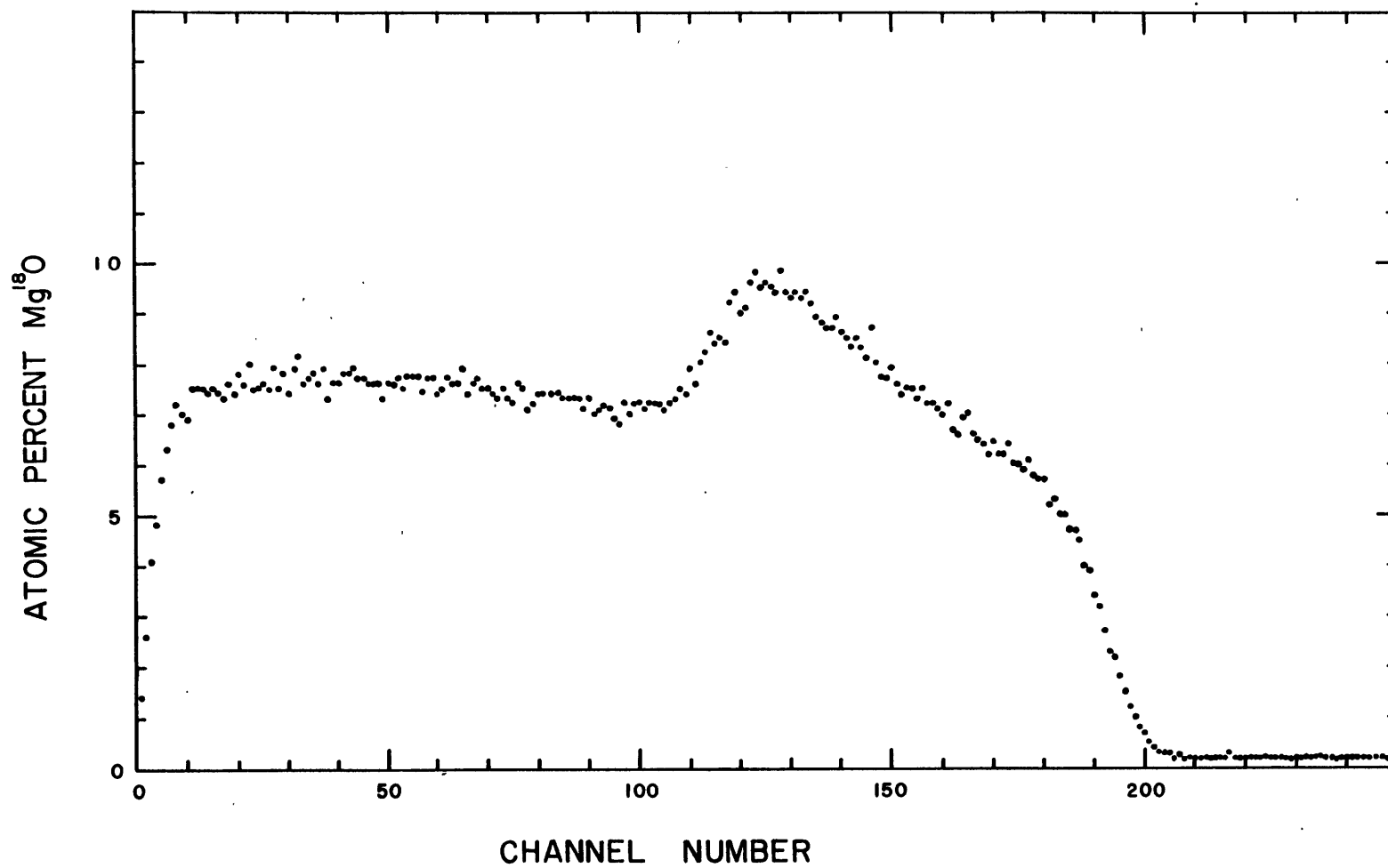


Fig. 13. Replot of Fig. 12. on a linear scale, atomic % Mg¹⁸O as a function of depth.

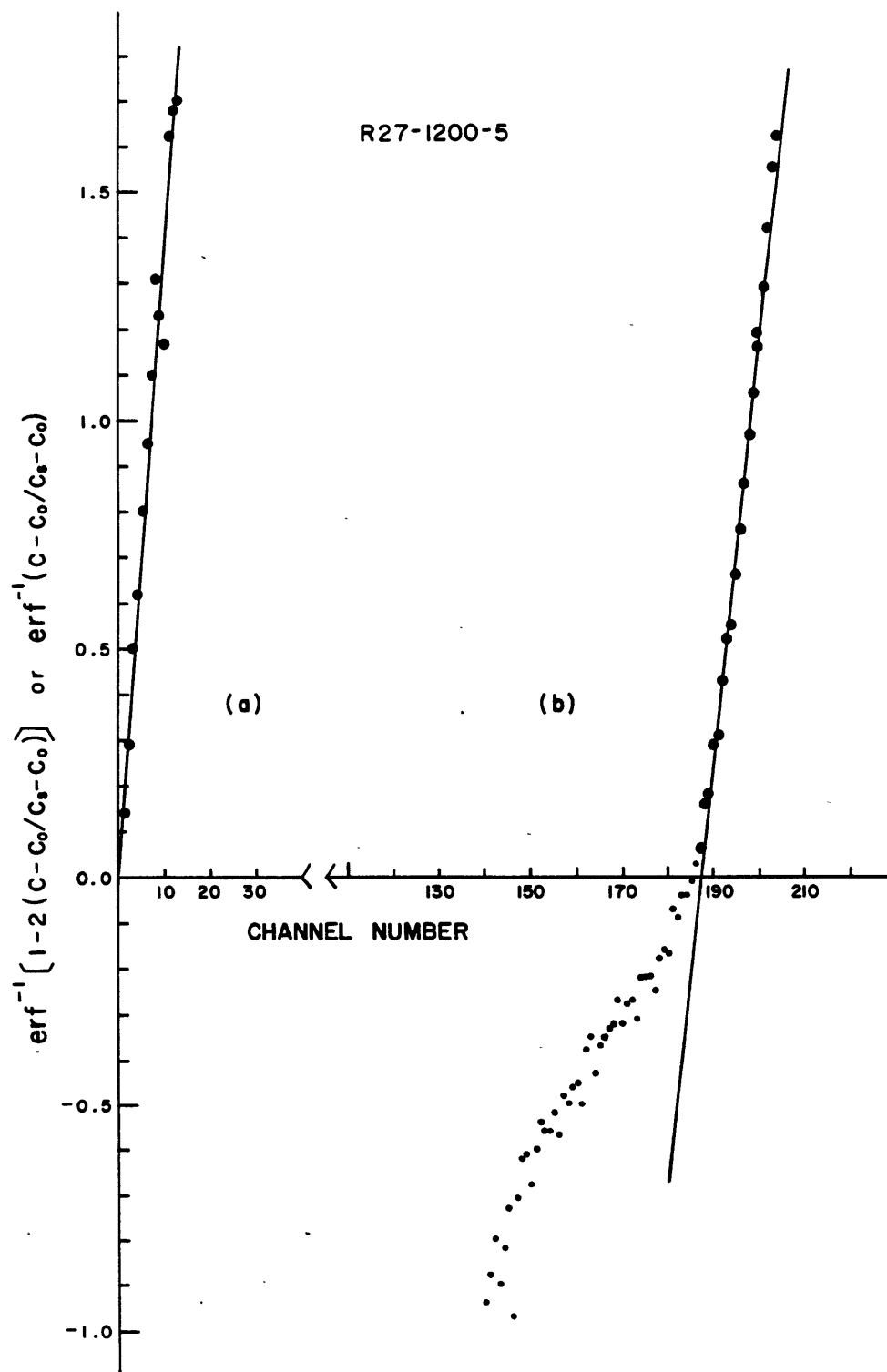


Fig. 14. Plot of the inverse error function corresponding to the profile in Fig. 13 for the gas-exchange (a) and for the isotopic interdiffusion (b).

as

$$D = (1.0 \pm 0.2) \times 10^{-17} \text{ cm}^2/\text{sec}, \quad \text{Eq. 29}$$

for the specimen R27-1200-5 which has been diffusion-annealed at 1200°C for 15 days.

The sputtering profile of the specimen, R27-1100-3, which was annealed at 1100°C for 20 days has been obtained with an $^{40}\text{Ar}^+$ primary beam of 9.65 KeV, 206 nA as in Fig. 15. The crater depth is $2.40 \pm 0.05 \text{ }\mu\text{m}$ which is reduced to a unit channel thickness,

$$\Delta x = (4.1 \pm 0.1) \times 10^{-7} \text{ cm/ch.} \quad \text{Eq. 30}$$

The plot of $\text{erf}^{-1} [1 - 2(X - X_0) / (X_\delta - X_0)]$ as a function of channel number which corresponds to the interdiffusion profile in Fig. 15 is shown in Fig. 16 (b). The initial abundance, X_δ , has been chosen as the maximum abundance, 0.0904 (obtained by averaging over channels of 380 to 400, Fig. 10), in order to preserve the consistency of analysis. A good gaussian nature of the spread is again demonstrated in the region corresponding to that of the initial profile, Fig. 9 or Fig. 11. For 43 data entries, the linear correlation coefficient is 0.99 and the slope is

$$A)_{t=t} = 0.040 \pm 0.001. \quad \text{Eq. 31}$$

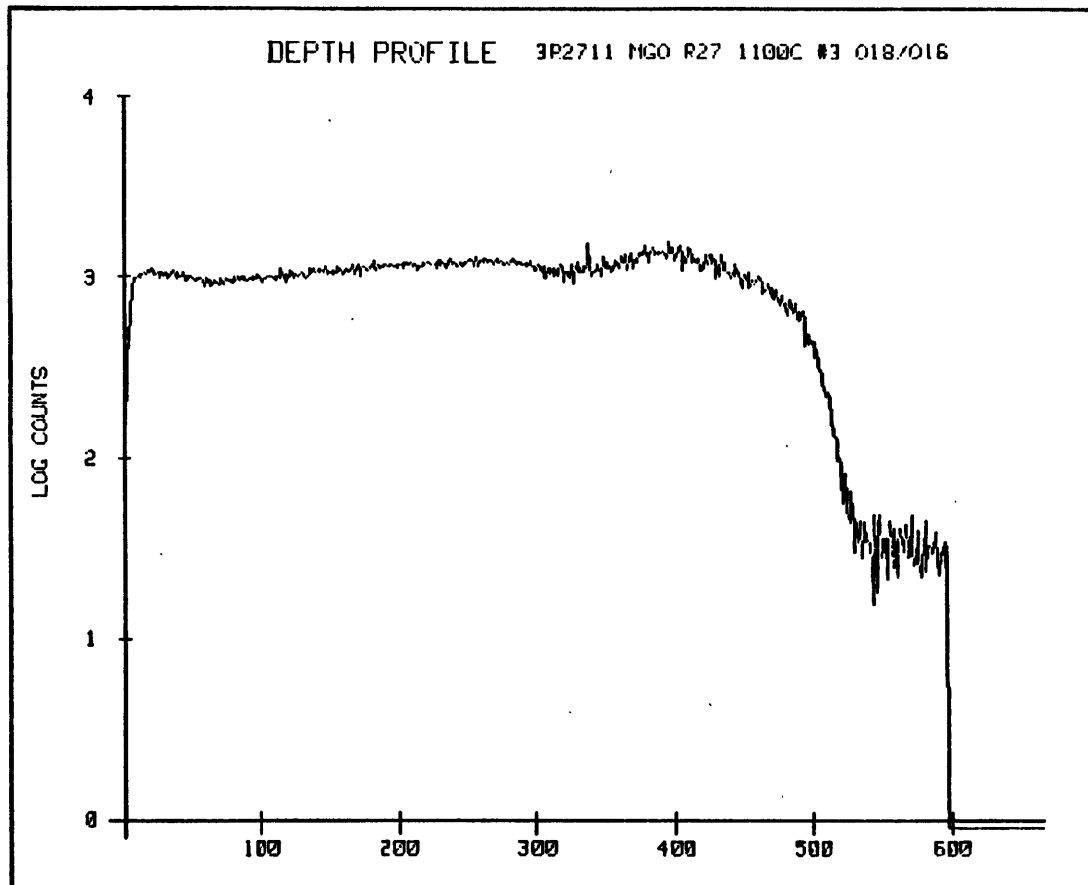


Fig. 15. Intensity ratio of ^{18}O to ^{16}O as a function of depth for the specimen annealed in air at 1100°C for 20 days and sputtered by a rastering $^{40}\text{Ar}^+$ beam of 206 nA, 9.65 KV.

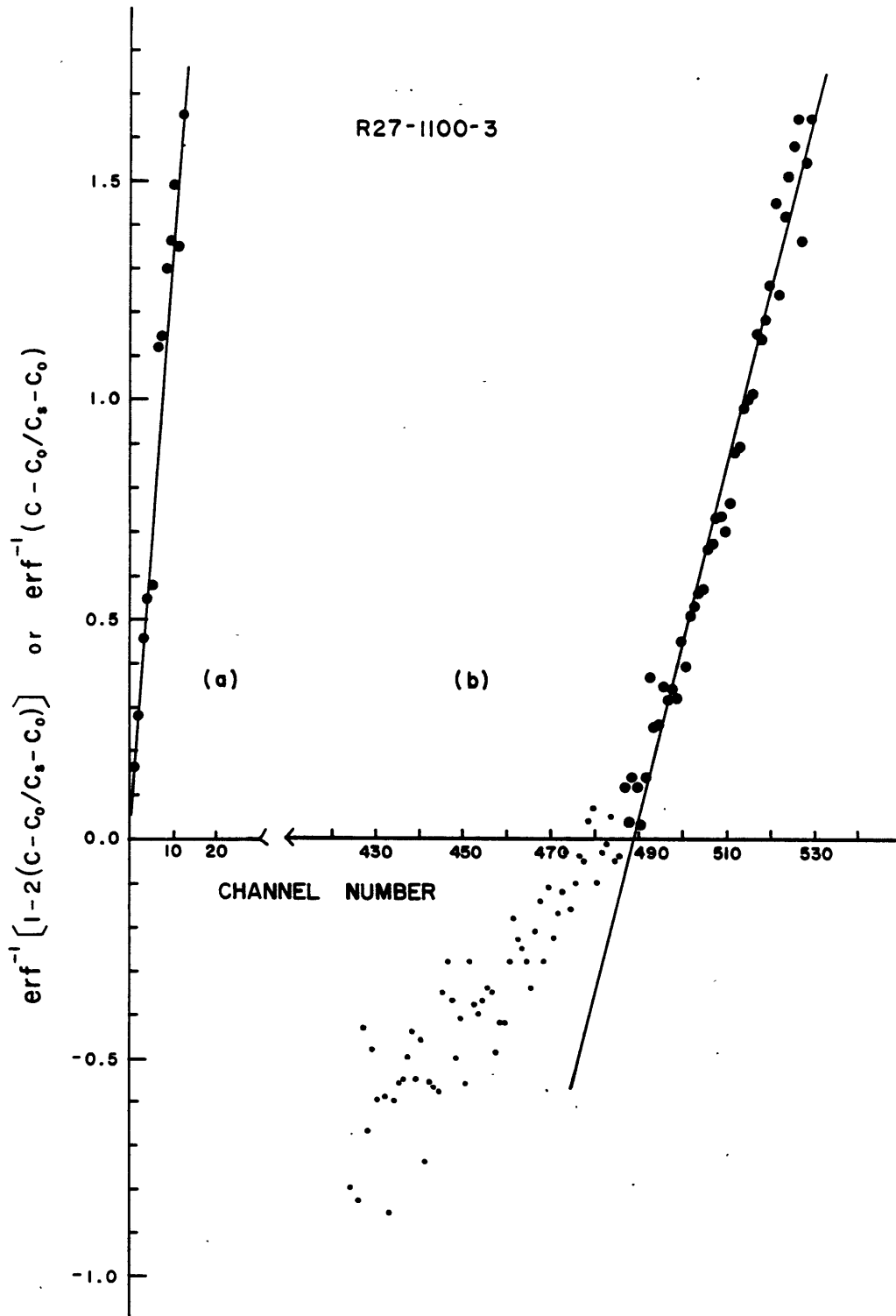


Fig. 16. Plot of the inverse error function corresponding to the profile in Fig. 15 for the gas-exchange (a) and for the isotopic interdiffusion (b).

From Eq.'s 30 and 31, the deconvolution, Eq. 24, yields the diffusion coefficient,

$$D = (8.0 \pm 1.3) \times 10^{-18} \text{ cm}^2/\text{sec} \quad \text{Eq. 32}$$

for the interdiffusion at 1100°C.

4.2.3. COMPARISON OF INTERDIFFUSION AND GAS-EXCHANGE GRADIENTS

Exchange profiles for the specimens, R27-1200-5 and R27-1100-3, shown in Fig. 12 and Fig. 15, respectively, have been already analyzed in the preceding chapter (see also Appendix 2). For direct comparison, the plot of erf^{-1} as a function of penetration produced by exchange in the surface region is also given in Fig. 14(a) and Fig. 16(a), respectively, on the same scale as the interdiffusion gradient. The two diffusion coefficients obtained therefrom are compared in Table 6.

Table 6. Comparison of Diffusion Coefficients

Temp (°C)	diffusion coefficients (cm ² /sec)	
	interdiffusion	gas-exchange
1200	$(1.0 \pm 0.2) \times 10^{-17}$	$(1.0 \pm 0.13) \times 10^{-17}$
1100	$(8.0 \pm 1.3) \times 10^{-18}$	$(2.1 \pm 0.4) \times 10^{-18}$

It is noted that the diffusion coefficient obtained from the interdiffusion gradient is in agreement with the diffusion coefficient obtained from the gas-exchange, taking into account the prevailing experimental error.

Reddy and Cooper¹³ have shown that, for MgO, the values of $k\sqrt{t}/\bar{D}$ in Eq. 5 are greater than 3 and hence that the surface exchange process does not influence the overall kinetics at temperatures of 1300° to 1600°C. The direct comparison in the present work shows that this conclusion is justified at temperatures at least down to 1100°C. This conclusion is also in keeping with the fact that all exchange profiles could be successfully interpreted (i.e., gave highly linear results, Appendix 2) under the assumption that the concentration of ¹⁸O at the phase boundary of the gas/solid diffusion couple, $(^{16}\text{O}_{1-\chi_{\text{O}}} \text{ } ^{18}\text{O}_{\chi_{\text{O}}})_2$ (in air) / $\text{Mg} (^{16}\text{O}_{1-\chi_{\text{S}}} \text{ } ^{18}\text{O}_{\chi_{\text{S}}})$, was its natural abundance χ_{O} or 0.002039.

The justification probably extends to the exchange profile established at 1000°C within the limits of the present experimental uncertainty since the diffusion coefficient extracted as such is not different from what is expected from the Arrhenius plot of diffusion coefficients measured between 1650° to 1100°C. According to Table 5, the best fit of the first 8 data ($r = 0.995$) yields

$$D = (6.8_{-4.3}^{+11.7}) \times 10^{-6} \exp(-3.44 \pm 0.14 \text{ eV}/kT) \text{ cm}^2/\text{sec},$$

Eq. 33

from which a diffusion coefficient at 1000°C is expected to be $D = 1.6 \times 10^{-19} \text{ cm}^2/\text{sec}$ with the relative uncertainty $\sigma_D/D \sim 2$. The measured value, in comparison, is $D = (4.5 \pm 1.0) \times 10^{-19} \text{ cm}^2/\text{sec}$.

Therefore, the diffusion coefficient represented by Eq. 16 may be regarded as the best estimate of the oxygen diffusivity in MgO.

5. DISCUSSION OF RESULTS

The results of the present analyses are compared in Fig. 17 with the oxygen self-diffusion coefficients reported in previous studies summarized in Table 1. The magnitudes of the present diffusion coefficients are two orders of magnitude smaller than those obtained by early exchange measurements^{1,9} but Oishi *et al.*⁸ showed that chemical polishing to remove the surface damage introduced in crushed samples considerably lowered the apparent diffusivity. In addition, certain heat treatments could increase the apparent diffusivity by creating etch pits which increased the area available for exchange.

In contrast, the present results are in good agreement with those of Rovner¹⁰ and in magnitude, if not activation energy, with results obtained by Reddy¹³ through proton-activation measurements of the gradients produced by ¹⁸O exchange. The latter agreement is of particular interest as discrepancies which could not be satisfactorily explained were present between the results of SIMS analysis^{4,8} and proton-activation analysis^{4,9} of anion self-diffusion in Al_2O_3 . Also included in Fig. 17 are results of indirect determinations of diffusion coefficients based upon measurement of dislocation movement with the aid of transmission electron microscopy. The activation energy for subgrain boundary formation obtained by Moriyoshi *et al.*¹⁵ is in

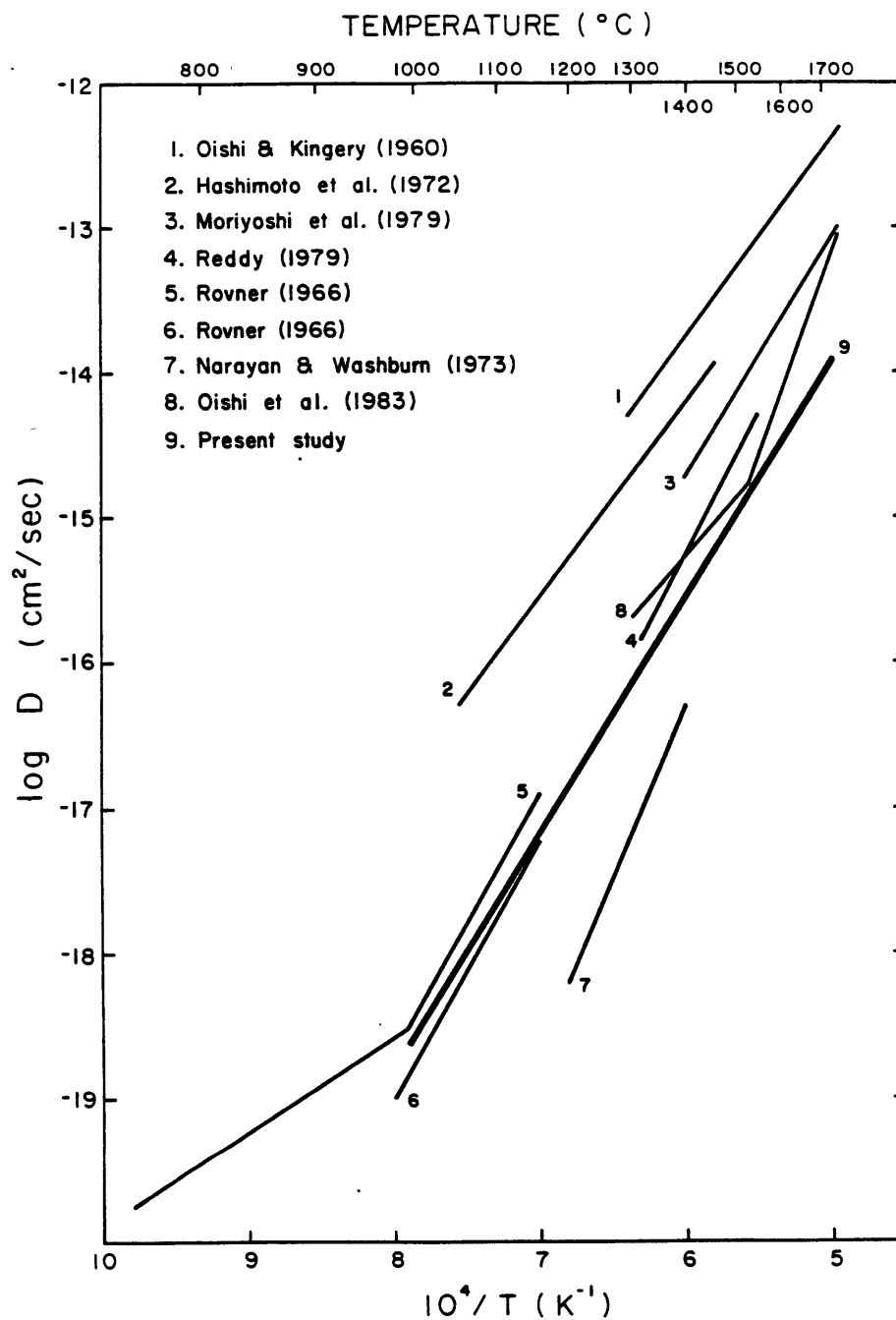


Fig. 17. Comparison of the oxygen self-diffusion coefficients of the present work with previously reported values.

good agreement, perhaps fortuitously, with the present value. The diffusivities deduced by Narayan and Washburn¹⁶ from dislocation-loop shrinkage rate are smaller than any directly measured coefficients. The values hinge, however, on the model assumed for dislocation movement.

The activation energies reported in previous studies vary from 2.6 to 3.8 eV for oxygen diffusion measured with the gas-exchange techniques. The activation energy obtained in the present work, 3.24 ± 0.13 eV, is squarely in the middle of this range. It is difficult to decide whether individual differences are truly significant in view of the limited temperature range and uncertain error limits of most studies.

An activation energy on the order of 3.2 eV is very difficult to interpret in terms of the available theoretical estimates of energies relevant to the defect structure of MgO and the prevailing interpretation of cation transport mechanisms. By virtue of good agreement between the calculated and experimental energy for cation vacancy migration as well as the magnitudes of ionic electrical conductivity and cation self-diffusion, it seems well established that cationic transport in MgO occurs by a vacancy mechanism, and that vacancy concentrations are determined by aliovalent cationic impurities.^{11,12} If such is the case and if Schottky equilibrium is maintained, anion vacancy concentrations and anion self-diffusion coefficients should be depressed - probably much more so than the ca.3 orders of magnitude difference presently observed between the measured anion and cation

self-diffusion coefficients. Moreover, the activation energy anticipated for anion self-diffusion in a crystal whose defect structure is controlled by cation impurities of higher valence state, or e.g. $[V_{Mg}^{''}] \sim [F_{Mg}^{\bullet}]$ in Kröger-Vink notation, should be given by $h_s + h_{m-}$ where h_s and h_{m-} are the enthalpies for Schottky vacancy-pair formation and anion vacancy migration, respectively. The sum of theoretical estimates for these enthalpies, namely 7.5 or 7.72 eV plus 2.38 or 2.11 eV (see Table 2), is clearly incompatible with the experimental values. If the defect structure is governed by cationic impurities of lower valence state, or e.g. $[V_O^{\bullet}] \sim [F_{Mg}^{\bullet}]$, the activation energy will be anticipated to be the enthalpy for anion vacancy migration, h_{m-} or 2.38 or 2.11 eV. The difference between experiment and the theoretical values for h_{m-} seems too great for all investigations to date to provide a satisfactory interpretation. Furthermore, judging from the SIMS mass spectrum of the impurity contents of an as-grown epitaxial layer, shown in Fig. 3, domination of the defect structure by cation impurities of lower valence is a highly improbable situation for the present study. Even if the crystal remains in an intrinsic regime and $[V_O^{\bullet}] = [V_{Mg}^{''}]$, the activation energy must be $\frac{1}{2}h_s + h_{m-}$ or about 6 eV for the oxygen diffusion. Even consideration of cation-anion divacancy as a corresponding diffusion mechanism leads to the activation energy of $h_s + h_a + h_m'$, where h_a and h_m' are the enthalpies for divacancy formation and migration, respectively. h_a has been theoretically estimated to be -2.55 eV (see

Table 2) and h_m' has been shown to be comparable with or greater than the activation energy for single vacancy movement.⁵⁰ The activation energy is thus at least $7.5 - 2.55 + 2.38$ or about 7 eV , which is far greater than the observed value, 3.2 eV . The nature of the anion transport mechanism accordingly remains unclear and is not satisfactorily interpretable in terms of any obvious model for defect structure.

6. SUMMARY

The anion self-diffusion coefficient of MgO has been determined in the present work by the gas/solid ^{18}O exchange technique, and by a limited number of solid/solid inter-diffusion measurements. Unlike the conventional method in which a normal MgO crystal was diffusion-annealed in a limited volume of ^{18}O -enriched atmosphere, a layer of ^{18}O -enriched single crystal was grown epitaxially on the substrate of commercially available MgO single crystal through chemical vapor transport with HCl and annealed in an air atmosphere to accomplish replacement of ^{18}O in the layer by ^{16}O in air. The concentration gradients of ^{18}O were established by secondary ion mass spectrometry. The charge build-up on an insulator surface during SIMS in-depth profiling was almost completely eliminated both by depositing a thin Au film on the sample surface and by flooding electrons on the sputtered area and hence an in-depth profile could be extended as deep as $3 \mu m$. The excellent depth resolution of SIMS as well as the unique characteristic of the diffusion sample allowed the diffusion coefficient to be measured at a temperature as low as $1000^{\circ}C$ (diffusion coefficients as low as $10^{-19} \text{ cm}^2/\text{sec}$, previously accessible to measurement only with great difficulty) in a reasonable time.

At temperatures of $1700^{\circ}C$ to $1000^{\circ}C$, the best estimate of the oxygen diffusivity is represented by

$$D_{best} = (1.8_{-1.1}^{+2.9}) \times 10^{-6} \exp(-3.24 \pm 0.13 \text{ eV}/kT) \text{ cm}^2/\text{sec},$$

which is precise within a factor of 2, or

$$\sigma_D/D_{best} \sim 2.$$

The present diffusion sample is unique in that one may compare two diffusion profiles in one specimen: one developed by the gas exchange at the surface of the epitaxial layer and the other developed by the isotopic interdiffusion at the interface between the epitaxial layer and the substrate crystal. At temperatures of 1100°C and 1200°C, diffusion coefficients obtained by the gas-exchange were not in disagreement with those obtained by the isotopic interdiffusion within the limits of experimental uncertainty. Based on this comparison and the previous observation by Reddy and Cooper,^{1,3} the overall gas exchange kinetics are not influenced by the isotope exchange reaction rate at the phase boundary but governed by the diffusion in the solid phase, MgO. Similarly, it is concluded that surface flaws or dislocations have no appreciable influence on the apparent exchange diffusion coefficient. The best estimated diffusion coefficient extracted from the gas exchange thus well represents the oxygen self-diffusion coefficient in single crystal MgO.

The activation energy in the neighborhood of 3.2 eV, how-

ever, still defies any atomistic interpretation based on the prevailing defect model for MgO -like ionic solids, which has mainly been established on the basis of experimental studies of transport phenomena on the cationic sublattice but by theoretical calculations of defect energies as well. It is implied that our present understanding of even the simplest oxide is still incomplete in so far as the anionic sublattice is concerned.

7. SUGGESTIONS FOR FUTURE WORK

For almost the past three decades, MgO has been a most beloved material as a model system for ceramic oxides. By virtue of extensive studies especially of cationic transport phenomena, there has been accumulated a great deal of information on the basis of which a self-consistent model for a defect structure has been established for MgO . It is now generally believed that cations migrate via a vacancy mechanism and the predominant defect is the Schottky disorder. This concensus is substantiated by the recent theoretical calculation of defect enthalpies.

Unfortunately, however, the present work has shown that such a defect model cannot explain successfully the diffusion mechanism on the anionic sublattice. Experimental figures for the activation energy of anion self-diffusion are inconsistent with the established defect model for MgO -like ionic systems. Is it implied that the uncertainty of experimental measurements veils the truth or, if not, a naive defect model is not appropriate as the oxygen diffusion mechanism? Could absolutely unexpected defect species due to, for example, anionic impurities be responsible for the discrepancy?

In the conventional gas-exchange technique where the crystal has to be annealed in a limited volumes of ^{18}O -enriched atmosphere because $^{18}O_2$ gas is very expensive (\$400

per gram!!), the direct measurement of oxygen diffusion is accordingly subject to various difficulties or limitations. It is now believed that those experimental hurdles have been obviated by the present diffusion sample bearing an ^{18}O -enriched epitaxial layer. With the present sample, an arbitrarily long diffusion anneal can be done in any kind of ^{16}O -reservoir. It may be an atmosphere whose oxygen partial pressure is controlled. In addition, SIMS in-depth profiling provides the most accurate analytic tool to establish a diffusion profile extending to 2-3 μm depth with an excellent depth resolution and no serious charging problem as well. The limitations on the precision in \mathcal{D} encountered in the present work are not inherent to the method, but may be improved by careful attention to surface planarity or reduction of the rastered area.

The following suggestions are thus offered for future work to provide answers to the questions raised earlier:

- i) It would be desirable to remeasure the oxygen diffusion coefficient with higher reliability over a far wider temperature range. In order to improve the accuracy, the diffusion annealing has to be long enough to let the diffusion distance be 1 μm at least. It is noted that the overall uncertainty has been propagated overwhelmingly from the depth measurement of sputtered craters. In any case, SIMS depth resolution is not accuracy-limiting. With respect to annealing temperature, approximately 1800°C may be the

realistic upper limit for gas exchange measurements due to high vapor pressure of MgO . There is no such limit to solid/solid interdiffusion measurements and cation self-diffusion measurements²⁰ have been performed to $2500^{\circ}C$. There need be no lower limit since the present specimen allows arbitrarily long anneal.

ii) The oxygen partial pressure dependence of the oxygen diffusivity is suggested for measurement for a clearer understanding of defect structure. Arbitrary control of oxygen partial pressure in the annealing atmosphere is now easily allowed with the present diffusion sample.

iii) Simultaneous measurement of cation self-diffusion may provide the critical clue to the understanding of the oxygen diffusion mechanism. For a diffusion specimen, one may grow with ease an epitaxial layer of e.g. $^{26}Mg^{18}O$ on usual single crystal MgO , or $^{26}Mg^{16}O$ on $Mg^{18}O$ through the chemical vapor transport with HCl . Since the simultaneous counting of various kinds of secondary ions is possible in SIMS in-depth profiling, diffusion characteristics on both sublattices can be directly compared.

iv) It is necessary to identify anionic impurities. In contrast to cationic impurities, little is known about anionic impurities in MgO . With the use of well-prepared standard-reference-materials, one may perform a quantitative analysis through, for example, the SIMS mass spectrum.

APPENDIX 1: ASSESSMENT OF ERRORS

In order to meaningfully compare experimental diffusivities and the diffusion parameters derived therefrom, it is necessary to assign the reliability to the measured diffusion coefficients. The reliability of a measured physical quantity is usually quantified by its random error and systematic error representing the precision and accuracy of the quantity, respectively. In most cases, however, it is very difficult, if not impossible, to evaluate the systematic error but it can be minimized or eliminated by the calibration of measuring instruments or specifically incorporating the correct systematic dependence in the model for the measurement of the physical quantity. The systematic error is thus disregarded in the present assessment under the assumption that all the related instruments, e.g. the profilometer and the thermocouple have been well calibrated. Hence, only the random error is put under consideration. As a measure of the random error, the standard deviation is introduced.

1.1. ERROR PROPAGATION AND LINEAR REGRESSION

Most physical quantities usually cannot be measured in a single direct measurement, but are calculated from one or more quantities which can be directly measureable. The errors associated with each measurement are propagated through this procedure. The propagation of errors has been given extensive

consideration^{40, 44, 45}

Suppose that a set of physical quantities, $\{p_i\}$, are directly measured with the uncertainties, $\{\delta p_i\}$, and they are used to calculate another quantity, q , via a functional dependence,

$$q = q(\{p_i\}). \quad \text{Eq. 1-1}$$

If the uncertainties, $\{\delta p_i\}$, are random and independent of each other, then the error in the calculated quantity, δq , is given by⁴⁰

$$\delta q = \left[\sum_i \left(\frac{\partial q}{\partial p_i} \delta p_i \right)^2 \right]^{1/2}. \quad \text{Eq. 1-2}$$

In any case, it is never larger than the ordinary sum,

$$\delta q \leq \sum_i \left| \frac{\partial q}{\partial p_i} \right| \delta p_i, \quad \text{Eq. 1-3}$$

which is often probably an overstatement of δq , since there may be partial cancellation of the errors in p_i .⁴⁰ If the measurements of p_i are governed by independent normal distributions, with standard deviations σ_{p_i} , then the values of $q(\{p_i\})$ are also normally distributed with standard deviation,

$$\sigma_q = \left[\sum_i \left(\frac{\partial q}{\partial p_i} \sigma_{p_i} \right)^2 \right]^{1/2}. \quad \text{Eq. 1-4}$$

When a set of directly measured diads $\{(x_i, y_i)\}$ are obtained and the variables, x and y , are known to be linearly related, on the other hand, the best straight line $y = Ax + B$ to fit a set of measured diads $\{(x_1, y_1), (x_2, y_2), \dots, (x_N, y_N)\}$ is usually found by a method of least squares. If x 's are subject to negligible errors, and y 's are equally uncertain, the slope, A , and the intercept, B , are respectively obtained from the principle of maximum likelihood⁴⁰ as

$$A = \frac{N(\sum x_i y_i) - (\sum x_i)(\sum y_i)}{\Delta} \quad \text{Eq. 1-5}$$

and

$$B = \frac{(\sum x_i)(\sum y_i) - (\sum x_i)(\sum x_i y_i)}{\Delta}, \quad \text{Eq. 1-6}$$

where

$$\Delta \equiv N(\sum x_i^2) - (\sum x_i)^2. \quad \text{Eq. 1-7}$$

The uncertainties in A and B are generated only from a constant uncertainty in y or σ_y since $\sigma_x \sim 0$. Due to Eq. 1-4,

$$\sigma_A^2 = N\sigma_y^2/\Delta \quad \text{Eq. 1-8}$$

and

$$\sigma_B^2 = \sigma_y^2 \sum x_i^2 / \Delta, \quad \text{Eq. 1-9}$$

where

$$\sigma_y^2 = \frac{1}{N-2} \sum_{i=1}^N (y_i - A - Bx_i)^2. \quad \text{Eq. 1-10}$$

The extent to which a set $\{(x_i, y_i)\}$ supports a linear relation $y = Ax + B$ or how well the set $\{(x_i, y_i)\}$ fits a straight line is measured by the linear correlation

coefficient^{40,46}

$$r = \frac{\sum (x_i - \bar{x})(y_i - \bar{y})}{[\sum (x_i - \bar{x})^2 \sum (y_i - \bar{y})^2]^{\frac{1}{2}}}, \quad \text{Eq. 1-11}$$

where (\bar{x}, \bar{y}) is the center-of-mass of the set $\{(x_i, y_i)\}$ or

$$\bar{x} = \frac{1}{N} \sum x_i \quad \text{and} \quad \bar{y} = \frac{1}{N} \sum y_i. \quad \text{Eq. 1-12}$$

The probability that ten or more measurements of two uncorrelated variables x and y , for example, would produce a correlation coefficient $|r| \geq 0.9$ is less than 0.001 % or negligible.⁴⁷ If this probability is sufficiently small, then we can conclude that it is very improbable that x and y are uncorrelated, and hence very probable that they are really correlated linearly.

1.2. ERROR EVALUATION

In the present determination of the diffusion coefficients, errors have been propagated from four independent sources. They are 1) the sputtered crater depth, d_0 , from which a unit channel thickness Δx is derived, 2) the slope, A , of the inverse error-function plot against channel number which is generated by a measured sputtering profile, 3) the diffusion annealing time, t , and 4) the annealing temperature, T . The first three sources attach the error to individual diffusion coefficients through Eq. 12 in the text,

or

$$D = \frac{1}{t} \left(\frac{\Delta x}{2A} \right)^2.$$

Due to Eq. 1-2, the uncertainty of a diffusion coefficient is

$$\frac{\delta D}{D} = \left[\left(2 \frac{\delta \Delta x}{\Delta x} \right)^2 + \left(2 \frac{\delta A}{A} \right)^2 + \left(\frac{\delta t}{t} \right)^2 \right] \quad \text{Eq. 1-13}$$

since the uncertainties in Δx , A and t are independent and considered random. The typical uncertainty in an annealing time was about 2 minutes or less, which was attributed to the elapsed time for the rise and fall of the sample temperature to and from the preset annealing temperature. It has thus been ignored compared to the other sources.

The uncertainty in a unit channel thickness, Δx , was estimated from the directly measured crater depths, $\{d_{o,i} \pm \delta d_{o,i}\}$. The uncertainty in the depth of the i th crater, $\delta d_{o,i}$, was taken as the maximum range of the true value with 100 % confidence, or $[d_{o,i} - \delta d_{o,i}, d_{o,i} + \delta d_{o,i}]$. Although the relative uncertainties, $|\delta d_{o,i}/d_{o,i}|$ were mostly about 10 %, some of them amounted to as much as 50 %. In order to even up these uncertainties, the measured crater depths normalized with respect to the primary ion beam current, d_o/I_p , were least-square fitted to a linear dependence on the sputtering times, t , assuming that the sputtering rate was constant for a constant primary accelerating voltage. The straight line of best fit was represented by Eq. 1 in the text

or

$$\bar{d} = (At + B)I_p \text{ cm,} \quad \text{Eq. 1-14}$$

where, due to Eq.'s 1-5 to 1-10,

$$A = (1.3 \pm 0.2) \times 10^{-10} \text{ cm sec}^{-1} \text{ nA}^{-1}$$

and

$$B = (3.2 \pm 0.7) \times 10^{-7} \text{ cm nA}^{-1} .$$

For the set, $\{(t_i, d_{o,i}/I_{p,i})\}$ of size $1 \leq i \leq 10$ as shown in Fig. 4 in the text, the linear correlation coefficient was

$$r = 0.97.$$

The error in a corrected depth, \bar{d} , was then evaluated from Eq. 1-14 on the basis of Eq. 1-3 rather than Eq. 1-2 to improve its reliability. Since the errors associated with the sputtering time and the primary ion beam current were negligibly small, $\sigma_{\bar{d}}$ was assessed as

$$\sigma_{\bar{d}} = I_p (t\sigma_A + \sigma_B) \quad \text{Eq. 1-15}$$

or

$$\sigma_{\bar{d}} = I_p [(2 \times 10^{-11})t + (7 \times 10^{-8})] \text{ cm,}$$

which was rather an overestimation as already pointed out. The corrected crater depth was subsequently converted to a unit channel thickness by dividing by the total number of channels, N , or

$$\Delta x = d/N \quad \text{Eq. 2}$$

with a uncertainty

$$\sigma_{\Delta x} = \frac{1}{N} \sigma_d \quad \text{Eq. 1-16}$$

again due to Eq. 1-2 or Eq. 1-4. The relative errors, $\sigma_{\Delta x}/\Delta x$ based on Eq. 2 and Eq. 1-16 were 20-30 % in the present work as shown in Table 2-2 in Appendix 2.

The uncertainty in the slope δA in Eq. 1-13 was also evaluated by Eq. 1-8, from the straight line of best fit,

$$\text{erf}^{-1} \frac{C-C_0}{C_s-C_0} = An + B, \quad \text{Eq. 1-17}$$

for a data set $\{n, \text{erf}^{-1} \frac{C-C_0}{C_s-C_0}\}$ which was extracted from the sputtering profile as described in Chapter 4. The standard deviation, σ_A , may be regarded as representing the various errors originated from SIMS in-depth profiling. The relative errors of the slopes, σ_A/A , varied from 1 % to 9 % with one-half of them falling between 1 and 2 %. The correlation factors were also larger than 0.97 as shown in Table 2-1 in Appendix 2.

Therefore, the uncertainty in a diffusion coefficient determined in the present work was represented in terms of the standard deviation,

$$\frac{\sigma_D}{D} = 2 \left[\left(\frac{\sigma_{\Delta x}}{\Delta x} \right)^2 + \left(\frac{\sigma_A}{A} \right)^2 \right]^{1/2}, \quad \text{Eq. 1-18}$$

which was somewhat of an overestimation in view of Eq. 1-15. As shown in Table 5 in the text, they ranges from 20 % to 60 %.

These diffusion coefficients with the assessed standard deviation were then used to derive the diffusion-related parameters on the basis of the empirical equation,

$$D = D_0 \exp(-Q/kT), \quad \text{Eq. 1-19}$$

in which the fourth source of error would come into play. The method of least squares was again employed for the set of $\{1/T, \ln D\}$. Since the uncertainties in the diffusion coefficients were comparable in size and those in the annealing temperatures were negligibly small compared to the standard deviations of diffusion coefficients, Eq. 1-5 to Eq. 1-10 were used to calculate the slope along with the standard deviation, from which the activation energy, $Q \pm \sigma_Q$, was extracted, and the intercept along with the standard deviation, from which the preexponential factor, $\ln D_0 \pm \sigma_{\ln D_0}$, was extracted. The result is Eq. 16 in the text or

$$\ln D_{\text{best}} = - (13.22 \pm 0.96) - \frac{3.24 \pm 0.13 \text{ eV}}{kT} ,$$

from which the precision of D_{best} is estimated as

$$\frac{D}{D_{\text{best}}} \leq 0.96 + \frac{0.13 \text{ eV}}{kT} .$$

In the temperature range of 1700°C to 1000°C, the relative standard deviation of the diffusion coefficient varies from 1.7 to 2.2. Thus, the diffusion coefficient determined in the present work may be claimed to be precise within approximately a factor 2, but it is rather an overestimation in view of Eq. 1-3.

APPENDIX 2. EXPERIMENTAL DATA

Measured sputtering profiles, intensity ratio of ^{18}O to ^{16}O vs. channel number, for surface gas-exchange are provided in what follows along with the corresponding plots of $\text{erf}^{-1}(C/C_0)/(C_s - C_0)$ as a function of channel number, where C , C_0 and C_s are measured concentration ^{18}O , natural abundance, and artificial abundance, respectively. A sputtering profile and the corresponding erf^{-1} plot are designated as (a) and (b), respectively, behind a specimen designation, for example, R29-1650-1(a) and R29-1650-1(b), respectively. Results of analyses are summarized in Table 2-1, where uncertainties associated with slopes, A , and intercepts, B , of the inverse error function plots are represented by standard deviations σ_A and σ_B , respectively. The standard deviations and the linear correlation factors have been calculated by Eq.'s 1-8, 1-9, and 1-11 in Appendix 1.

Diffusion coefficients extracted from the slopes, A , are given in Table 2-2. *Measured diffusion coefficients* in the 6th column of the table are based on the as-measured thicknesses of a unit channel in the 4th column, that is, derived from direct measurement of the final depth of the specific sputtered crater. On the other hand, *calibrated diffusion coefficients* in the last column are based on the corrected (or calibrated) unit channel thickness of column 5, obtained by using sputtering rate averaged over the entire data set

according to Eq. 1. One set of the best estimates, given in Table 5 in the text has been obtained by taking weighted averages of the calibrated D's at temperatures where multiple diffusion coefficients are available. A weighted average, $D \pm \sigma_D$, of a set $\{D_i \pm \sigma_{D_i}\}$ is defined⁴⁰ as

$$D = \Sigma W_i D_i / \Sigma W_i \quad \text{Eq. 2-1}$$

and

$$\sigma_D = (\Sigma W_i)^{-\frac{1}{2}} \quad \text{Eq. 2-2}$$

where

$$W_i = 1/\sigma_{D_i}^2 .$$

Especially for the 1400°C samples, the weighted average of R31-1400-1 and -2 has been averaged again with R27-1400 arithmetically or with the same weights since the datum for R27-1400 is statistically independent of the others. Similarly, the independently determined diffusion coefficient for R27-1000 has been employed as a best estimate of diffusion coefficient at 1000°C. For a comparison, the diffusion coefficients in the 6th column, which were determined from the measured values of the sputtered crater depths, are plotted against reciprocal temperature in Fig. 2-31. When equivalent weights are assigned to each element of the data set $\{1/T, \ln D\}$ to simplify the method of least squares though it is not a very rigorous way,^{40,44} the set of 15 elements may well be represented by

$$D = (4.0_{-3.6}^{+12.7}) \times 10^{-6} \exp \left(- \frac{3.35 \pm 0.19 \text{ eV}}{kT} \right) \text{ cm}^2/\text{sec}$$

Eq. 2-3

where the linear correlation coefficient is -0.98. This diffusion coefficient is, as a matter of fact, the same as the diffusion coefficient based on the calibrated crater depths, Eq. 16 in the text. It is, however, noted that, by evening up uncertainties associated with raw measurements of the sputtered crater depths with the help of Eq. 1, the precision of the activation energy and the preexponential factor in Eq. 2-3 are improved from 6 % to 4 % and 11 % to 7 %, respectively.

Table 2-1. Linear Regression Data of Diffusion Profiles, $Y=An+B$

where $Y=\text{erf}^{-1}(C-C_0)/(C_s-C_0)$

Specimen Designation	Artificial Abundance Mg ¹⁸ O at % [*]	Slope ($A \pm \sigma_A$) $\times 10^2$	Intercept ($B \pm \sigma_B$) $\times 10^2$	Correlation r	Entry ⁺ N
R29-1650-1	9.24	1.24 \pm 0.02	-3.8 \pm 0.7	0.995	110
R29-1600-2	7.96	0.641 \pm 0.012	-4.2 \pm 1.4	0.993	39
R29-1550-1	13.82	1.43 \pm 0.09	-4.2 \pm 3.4	0.955	65
R31-1500-1	44.63	1.75 \pm 0.03	4.8 \pm 1.0	0.994	57
R31-1500-3	37.78	1.60 \pm 0.02	-8.3 \pm 0.7	0.996	67
R31-1400-1	33.89	2.09 \pm 0.04	-4.7 \pm 0.9	0.995	36
R31-1400-2	42.32	1.519 \pm 0.013	-8.7 \pm 0.5	0.998	56
R27-1400	8.03	4.1 \pm 0.3	26 \pm 3	0.972	14
R31-1300-1	48.15	2.41 \pm 0.03	-10 \pm 1	0.997	37
R31-1300-2	52.53	2.24 \pm 0.03	0.80 \pm 0.82	0.996	50
R27-1200-5	7.64	13.0 \pm 0.8	10 \pm 6	0.980	13
R27-1100-1	7.22	6.9 \pm 0.3	10 \pm 3	0.990	18
R27-1100-2	8.23	8.0 \pm 0.5	12 \pm 3	0.986	10
R27-1100-3	7.05	10.6 \pm 1.0	6.7 \pm 6.0	0.968	10
R27-1000	9.85	15.3 \pm 0.7	24 \pm 3	0.995	10

* calculated from the secondary ion intensity ratio of ¹⁸O to ¹⁶O according to Eq. 13

+ size of a data set {n,Y}

Table 2-2. Diffusion Data

Specimen Designation	Annealing		$\Delta x (\times 10^{-7} \text{ cm})$		$D (\text{cm}^2/\text{sec})$	
	Temp ($^{\circ}\text{C}$)	Time (hr)	measured	calibrated	measured	calibrated
R29-1650-1	1650	2.0	2.2 ± 0.2	1.5 ± 0.4	$(1.1 \pm 0.2) \times 10^{-14}$	$(5.2 \pm 2.7) \times 10^{-15}$
R29-1600-2	1600	3.0	1.03 ± 0.05	1.0 ± 0.2	$(6.0 \pm 0.6) \times 10^{-15}$	$(5.9 \pm 2.4) \times 10^{-15}$
R29-1550-1	1550	4.7	1.5 ± 0.1	1.4 ± 0.4	$(1.6 \pm 0.3) \times 10^{-15}$	$(1.4 \pm 0.8) \times 10^{-15}$
R31-1500-1	1500	4.0	1.18 ± 0.06	1.6 ± 0.4	$(0.79 \pm 0.08) \times 10^{-15}$	$(1.5 \pm 0.8) \times 10^{-15}$
R31-1500-3	1500	4.0	1.67 ± 0.07	1.7 ± 0.5	$(1.9 \pm 0.2) \times 10^{-15}$	$(2.0 \pm 1.3) \times 10^{-15}$
R31-1400-1	1400	12.0	1.9 ± 0.2	2.1 ± 0.7	$(4.8 \pm 0.9) \times 10^{-16}$	$(5.7 \pm 3.6) \times 10^{-16}$
R31-1400-2	1400	12.0	2.0 ± 0.2	1.8 ± 0.6	$(10 \pm 2) \times 10^{-16}$	$(8.1 \pm 5.2) \times 10^{-16}$
R27-1400*	1400	15.0	1.81 ± 0.01		$(0.9 \pm 0.13) \times 10^{-16}$	*
R31-1300-1	1300	74.5	1.2 ± 0.4	2.0 ± 0.6	$(2.3 \pm 1.5) \times 10^{-17}$	$(6.4 \pm 4.1) \times 10^{-17}$
R31-1300-2	1300	74.5	1.5 ± 0.7	1.7 ± 0.5	$(4.2 \pm 3.9) \times 10^{-17}$	$(5.2 \pm 2.9) \times 10^{-17}$
R27-1200-5	1200	360.0	9.4 ± 0.2	9.4 ± 1.8	$(1.0 \pm 0.13) \times 10^{-17}$	$(1.0 \pm 0.4) \times 10^{-17}$
R27-1100-1	1100	480.0	2.35 ± 0.05	2.4 ± 0.4	$(1.7 \pm 0.2) \times 10^{-18}$	$(1.7 \pm 0.6) \times 10^{-18}$
R27-1100-2	1100	480.0	3.08 ± 0.08	3.2 ± 0.6	$(2.1 \pm 0.3) \times 10^{-18}$	$(2.3 \pm 0.9) \times 10^{-18}$
R27-1100-3	1100	480.0	4.03 ± 0.08	4.1 ± 1.3	$(2.1 \pm 0.4) \times 10^{-18}$	$(2.2 \pm 1.5) \times 10^{-18}$
R27-1000*	1000	960.0	3.8 ± 0.4		$(4.5 \pm 1.0) \times 10^{-19}$	*

* Sputtering data of these two specimens, obtained toward the completion of the series of measurements, were not included in the establishment of the linear sputtering rate equation, Eq. 1 in the text because the sputtering condition was different. The corresponding diffusion coefficients must therefore be taken to be independent of the others.

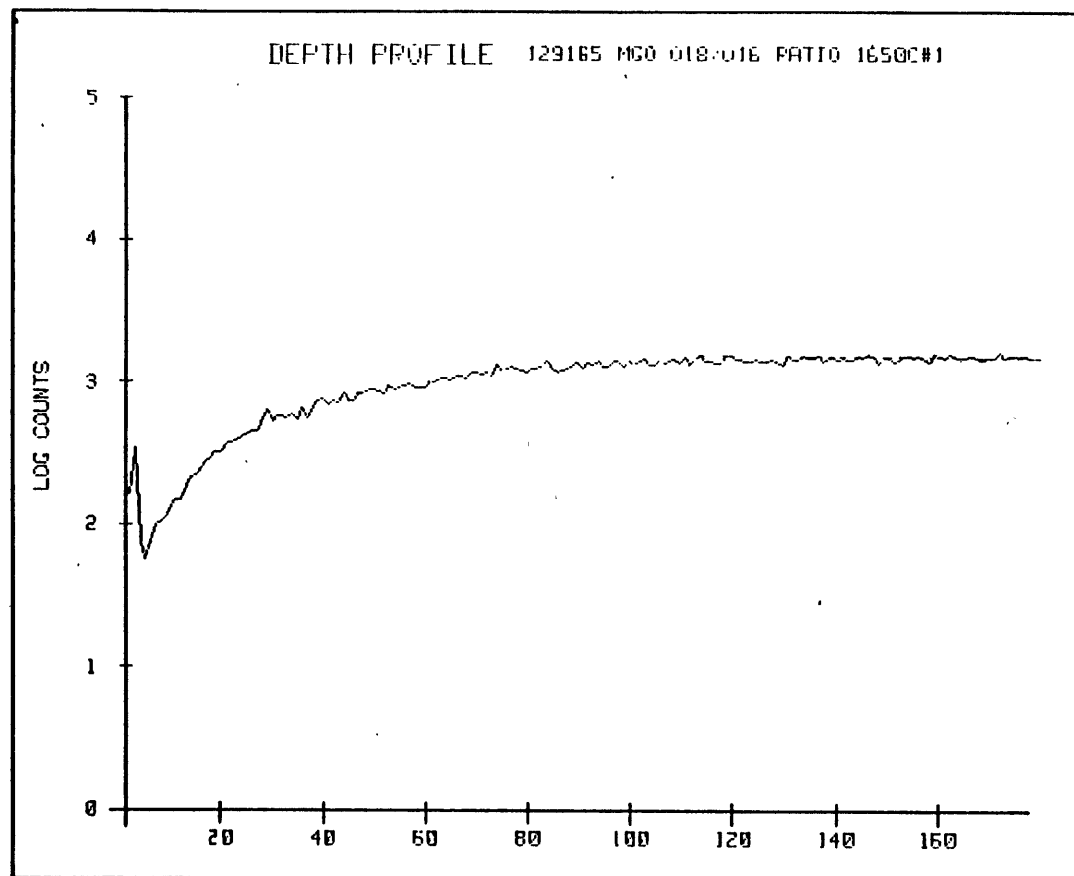


Fig. 2-1. R29-1650-1 (a)

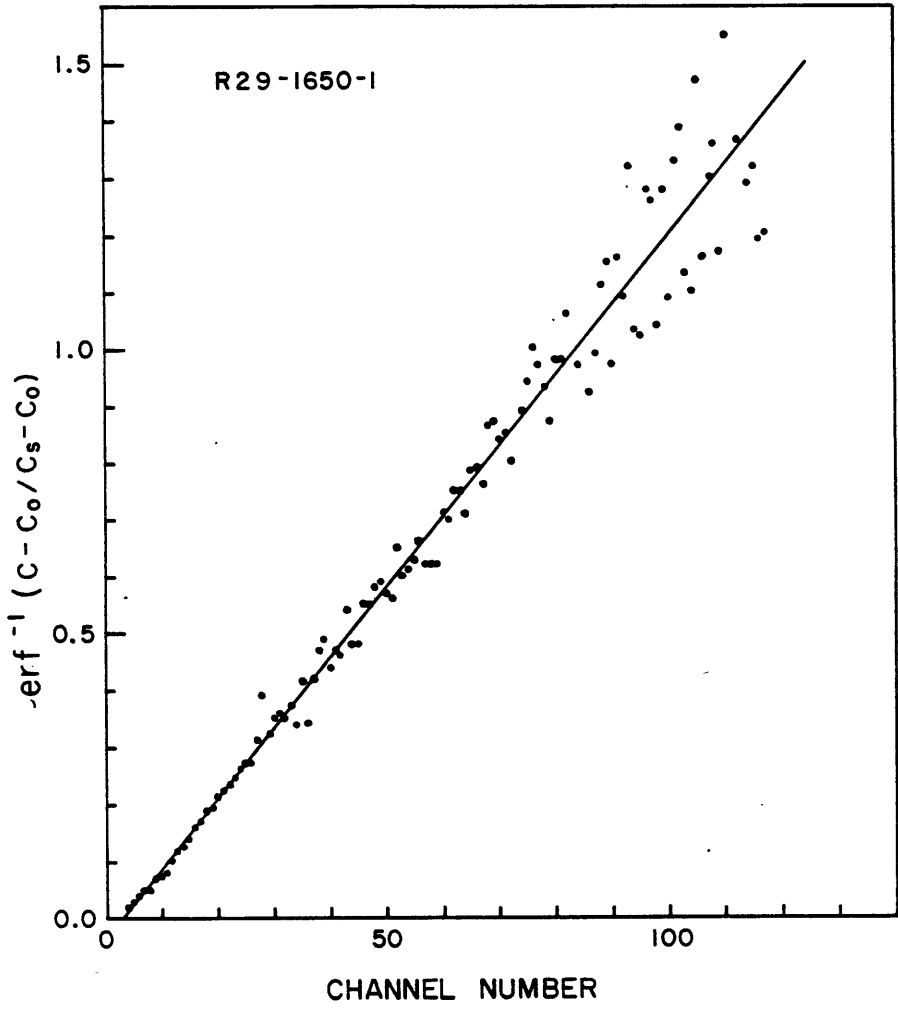


Fig. 2-2. R29-1650-1 (b)

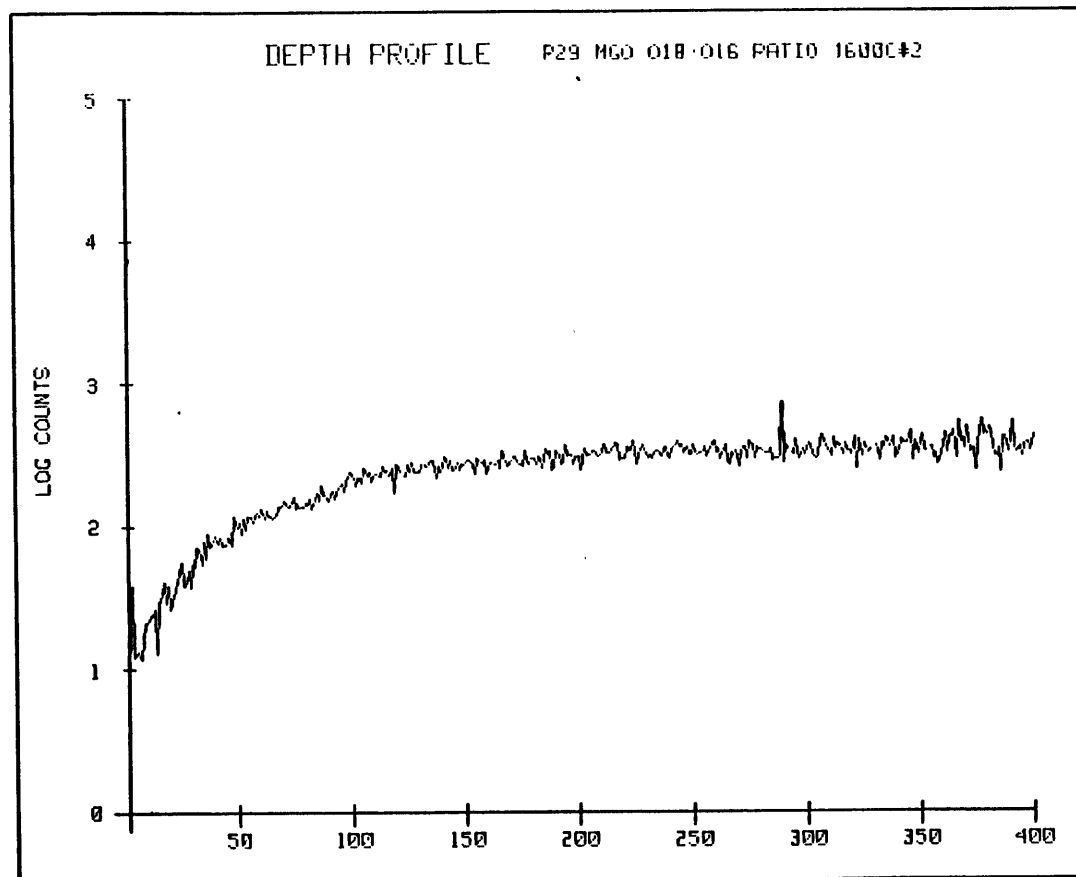


Fig. 2-3. R29-1600-2 (a)

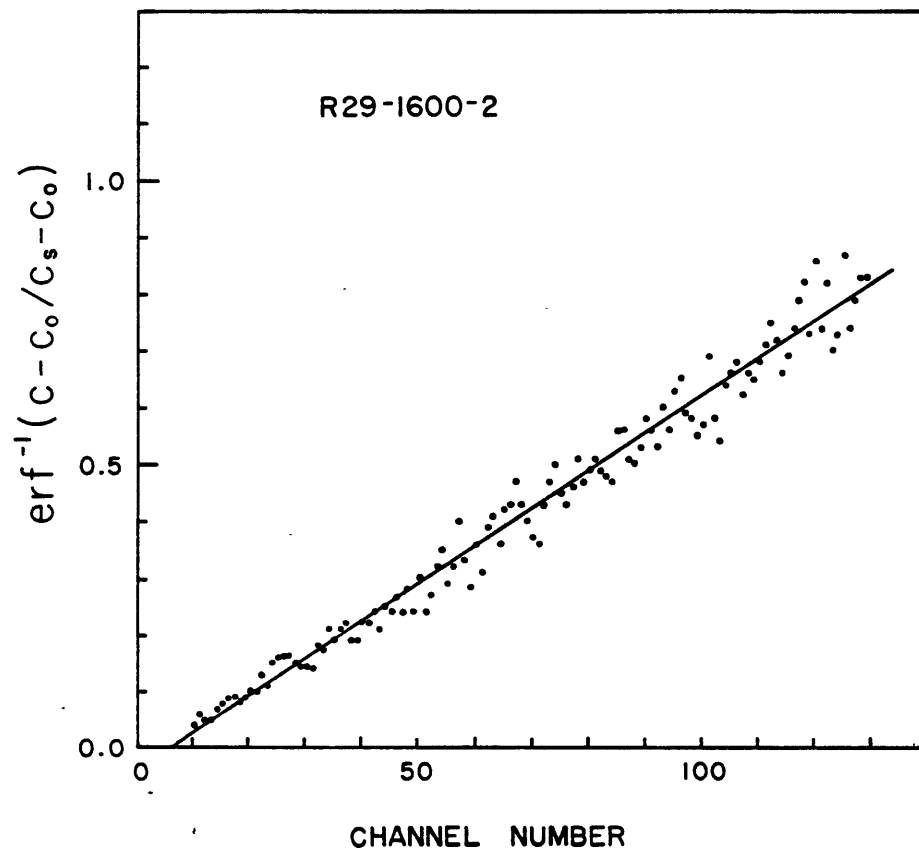


Fig. 2-4. R29-1600-2 (b)

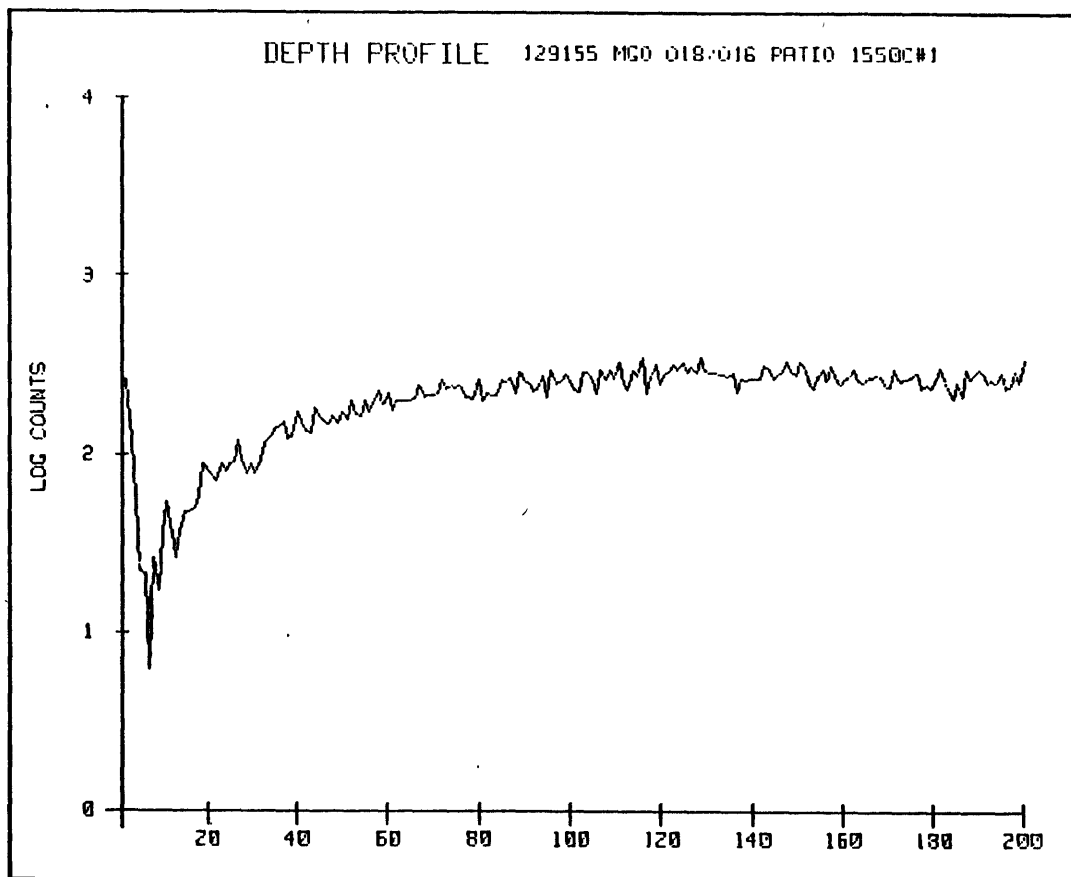


Fig. 2-5. R29-1550-1 (a)

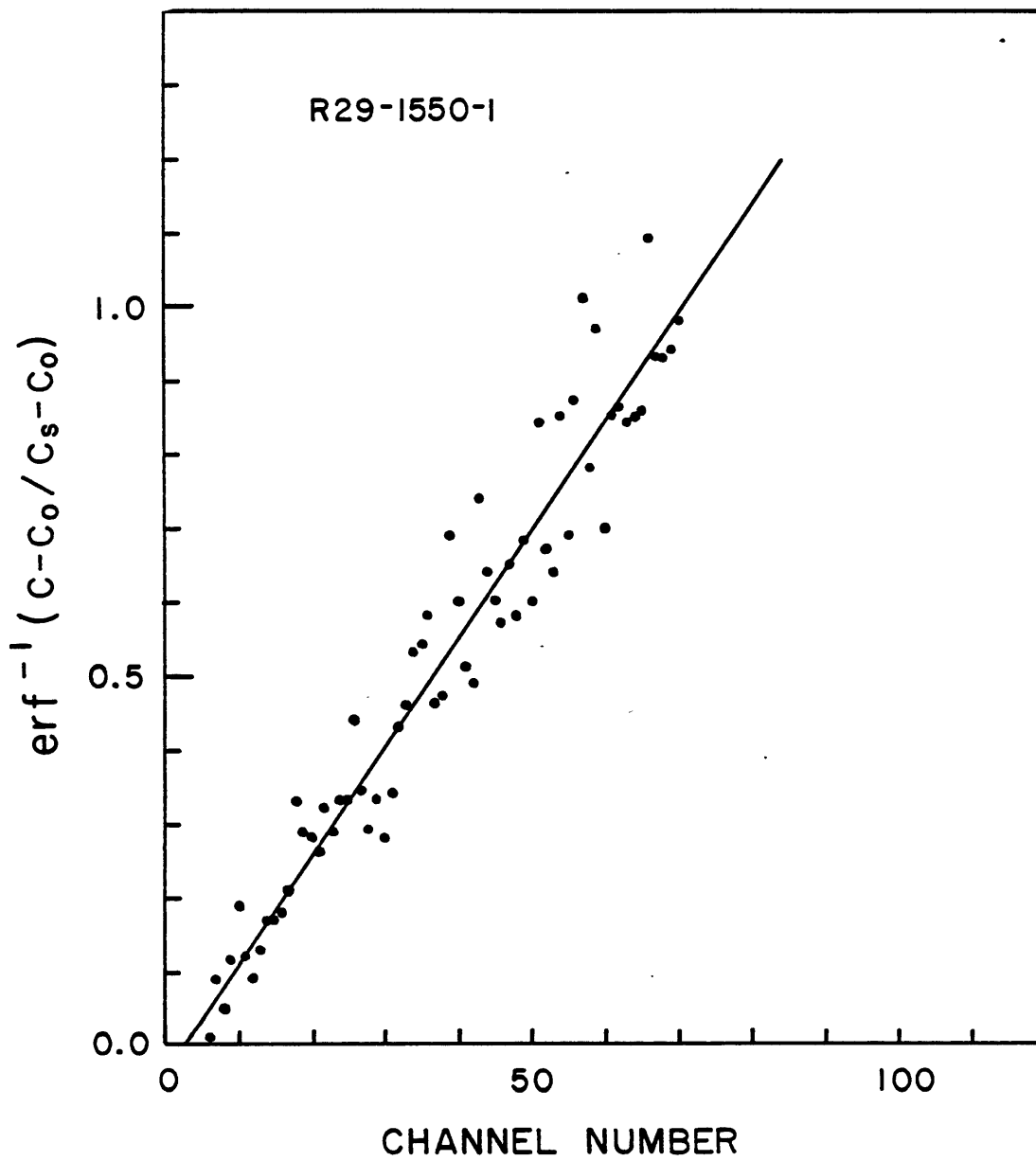


Fig. 2-6. R29-1550-1 (b)

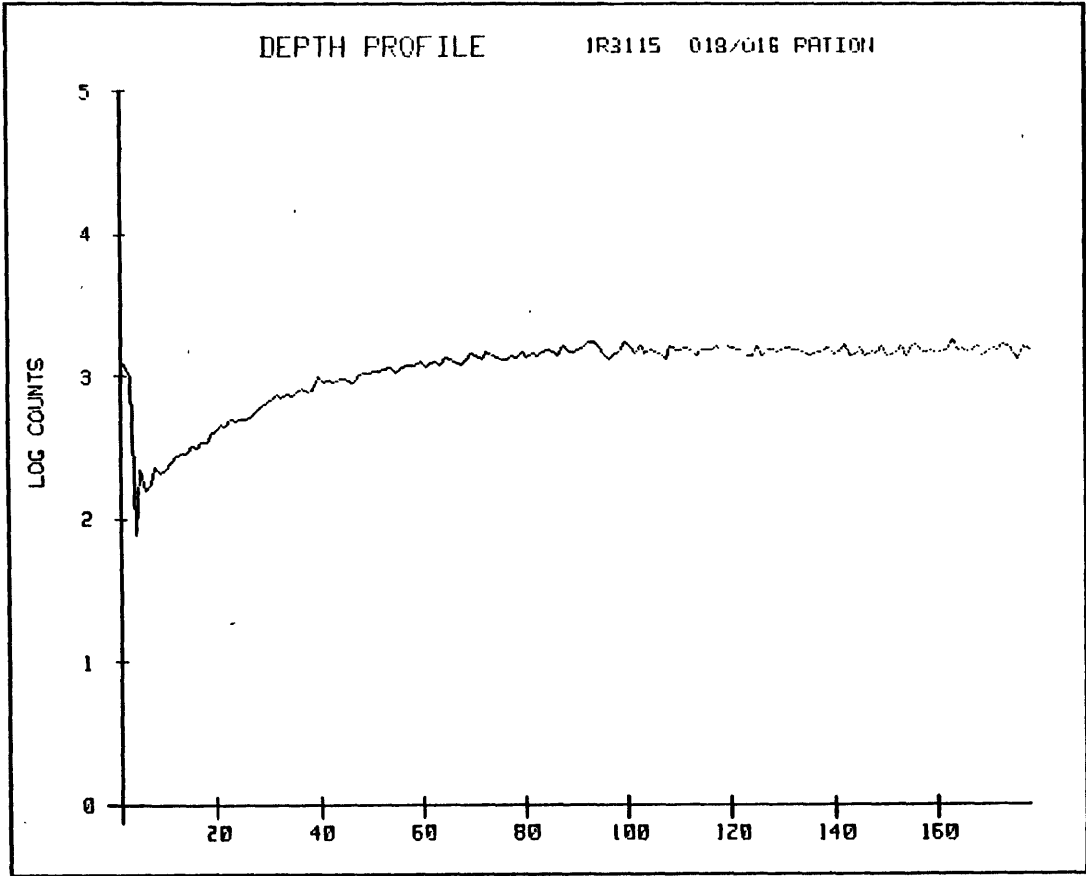


Fig. 2-7. R31-1500-1 (a)

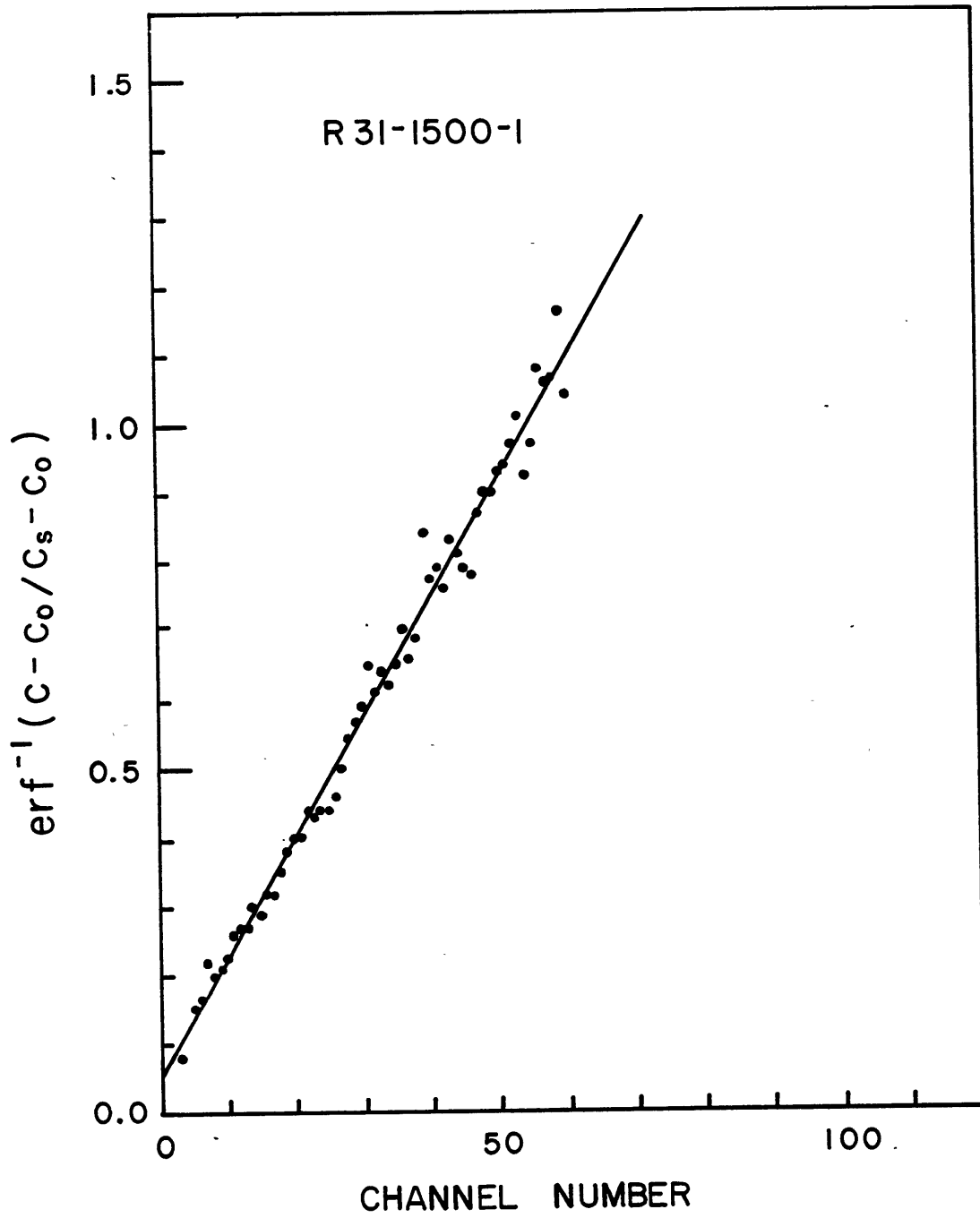


Fig. 2-8. R31-1500-1 (b)

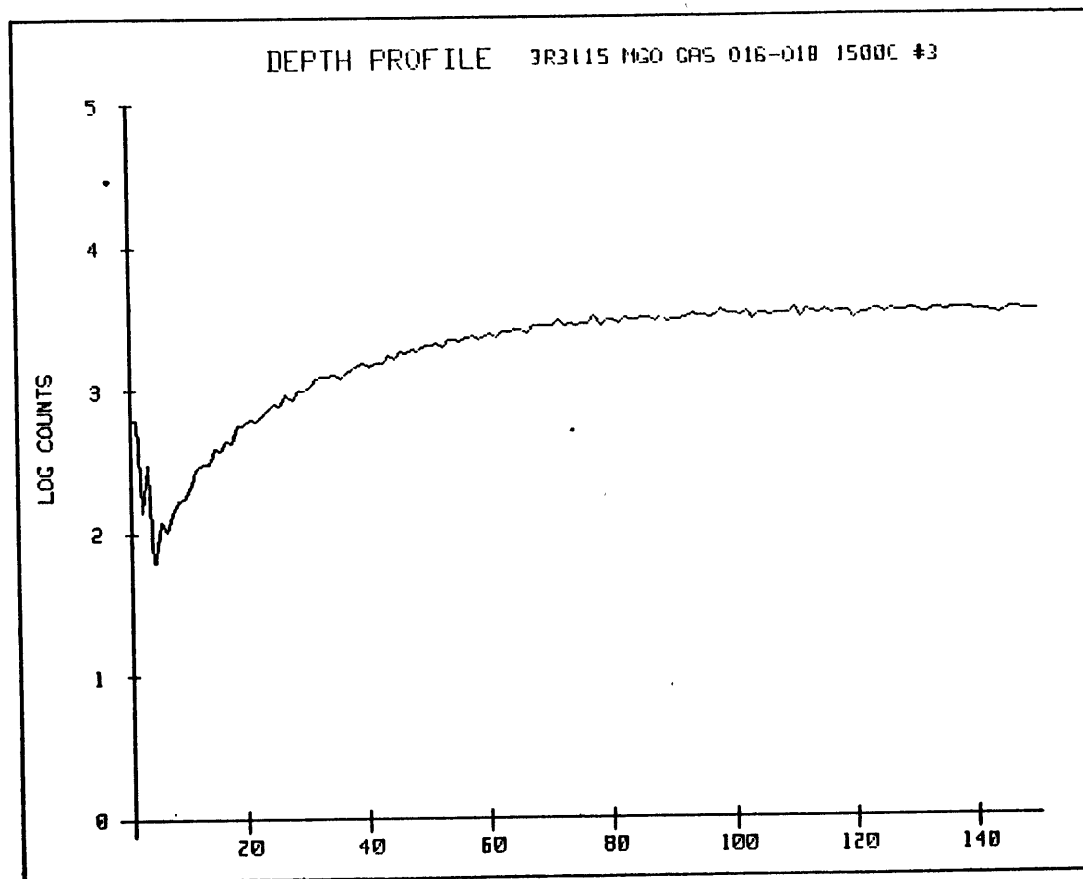


Fig. 2-9. R31-1500-3 (a)

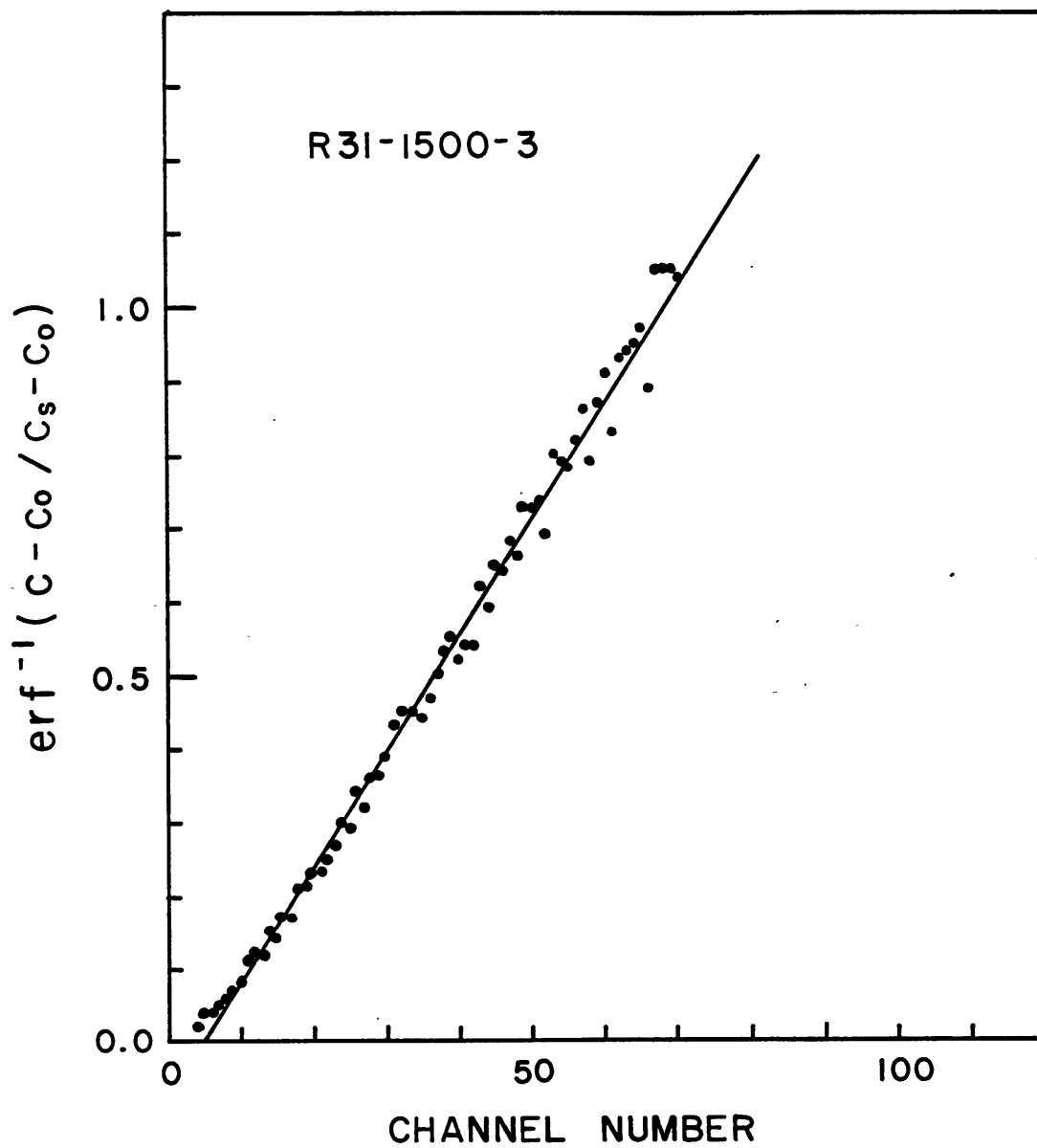


Fig. 2-10. R31-1500-3 (b)

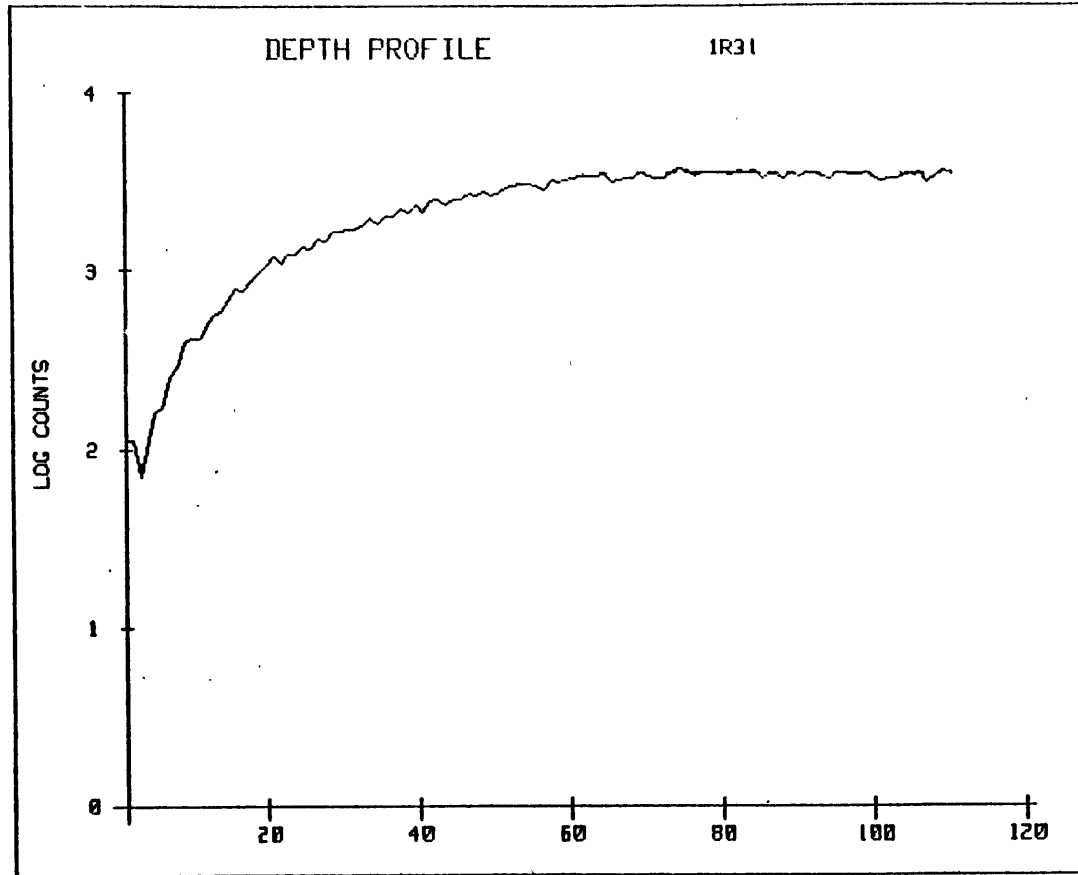


Fig. 2-11. R31-1400-1 (a)

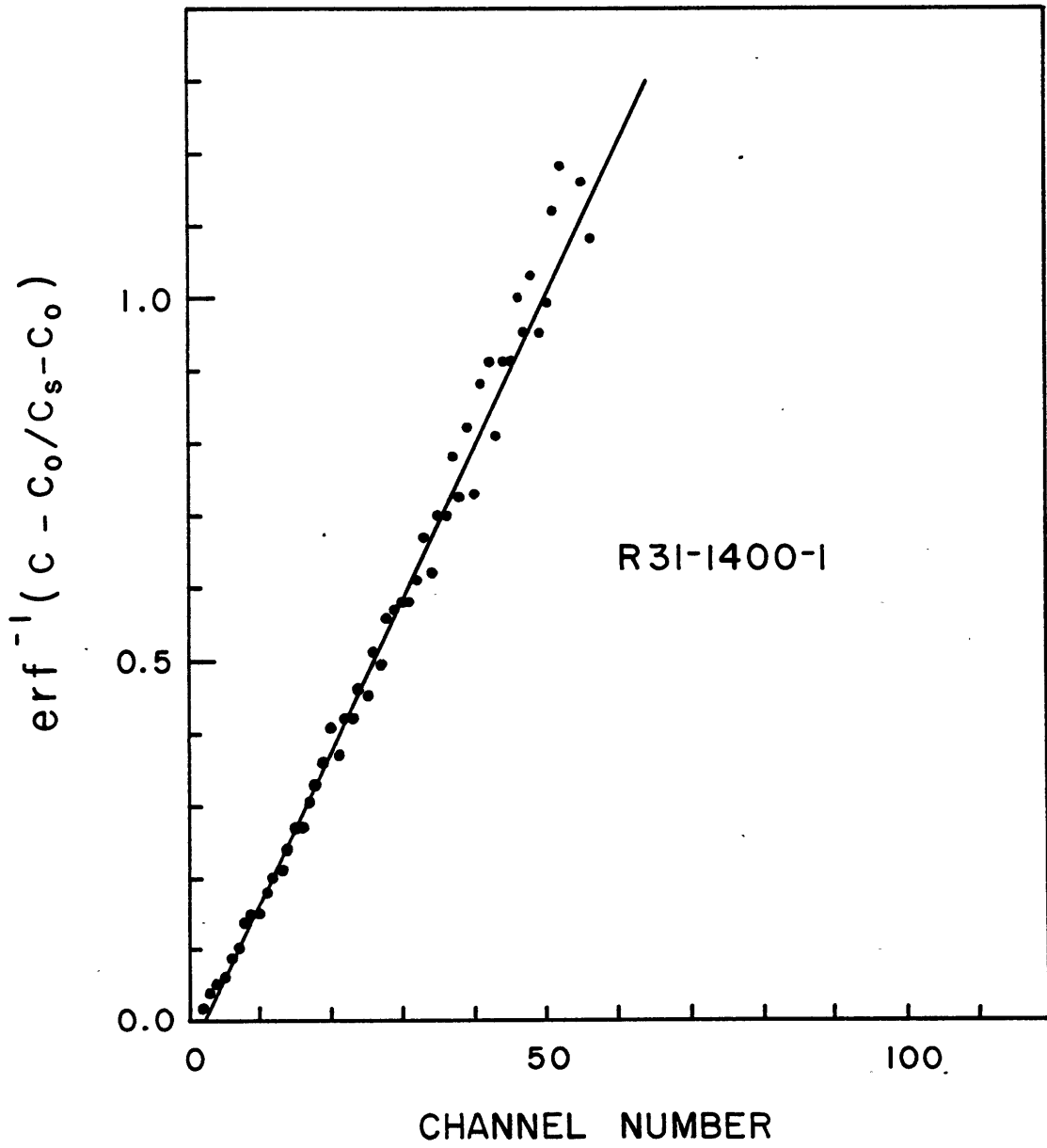


Fig. 2-12. R31-1400-1 (b)

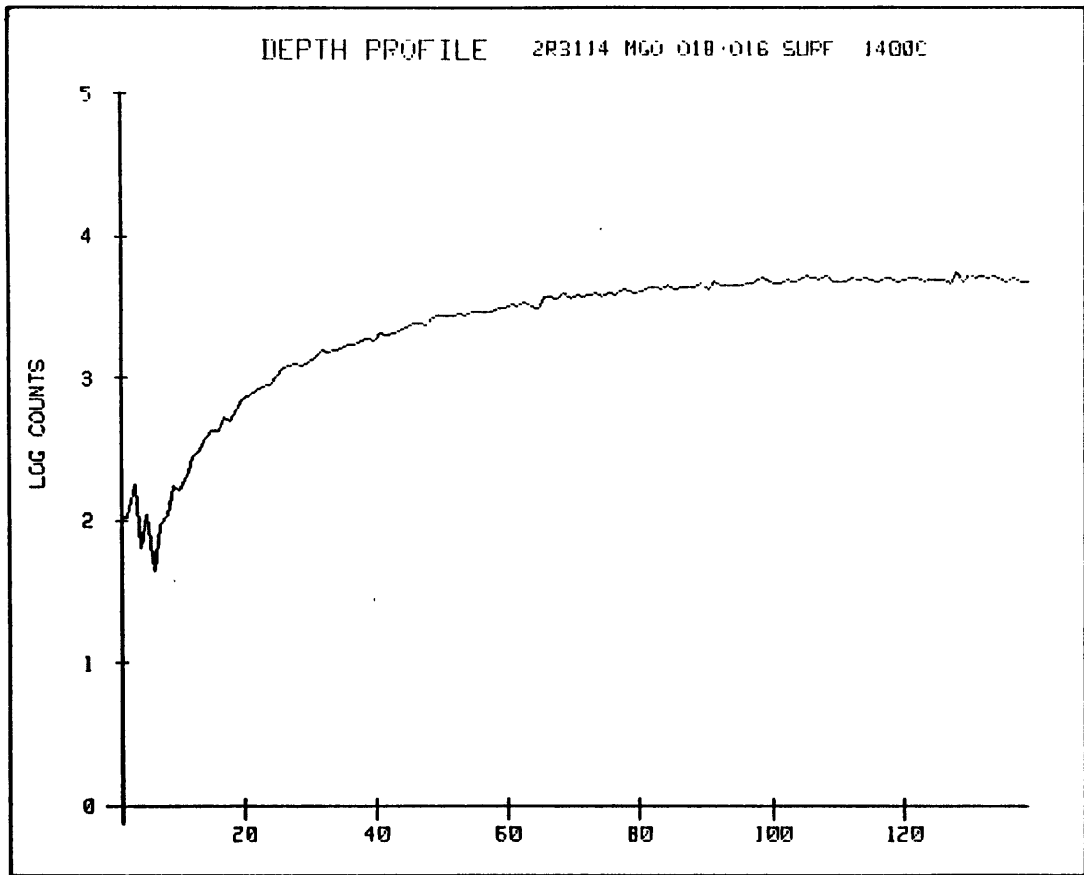


Fig. 2-13. R31-1400-2 (a)

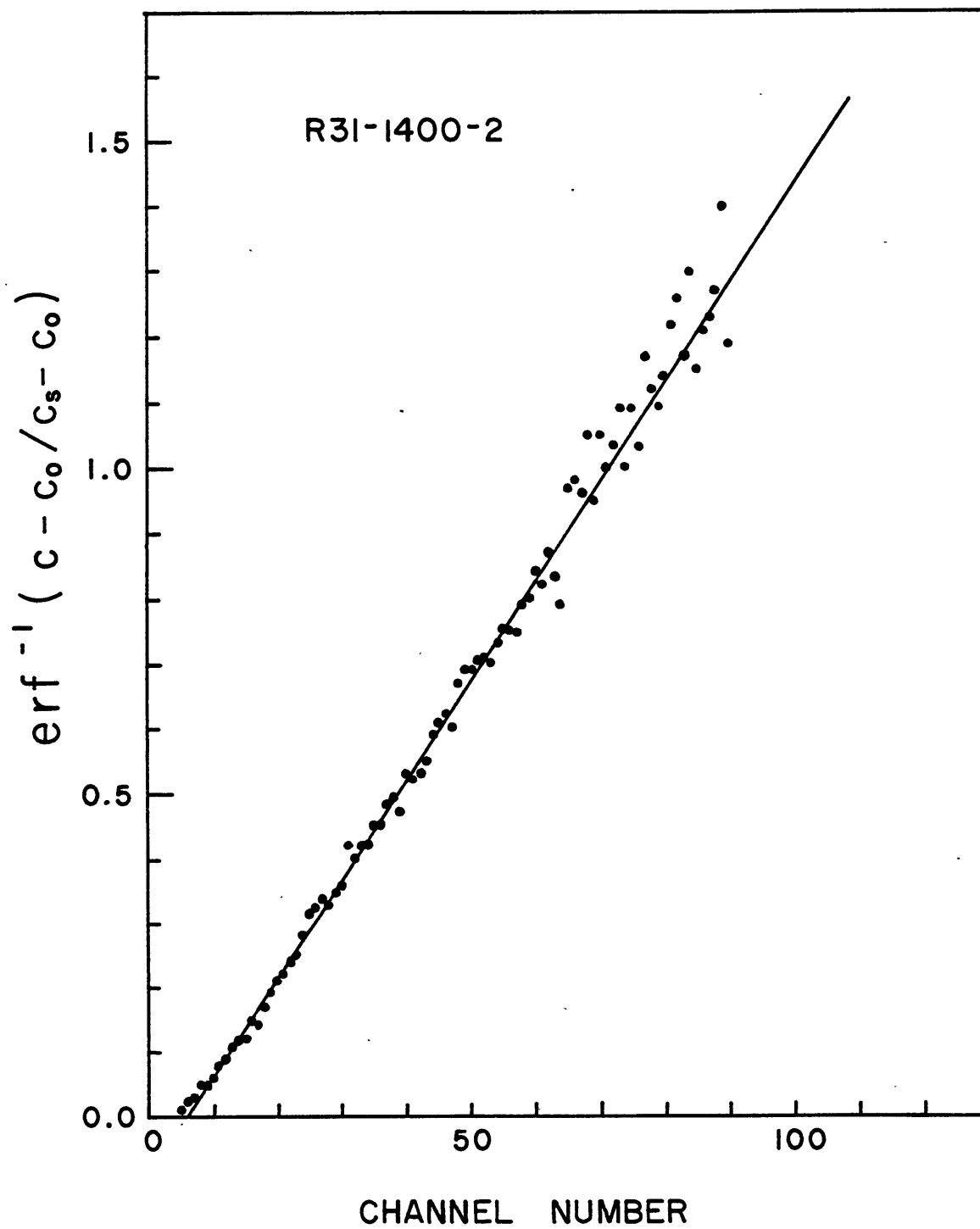


Fig. 2-14. R31-1400-2 (b)

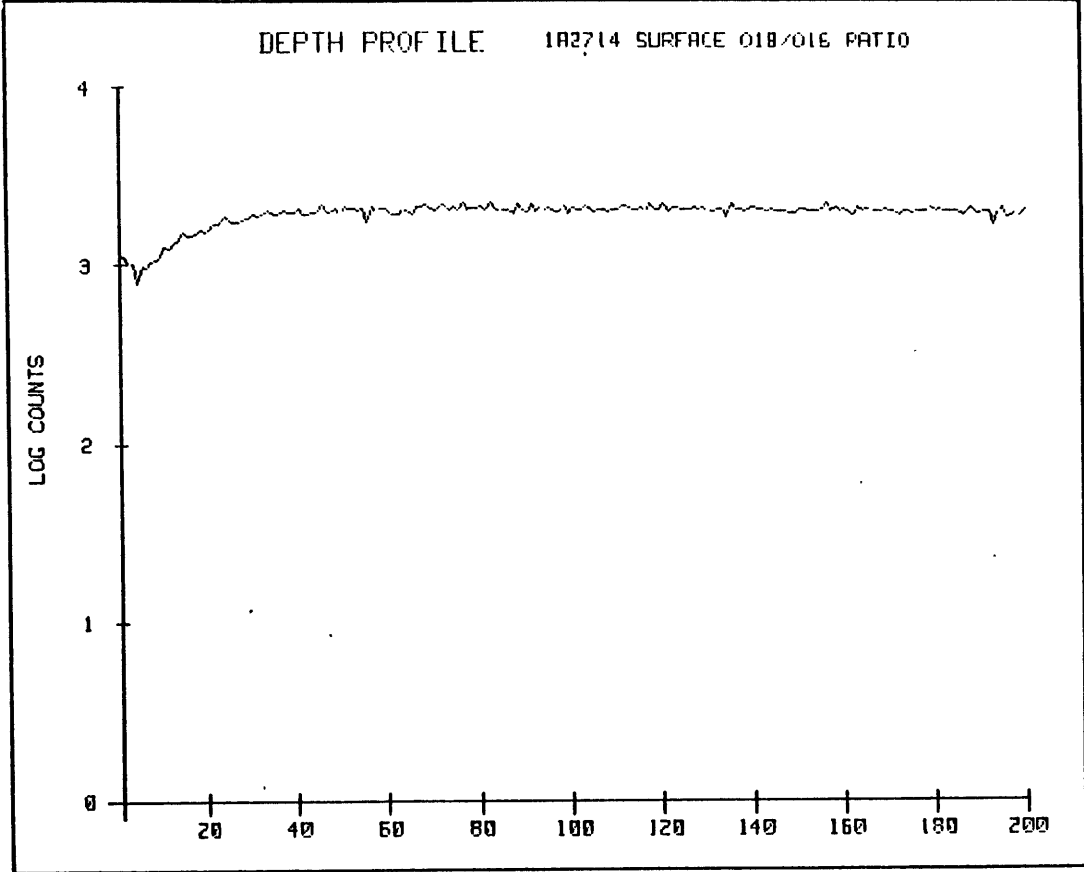


Fig. 2-15. R27-1400 (a)

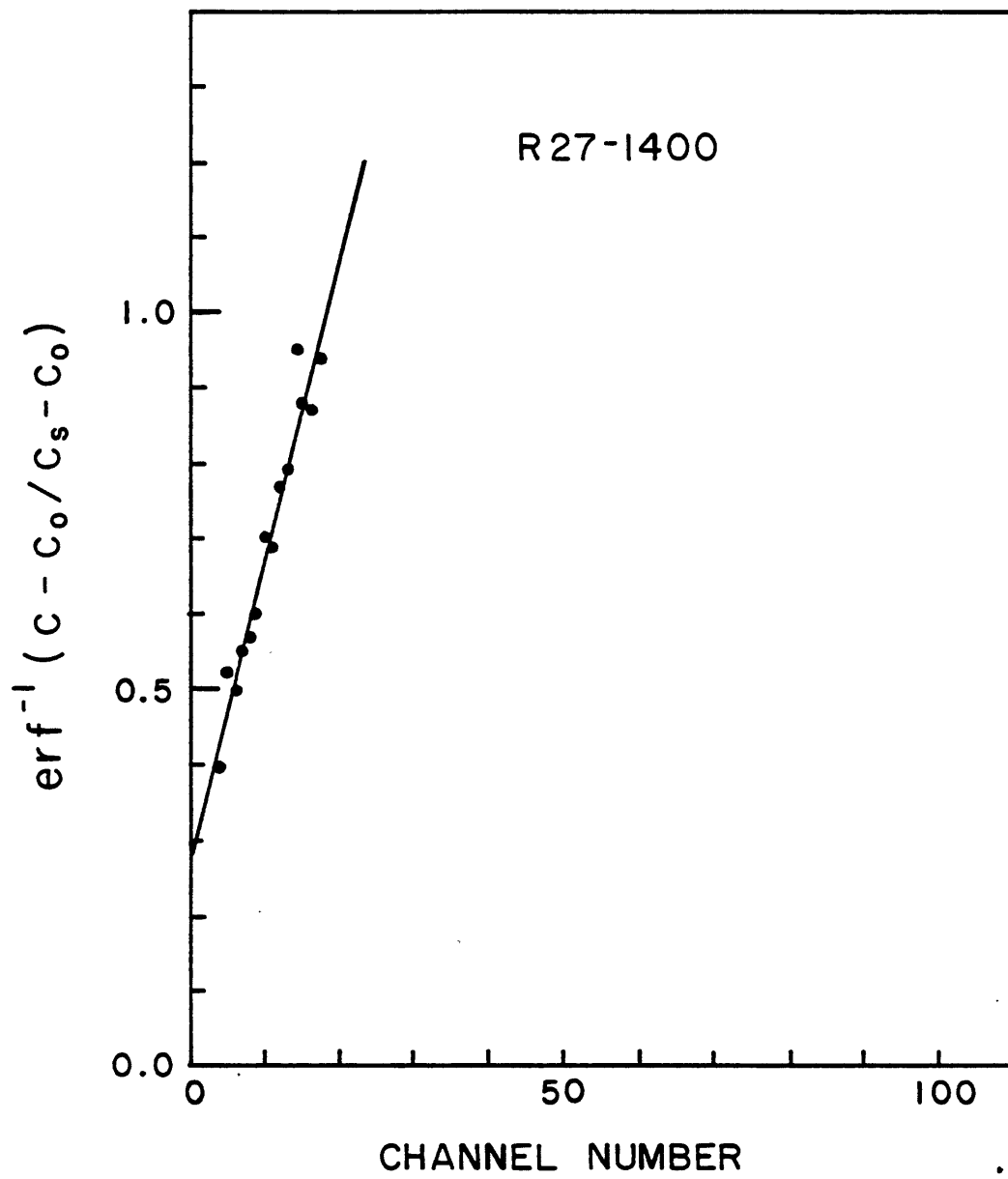


Fig. 2-16. R27-1400 (b)

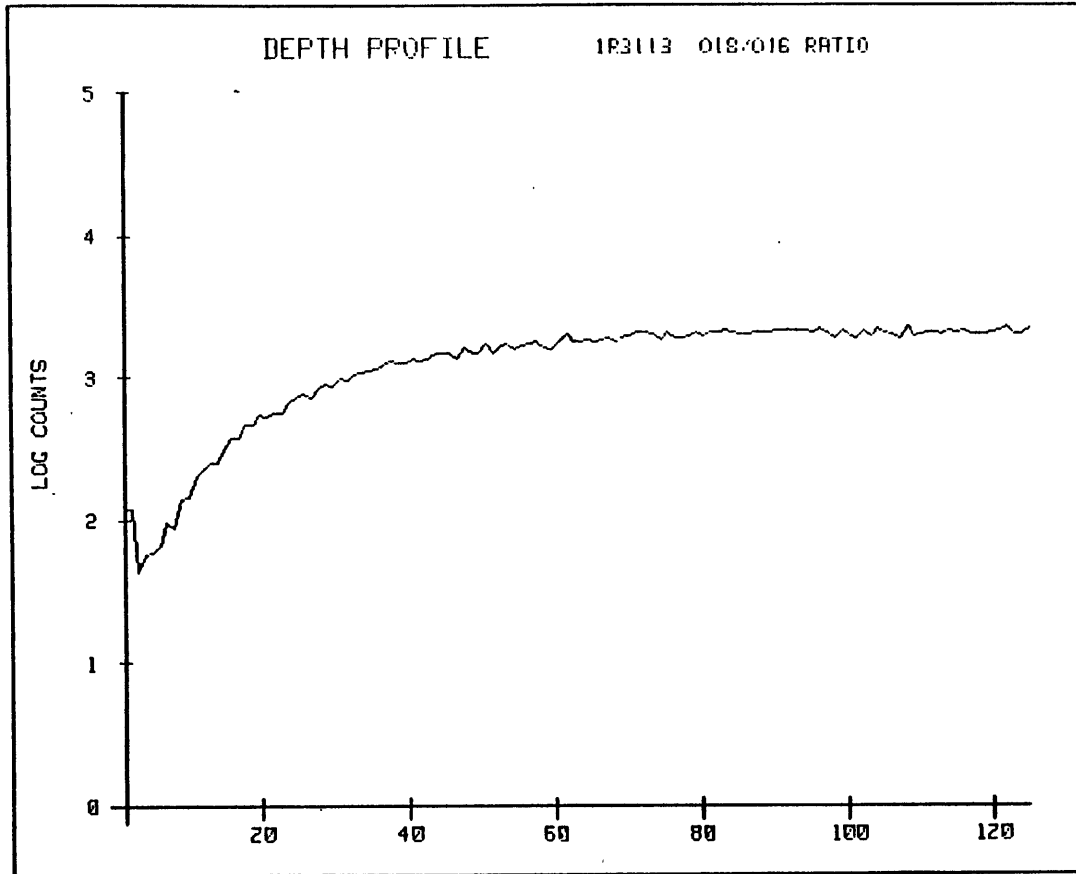


Fig. 2-17. R31-1300-1 (a)

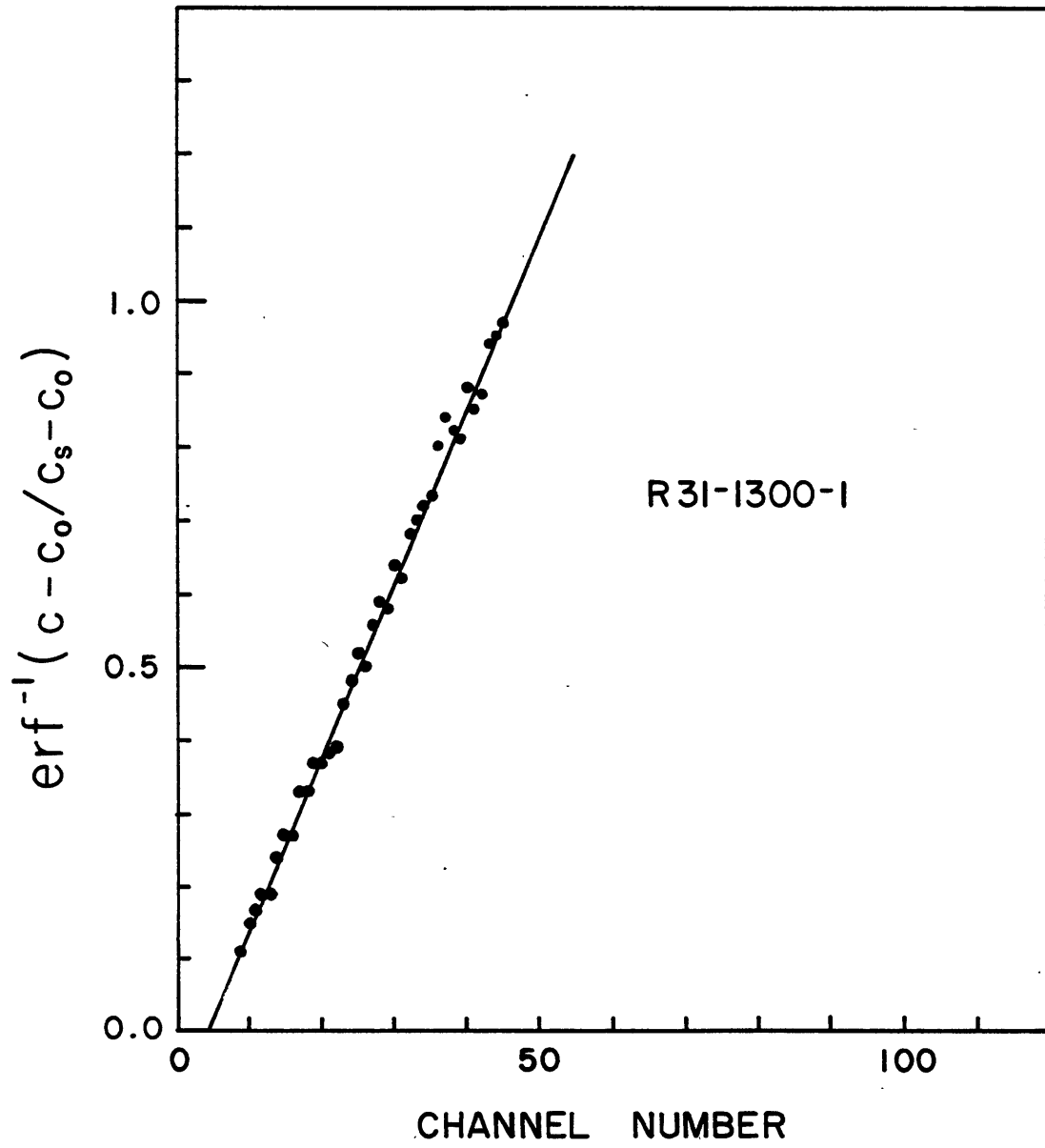


Fig. 2-18. R31-1300-1 (b)

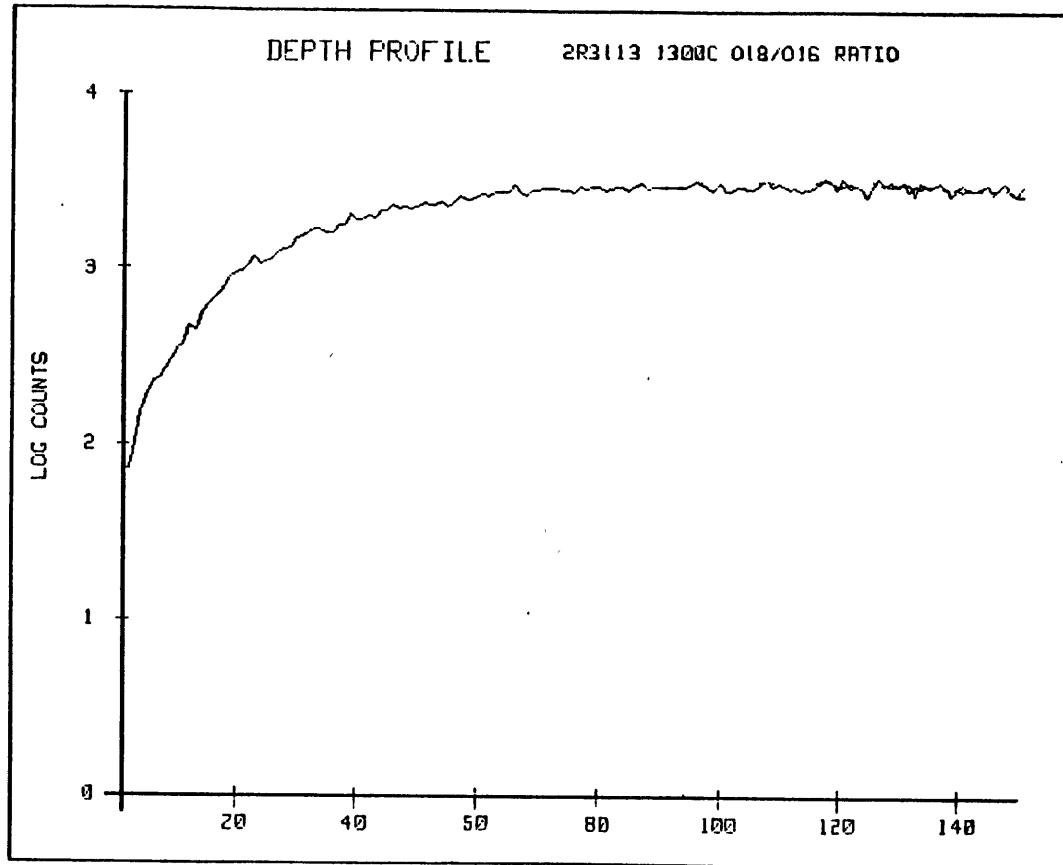


Fig. 2-19. R31-1300-2 (a)

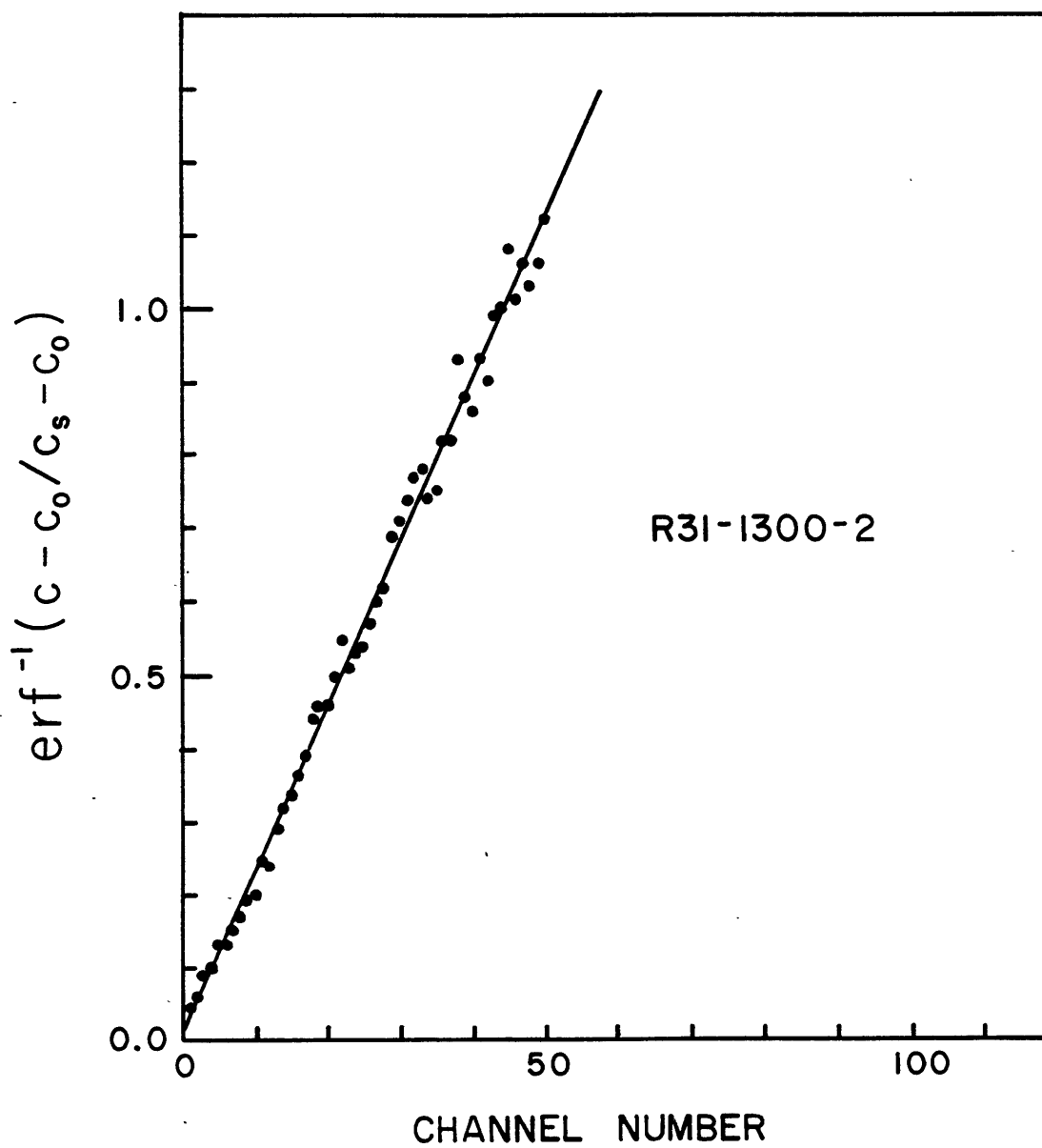


Fig. 2-20. R31-1300-2 (b)

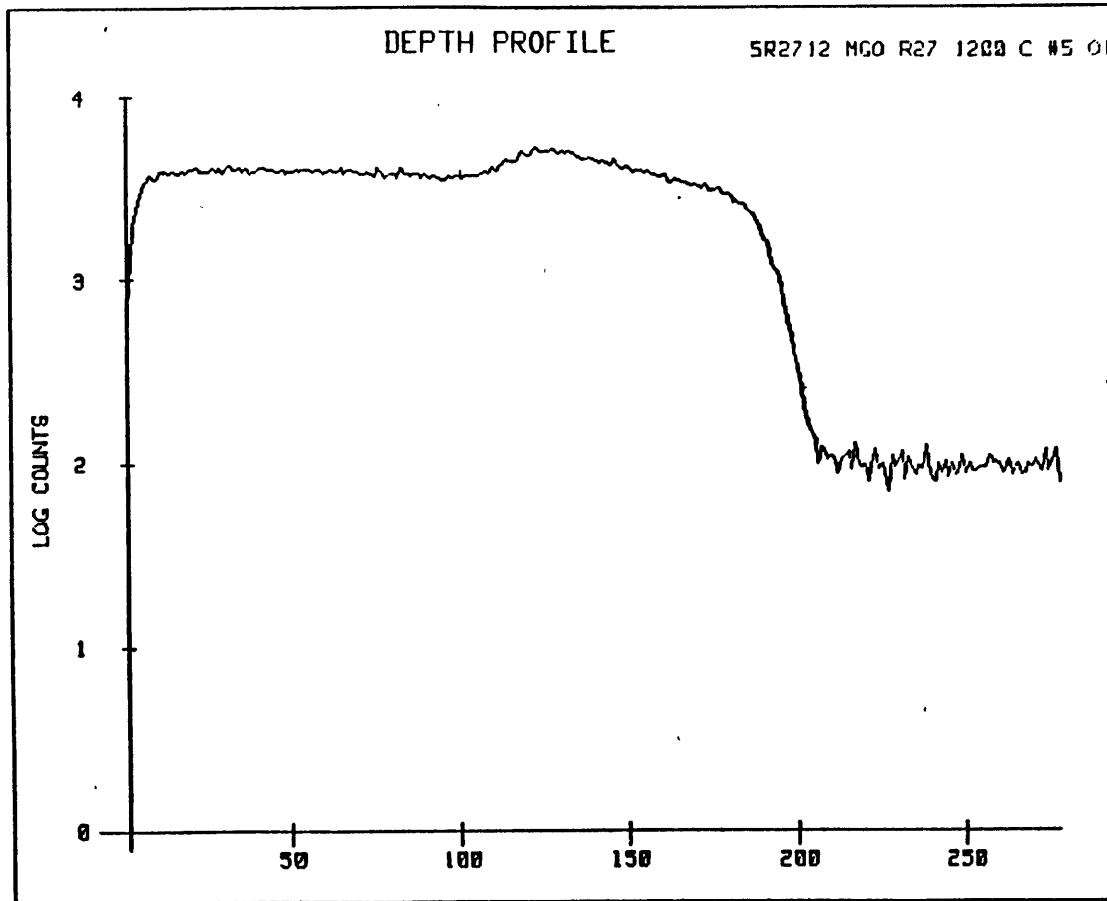


Fig. 2-21. R27-1200-5 (a)

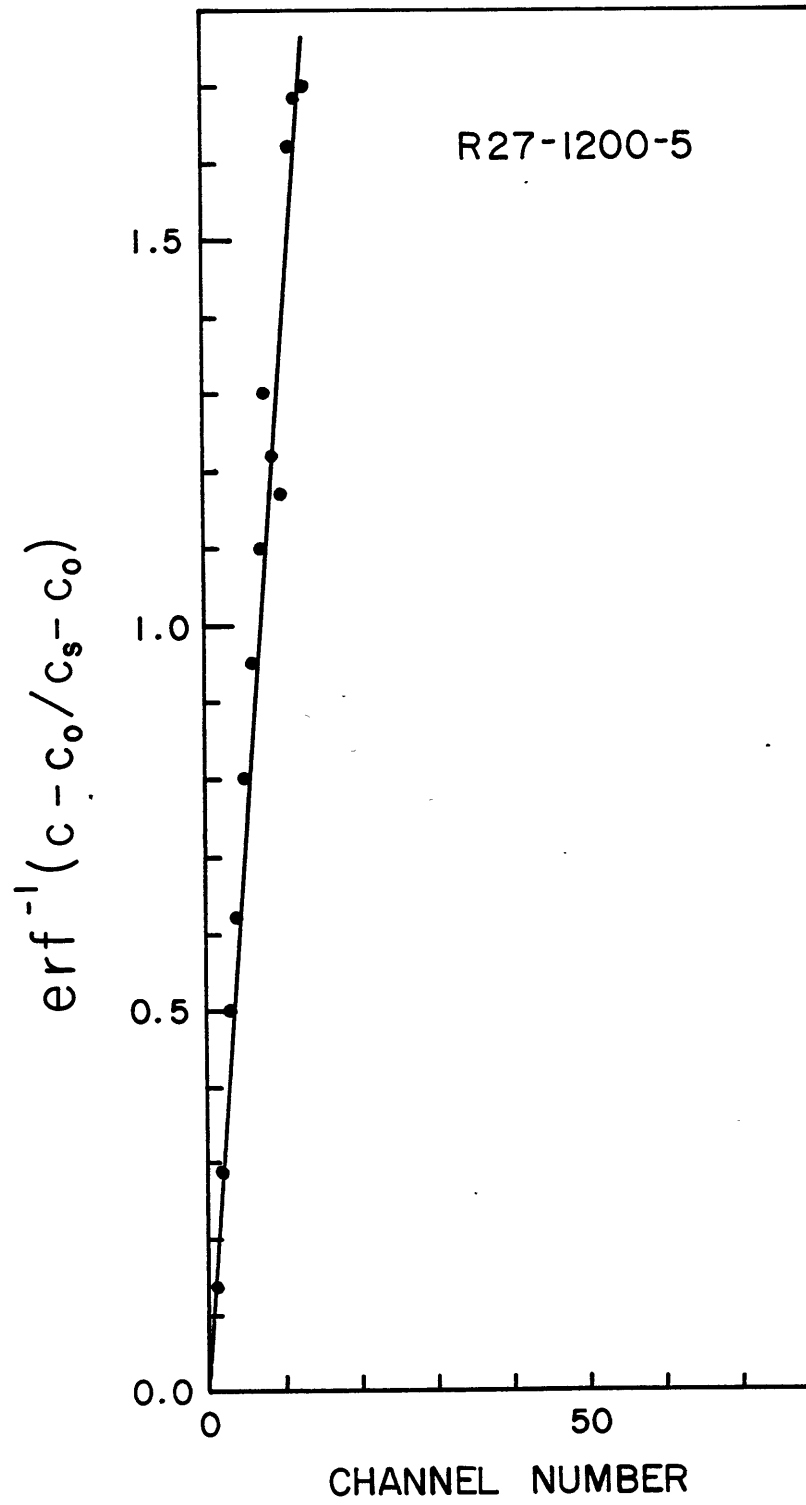


Fig. 2-22. R27-1200-5 (b)

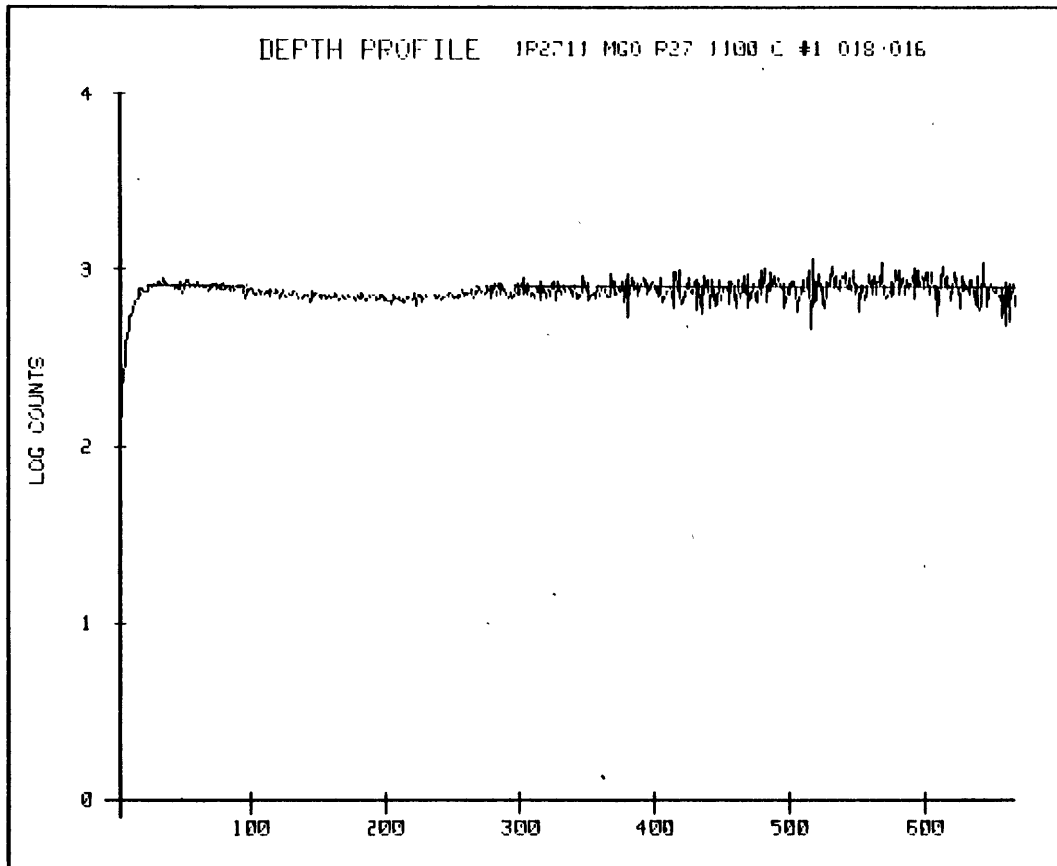


Fig. 2-23. R27-1100-1 (a)

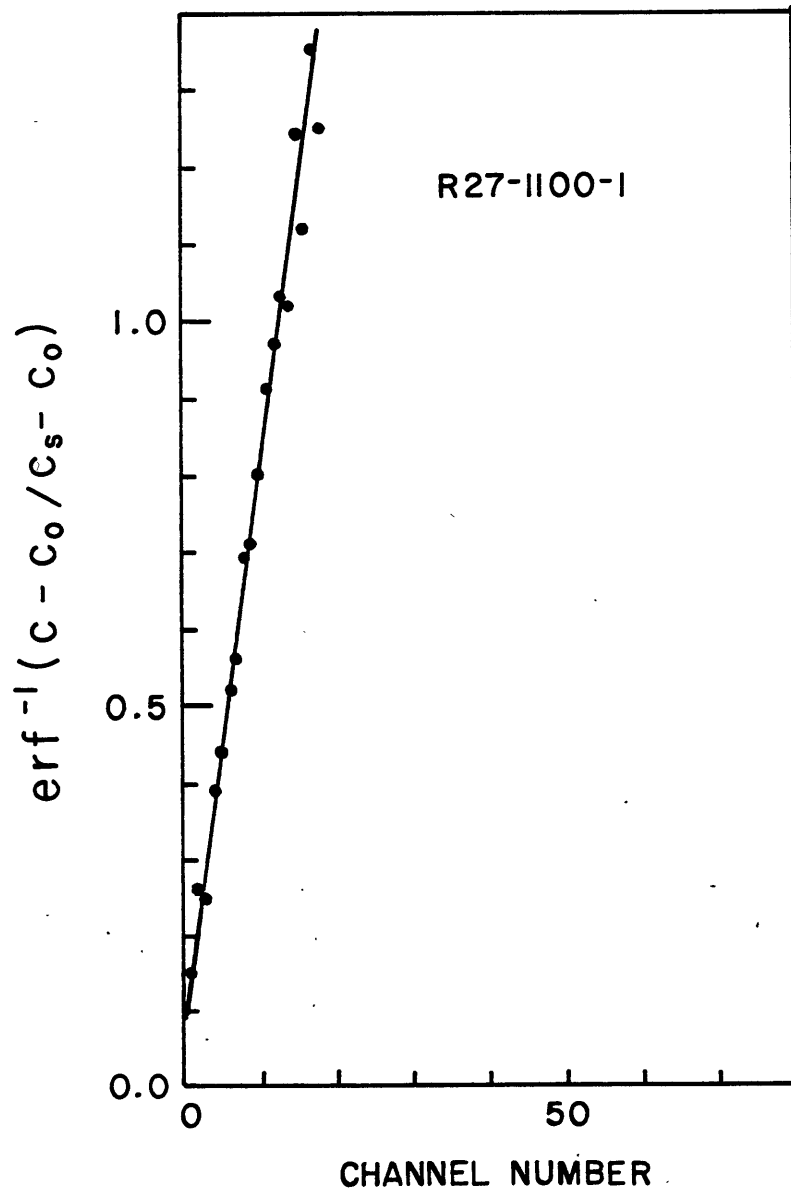


Fig. 2-24. R27-1100-1 (b)

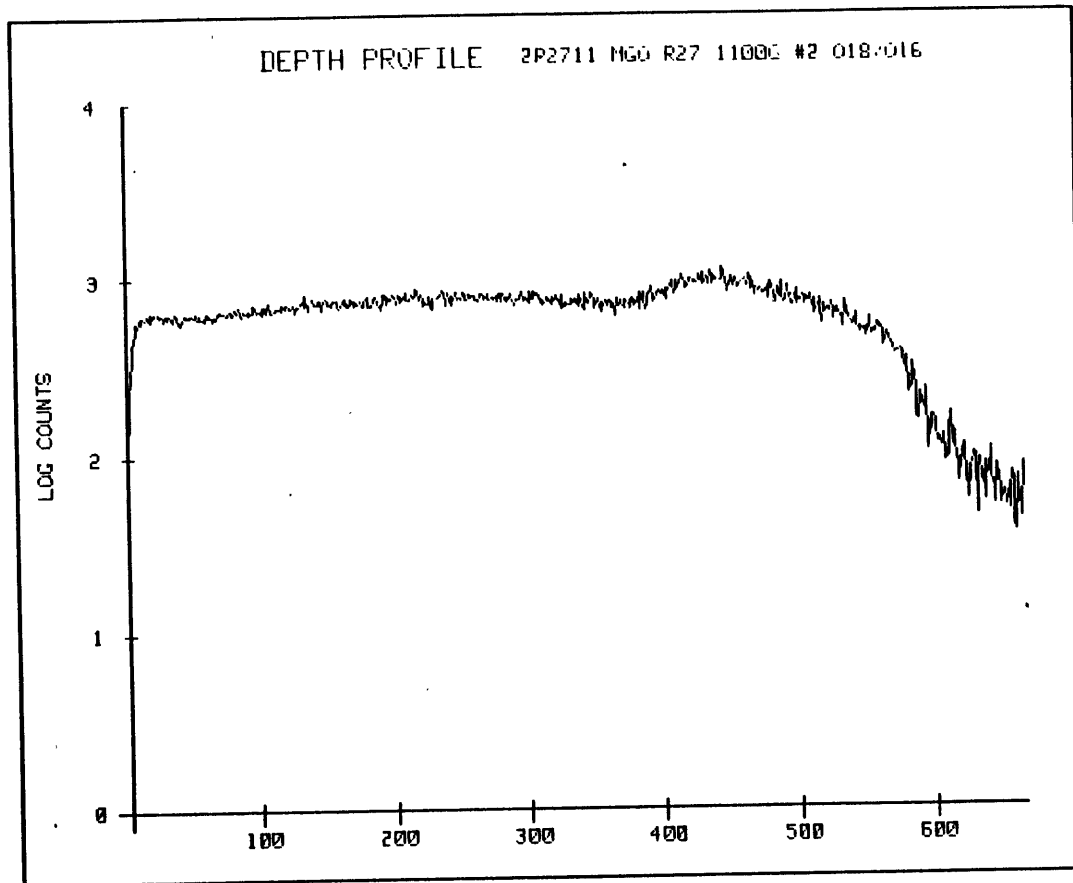


Fig. 2-25. R27-1100-2 (a)

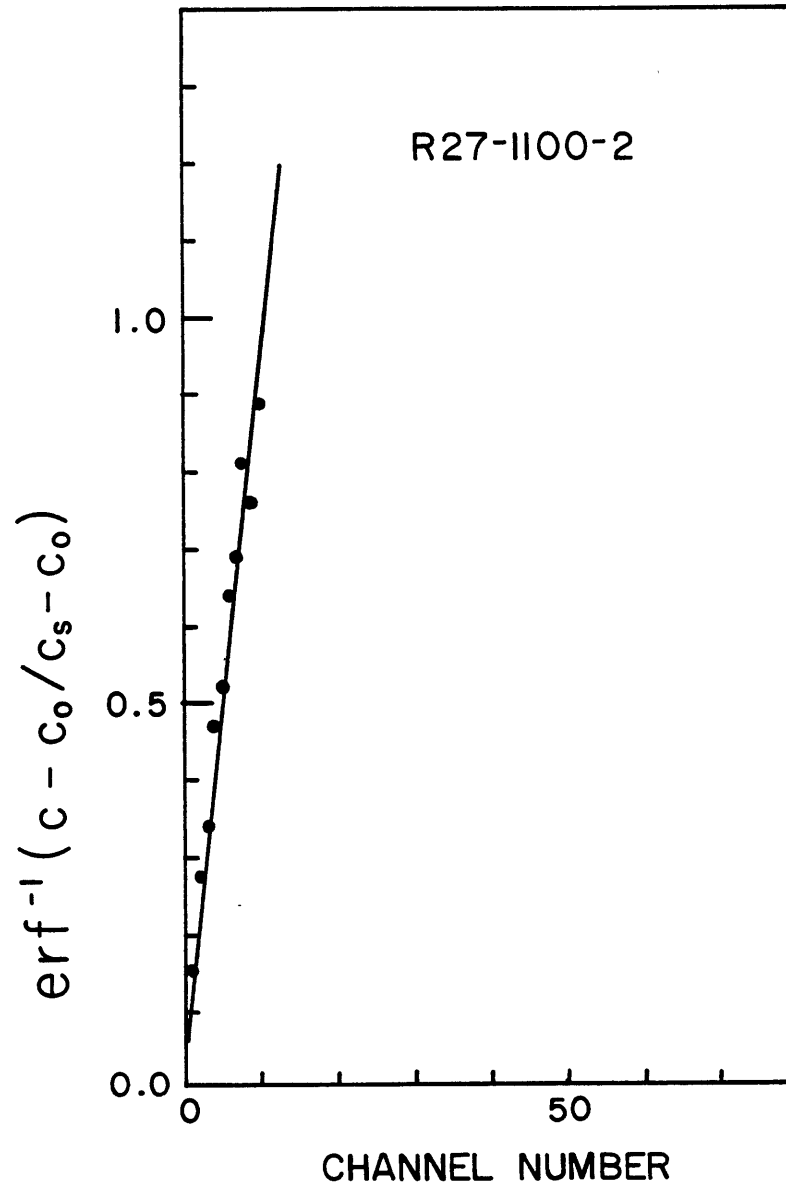


Fig. 2-26. R27-1100-2 (b)

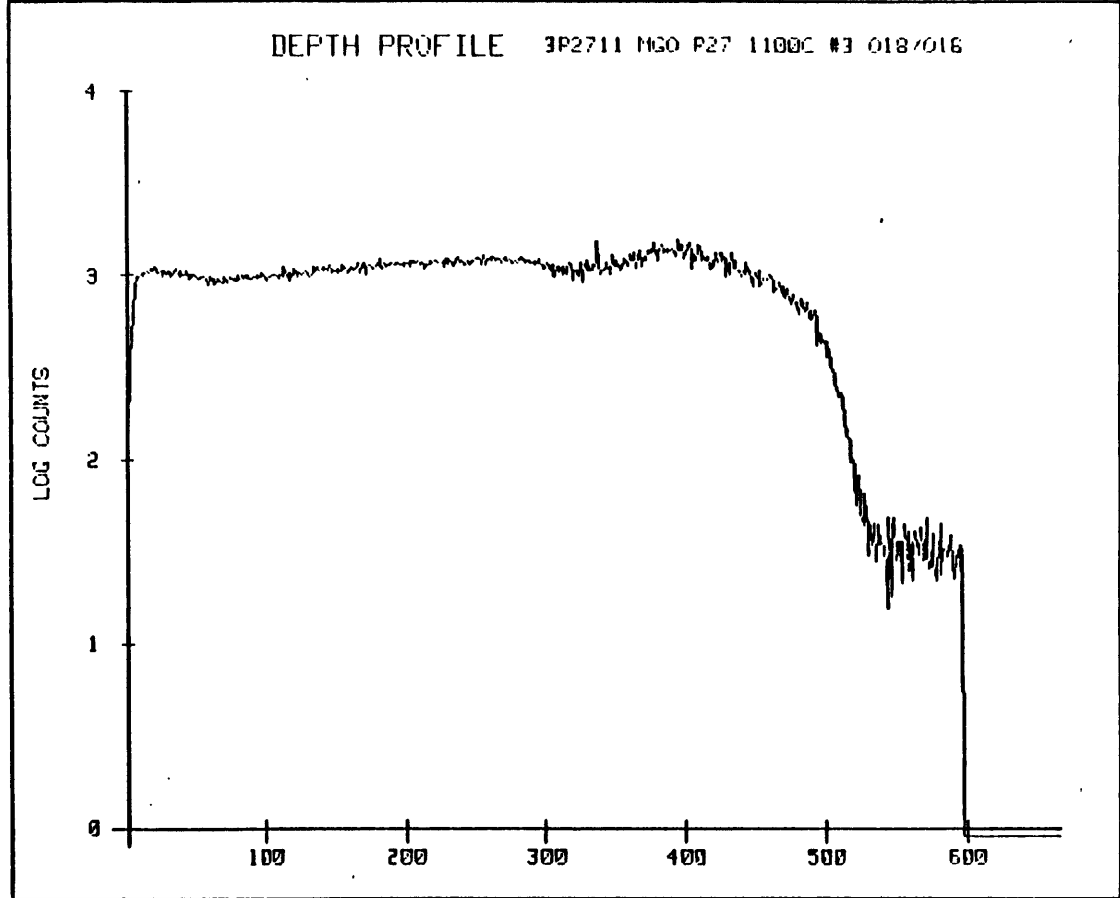


Fig. 2-27. R27-1100-3 (a)

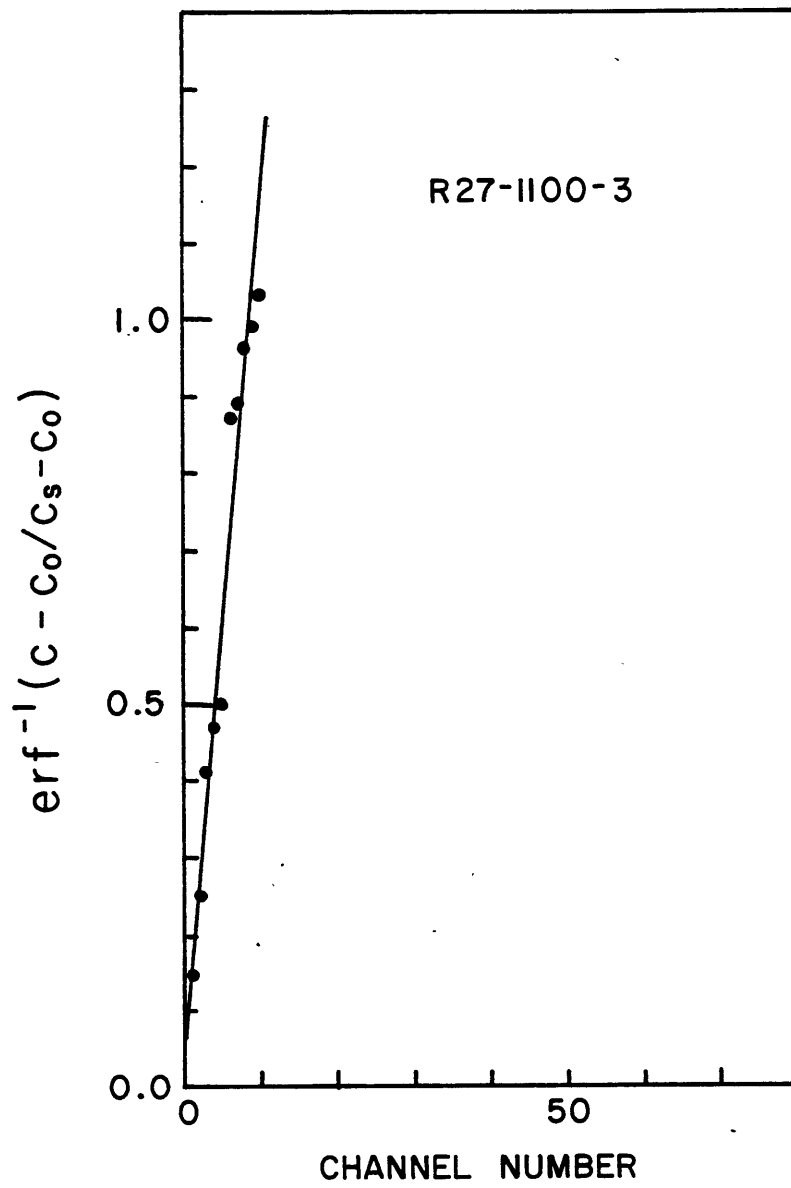


Fig. 2-28. R27-1100-3 (b)

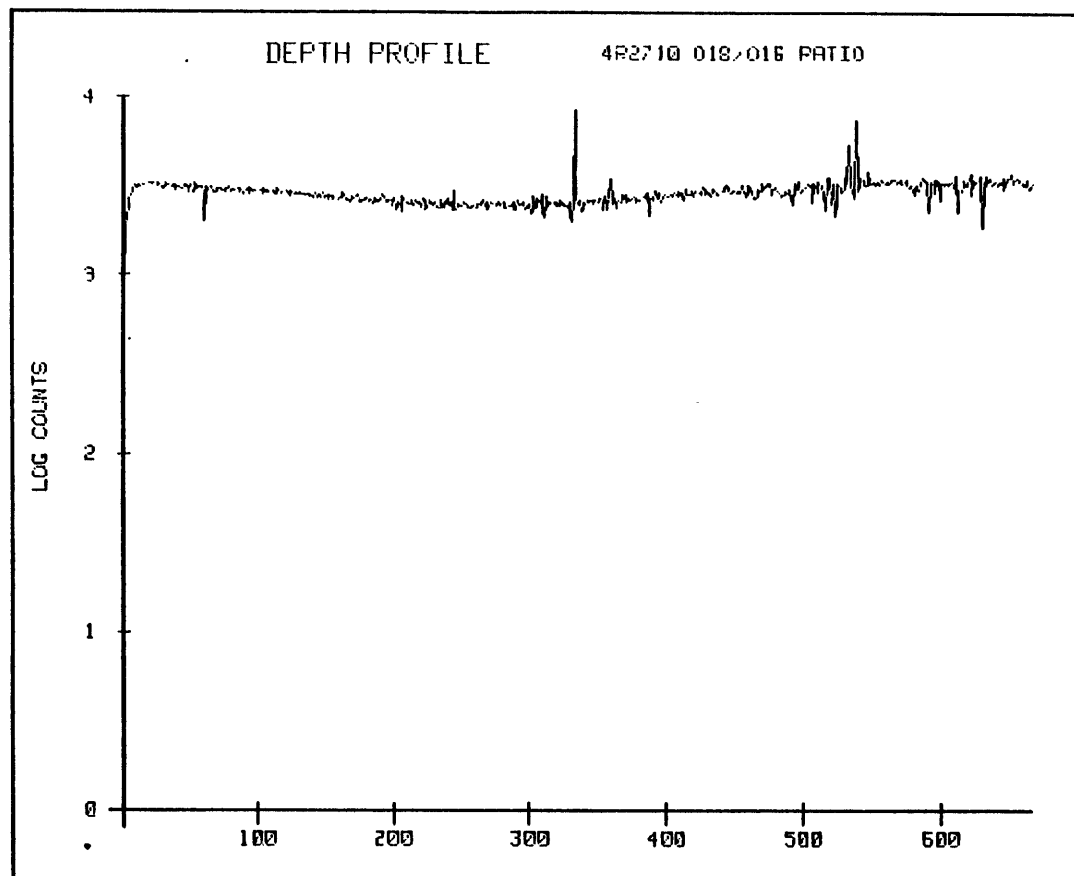


Fig. 2-29. R27-1000 (a)

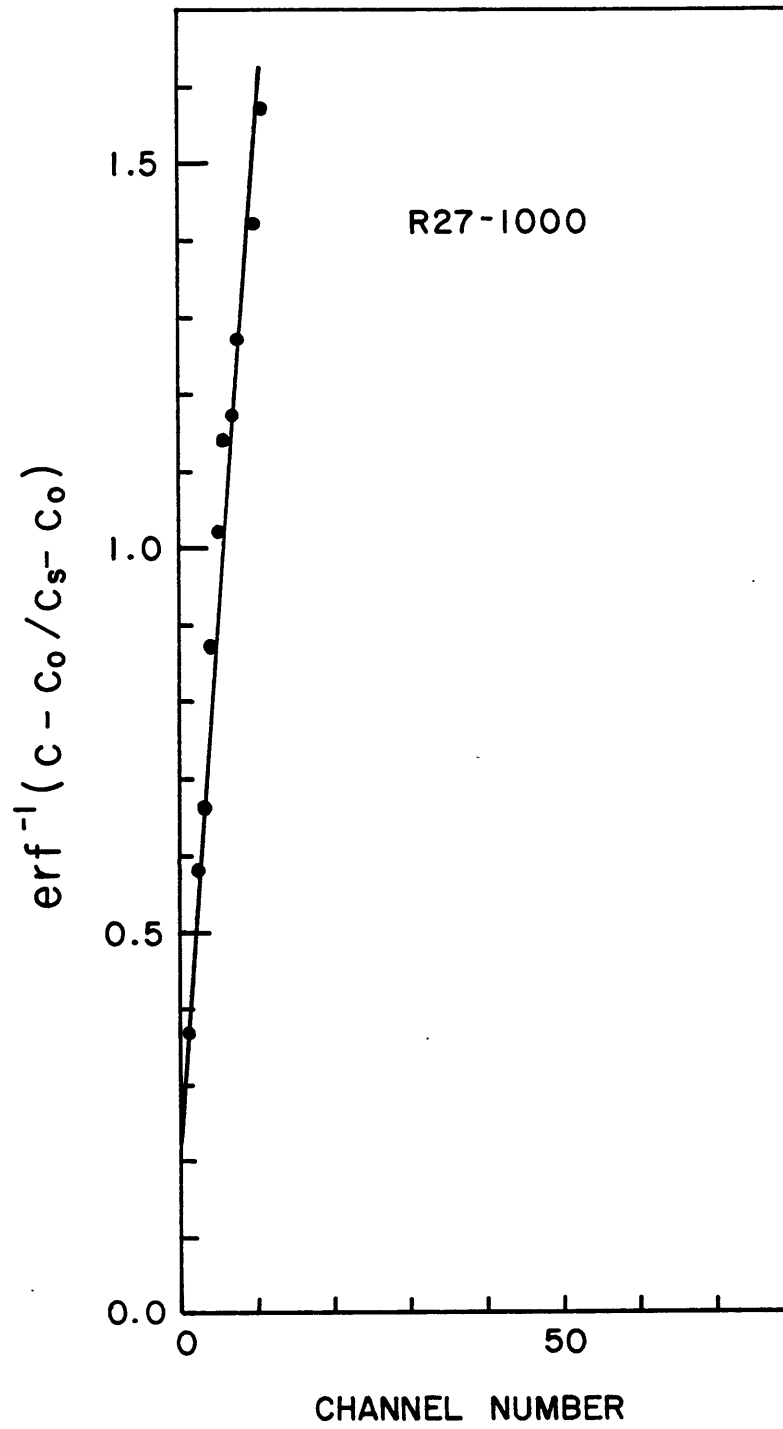


Fig. 2-30. R27-1000 (b)

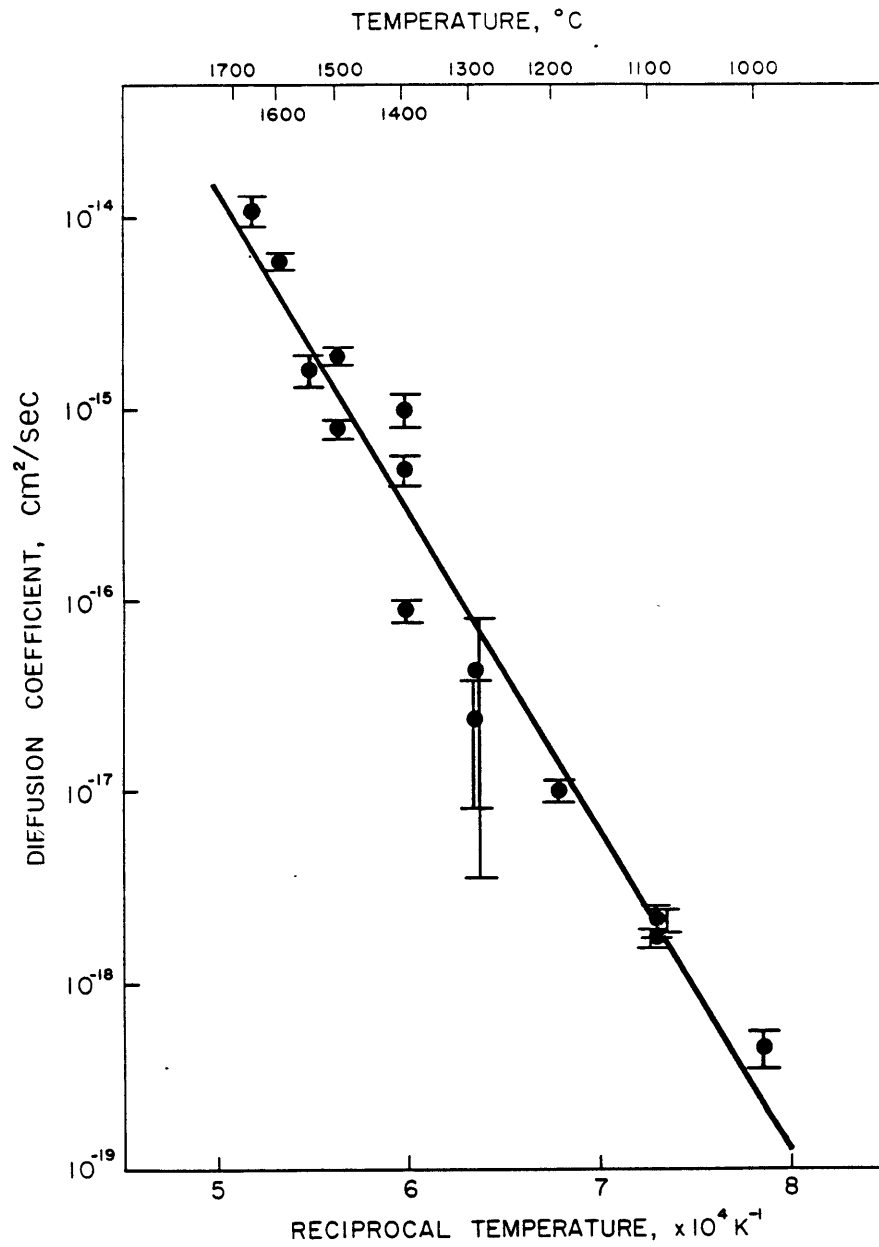


Fig. 2-31. An Arrhenius plot of measured diffusion coefficients based on the as-measured crater depths.

References

1. Y. Oishi and W. D. Kingery, *J. Chem. Phys.*, 33, 905, 1960
2. W. C. Mackrodt and R. F. Stewart, *J. Phys. C: Solid State Phys.*, 12, 5015, 1979
3. M. J. L. Sangster and D. K. Rowell, *Phil. Mag. A*, 44, 613, 1981
4. E. A. Colbourn and W. C. Mackrodt, *Cera. Intern.*, 8, 90, 1982
5. J. CRANK, *The Mathematics of Diffusion*, 2nd edition, Oxford University Press, London, 1975
6. Y. Oishi, K. Ando, and N. Suga, *J. Am. Ceram. Soc.*, 66, C-130, 1983
7. Y. Oishi and W. D. Kingery, *J. Chem. Phys.*, 33, 480, 1960
8. Y. Oishi, K. Ando, H. Kurokawa, and Y. Hiro, *J. Am. Ceram. Soc.*, 66, C-60, 1983
9. H. Hashimoto, M. Hama, and S. Shirasaki, *J. Appl. Phys.*, 43, 4828, 1972
10. L. H. Rovner, Ph. D. Thesis, Department of Physics, Cornell University, 1966, quoted from Ref. 11.
11. B. J. Wuensch, in *Mass Transport Phenomena in Ceramics*, edited by A. R. Cooper and A. H. Heuer, Plenum Press, New York, New York, 1975, pp 211-231

12. B. J. Wuensch, in *Mass Transport in Solids*, edited by F. Beniere and C. R. A. Catlow, Plenum Press, New York, New York, 1983, pp 353-376
13. a) K. P. R. Reddy, Ph. D. Thesis, Department of Metallurgy and Materials Science, Case Western Reserve University, 1979
b) K. P. R. Reddy and A. R. Cooper, *J. Am. Ceram. Soc.*, 66, 664, 1983
14. J. M. Calvert, D. J. Derry, and D. G. Lees, *J. Phys. D: Appl. Phys.*, 7, 940, 1974
15. Y. Moriyoshi, T. Ikegami, S. Matsuda, Y. Bando, Y. Sekikawa, and S. Shirasaki, *Z. Phys. Chem, N.F.* 118, 187, 1979
16. J. Narayan and J. Washburn, *Acta Metall.*, 21, 533, 1973
17. W. C. Mackrodt and R. F. Stewart, *J. Phys. C: Solid State Phys.*, 12, 431, 1979
18. M. Duclot and C. Deportes, *J. Solid State Chem.*, 31, 377, 1980
19. D. R. Sempolinski and W. D. Kingery, *J. Am. Ceram. Soc.*, 63, 664, 1980
20. B. J. Wuensch, W. C. Steele and T. Vasilos, *J. Chem. Phys.*, 58, 5258, 1973
21. W. H. Gourdin and W. D. Kingery, *J. Mat. Sci.*, 14, 2053, 1979
22. E. A. Gulbransen, *Trans. Electrochem. Soc.*, 87, 589, 1945
23. T. E. Leontis and F. N. Rhines, *Trans. AIME*, 166, 265,

- 1946
24. R. Sh. Mikhail and V. K. Gouda, *J. Appl. Chem.*, 10, 384, 1960
 25. R. J. Stokes, T. L. Johnston and C. H. Li, *Phil. Mag.*, 3, 718, 1958
 26. P. E. Gruber, *J. Cryst. Growth*, 18, 94, 1973
 27. J. A. McHugh, *NBS Spec. Pub.* 427, 179, 1975
 28. J. W. Colby, in *Practical Scanning Electron Microscopy*, edited by J. I. Goldstein, Plenum Press, New York, New York, 1975, pp 529-572
 29. E. Zinner, *Scanning*, 3, 57, 1979
 30. S. Hofmann, *Surf. Interf. Anal.*, 2, 148, 1980
 31. H. W. Werner, *Surf. Interf. Anal.*, 2, 56, 1980
 32. C. W. Magee and R. E. Honig, *Surf. Interf. Anal.*, 4, 35, 1982
 33. H. W. Werner and A. E. Morgan, *J. Appl. Phys.*, 47, 1232, 1976
 34. G. Müller, *Appl. Phys.*, 10, 317, 1976
 35. K. Wittmaack, *J. Appl. Phys.*, 50, 493, 1979
 36. C. P. Hunt, C. T. H. Stoddart and M. P. Seah, *Surf. Interf. Anal.*, 3, 157, 1981
 37. N. Shimizu and S. R. Hart, *Ann. Rev. Earth Planet. Sci.*, 10, 483, 1982
 38. N. Shimizu and S. R. Hart, *J. Appl. Phys.*, 53, 1303, 1982
 39. G. Friedlander, J. W. Kennedy and J. M. Miller, *Nuclear and Radiochemistry*, 2nd edition, John Wiley & Sons Inc.,

- New York, New York, 1964
40. J. R. Taylor, *An Introduction to Error Analyses*, University Science Books, Mill Valley, California, 1982
 41. P. M. Hall and J. M. Morabito, *Surf. Sci.*, 54, 79, 1976
 42. C. C. Lo and D. E. Schuele, *J. Appl. Phys.*, 46, 5005, 1975
 43. H. W. Werner, *Surf. Interf. Anal.*, 4, 1, 1982
 44. H. D. Young, *Statistical Treatment of Experimental Data*, McGraw-Hill Book Co. Inc., New York, New York, 1962
 45. Y. Beers, *Introduction to the Theory of Error*, Addison-Wesley Publishing Co., Reading, MA, 1957.
 46. J. W. Richards, *Interpretation of Technical Data*, D. Van Nostrand Co. Inc., Princeton, NJ, 1967
 47. J. Murdoch and J. A. Barnes, *Statistical Tables*, 2nd edition, John Wiley and Sons, New York, New York, 1977
 48. D. J. Reed and B. J. Wuensch, *J. Am. Ceram. Soc.*, 63, 88, 1980
 49. K. P. R. Reddy and A. R. Cooper, *J. Am. Ceram. Soc.*, 65, 634, 1982
 50. K. Tharmalingam and A. B. Lidiard, *Phil. Mag.*, 6, 1157, 1961

PART II:

NONISOTHERMAL ANION SELF-DIFFUSION IN MgO

1. INTRODUCTION

How the intermixing of oxygen isotopes, ^{18}O and ^{16}O , in our system MgO proceeds in a temperature gradient can be described through the application of *Irreversible Thermodynamics*, in which the coupling of the temperature gradient with a mass flow (i.e. thermomigration) is attributed to a defined quantity, called the *heat of transfer*. By doing so, a set of phenomenological equations is established for the system, from which, in principle, a time-dependent intermixing profile of oxygen isotopes may be obtained. From this profile, in turn, it should be possible to extract a value for the heat of transfer of oxygen in MgO. In anticipation of the final result, however, it has been found that no cross effect is left in the intermixing profile when diffusion proceeds via a vacancy mechanism. As this is presumed to be the transport mechanism in MgO, the heat of transfer of oxygen can never be obtained from an experiment of the type originally envisioned.

In order to develop an understanding of the phenomenon in a clear way, irreversible thermodynamics is reviewed first with an emphasis on its intrinsic limitations. This is followed by its application to the simple case of the thermomigration of interstitial impurities in an elementary metal. This treatment leads to a useful result which stands in conspicuous contrast to the thermomigration via a vacancy

mechanism, and suggests a more efficient experiment for measurement of the effect. Finally, the intermixing of the oxygen-isotopes in the system MgO will be tackled in a rigorous way.

2. IRREVERSIBLE THERMODYNAMICS

When a system is displaced from thermodynamic equilibrium, it evolves towards a stationary state which is compatible with the imposed constraints. There may be chemical reactions, mass and energy transfer, and momentum transfer as evolutionary processes of the system. A systematic treatment of these processes makes the subject of the *Thermodynamics of Irreversible Processes* or, more concisely, *Irreversible* or *Nonequilibrium Thermodynamics*. This branch of thermodynamics has been discussed extensively in the linear regime¹⁻⁵ and more recently attention has been paid to the non-linear regime⁶.

The principles of Irreversible Thermodynamics, in general, stand on the hypothesis that any irreversible process produces entropy. In its linear regime, the method of this discipline is to calculate the rate of entropy production, to identify generalized thermodynamic fluxes (or rates) and forces (or affinities), to set up linear phenomenological equations, and to apply the reciprocity theorem of Onsager⁷. Usually, all the transport phenomena may be described satisfactorily in the linear regime⁴. In what follows, the linear irreversible thermodynamics will be summarized to the extent necessary for the development of understanding in the subsequent Chapters 3 and 4.

2.1. Entropy Production

For a continuous system in which the intensive state variables are not only functions of time but also continuous functions of the space coordinates, the rate of entropy production in a unit volume, σ , is calculated, with the help of three conservation laws for mass, energy, and momentum, on the basis of a local formulation of the Gibbs equation.²⁻⁵ The Gibbs equation in the form of its total time derivative with respect to the center-of-mass frame of reference is

$$T \frac{dS}{dt} = \frac{dU}{dt} + P \frac{dV}{dt} - \sum_{k=1}^n \mu_k \frac{dn_k}{dt}, \quad \text{Eq. 1}$$

where, as usual, T , P , V , S and U are respectively temperature, pressure, volume, total entropy and total internal energy. μ_k and n_k are respectively chemical potential and the amount of substance k in an n -component system. Equation 1 is not affected by the choice of species as the substance k provided that all possible chemical equilibrium between species have been established. Use of the local Gibbs formula for a state displaced from an overall thermodynamic equilibrium is justified, due to Prigogine⁹, provided that the distribution functions of particle momenta and relative positions are maintained, locally, close to the equilibrium distributions. According to Nicolis⁶, more specifically this implies:

i) Spatial and temporal variations of thermodynamic variables must be small enough over the mean free path and the relaxation time, respectively, which characterize the thermal motion of constituent particles. This implies that dissipative processes, arising primarily from the frequent elastic collisions, are very efficient in establishing some kind of *local equilibrium* in the system.

ii) Reactive collisions are sufficiently rare events so that elastic collisions may restore the equilibrium distribution to a good approximation. This can be achieved if the energies of activation are sufficiently large with respect to thermal energies.

The result is the balance equation for the local entropy per unit volume, s_v^{1-5} ,

$$\frac{ds_v}{dt} = -\text{div } \vec{J}_s + \sigma, \quad \text{Eq. 2}$$

where \vec{J}_s represents the entropy flux across the imaginary boundary of a local volume element which is moving at its center-of-mass velocity, \vec{u}_M . The *center-of-mass (or barycentric) frame of reference* is a natural coordinate system for this formulation, since any bulk motion of the system, as a whole, makes no contribution to entropy production. The rate of entropy creation, σ , is never negative by virtue of the second law of thermodynamics.

Entropy is produced by chemical reactions (σ_{chem}), diffusion ($\sigma_{\text{diffusion}}$), heat conduction (σ_{thermal}), and viscous flow (σ_{viscous}).

According to Curie's symmetry principle⁴ which says that *macroscopic causes always have fewer elements of symmetry than the effects they produce*, fluxes and forces of different tensorial character do not couple in an isotropic system within the domain of linear irreversible thermodynamics³. The total rate of entropy production, σ , may thus be split up into the three positive-definite components;

$$\sigma = \sigma_{\text{chem}} + (\sigma_{\text{diffusion}} + \sigma_{\text{thermal}}) + \sigma_{\text{viscous}} \quad \text{Eq. 3}$$

with

$$\begin{aligned} \sigma_{\text{chem}} &\geq 0 \\ \sigma_{\text{diffusion}} + \sigma_{\text{thermal}} &\geq 0 \\ \sigma_{\text{viscous}} &\geq 0 \end{aligned}$$

where equalities hold only for reversible processes.

In such a non-viscous system of n -components with no chemical reaction involved, the rate of entropy production, σ , solely due to vectorial phenomena – diffusion and heat conduction is given in a bilinear form of fluxes and forces;¹⁻⁵

$$T\sigma = \tilde{J}X \quad \text{Eq. 4}$$

where the transposed matrix (denoted by tilde) of vectorial fluxes, \tilde{J} , and the matrix of generalized forces, X , are, respectively, defined as

$$J \equiv \begin{pmatrix} J_M \\ J_U \end{pmatrix} \quad \text{Eq. 5}$$

and

$$X \equiv \begin{pmatrix} X_M \\ X_U \end{pmatrix}. \quad \text{Eq. 6}$$

In Eq. 5, the $(n \times 1)$ submatrix J_M represents a column matrix of n -diffusion fluxes J_1, J_2, \dots, J_n , namely,

$$J_M \equiv \begin{pmatrix} J_1 \\ J_2 \\ \vdots \\ J_n \end{pmatrix}$$

and the (1×1) submatrix J_U is the energy flow J_U itself or

$$J_U \equiv (J_U).$$

Corresponding thermodynamic forces are represented respectively by the $(n \times 1)$ submatrix X_M and the (1×1) submatrix X_U in Eq. 6, which are defined as

$$X_M \equiv \begin{pmatrix} X_1 \\ X_2 \\ \cdot \\ \cdot \\ X_n \end{pmatrix} \quad \text{and} \quad X_U \equiv (X_u).$$

The introduction of submatrices, J_M , J_U , X_M and X_U , instead of their element forms somewhat facilitates some manipulations with fluxes and forces, e.g., their transformations, to be described later on. The diffusion flux of a component k , \vec{J}_k , is defined with respect to the barycentric frame of reference as²⁻⁵

$$\vec{J}_k \equiv C_k (\vec{u}_k - \vec{u}_M), \quad \text{Eq. 7}$$

where C_k and u_k are, respectively, local molecular density and velocity of the component k . Such fluxes for n components are automatically interdependent through the definition of a local center-of-mass velocity, \vec{u}_M , as

$$\sum_{k=1}^n m_k \vec{J}_k = 0 \quad \text{Eq. 8}$$

where m_k is the molecular weight of k . When the component k is acted upon by an external non-electrical force, \vec{F}_k , the generalized thermodynamic force, \vec{X}_k , is represented by¹⁻⁵

$$\vec{X}_k \equiv \vec{F}_k - T \vec{\nabla} \left(\frac{\mu_k}{T} \right), \quad \text{Eq. 9}$$

in which μ_k is the chemical potential of k . If the constituent is electrically charged, then the corresponding chemical potential is replaced by its electrochemical potential, η_k .^{1,0}

The energy flux, \vec{J}_u , is also by construction referred to the local center-of-mass frame and its conjugate force, \vec{X}_u is¹⁻⁵

$$\vec{X}_u \equiv T \vec{\nabla} \left(\frac{1}{T} \right). \quad \text{Eq. 10}$$

It should be noted that the rate of entropy creation decreases as the system evolves with time and becomes minimum at a (non-equilibrium) stationary state.²⁻⁴ At thermodynamic equilibrium, as a special case of stationary state, both the fluxes and forces for all irreversible processes disappear simultaneously with no entropy produced;

$$J = 0 \quad \text{and} \quad X = 0. \quad \text{Eq. 11}$$

2.2. PHENOMENOLOGICAL LAWS AND ONSAGER THEOREM

A flux may be expressed in Taylor series about thermodynamic equilibrium with respect to forces of the same tensorial character.⁶ For example, a diffusion flux, J_k , in an isotropic system is represented by

$$\begin{aligned}
J_k(\{X_1\}) &= J_k(\{X_1=0\}) + \sum_1 \left(\frac{\partial J_k}{\partial X_1} \right)_{X_1=0} X_1 + \\
&+ \frac{1}{2} \sum_1 \sum_m \left(\frac{\partial^2 J_k}{\partial X_1 \partial X_m} \right)_{X_1=0, X_m=0} X_1 X_m + \dots \quad \text{Eq. 12}
\end{aligned}$$

where the first term is identically zero due to Eq. 11. In the neighborhood of thermodynamic equilibrium, the third and higher order terms may be disregarded to provide the *phenomenological laws or thermodynamic equations of motion*¹ in the matrix form,

$$J = L X \quad \text{Eq. 13}$$

or, due to Eq. 5 and Eq. 6,

$$J_M = L_{MM} X_M + L_{MU} X_U \quad \text{Eq. 14}$$

$$J_U = L_{UM} X_M + L_{UU} X_U, \quad \text{Eq. 15}$$

in which the matrix of phenomenological coefficients or transport coefficients L is defined as⁶

$$L = (L_{kl}) \equiv \left(\left(\frac{\partial J_k}{\partial X_l} \right)_{X_l=0} \right). \quad \text{Eq. 16}$$

Empirical relations such as Fourier's law of heat conduction, Fick's law of diffusion and Ohm's law of electrical conduction belong automatically to this scheme. The

existence of phenomenological laws is considered an *extra-thermodynamic hypothesis*⁴. But it has been shown⁴ that they are valid whenever the relative variation of a state variable such as, for example, temperature T is small over a length of the mean free path, λ , or

$$\frac{\lambda}{T} \frac{\partial T}{\partial x} \ll 1. \quad \text{Eq. 17}$$

This condition is satisfied in most of the usual cases and in general the phenomenological laws are considered to give good approximations for transport processes⁴. We may notice that the domain of validity of the phenomenological laws coincides with that of the local Gibbs equation described in Section 2.1.

The grand assumption which plays the key role in the application of the phenomenological laws, Eq. 13 or Eq.'s 14 and 15, is the celebrated reciprocity theorem of Onsager⁷. Without this theorem, the phenomenological laws are nothing but a known condition of thermodynamic equilibrium, Eq. 11, and the empirical linear laws themselves⁹. The Onsager theorem states that, in the absence of Lorentz force and Coriolis force, the matrix of the phenomenological coefficients, L , is symmetrical for *appropriately-chosen, independent* fluxes and forces, or

$$L = \tilde{L}, \quad \text{Eq. 18}$$

the proof of which is readily found in the well-known textbooks²⁻⁴ of irreversible thermodynamics.

The appropriately-chosen conjugate flux and force are originally selected to be the time derivative of a thermodynamic state variable (scalar flux) and the first partial derivative of the entropy of the given system with respect to the same variable (scalar force), respectively. The validity of the theorem has thus been questioned for vectorial fluxes and forces since there is no evidence that these are appropriately chosen in the rigorous Onsager sense.¹ Furthermore, the vectorial fluxes are frequently subject to a linear homogeneous relation among themselves such as Eq. 8 and/or the vectorial forces also. Due to Mazur and de Groot,³ however, the Onsager theorem is taken as verified even for vectorial fluxes and forces. It has also been proved that a linear homogeneous dependency among the fluxes leaves the theorem unimpaired. Even when there are linear interdependencies for both fluxes and forces, it has been shown that the L-matrix can be chosen in such a way that the theorem holds due to the indeterminacies of the phenomenological coefficients.^{3, 12}

The Onsager theorem, Eq. 18, reduces the production of entropy to

$$T\sigma = \tilde{X}LX,$$

Eq. 19

in view of Eq.'s 4 and 13. Since the entropy production must be positive definite, the L-matrix is required to be positive definite, or

$$|L| \geq 0. \quad \text{Eq. 20}$$

2.3. TRANSFORMATION OF FLUXES AND FORCES

In principle, there can be an infinite number of equivalent sets of flux and force, $\{J, X\}$, to describe an irreversible system, but it occurs quite often that a specific set is particularly convenient for the system.^{4,13} We are thus in need of the transformation of a given set, $\{J, X\}$ into another equivalent $\{J', X'\}$ subject to the requirement that entropy production remains invariant and the Onsager theorem unimpaired. According to Meixner,¹⁴ a new set, $\{J', X'\}$ obtained by a congruent transformation through α such that

$$J' = \alpha J \quad ; \quad X' = \tilde{\alpha}^{-1} X \quad \text{Eq. 21}$$

leaves the entropy production invariant,

$$T\sigma = \tilde{J}X = \tilde{J}'X' \quad \text{Eq. 22}$$

and the Onsager theorem remains valid,

$$L' = \alpha L \tilde{\alpha} = \tilde{L}'. \quad \text{Eq. 23}$$

Such transformation, α , has been shown to be the only admissible one for the (scalar) fluxes and forces^{1,5}. The same is presumably true for vectorial fluxes and forces in such a way that the Onsager theorem itself is true for these due to Mazur and de Groot³. It should be noted that, for a nonsingular matrix, α , to exist, either the fluxes have to be independent of each other or equivalently, the forces so.

One of the most frequently used set of fluxes and forces is obtained through the transformation α ²⁻⁵,

$$\alpha \equiv \begin{pmatrix} I & 0 \\ -\tilde{h}_M & 1 \end{pmatrix} \quad \text{Eq. 24}$$

where I denotes an $(n \times n)$ identity matrix and \tilde{h}_M is a $(1 \times n)$ row matrix of partial molar enthalpies of constituents or

$$\tilde{h}_M \equiv (h_1, h_2, \dots, h_n). \quad \text{Eq. 25}$$

By operation of the transformation, α , the new fluxes and forces expressed in terms of the old ones are, respectively, obtained as

$$\begin{pmatrix} J'_M \\ J'_U \end{pmatrix} = \begin{pmatrix} J_M \\ J_U - \tilde{h}_M J_M \end{pmatrix} \quad \text{Eq. 26}$$

and

$$\begin{pmatrix} X'_M \\ X'_U \end{pmatrix} = \begin{pmatrix} X_M + h_M X_U \\ X_U \end{pmatrix}. \quad \text{Eq. 27}$$

The new phenomenological laws may be written as

$$J' = L'X' \quad \text{Eq. 28}$$

or

$$J'_M = L'_{MM}X'_M + L'_{MU}X'_U \quad \text{Eq. 29}$$

$$J'_U = L'_{UM}X'_M + L'_{UU}X'_U \quad \text{Eq. 30}$$

where the L' -matrix has been transformed following Eq. 23

as

$$L' \equiv \begin{pmatrix} L'_{MM} & L'_{MU} \\ L'_{UM} & L'_{UU} \end{pmatrix} = \begin{pmatrix} L_{MM} & L_{MU} - L_{MM}h_M \\ L_{UM} - \tilde{h}_M L_{MM} & L_{UU} - L_{UM}h_M - \tilde{h}_M L_{MU} + \tilde{h}_M L_{MM}h_M \end{pmatrix} \quad \text{Eq. 31}$$

During the transformation, whereas the diffusion flux, J'_M , remains the same (i.e. $J'_M = J_M$), the energy flux, J'_U , transforms (see Eq. 26) as

$$J'_U = J_U - \tilde{h}_M J_M.$$

The enthalpies carried by diffusion fluxes have been subtracted from J_U , the energy flux conducted across the imaginary boundary of a local volume element moving at the center-of-mass velocity. The transformed energy flux J'_U , especially called the *reduced heat flux*⁴, is found to be independent of the frame of reference (or reference velocity)⁵ and will be replaced by a new symbol, J_q , in its application to a crystalline solid.

With respect to the thermodynamic forces, only the direct causes for mass flows take a different form (see Eq. 27), i.e.,

$$X'_M = X_M + h_{MU} X_U$$

or in its elementary form,

$$\vec{X}'_k = \vec{X}_k + h_{ku} \vec{X}_u$$

which is rewritten, in view of Eq.'s 9 and 10, as

$$\vec{X}'_k = \vec{F}_k - (\vec{\nabla}\mu_k)_T. \quad \text{Eq. 32}$$

The last term on the right-hand-side of Eq. 32 is the isothermal part of $\vec{\nabla}\mu_k$,

$$(\vec{\nabla}\mu_k)_T = T\vec{\nabla}\left(\frac{\mu_k}{T}\right) + \left(\frac{h_k}{T}\right)\vec{\nabla}T, \quad \text{Eq. 33}$$

which is, of course, a function of other thermodynamic variables, e.g. pressure and composition. \vec{X}'_k may be called a *reduced (thermodynamic) force*. The reduced force $\vec{X}'_u (= \vec{X}_u)$ will be specially denoted as \vec{X}'_q . The *reduced fluxes and forces*, $\{J', X'\}$, obtained by a transformation α in Eq. 24, make obviously a very convenient set in the description of non-isothermal phenomena such as thermomigration because the diffusional driving force, \vec{X}_k , has been set free from its temperature dependence. This set, $\{J', X'\}$, will be used exclusively in

the following chapters.

2.4. HEATS OF TRANSFER

The phenomenological law,

$$J_M = L_{MM}X_M + L_{MU}X_U \quad \text{Eq. 14}$$

or

$$J'_M = L_{MM}'X'_M + L_{MU}'X'_U, \quad \text{Eq. 29}$$

implies that a mass flux is induced not only by its direct cause—diffusional driving force, X_M or X'_M , but also by an indirect cause—thermal driving force (i.e. temperature gradient), $X_U (=X'_U)$. The former, the direct effect, reduces to the well-established *Fick's First Law* under isothermal conditions. The latter, the indirect effect or cross effect which relates a mass flux to the temperature gradient is called the (Ludwig-) *Soret effect*². The processes themselves may be called, respectively, (ordinary-) *diffusion* and *thermal-diffusion* or *thermomigration*. The term *thermomigration*, however, is preferred to avoid a possible confusion of the *thermal-diffusion* with the *thermal diffusivity*. When a system is of one-component, the cross phenomena may be called a *self-thermomigration* or *thermal self-diffusion*. Similarly, according to the phenomenological equation,

$$J_U = L_{UM}X_M + L_{UU}X_U \quad \text{Eq. 15}$$

or

$$J'_U = L_{UM} X'_M + L_{UU} X'_U, \quad \text{Eq. 30}$$

the energy flux is caused by the diffusional driving force as well as by the temperature gradient. The direct phenomenon is subject to the *Fourier's Law* of heat conduction. The cross phenomenon is called the *Dufour effect*²; which is reciprocal to the *Soret effect*.

These cross phenomena or interferences are attributed to a quantity called the *heat of transfer* and their exact reciprocity is established by the Onsager theorem. Let us first consider an isothermal diffusion system. The phenomenological law will then be

$$J_M = L_{MM} X_M \quad \text{Eq. 34}$$

$$J_U = L_{UM} X_M \quad \text{Eq. 35}$$

since $X_U=0$ in Eq.'s 14 and 15. Substitution of Eq. 34 into Eq. 35 is followed by

$$J_U = \tilde{Q}_M^* J_M \quad \text{Eq. 36}$$

where an $(1 \times n)$ row matrix \tilde{Q}_M^* is defined as

$$\tilde{Q}_M^* \equiv L_{UM} L_{MM}^{-1}. \quad \text{Eq. 37}$$

It is implied that an energy as much as Q_k^* is transported by the diffusion flux, J_k , even in the absence of its direct cause. Q_k^* is, thus, called the *heat of transport* or *heat of transfer* of the constituent k . Through the application of the Onsager theorem,

$$\tilde{L}_{UM} = L_{MU} \quad ; \quad \tilde{L}_{MM} = L_{MM},$$

a column matrix of the heat of transfer, Q_M^* , is obtained as

$$Q_M^* = L_{MM}^{-1} L_{MU}. \quad \text{Eq. 38}$$

Substituting from Eq. 37 or Eq. 38 into the phenomenological equations, Eq.'s 14 and 15,

$$J_M = L_{MM} X_M + L_{MM} Q_M^* X_U \quad \text{Eq. 39}$$

$$J_U = \tilde{Q}_M^* L_{MM} X_M + L_{UU} X_U, \quad \text{Eq. 40}$$

in which the reciprocity of the interference between the two vectorial phenomena has been established by virtue of the heats of transport. A diffusion process is coupled to an applied temperature gradient because the diffusing species are thermally energized with their heats of transport quite similarly to the way in which a diffusion of charged particles is coupled to an applied electric potential gradient because the diffusing species are electrically charged.

The same isothermal diffusion system can also be described

in terms of the reduced fluxes and forces, $\{J', X'\}$, as

$$J'_M = L_{MM} X'_M \quad \text{Eq. 41}$$

$$J'_U = L_{UM} X'_M. \quad \text{Eq. 42}$$

Combining Eq. 41 and Eq. 42, we obtain a reduced heat flux transported by the diffusion flux,

$$J'_U = \tilde{q}_M^* J'_M, \quad \text{Eq. 43}$$

where the row matrix of the corresponding heat of transport is defined as

$$\tilde{q}_M^* \equiv L_{UM} L_{MM}^{-1}. \quad \text{Eq. 44}$$

Again due to the Onsager theorem, the column matrix, q_M^* , becomes

$$q_M^* = L_{MM}^{-1} L_{MU}. \quad \text{Eq. 45}$$

In view of Eq. 44 and Eq. 45, the phenomenological laws, Eq. 29 and Eq. 30, are rewritten as

$$J'_M = L_{MM} X'_M + L_{MM} q_M^* X'_U \quad \text{Eq. 46}$$

$$J'_U = \tilde{q}_M^* L_{MM} X'_M + L_{UU} X'_U. \quad \text{Eq. 47}$$

The corresponding heat of transport in this reduced scheme is

accordingly called the *reduced heat of transfer*.

The reduced heat of transfer, q_M^* , is related to Q_M^* through the transformation α in Eq. 24. Since, from Eq. 31,

$$L_{MM}' = L_{MM} \quad ; \quad L_{MU}' = L_{MU} - L_{MM}h_M$$

and, from Eq. 39,

$$L_{MU}' = L_{MM}Q_M^*,$$

Eq. 45 reduces to

$$q_M^* = Q_M^* - h_M \quad \text{Eq. 48}$$

or, in its element form,

$$q_k^* = Q_k^* - h_k. \quad \text{Eq. 49}$$

The reduced heat of transfer, q_k^* , is a thermal energy carried by a diffusing species k less its own enthalpy. According to Eastman¹⁶ and Wagner,¹⁷ who independently introduced the concept of the *heat of transfer*, the reduced heat of transfer of a component, q_k^* , can be defined as the heat which must be absorbed by an arbitrarily isolated part of a system in order to keep its temperature and pressure constant when unit quantity of the component in question is removed from it. No successful kinetic interpretation, however, has yet been avail-

able for a condensed system:^{18,19}

2.5. APPLICATION TO CRYSTALLINE SOLIDS

The irreversible thermodynamics has been reviewed so far for vectorial phenomena with respect to a natural reference frame—the center-of-mass frame of reference. In this section, we will see how the results must be modified to be applicable to a crystalline solid. Our system will be an isotropic crystalline solid. The system is assumed to be isobaric and, consequently, to be in mechanical equilibrium. The effect of external conservative force fields such as gravitational or centrifugal forces are usually neglected for a solid system, i.e., in Eq. 9 or in Eq. 32,

$$\vec{F}_k = 0.$$

We will assume that no space charge build-up is to be allowed in the system, if constituents are charged electrically, even in a volume element which is macroscopically small but microscopically large.²⁰ Actually, mechanical equilibrium is readily achieved through a bulk movement of the system itself.⁹

In the irreversible thermodynamical description of the transport phenomena in a crystalline solid, it is convenient as well as reasonable to take into account atomic (or ionic) defects in addition to all the atomic (or ionic) species,⁹ since the latter are rendered mobile only through the pertinent lattice defects. In an actual material, defects do not

necessarily have to be in internal thermodynamic equilibrium with respect to their local concentrations. In such a case, a definite value cannot be assigned to the (electro-) chemical potential of a thermodynamic component.^{2,1} If the kinetics of the defect annihilation or production remains in the domain in which the local Gibbs formula is valid, as described in Section 2.1, we instead employ the (electro-) chemical potentials and other pertinent partial thermodynamic quantities of atomic (or ionic) species and individual defects. A treatment of this non-equilibrium case is developed in Appendix 2.

In view of the well-defined localities of constituent entities in a crystalline solid, a vectorial flux relative to the local lattice rather than the local center-of-mass may better represent intrinsic characteristics. An atomic (or ionic) flux, \vec{J}_k , is usually defined as the number of chemical species crossing a unit area per unit time, which is moving at a velocity \vec{u} relative to the fixed laboratory coordinate system of reference^{5, 22} or

$$\vec{J}_k \equiv C_k (\vec{u}_k - \vec{u}), \quad \text{Eq. 50}$$

where \vec{u}_k is the velocity of k with respect to the laboratory frame of reference. The relative velocity, \vec{u} , thus defines a reference frame, which is, in general, taken as a weighted mean of velocities of chemical constituent, \vec{u}_k ^{5, 22};

$$\vec{u} = \sum_k w_k \vec{u}_k \quad \text{Eq. 51}$$

in which the weighting factors, w_k , have been normalized to be

$$1 = \sum_k w_k. \quad \text{Eq. 52}$$

The relative velocity \vec{u} is often called a *reference velocity*. In view of Eq. 51, the atomic (or ionic) fluxes are inter-related via a linear homogeneous relation,

$$\sum_k \frac{w_k}{C_k} \vec{J}_k = 0. \quad \text{Eq. 53}$$

By choosing mass fraction as the weighting factor or

$$w_k = m_k C_k / \sum_k m_k C_k,$$

we define the *center-of-mass* or *mass-fixed frame of reference* or the *barycentric frame of reference*, \vec{u}_M ,

$$\vec{u}_M = \frac{\sum_k m_k C_k \vec{u}_k}{\sum_k m_k C_k}, \quad \text{Eq. 54}$$

which has provided the natural reference frame in the calculation of the entropy production since it is automatically introduced by the law of momentum conservation. In this frame, a flux is defined as Eq. 7 and satisfies Eq. 8 or Eq. 53, which implies that no net transfer of mass occurs in this frame.

If we choose a volume fraction for w_k ,

$$w_k = \bar{V}_k C_k / \sum_k \bar{V}_k C_k \quad \text{Eq. 55}$$

where \bar{V}_k is the partial volume of k , satisfying $\sum_k \bar{V}_k C_k = 1$, we have the Fick or the volume-fixed frame of reference, \vec{u}_F ,

$$\vec{u}_F = \sum_k \bar{V}_k C_k \vec{u}_k. \quad \text{Eq. 56}$$

A flux in the Fick frame, \vec{J}_k , is given by

$$\vec{J}_k = C_k (\vec{u}_k - \vec{u}_F), \quad \text{Eq. 57}$$

which satisfies the linear homogeneous relation,

$$\sum_k \bar{V}_k \vec{J}_k = 0. \quad \text{Eq. 58}$$

Eq. 58 implies that there is no net volume transfer in the volume-fixed frame of reference. This frame provides a geometrical coordinate system in which matter transport is experimentally measured.

When the weighting factor is taken as the mole fraction or

$$w_k = C_k / \sum_k C_k, \quad \text{Eq. 59}$$

the *molecular* or the *number-fixed* frame of reference is defined with the reference velocity, \vec{u}_N ,

$$\vec{u}_N = \frac{\sum_k C_k \vec{u}_k}{\sum_k C_k} . \quad \text{Eq. 60}$$

A diffusion flux in this frame, ${}_N \vec{J}_k$, is represented by

$${}_N \vec{J}_k = C_k (\vec{u}_k - \vec{u}_N) , \quad \text{Eq. 61}$$

and no net particle flux exists,

$$\sum_k {}_N \vec{J}_k = 0 . \quad \text{Eq. 62}$$

The number-fixed frame of reference coincides with the *Matano interface*^{2,3,24}

The choice of velocity of the solvent atoms (or ions) as a reference velocity defines the *Hittorf* or the *solvent-fixed* frame of reference, \vec{u}_S , in which any diffusion flux is defined relative to the solvent. It is obviously a convenient frame to describe, for example, transport of interstitial impurities in a crystalline solid.

Likewise, the *lattice (-fixed)* frame of reference is represented by the reference velocity, \vec{u}_L , with which the local crystalline lattice is moving. By introducing the vacancy as a constituent in addition to chemical species, we define \vec{u}_L as

$$\vec{u}_L = \frac{\sum_k C_k \vec{u}_k + C_v \vec{u}_v}{\sum_k C_k + C_v}, \quad \text{Eq. 63}$$

where the concentration and the velocity of vacancies are, respectively, denoted as C_v and \vec{u}_v . The denominator, $\sum_k C_k + C_v$, may be replaced by the concentration of lattice points, C , since the interstitials are not taken into account in the definition of \vec{u}_L in Eq. 63. In the present discussion, C is assumed to be constant. A diffusion flux is then measured relative to the local lattice or

$$L^J_k = C_k (\vec{u}_k - \vec{u}_L) \quad \text{Eq. 64}$$

and, in view of Eq. 53,

$$\sum_k L^J_k + L^J_v = 0, \quad \text{Eq. 65}$$

which implies the conservation of the local crystalline lattice. The lattice frame of reference is congruent with the frame represented by the *inert chips* in Darken's analysis²⁵ of the Kirkendall effect and accordingly often called the *Kirkendall frame of reference*²⁶. The local lattice flow velocity, \vec{u}_L , can be derived purely phenomenologically in an isothermal diffusion system without recourse to the introduction of vacancy flux²⁷.

Of these possible choices of the reference velocities,

it will be shown that the Fick frame and the lattice frame of reference are the most appropriate frames to describe the matter transport via the vacancy mechanism with the provision that the partial volume is constant. The former provides the proper geometrical coordinate system in view of the experiment and the latter in view of the physics of matter transport within a lattice. These two frames are related to each other through their relative velocity as

$$\vec{J}_k^F = \vec{J}_k^L + C_k(\vec{u}_L - \vec{u}_F). \quad \text{Eq. 66}$$

Due to Eq.'s 58 and 65, the relative velocity, $\vec{u}_L - \vec{u}_F$, is obtained as

$$\vec{u}_L - \vec{u}_F = \frac{\vec{J}_v^L}{\sum_k C_k} \quad \text{Eq. 67}$$

in which the partial volume of a chemical component has been assumed to be constant. Since usually the concentration of vacancies, C_v , is negligibly small compared with the concentration of lattice points, C , the denominator in Eq. 67 may be taken as C , which reduces Eq. 67 to

$$\vec{u}_L - \vec{u}_F \cong \frac{\vec{J}_v^L}{C}. \quad \text{Eq. 68}$$

The choice of the lattice reference frame, \vec{u}_L , may not lead to the bilinear form of the entropy production, Eq. 4 which in turn renders the Onsager theorem invalid. Under

mechanical equilibrium, however, it has been shown that the rate of entropy production remains bilinear due to *Prigogine's theorem*.^{2,4,9} The theorem says that, for an n-component system in mechanical equilibrium, the generalized forces, X_k , are related to each other as

$$\sum_{k=1}^n C_k X_k = 0, \quad \text{Eq. 69}$$

at constant temperature. This is an extension of the Gibbs-Duhem equation to an irreversible system.^{8,29} As a corollary, the rate of entropy production is then invariant with an arbitrary choice of reference velocity. The theorem is extended to the non-isothermal system by employing the reduced set of fluxes and forces, $\{J', X'\}$, in Eq. 26 due to Eq. 32 or

$$\sum_{k=1}^n C_k X'_k = 0. \quad \text{Eq. 70}$$

Especially for a crystalline solid with a vacancy diffusion mechanism, the theorem will be rewritten as

$$\sum_{k=1}^n C_k X'_k + C_v X'_v = 0 \quad \text{Eq. 71}$$

and the entropy production as

$$T\sigma = \sum_{k=1}^n L_{J'_k X'_k} J'_k X'_k + L_{J'_v X'_v} J'_v X'_v + J_q X_q. \quad \text{Eq. 72}$$

The $(n+2) \times (n+2)$ matrix, L' , for the set $\{J', X'\}$ satisfying Eq. 72 cannot be defined uniquely because the fluxes and the forces are respectively dependent, i.e., Eq.'s 65 and 71.^{2,3,12} In order to avoid the arbitrariness of the L' -matrix, we may choose to eliminate the vacancy terms with the use of Eq. 65, according to a procedure introduced by de Groot, with n dependent fluxes in the fluid system.^{2,9} The rate of entropy production, Eq. 72, is then reduced to

$$T\sigma = \sum_{k=1}^n J_k \cdot (X_k - X_v) + J_q \cdot X_q \quad \text{Eq. 73}$$

where the subscript L (which denotes the lattice frame of reference defined by Eq. 63) and the superscript ' (prime) (indicating reduced set defined by Eq. 24) have been dropped for the sake of simplicity. In what follows, all fluxes and forces are to be understood as the reduced quantities referred to the lattice reference frame, unless otherwise specifically indicated. It should be noted that the fluxes of chemical components are independent, whereas the forces remain dependent, i.e., they are related by Eq. 71. We may recall that, in such a case, the $(n+1) \times (n+1)$ matrix, L , can be uniquely defined and it is symmetric due to the Onsager theorem.³

The phenomenological laws are then written as

$$J_k = \sum_{l=1}^n L_{kl} (X_l - X_v) + L_{kq} X_q \quad (k = 1, 2, \dots, n)$$

Eq. 74

$$J_q = \sum_{l=1}^n L_{ql} (X_l - X_v) + L_{qq} X_q, \quad \text{Eq. 75}$$

in which Onsager reciprocity relations hold, i.e.,

$$L_{kl} = L_{lk} ; L_{kq} = L_{qk}. \quad \text{Eq. 76}$$

Accordingly, n independent reduced heats of transport are defined as

$$L_{kq} = \sum_{l=1}^n L_{kl} q_l^* . \quad \text{Eq. 77}$$

In view of Eq. 77, a diffusion flux, J_k , with respect to the local lattice reference frame is represented by

$$J_k = \sum_{l=1}^n L_{kl} (X_l - X_v + q_l^* X_q). \quad \text{Eq. 78}$$

3. DEVELOPMENT OF A MODEL FOR THERMOMIGRATION OF INTERSTITIALS

Having reviewed the foundations of irreversible thermodynamics in the preceding chapter, we will now use these principles to develop a description of the thermomigration of interstitial impurities. This analysis will be performed before treating our favorite MgO system since the analysis for an interstitial mechanism is very simple in concept, and the involved mathematics is quite similar to that of the intermixing of oxygen isotopes in a temperature gradient.

For interstitial impurities in metals, about twenty measurements of thermomigration have thus far been performed as summarized in Table 1. Most of measurements were made with the stationary state technique in which the application of a stationary temperature gradient produced a stationary concentration gradient from an initially homogeneous matrix. According to Shewmon,^{3,1} this technique is considered more accurate than any other possible technique probably involving a non-zero flux of the solute. It is because the disappearance of the solute flux in the stationary state renders both the diffusion coefficient and the absolute concentration of the interstitial solute unnecessary for the extraction of a heat of transfer from the stationary concentration gradient (see Eq. 86). Experimentally, however, a very long time is usually required to reach a stationary state. The difference between initial

Table 1. Experimental Heats of Transfer
for Interstitial Solutes^a

Solute	Solvent	q_i^* eV ^b ($ T_i^* $ °K) ^c	Q eV ^d (T_m °K) ^e	Ref.
C	α -Fe (bcc)	-1.04±0.07 (12000)	1.04 (12000)	30, 31
C	γ -Fe (fcc)	-0.10±0.07 (1200)	1.56 (18000)	30, 31
H	α -Fe (bcc)	-0.35~-0.24 (4100~2800)	0.12 (1400)	32
D	α -Fe (bcc)	-0.34~-0.23 (4000~2700)	0.12 (1400)	32
H	γ -Fe _{0.6} Ni _{0.4} (fcc)	-0.07~-0.05 (810~580)	0.43 (5000)	32
H	Ni (fcc)	-0.07~-0.01 (810~120)	0.36 (4200)	32
D	Ni (fcc)	-0.06~-0.03 (700~350)	0.36 (4200)	32
H	α -Zr (hcp)	0.26 (3000)	0.41 (4800)	33
D	α -Zr (hcp)	0.28 (3300)	0.37 (4300)	33
H	β -Zr (bcc)	0.26~0.52 (3000~6000)		34
H	Ti (bcc)	0.23 (2700)		35
H	8Al-1V-Mo titanium alloy	0.13 (1500)		35
H	6Al-4V titanium alloy	0.08 (930)	0.54 (6300)	35

(cont'd)

Table 1. (cont'd)

Solute	Solvent	q_i^* eV ^b ($ T_i^* $ K) ^c	Q eV ^d (T_m K) ^e	Ref.
H	δ -ZrH _{1.69} (fcc)	0.06±0.02 (670)	0.49 (5700)	36
N	α -Fe (bcc)	-0.78 (9100)	0.78 (9100)	
N	β -Zr (bcc)	positive		
N	Nb (bcc)	0 (0)		39
N	Ta (bcc)	-0.30~0 (3500~0)		39
O	β -Zr (bcc)	0.87±0.09 (10000)		37, 38
O	Nb (bcc)	-0.69 ^f (8000)		39
O	Ta (bcc)	-0.82 ^g (9500)		39
Si	Bi ₂ Te ₃ ^h	0.26±0.04 (3000)		

a. Most of data are reproduced from References 18 and 48.

b. reduced heat of transport as defined in Eq. 43, Chapter 2.

c. $T_i^* \equiv q_i^*/k$ where k is the Boltzmann constant, 8.617×10^{-5} eV/K

d. activation energy for the isothermal diffusion

e. $T_m \equiv Q/k$, activation temperature

f. for oxygen concentration less than 0.15 at %

g. for oxygen concentration less than 0.5 at %

h. rhombohedral

and final concentration decreases approximately as $\exp(-t/\theta)^{40,41}$ where $\theta=L^2/\pi^2D_i^2$, L is the specimen thickness along the gradient and the diffusion coefficient for the impurity in question is denoted as D_i . A time at least as long as 5θ is required to bring a sample within 99.3 % of the stationary state. Depending on D_i , this sometimes can be hopelessly long. Some have thus tried to develop a solution for the time-dependent concentration which is developed from the initially homogeneous distribution of impurities with a method of quantum mechanical perturbation theory.^{42,43} But the related mathematics is quite involved.

In this chapter, an approximate solution, valid for short annealing times, which is experimentally operable, explicit and mathematically simple, will be introduced under the initial conditions of a semi-infinite source, a thin film source and a finite (or thick-film) source, in order to provide an analysis analogous to oxygen-intermixing in MgO in a temperature gradient. We will see, in addition, that an experiment designed on the basis of the present time-dependent solution may be an advantageous replacement for the above mentioned stationary state technique to measure the heat of transport of interstitial impurities in a metal system.

3.1. PHENOMENOLOGICAL LAWS

Consider an isotropic crystalline system containing interstitial impurities of one kind denoted with the subscript "i", such as, for example, carbon in austenite. The system is

assumed to be in mechanical equilibrium (as outlined in Section 2.5), and subject to both a concentration gradient of interstitials and a temperature gradient. With respect to the local temperature, a stationary state is assumed or

$$\left(\frac{\partial T}{\partial t}\right)_{\vec{r}} = 0 \quad \text{Eq. 79}$$

since heat conduction is usually much faster than a concentration change by diffusion in most material systems. The validity of the following analysis is, thus, guaranteed only when the stationary state with respect to the temperature is reached in a negligibly short time compared with the time required for a measurable change in concentration.

We may assume that movements of interstitials are not coupled to those of host atoms. The host lattice is relatively immobile so that it may be regarded as a cage for interstitials. The host lattice thus provides the most appropriate frame of reference relative to which the flux of interstitials, \vec{J}_i , is measured. This frame corresponds to the *Hittorf* or the *solvent-fixed frame of reference* (see Section 2.5 for details), which is approximately coincident with the *Fick* or the *volume-fixed frame of reference* if one may neglect the volume change which accompanies the incorporation of an interstitial. The flux, \vec{J}_i , in the present example is therefore experimentally determinable.

The flux of interstitials, \vec{J}_i , referred to the solvent-fixed frame of reference may be written in view of Eq. 46 as

$$\vec{J}_i = L_{ii} (\vec{X}_i + q_i^* \vec{X}_q). \quad \text{Eq. 80}$$

Substituting Eq. 32 and Eq. 10, we have

$$J_i = - D_i \frac{\partial C_i}{\partial z} - D_i C_i \frac{q_i^*}{kT^2} \frac{dT}{dz} \quad \text{Eq. 81}$$

for planar thermomigration along z-direction, where the ordinary diffusion coefficient of interstitials, D_i , has been defined as

$$D_i \equiv \frac{kTL_{ii}}{C_i}. \quad \text{Eq. 82}$$

According to de Groot², the coefficient of the temperature gradient in Eq. 81 is called the *thermal diffusion coefficient*, D'_i , or

$$D'_i \equiv D_i \frac{q_i^*}{kT^2} \quad \text{Eq. 83}$$

and the ratio of the thermal diffusion coefficient to the ordinary diffusion coefficient is the *Soret coefficient*, S_T ,

$$S_T \equiv \frac{D'_i}{D_i}. \quad \text{Eq. 84}$$

The reduced heat of transfer of an interstitial, q_i^* , is defined relative to the host lattice.

In the stationary state, the flux of interstitials

disappears relative to the solvent,

$$\vec{J}_i = 0 \quad \text{Eq. 85}$$

which reduces Eq. 81 to

$$\frac{d \ln C_i}{d(1/T)} = \frac{q_i^*}{k} \quad \text{Eq. 86}$$

Eq. 86 is the principle of the stationary state technique which has been almost exclusively used to measure the heat of transport of interstitials.^{3, 4, 8}

Since the solvent-fixed frame is taken to approximately coincide with the Fick frame of reference, the continuity equation for the interstitials is obtained as

$$\frac{\partial C_i}{\partial t} = - \operatorname{div} \vec{J}_i \quad \text{Eq. 87}$$

or, due to Eq. 81,

$$\frac{\partial C_i}{\partial t} = \frac{\partial}{\partial z} \left(D_i \frac{\partial C_i}{\partial z} \right) - T_i^* \frac{\partial}{\partial z} \left[D_i C_i \frac{\partial}{\partial z} \left(\frac{1}{T} \right) \right], \quad \text{Eq. 88}$$

where

$$T_i^* \equiv \frac{q_i^*}{k} \quad \text{Eq. 89}$$

The intermixing profile of the interstitial isotopes,

say i and i^* , will also follow the same equation if the interference between the two isotopes is neglected. In such a case, C_i must represent the concentration of the i isotopes.

It should be noted from Eq. 88 that the development of the concentration profile, $C_i(z,t)$, is influenced by the thermomigration via the reduced heat of transport (T_i^*). If a time-dependent solution of Eq. 88, $C_i(z,t)$, is available, one may thus extract the information of the thermomigration from it or design a time-saving experiment to measure the reduced heat of transport, q_i^* . We will see what a time-dependent solution looks like in the next section.

3.2. TIME-DEPENDENT SOLUTIONS

One may assume that, even in a temperature gradient, the local diffusion coefficient, $D_i(z)$, will be the isothermal diffusion coefficient at the local temperature, $T(z)$, in view of the postulate of the local thermodynamic equilibrium discussed in Section 2.1. The temperature dependence of an ordinary diffusion coefficient has been well established both theoretically and experimentally⁴⁴ as

$$D = D_o \exp(-T_m/T) \quad \text{Eq. 90}$$

in which T_m denotes the activation energy for the diffusion, Q , divided by the Boltzmann constant, k , i.e.,

$$T_m = Q/k. \quad \text{Eq. 91}$$

It may be called an *activation temperature*.

Substituting from Eq. 90 into the continuity equation, Eq. 88, we obtain a differential equation,

$$\begin{aligned} \frac{\partial C_i}{\partial t} = & D_i \frac{\partial^2 C_i}{\partial z^2} + D_i \frac{T_m + T_i^*}{T^2} \frac{\partial C_i}{\partial z} \frac{dT}{dz} \\ & + D_i \frac{T_i^* (T_m - 2T)}{T^4} C_i \left(\frac{dT}{dz}\right)^2 + D_i \frac{T_i^*}{T^2} C_i \frac{d^2 T}{dz^2}. \end{aligned} \quad \text{Eq. 92}$$

An exact solution is by no means possible but an approximate solution may be obtained with a perturbation method^{4,5,6} over a very thin region δ , in which the thermomigration is observed, such as

$$\frac{\delta}{L} \sim \varepsilon^2 ; \quad \varepsilon^2 \ll 1, \quad \text{Eq. 93}$$

where a typical dimension of the system is again denoted as L .

In the neighborhood δ of $z=0$, $(-\frac{1}{2}\delta, \frac{1}{2}\delta)$, the spatial variation of the stationary temperature (Eq. 79) may be taken as linear, viz.,

$$T = T_0 + a \cdot z \quad \text{Eq. 94 a}$$

or

$$T = T_0 \left(1 + \frac{az}{T_0}\right) \quad \text{Eq. 94 b}$$

and, for the temperature usually employed in a solid-state diffusion-related experiment, the relative variation of temperature may be only on the order of magnitude ε^2 or

$$\left| \frac{a\delta}{T_0} \right| \sim \varepsilon^2 \quad \text{Eq. 95}$$

where T_0 is the temperature at $z=0$ and "a" is the temperature gradient in $(-\frac{1}{2}\delta, \frac{1}{2}\delta)$. Equation 93 and Eq. 95 imply that a temperature gradient is on the order of magnitude, $a \sim T_0/L$, but, as far as Eq. 95 remains valid, Eq. 93 need not be necessarily true as shown in Appendix 1 (L, as a symbolic representation of a macroscopic dimension, was introduced to stress that δ is relatively thin). If it is expanded in a Taylor series about $z=0$ ($T=T_0$), the diffusion coefficient, Eq. 90, is then well represented within the accuracy of ε^2 in this region δ by

$$D_i = \Delta_0 + \Delta_1 z, \quad \text{Eq. 96}$$

where

$$\Delta_0 \equiv D_i(T_0) \quad ; \quad \Delta_1 \equiv (a/T_0)(T_m/T_0)D_i(T_0).$$

In usual temperature conditions of a diffusion-related experiment, we may set

$$\frac{T_m}{T_0} \sim \frac{1}{\varepsilon} \quad \text{Eq. 97}$$

and

$$\left| \frac{T_i^*}{T_0} \right| \sim \frac{1}{\varepsilon} \quad \text{Eq. 98}$$

on the basis of experience^{18,47,48,77} (see also Table 1).

In the neighborhood δ characterized by "a" and T_0 as such,

the solutions to Eq. 92 are obtained, within the accuracy of ϵ^2 , as follows (see, for details, Appendix 1):

For the semi-infinite source initial and boundary conditions,

$$\left. \begin{aligned} C_i(z < 0 ; t = 0) &= C_s \\ C_i(z > 0 ; t = 0) &= 0 \\ C_i(z = -\infty ; t > 0) &= C_s \\ C_i(z = \infty ; t > 0) &= 0 \end{aligned} \right\}, \quad \text{Eq. 99}$$

the time-dependent solution is

$$\begin{aligned} \frac{C_i(z, t)}{C_s} &= \frac{1}{2} \operatorname{erfc}\left(\frac{z}{2\sqrt{\Delta_o t}}\right) - \frac{1}{4\sqrt{\pi}} \cdot \frac{a(T_m + 2T_i^*)}{T_o^2} \cdot \sqrt{\Delta_o t} \cdot \exp\left(-\frac{z^2}{4\Delta_o t}\right) \\ &+ \frac{1}{8\sqrt{\pi}} \cdot \frac{aT_m}{T_o^2} \cdot \frac{z^2}{\sqrt{\Delta_o t}} \cdot \exp\left(-\frac{z^2}{4\Delta_o t}\right). \end{aligned} \quad \text{Eq. 100 a}$$

Rearranging, we obtain

$$\begin{aligned} \frac{C_i(\eta, \xi)}{C_s} &= \frac{1}{2} \operatorname{erfc}(\eta) - \frac{1}{4\sqrt{\pi}} \cdot \frac{aT_i^*}{T_o^2} \cdot \xi \cdot \exp(-\eta^2) \\ &+ \frac{1}{8\sqrt{\pi}} \cdot \frac{aT_m}{T_o^2} \cdot \xi \cdot (2\eta^2 - 1) \cdot \exp(-\eta^2) \end{aligned} \quad \text{Eq. 100 b}$$

where

$$\xi \equiv 2\sqrt{\Delta_o t} \quad ; \quad \eta \equiv z/\xi. \quad \text{Eq. 101}$$

For the thin-film source initial and boundary conditions,

$$\left. \begin{aligned} C_i(z = 0; t = 0) &= \infty \\ C_i(|z| > 0; t = 0) &= 0 \\ C_i(|z| = \infty; t > 0) &= 0 \end{aligned} \right\}, \quad \text{Eq. 102}$$

the solution is

$$\begin{aligned} \frac{\sqrt{\pi}}{M} C_i(z, t) &= \frac{1}{2\sqrt{\Delta_0 t}} \cdot \exp\left(-\frac{z^2}{4\Delta_0 t}\right) - \frac{1}{8} \cdot \frac{a(T_m + 2T_i^*)}{T_0^2} \cdot \frac{z}{\sqrt{\Delta_0 t}} \\ &\cdot \exp\left(-\frac{z^2}{4\Delta_0 t}\right) + \frac{1}{16} \cdot \frac{aT_m}{T_0^2} \cdot \frac{z^3}{(\Delta_0 t)^{3/2}} \cdot \exp\left(-\frac{z^2}{4\Delta_0 t}\right) \end{aligned} \quad \text{Eq. 103 a}$$

or, due to Eq. 101,

$$\begin{aligned} \frac{\sqrt{\pi}}{M} C_i(\eta, \xi) &= \frac{1}{\xi} \cdot \exp(-\eta^2) - \frac{1}{2} \cdot \frac{aT_i^*}{T_0^2} \cdot \eta \cdot \exp(-\eta^2) \\ &+ \frac{1}{4} \cdot \frac{aT_m}{T_0^2} \cdot \eta(2\eta^2 - 1) \cdot \exp(-\eta^2), \end{aligned} \quad \text{Eq. 103 b}$$

where M is the total amount of source, i.e.,

$$M \equiv \int_{-\infty}^{\infty} C_i(z, t) dz. \quad \text{Eq. 104}$$

For a finite source of $2h$ thickness represented by the initial and boundary conditions,

$$\begin{aligned} C_i(|z| < h ; t = 0) &= C_s \}, \\ C_i(|z| > h ; t = 0) &= 0 \end{aligned} \quad \text{Eq. 105}$$

the solution is given by

$$\begin{aligned} \frac{C_i(z, t)}{C_s} &= \frac{1}{2} \left[\operatorname{erf} \left(\frac{h+z}{2\sqrt{\Delta_0 t}} \right) + \operatorname{erf} \left(\frac{h-z}{2\sqrt{\Delta_0 t}} \right) \right] \\ &+ \frac{1}{4\sqrt{\pi}} \left(\frac{a}{T_0} \right) \left(\frac{T_m + 2T_i^*}{T_0} \right) \sqrt{\Delta_0 t} \left\{ \exp \left[- \left(\frac{h+z}{2\sqrt{\Delta_0 t}} \right)^2 \right] \right. \\ &- \left. \exp \left[- \left(\frac{h-z}{2\sqrt{\Delta_0 t}} \right)^2 \right] \right\} + \frac{1}{8\sqrt{\pi}} \left(\frac{a}{T_0} \right) \left(\frac{T_m}{T_0} \right) \frac{(h^2 - z^2)}{\sqrt{\Delta_0 t}} \\ &\left\{ \exp \left[- \left(\frac{h+z}{2\sqrt{\Delta_0 t}} \right)^2 \right] - \exp \left[- \left(\frac{h-z}{2\sqrt{\Delta_0 t}} \right)^2 \right] \right\} \end{aligned} \quad \text{Eq. 106 a}$$

or

$$\begin{aligned} \frac{C_i(\rho, \zeta)}{C_s} &= \frac{1}{2} \left[\operatorname{erf} \left(\frac{1+\rho}{\zeta} \right) + \operatorname{erf} \left(\frac{1-\rho}{\zeta} \right) \right] \\ &+ \frac{1}{4\sqrt{\pi}} \left(\frac{a}{T_0} \right) \left(\frac{T_i^*}{T_0} \right) h\zeta \left\{ \exp \left[- \left(\frac{1+\rho}{\zeta} \right)^2 \right] - \exp \left[- \left(\frac{1-\rho}{\zeta} \right)^2 \right] \right\} \\ &+ \frac{1}{4\sqrt{\pi}} \left(\frac{a}{T_0} \right) \left(\frac{T_m}{T_0} \right) h\zeta \left[\frac{1}{2} + \left(\frac{1+\rho}{\zeta} \right) \left(\frac{1-\rho}{\zeta} \right) \right] \left\{ \exp \left[- \left(\frac{1+\rho}{\zeta} \right)^2 \right] \right. \\ &- \left. \exp \left[- \left(\frac{1-\rho}{\zeta} \right)^2 \right] \right\}, \end{aligned} \quad \text{Eq. 106 b}$$

where

$$\rho \equiv z/h \quad ; \quad \zeta \equiv 2\sqrt{\Delta_0 t} / h. \quad \text{Eq. 107}$$

This finite source of $2h$ thickness may be regarded as an

intermediate between the two extreme cases, the thin-film source and the semi-infinite source.

It is shown in Appendix 1 that Eq.'s 95, 97 and 98,

$$|a\delta/T_0| \sim \varepsilon^2 ; T_m/T_0 \sim 1/\varepsilon ; |T_i^*/T_0| \sim 1/\varepsilon,$$

are the sufficient conditions for these approximate solutions, $C_i(z,t)$ or $C_i(\eta,\xi)$ in Eq. 100 and Eq. 103 and $C_i(\rho,\zeta)$ in Eq. 106 to be accurate within ε^2 .

Expected concentration profiles, $C_i(\eta,\xi)$ of Eq. 100 and Eq. 103 and $C_i(\rho,\zeta)$ in Eq. 106 are shown in Fig. 1, Fig. 2 and Fig. 3, respectively, where an overall profile will be generated by combining the leading isothermal diffusion profile (a) and the two corrective curves (b) and (c), both of order of magnitude ε , namely, $(a)+\varepsilon(b)+\varepsilon(c)$. The curves (b) and (c) represent the perturbations produced by thermomigration and by the temperature dependence of the isothermal diffusivity D_i , respectively. As would be expected, the perturbation due to thermomigration is governed by the heat of transfer (T_i^*) and that due to the temperature dependence of D_i is governed by its activation energy (T_m). Both perturbations are proportional to the temperature gradient "a" to the extent to which the condition, $|a\delta/T_0| \sim \varepsilon^2$, remains valid. Strangely enough in this connection, the perturbation due to the temperature dependence of D_i turns out to be suppressed around $z \sim \pm\sqrt{2\Delta_0 t}$ or $\eta \sim \pm 0.7$ for both the semi-infinite and the thin-film sources (see the curve (c) in Fig. 1 and Fig. 2, and the third term on the

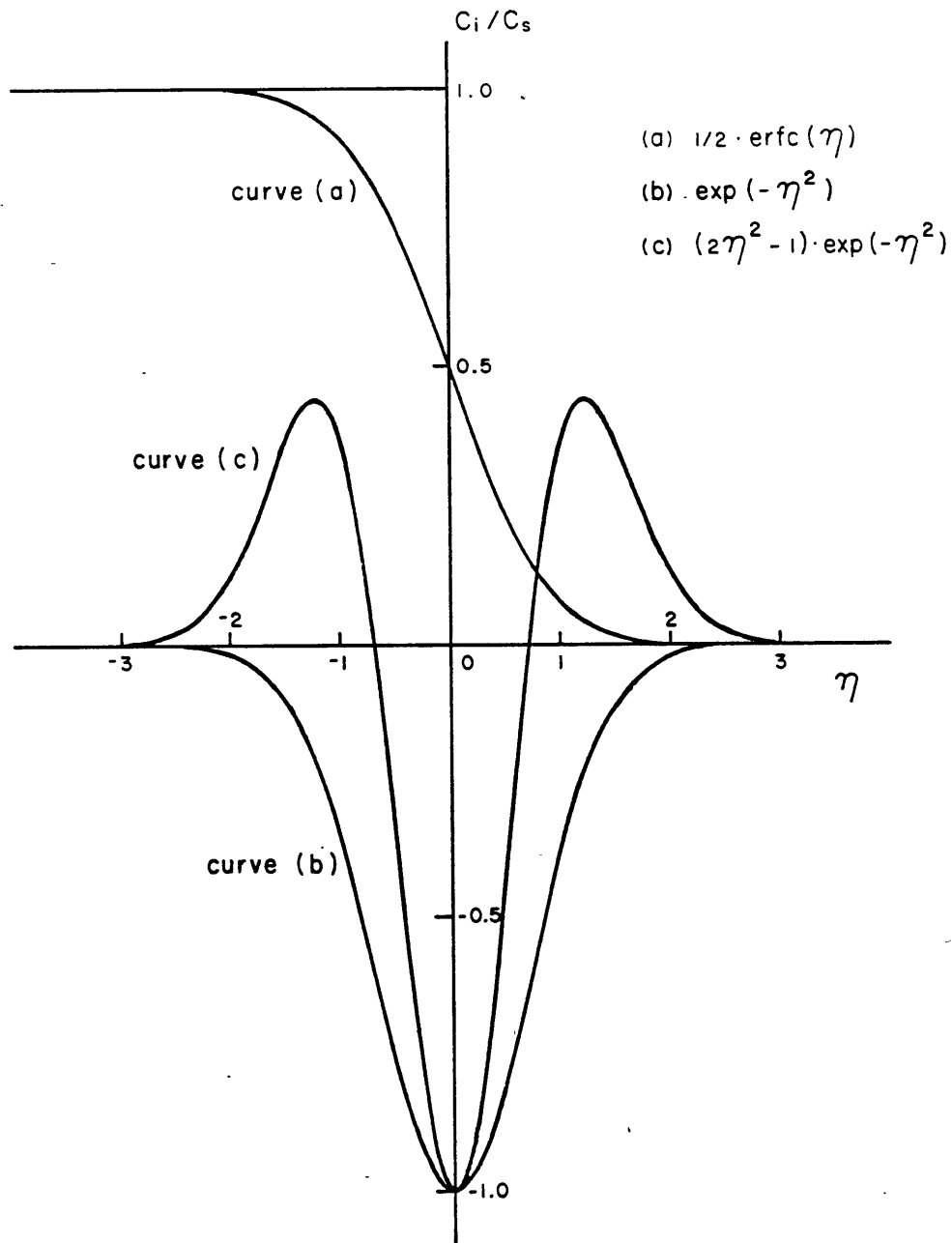


Fig. 1. The nonisothermal diffusion profile developed from a semi-infinite source is expected to be a combination, $(a) + \epsilon(b) + \epsilon(c)$.

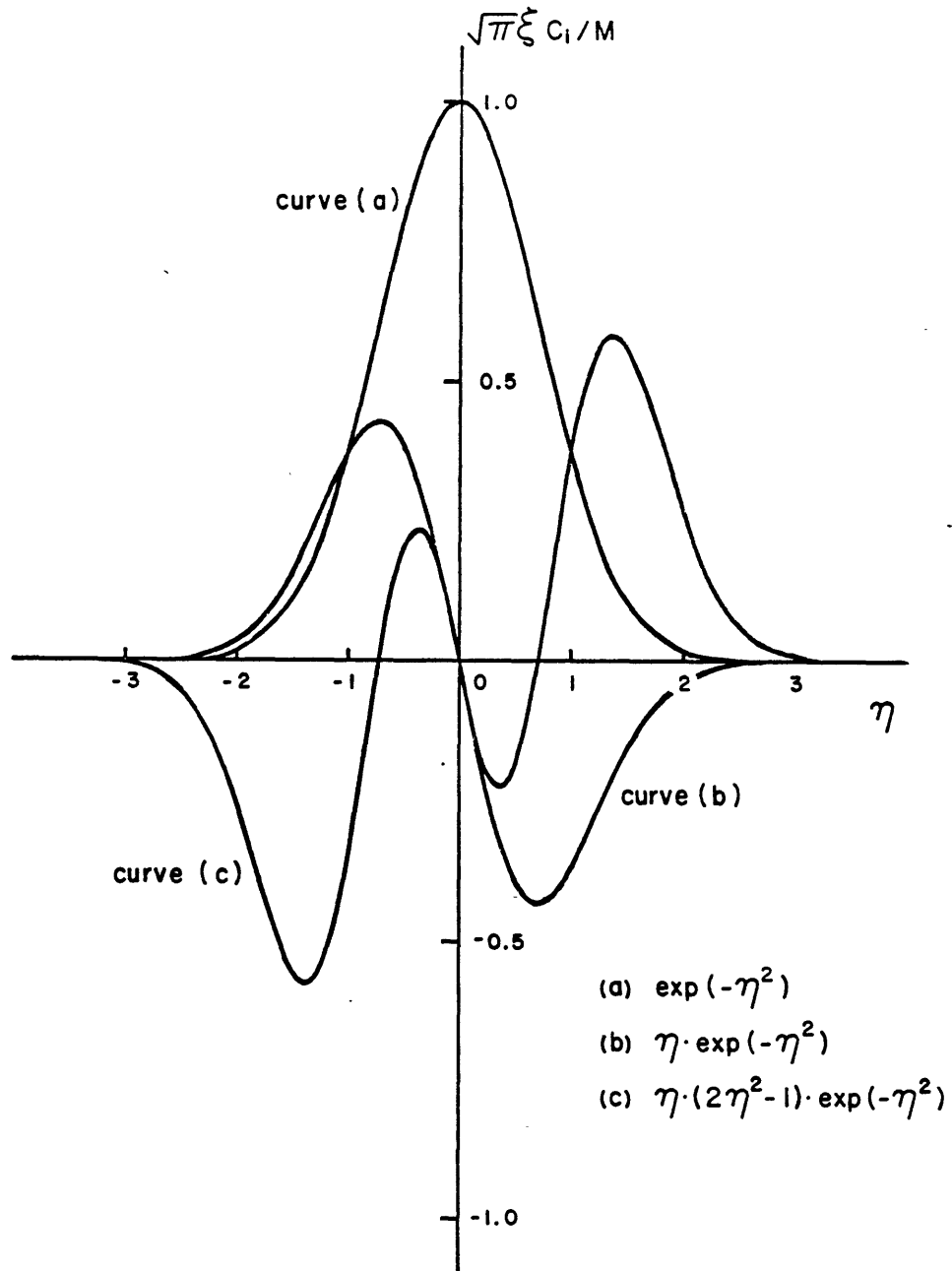


Fig. 2. The nonisothermal diffusion profile developed from a thin-film source is expected to be a combination, $(a) + \epsilon(b) + \epsilon(c)$.

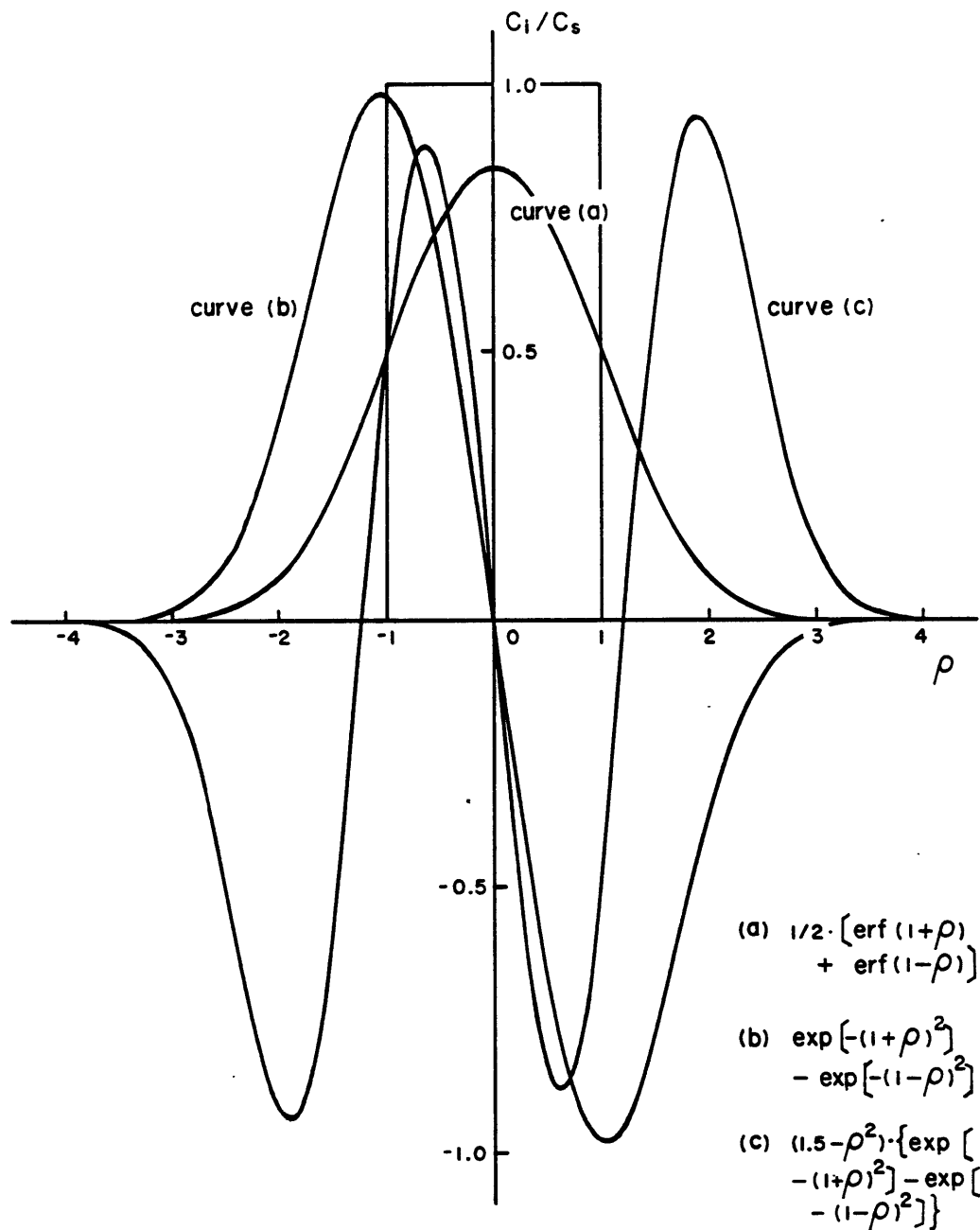


Fig. 3. The nonisothermal diffusion profile developed from a finite source of $2h$ thickness is expected to be a combination, $(a) + \epsilon(b) + \epsilon(c)$. ζ has been arbitrarily taken as 1 in Eq. 188 b.

right-hand-side of Eq. 100 b and Eq. 103 b . For the finite source of $2h$ thickness, this suppression takes place at $z \sim \pm\sqrt{h^2+2\Delta_0 t}$ or $\rho \sim \sqrt{1+\frac{1}{2}\zeta^2}$ (see the curve (c) in Fig. 3 and the third term on the right-hand-side of Eq. 106 b). As a consequence, any disturbance on an antisymmetric or symmetric isothermal-diffusion profile in these regions is mainly caused by thermomigration.

It is noteworthy, in Fig. 1 or in Eq. 100 for a semi-infinite source, that the isothermal diffusion profile of an odd function, $\text{erfc}(\eta)$, is modified by two even functions, $\exp(-\eta^2)$ and $(2\eta^2-1)\exp(-\eta^2)$, to leave the law of mass conservation unimpaired, namely,

$$\int_0^C C_i(\eta, \xi) dC = 0. \quad \text{Eq. 108}$$

In Fig. 2 or in Eq. 103 for a thin film source, however, the leading profile of an even function, $\exp(-\eta^2)$, is modified by the two odd functions, $\eta \exp(-\eta^2)$ and $\eta(2\eta^2-1)\exp(-\eta^2)$, and the law of mass conservation again remains unimpaired, namely,

$$\int_{-\infty}^{\infty} C_i(\eta, \xi) \xi d\eta = M. \quad \text{Eq. 109}$$

The same is true for a finite source of $2h$ thickness as shown in Fig. 3 or in Eq. 106. The leading term of an even function is again modified by the two odd functions.

3.3. DETERMINATION OF HEAT OF TRANSPORT

From the experimental point of view, we may have some degrees of freedom to adjust the accuracy of the time-dependent solutions, Eq. 100, Eq. 103 and Eq. 106. A diffusion zone δ , over which the cross effect is supposed to be observed, can be diminished as much as is allowed by the spatial resolution (or depth resolution) of an instrument such as, for example, the secondary ion mass spectrometer employed to establish the concentration profile, $C_i(z,t)$. Equivalently, the accuracy ϵ^2 can also be controlled by adjusting the temperature and its gradient at $z=0$ for a given δ (see Eq. 95). If we take, for example, $\delta \sim 10 \mu$ and $L \sim 1 \text{ cm}$ or $a \sim 10^3 \text{ K/cm}$ and $T_0 \sim 10^3 \text{ K}$ for the given $\delta \sim 10 \mu$, then ϵ^2 will be $\sim 10^{-3}$ or 0.1 %.

The reduced heat of transport, q_i^* , can be determined by curve-fitting an experimental diffusion profile to either one of Eq. 100, Eq. 103 and Eq. 106 depending on the initial and boundary conditions, Eq. 99, Eq. 102 or Eq. 105, respectively. Alternatively, it is possible to determine q_i^* from the characteristics of the profile itself. Let's first examine the non-isothermal diffusion profile developed from a semi-infinite source, Fig. 1 or Eq. 100. It is observed in Fig. 1 that the position where $C_i/C_s = 1/2$, z_0 or $\eta_0 (\equiv z_0/2\sqrt{\Delta_0 t})$, will be displaced from $z=0$ or $\eta=0$ where C_i/C_s would be 1/2 for an isothermal annealing under the semi-infinite source initial and boundary conditions. This is a result of the addition of the second term in the solution Eq. 100 a, which has maximum

magnitude at $z=0$ and which, moreover, is the term which contains information on the heat of transport. From Eq. 100 b,

$$\begin{aligned} \frac{1}{2} &= \frac{1}{2} \left(1 - \frac{2}{\sqrt{\pi}} \eta_0 + \dots \right) \\ &- \frac{1}{4\sqrt{\pi}} \frac{aT_i^*}{T_0^2} \xi \left(1 - \eta_0^2 + \frac{1}{2} \eta_0^4 - \dots \right) \\ &+ \frac{1}{8\sqrt{\pi}} \frac{aT_m}{T_0^2} \xi \left(-1 + 3\eta_0^2 - \frac{5}{2} \eta_0^4 + \dots \right) \end{aligned} \quad \text{Eq. 110}$$

where use has been made of infinite series expansions for the complementary error function and the exponential function.

For a small displacement or

$$\eta_0 \rightarrow 0, \quad \text{Eq. 111}$$

we may neglect the terms of the second and higher order in Eq. 110 to get

$$\eta_0 = -\frac{1}{8} \cdot \frac{a(T_m + 2T_i^*)}{T_0^2} \cdot \xi \quad \text{Eq. 112}$$

or, due to Eq. 101,

$$\left(\frac{z_0}{t} \right) = -\frac{1}{2} \cdot \frac{a(T_m + 2T_i^*)}{T_0^2} \cdot \Delta_0 \quad \text{Eq. 113}$$

Therefore, by measuring the shift velocity, $\dot{z}_0 \equiv (z_0/t)$, at $z=0$, we can determine the heat of transport, q_i^* ($=kT_i^*$) provided that the isothermal diffusion coefficient of the interstitial

impurities is known. In view of Eq. 113, the shift velocity, \dot{z}_0 , is obviously position-dependent. Thus, by measuring both a displacement, z_0 , and the elapsed time, t , in the stationary temperature gradient, we come to obtain a certain average velocity, \bar{z}_0 , such that

$$\bar{z}_0 = \frac{1}{z_0} \int_0^{z_0} \dot{z}_0(z) dz. \quad \text{Eq. 114}$$

The local velocity, $\dot{z}_0(z_0 \rightarrow 0)$, may thus be determined by extrapolating \bar{z}_0 up to $z_0=0$ or equivalently $t=0$.

The reduced heat of transport, q_i^* , can also be determined from the time rate of concentration change at $z=0$, $C_i(0,t)$ for the semi-infinite source. According to Eq. 100 a, $C_i(0,t)$ varies with time as

$$\frac{C_i(0,t)}{C_s} = \frac{1}{2} - \alpha \sqrt{t} \quad \text{Eq. 115}$$

where

$$\alpha \equiv \frac{a\sqrt{\Delta_0}}{4\sqrt{\pi T_0^2}} (T_m + 2T_i^*). \quad \text{Eq. 116}$$

The normalized concentration, C_i/C_s , at $z=0$ is expected to vary linearly with t . From its proportionality coefficient, α , we may extract q_i^* ($=kT_i^*$) both with the help of the isothermal diffusion coefficient which is presumed to be sufficiently accurate, and with the knowledge of the temperature and its gradient at $z=0$, i.e., T_0 and "a". These latter terms might

be the major source of error associated with the calculation of q_i^* . By choosing T_o for a given temperature gradient satisfying Eq. 95, $|a\delta/T_o| \sim \epsilon^2$, we may maximize α . Substituting Eq. 90, $D(T_o) = D_o \exp(-T_m/T_o)$, for Δ_o in Eq. 116, we obtain

$$\alpha = \frac{a(T_m + 2T_i^*)\sqrt{D_o} \exp(-T_m/2T_o)}{4\sqrt{\pi} T_o^2}, \quad \text{Eq. 117}$$

which goes to maximum,

$$\alpha_{\max} = \frac{8\sqrt{D_o}}{\sqrt{\pi}e^2} \frac{a}{T_m} \left(\frac{1}{2} + \frac{T_i^*}{T_m}\right) \quad \text{Eq. 118}$$

at the temperature,

$$T_o = T_m/4. \quad \text{Eq. 119}$$

To maximize the cross effect, thus, the choice of a proper combination of T_o and "a" is required. The temperature gradient, a, may be rather more restrictive due to the constraints necessary to achieve accuracy of the time-dependent solution, Eq. 95, and due to the possible alteration of the material itself at the hot end of the specimen such as, for example, melting or vaporization.

We next turn to an examination of the solution under thin film initial conditions, Eq. 103, to see if the expression might similarly suggest experiments which might provide value for the heat of transport in a simple and efficient way. It

may also be observed in Fig. 2 that the position, z_0 or η_0 , where the solute concentration is maximum, is displaced from $z=0$, the location of maximum concentration which would occur under isothermal annealing with the thin-film source initial and boundary conditions, Eq. 102. For this solution, however, the displacement occurs as a result of the asymmetry in the form of both (b) and (c), Fig. 2, only the former of which contains information on the heat of transport. Also the two perturbations may, in part, nullify one another depending on the sign and magnitude of the heat of transport. By differentiating Eq. 103 b with respect to η , we have

$$0 = \left[- \frac{a(T_m + 2T_i^*)}{4T_o^2} - \frac{2}{\xi} \eta_0 + \frac{a(2T_m + T_i^*)}{T_o^2} \eta_0^2 - \frac{aT_m}{T_o^2} \eta_0^4 \right] \cdot \exp(-\eta_0^2). \quad \text{Eq. 120}$$

For small η_0 , neglecting the second and higher order terms in η_0 analogous to the procedure in simplifying the expansion Eq. 110, we arrive at exactly the same expressions as Eq. 112 and Eq. 113. That is, the maximum in the concentration gradient of the thin-film sample moves at the same velocity as the relative concentration of 1/2 under semi-infinite source conditions. The reduced heat of transport, q_i^* , is thus determined by measuring the velocity, $\dot{z}_0(z_0 \rightarrow 0)$, with which the concentration maximum shifts from $z=0$. The determination of the local shift velocity, $\dot{z}_0(z_0 \rightarrow 0)$, follows the same procedure that has been discussed for the measurement of the local velocity with which the position where $C_i/C_s=1/2$ shifts for the semi-infinite source.

According to Eq. 113, the displacement of the concentration maximum or $C_i/C_s=1/2$ is governed by the temperature dependence of the diffusion rate via T_m or Q and by the interference with the applied temperature gradient via T_i^* or q_i^* . The former always shifts the concentration maximum or, alternatively, $C_i/C_s=1/2$ down the temperature gradient but the latter influence may shift this reference concentration either down or up the gradient depending on the sign of q_i^* . As a numerical estimation of the shift velocity, we may substitute $a \sim 10^3$ K/cm, $T_o \sim 10^3$ K, and $T_m + 2T_i^* \sim 10^4$ K in Eq. 113. The shift velocity is then given as

$$z_o/t \sim 10\Delta_o \text{ cm/sec.}$$

In other words, the system must be kept in the temperature gradient only for a time t as long as

$$t \sim z_o/10\Delta_o \text{ sec,}$$

for which an overall diffusion zone, δ , extends to

$$\delta \sim 10\sqrt{\Delta_o t} \sim \sqrt{z_o} \text{ cm.}$$

When z_o is taken as $\sim 1 \mu\text{m}$, δ will then be $\sim 100 \mu\text{m}$. In comparison, it is very interesting to compare the present time scale with that of a stationary state technique for which it has previously been shown that the relaxation time is $\theta = L^2/\pi^2 D_i$.

It has been already pointed out that it takes at least 50 to achieve 99 % of the stationary state. The ratio of the two time scales is approximately

$$\frac{t}{\theta} \sim \frac{z_0}{L^2} ,$$

which represents very well the efficiency of the present analysis. That is, the suggested method for determining the reduced heat of transport for diffusion by an interstitial mechanism should produce accurate results in experiments an order of magnitude less time in duration than the stationary state technique.

Finally, to a nonisothermal diffusion profile developed from a finite source, Eq. 106 and Fig. 3, one may apply the ideas similar or equivalent to those described above for the both extreme source conditions so as to determine the reduced heat of transport of the solute.

4. NONISOTHERMAL ANION SELF-DIFFUSION IN MgO

We will now turn to our initial problem, which motivated the present analyses, the intermixing of isotopes, ^{16}O and ^{18}O of MgO in a temperature gradient. The focus of the problem is on how the intermixing profile develops in a temperature gradient, namely, how it is affected by the thermomigration.

Understanding of the thermomigration in ionic crystals is still rather limited. Howard⁴⁹ and Allnatt and Chadwick⁵⁰ have provided theoretical analyses based on irreversible thermodynamics for an alkali halide crystal doped with divalent cations. In these analyses, the anion sublattice was regarded as perfect and immobile since the diffusion rate of anions is very sluggish compared with cations in the alkali halides. The principle of the analyses is based on the Soret effect confined at the cation sublattice - stationary unmixing of cation impurities in a temperature gradient. Experimental observation is made of the Soret gradient from which an effective heat of transport of impurity cations is extracted. Soret data are available only for alkali halide crystals: $^{85}\text{Sr}^{2+}$ in NaCl^{51,52} and in KCl⁵³; $^{54}\text{Mn}^{2+}$ in NaCl⁵⁴ and KCl⁵³; Sr^{2+} , Cd^{2+} and Mn^{2+} in AgCl⁵⁵; Cd^{2+} and Mn^{2+} in AgBr.⁵⁵ No study has yet been made of thermomigration in metallic oxides and furthermore, a thermal self-diffusion measurement has never been attempted even for alkali halides as far as we know. If or when a self-

thermomigration datum is available, it could be complemented by a measurement of the thermoelectric power to permit separation of the heats of transport of cations and anions because each provides the knowledge of a certain combination of two heats of transport (see Section 4.3). More attention has been paid to the measurement of thermoelectric power.^{5,6} The irreversible thermodynamical analyses of the thermoelectricity of ionic crystals have been provided by many authors.^{5,7-61}

In this chapter, we will analyze the thermomigration of oxygen in MgO and show what kind of information might be extracted from the time-dependent intermixing profile.

4.1. PHENOMENOLOGICAL LAWS

Consider a system of crystalline $\text{Mg}(\text{}^{16}\text{O}_{1-x}\text{}^{18}\text{O}_x)$, composed of two kinds of oxygen isotopes, ^{16}O and ^{18}O . It is presumed to be hypothetically pure and stoichiometric. The predominant defects are those of Schottky disorder which are fully ionized. The concentration of intrinsic electronic defects – free electron and holes is negligibly small compared with that of the ionic defects.

Now suppose that the system is subject both to an isotopic concentration gradient ($\partial C_1/\partial z \neq 0$) and to a stationary temperature gradient ($\partial T/\partial z \neq 0$; $\partial T/\partial t = 0$) along the z -direction. In such a system, we may observe fluxes of (1) $^{18}\text{O}_\text{O}^{-2}$, (2) $^{16}\text{O}_\text{O}^{-2}$ and (3) V_O^\bullet on the anionic sublattice and those of (4) Mg_Mg^{+2} and (5) V_Mg'' on the cationic sublattice,

induced relative to the local crystalline lattice or lattice frame of reference (see Section 2.5) as evolutionary processes. The numerical superscripts, -2 and +2 denote the actual charge states (valences) of the constituent ions on each sublattice, while the dots (·) and the primes (') represent the effective positive and negative charges, respectively, of the fully ionized defects according to the Kröger-Vink system of notation:^{6,2} For the sake of simplicity, we will employ numerical subscripts, k=1-5 to denote the mobile species in the order in which they have been introduced above: J_1 for flux of $^{18}\text{O}_\text{O}^{-2}$; J_2 for flux of $^{16}\text{O}_\text{O}^{-2}$; J_3 for flux of $\text{V}_\text{O}^{\cdot\cdot}$; J_4 for flux of Mg_Mg^{+2} ; J_5 for flux of V_Mg'' .

In an MgO-like stoichiometric ionic solid, the two sublattices are so intimately bound together that they are better regarded conceptually as a single molecular lattice with an electrically neutral quasi-molecule, $(\text{Mg}^{+2}\text{O}^{-2})^x$, on each lattice point. Thus, any kind of variation on one sublattice either closes itself or synchronizes with the reciprocal equivalent on the other under the macroscopic constraint,

$$C_- = C_+ \equiv C$$

Eq. 121

in which C_- and C_+ denote the densities of ionic positions on the anionic sublattice (denoted by the subscript "-") and the cationic sublattices (denoted by the subscript "+"), respectively. For the present system,

$$C_- = C_1 + C_2 + C_3 \quad \text{Eq. 122}$$

and

$$C_+ = C_4 + C_5. \quad \text{Eq. 123}$$

Since the misplacement of ions from their own sublattice to the other is prohibited energetically and each sublattice is preserved locally, the fluxes are subject to the constraints,

$$L^{\vec{J}}_1 + L^{\vec{J}}_2 + L^{\vec{J}}_3 = 0 \quad \text{Eq. 124}$$

and

$$L^{\vec{J}}_4 + L^{\vec{J}}_5 = 0. \quad \text{Eq. 125}$$

Due to these linear interdependencies between fluxes, the phenomenological equations for our system may be written, according to Eq. 78, Chapter 2, as

$$L^{\vec{J}}_1 = L_{11}(\vec{X}_1 - \vec{X}_3 + q_1^* \vec{X}_q) + L_{12}(\vec{X}_2 - \vec{X}_3 + q_2^* \vec{X}_q) + L_{14}(\vec{X}_4 - \vec{X}_5 + q_4^* \vec{X}_q) \quad \text{Eq. 126}$$

$$L^{\vec{J}}_2 = L_{21}(\vec{X}_1 - \vec{X}_3 + q_1^* \vec{X}_q) + L_{22}(\vec{X}_2 - \vec{X}_3 + q_2^* \vec{X}_q) + L_{24}(\vec{X}_4 - \vec{X}_5 + q_4^* \vec{X}_q) \quad \text{Eq. 127}$$

$$L^{\vec{J}}_4 = L_{41}(\vec{X}_1 - \vec{X}_3 + q_1^* \vec{X}_q) + L_{42}(\vec{X}_2 - \vec{X}_3 + q_2^* \vec{X}_q) + L_{44}(\vec{X}_4 - \vec{X}_5 + q_4^* \vec{X}_q) \quad \text{Eq. 128}$$

Since the constituents are electrically charged, the generalized forces in their reduced forms (see Eq. 32, Chapter 2) are written in terms of the corresponding electro-chemical potentials;

$$\vec{X}_k = - (\vec{\nabla} \eta_k)_T, \quad k = 1, 2, 3, 4, 5 \quad \text{Eq. 129 a}$$

or

$$\vec{X}_k = - (\vec{\nabla} \mu_k)_T - e_k \vec{\nabla} \phi, \quad \text{Eq. 129 b}$$

where e_k may be chosen as either the actual charge or the effective charge of species k and $\vec{\nabla} \phi$ is an electric field induced internally in our nonisothermal diffusion system of charged constituents. The thermodynamic forces of Eq. 129 are supposed to satisfy the electrochemical Gibbs-Duhem relation^{28,29} (or Prigogine's theorem, Eq. 71, Chapter 2);

$$\sum_{k=1}^5 C_k \vec{X}_k = 0. \quad \text{Eq. 130}$$

Assuming that vacancies do not interact with each other and are absolutely random in their placements, we may write

$$\mu_k = \mu_k^0 + kT \ln C_k/C, \quad k = 1, 2, 3, 4, 5 \quad \text{Eq. 131}$$

and hence Eq. 129 is rewritten as

$$\begin{aligned} \vec{X}_1 &= -kT \frac{\vec{\nabla} C_1}{C_1} + e \vec{\nabla} \phi & \text{for } {}^{18}\text{O}_\text{O}^{-2} \\ \vec{X}_2 &= -kT \frac{\vec{\nabla} C_2}{C_2} + e \vec{\nabla} \phi & \text{for } {}^{16}\text{O}_\text{O}^{-2} \\ \vec{X}_3 &= -kT \frac{\vec{\nabla} C_3}{C_3} & \text{for } V_\text{O}^{\bullet\bullet} \\ \vec{X}_4 &= -kT \frac{\vec{\nabla} C_4}{C_4} - e \vec{\nabla} \phi & \text{for } \text{Mg}_\text{Mg}^{+2} \end{aligned} \quad \text{Eq. 132}$$

$$\vec{X}_5 = -kT \frac{\vec{V}C_5}{C_5} \quad \text{for } V_{Mg}'' \quad \text{Eq. 132}$$

in terms of the actual cationic charge, e ($=2e_0$ for MgO in terms of the electronic charge e_0). If we further assume that local internal equilibrium for Schottky defect formation prevails,

$$\frac{\vec{V}C_3}{C_3} = \frac{\vec{V}C_5}{C_5} = \frac{h_s/2}{kT^2} \vec{V}T, \quad \text{Eq. 133}$$

since

$$C_3 C_5 = C_- C_+ \exp(-g_s/kT) \quad \text{Eq. 134}$$

and $C_3 = C_5$ and $C_- = C_+$.

Here the Gibbs free energy and the enthalpy for Schottky defect formation, g_s and h_s , respectively, are interrelated via the thermodynamic identity,

$$\frac{\partial}{\partial T} \left(\frac{g_s}{T} \right) = - \frac{h_s}{T^2}. \quad \text{Eq. 135}$$

Thermodynamic forces in the local defect equilibrium have been well derived by Howard and Lidiard⁹ and Lidiard^{6,3}

With respect to the phenomenological coefficients, we may assume, as Howard and Lidiard⁹ did in their treatment of the thermoelectricity of ionic solids, that

$$L_{14} = L_{41} = 0 \quad ; \quad L_{24} = L_{42} = 0, \quad \text{Eq. 136}$$

which implies that a diffusional driving force acting on the

cation confined to its own sublattice does not cause a diffusion flow of the anion confined to the other sublattice and *vice versa*. Of the other non-zero phenomenological coefficients, L_{11} , $L_{12}(=L_{21})$ and L_{22} are identified in terms of the anion tracer diffusion coefficient, D_{-}^{*} , and the corresponding correlation factor, f_{-} , with a close analogy to the isothermal self-diffusion in an elemental crystal.⁹ This is made possible only for a system in which local defect equilibrium is observed or in which the vacancy concentration, C_3 in the present case, is a single-valued function of the local temperature alone in view of the relation,^{6,4}

$$D_{-}^{*} = f_{-} \frac{C_3}{C_{-}} D_3. \quad \text{Eq. 137}$$

The vacancy diffusion coefficient, D_3 , is presumably dependent on the local temperature alone.

The identification is carried out by the two independent thought experiments. First consider an isothermal (i.e., $\vec{X}_q=0$) anion tracer diffusion in which

$$\vec{\nabla}C_1 + \vec{\nabla}C_2 = 0 \quad ; \quad \vec{\nabla}C_3 = 0. \quad \text{Eq. 138}$$

From Eq.'s 126 and 127 along with Eq.'s 132, 136 and 138, we can equate the anion tracer diffusion coefficient D_{-}^{*} with the combination of the phenomenological coefficients as

$$(L_{11}/C_1) - (L_{12}/C_2) = D_{-}^{*}/kT \quad \text{Eq. 139}$$

and

$$L_{22}/C_2 - L_{21}/C_1 = D_-^*/kT. \quad \text{Eq. 140}$$

It is noted that $\vec{L}_1\vec{J}_1 + \vec{L}_2\vec{J}_2 = 0$ is necessarily true.

Consider next a situation in which a concentration gradient of vacancies exists in an isothermal condition and in which the isotopic ratio remains constant, or

$$\vec{\nabla}C_1/C_1 = \vec{\nabla}C_2/C_2 \quad ; \quad \vec{\nabla}C_3 \neq 0. \quad \text{Eq. 141}$$

There will then be a net vacancy flux, $\vec{L}_3\vec{J}_3$, or

$$\vec{L}_3\vec{J}_3 = -D_3\vec{\nabla}C_3, \quad \text{Eq. 142}$$

which is counterbalanced by $\vec{L}_1\vec{J}_1$ and $\vec{L}_2\vec{J}_2$ proportional to the concentration of the isotope 1 and 2, respectively, viz.,

$$\vec{L}_1\vec{J}_1 = - [C_1/(C_1+C_2)] \vec{L}_3\vec{J}_3 \quad \text{Eq. 143}$$

$$\vec{L}_2\vec{J}_2 = - [C_2/(C_1+C_2)] \vec{L}_3\vec{J}_3. \quad \text{Eq. 144}$$

Substituting Eq.'s 126 and 127 along with Eq.'s 132, 136 and 141 into Eq. 143 and Eq. 144 combined with Eq. 142, we obtain another set of equations;

$$L_{11} + L_{12} = (C_1C_3D_3)/(CkT) \quad \text{Eq. 145}$$

and

$$L_{22} + L_{21} = (C_2C_3D_3)/(CkT) \quad \text{Eq. 146}$$

By solving simultaneously Eq.'s 139, 140, 145 and 146 along with Eq. 137, we obtain single-valued coefficients in terms of f_- and D_-^* as;

$$L_{11} = \frac{C_1 D_-^*}{f_- kT} \cdot \left[1 - \frac{C_2}{C_1 + C_2} (1 - f_-) \right] \quad \text{Eq. 147}$$

$$L_{21} = L_{12} = \frac{D_-^*}{f_- kT} \cdot \frac{C_1 C_2}{C_1 + C_2} \cdot (1 - f_-) \quad \text{Eq. 148}$$

$$L_{22} = \frac{C_2 D_-^*}{f_- kT} \cdot \left[1 - \frac{C_1}{C_1 + C_2} (1 - f_-) \right]. \quad \text{Eq. 149}$$

In another thought experiment in which a concentration gradient of the cation vacancy, $\vec{\nabla} C_5$, is imposed upon our system, we have a net vacancy flux on the cation sublattice, $L_{5'}^{\vec{J}}$,

$$L_{5'}^{\vec{J}} = - D_5 \vec{\nabla} C_5. \quad \text{Eq. 150}$$

This vacancy flux will be counterbalanced by a net cation flux $L_4^{\vec{J}}$ or

$$L_4^{\vec{J}} = - L_{5'}^{\vec{J}}. \quad \text{Eq. 151}$$

Equation 151 along with Eq. 150 yields an expression of L_{44} in terms of the cation self-diffusion coefficient D_+ due to Eq. 128 combined with Eq.'s 132 and 136;

$$L_{44} = \frac{C_4 D_+}{kT} \quad \text{Eq. 152}$$

where we employed a relation similar to Eq. 137,

$$C_5 D_5 = C_4 D_+ . \quad \text{Eq. 153}$$

The transport coefficient L_{44} , Eq. 152, corresponds to the combination, $L_{11}+L_{12}+L_{21}+L_{22}$, on the other sublattice, which is related to the anion self-diffusion coefficient, D_- , due to Eq.'s 147, 148 and 149;

$$L_{11} + L_{12} + L_{21} + L_{22} = \frac{(C_1 + C_2)D_-}{kT} \quad \text{Eq. 154}$$

since $D_-^* = f_- D_-$. It should be noted that, in this identification of transport coefficients L_{k1} , the vacancy concentrations, C_3 and C_5 , have been implicitly assumed to be negligibly small compared to both ion concentrations or

$$C_3 \ll C_1 + C_2 \quad ; \quad C_5 \ll C_4 . \quad \text{Eq. 155}$$

These assumptions allow Eq. 122 and Eq. 123, if necessary, to be rewritten as

$$C_- \cong C_1 + C_2 \quad ; \quad C_+ \cong C_5 . \quad \text{Eq. 156}$$

Substituting Eq.'s 132, 133, 136, 147, 148, 149 and 152 into Eq. 126, Eq. 127, and Eq. 128, we finally obtain the phenomenological equations respectively as:

$$L\vec{J}_1 = -D_-^* [\vec{\nabla}C_1 - \frac{C_1 e}{f_- kT} \vec{\nabla}\phi + \frac{C_1 (q_1^* - h_s/2)}{f_- kT^2} \vec{\nabla}T] \quad \text{Eq. 157}$$

$$L\vec{J}_2 = -D_-^* [\vec{\nabla}C_2 - \frac{C_2 e}{f_- kT} \vec{\nabla}\phi + \frac{C_2 (q_2^* - h_s/2)}{f_- kT^2} \vec{\nabla}T] \quad \text{Eq. 158}$$

$$L\vec{J}_4 = -D_+ [\vec{\nabla}C_4 - \frac{C_4 e}{kT} \vec{\nabla}\phi + \frac{C_4 (q_4^* - h_s/2)}{kT^2} \vec{\nabla}T] \quad \text{Eq. 159}$$

If we neglect the isotope effect originating from the difference of isotopic masses, we may set

$$q_1^* = q_2^* \equiv q_-^*. \quad \text{Eq. 160}$$

This effect has been already neglected when we define the tracer diffusivity D_-^* , Eq. 139 and Eq. 140. It should be noted that only two independent reduced heats of transfer, q_-^* and q_+^* ($=q_4^*$), one for each sublattice, is defined as has been already pointed out by Howard and Lidiard.⁹

Movements of ions are further restricted by an electro-neutrality field, $\vec{\nabla}\phi$, called the *thermal diffusion potential*, which originates from the incipient charge separation due to the difference of cation and anion mobilities. This field prohibit further separation by leveling ionic mobilities, i.e., "helping and retarding ions according to their needs so as to keep the situation as electroneutral as possible."^{6 5} In this sense, it may be called the electroneutrality field. As a sufficiency for the charge neutrality,

$$L\vec{J}_3 - L\vec{J}_5 = 0 \quad \text{Eq. 161}$$

in terms of effective charge flows, or

$$L\vec{J}_1 + L\vec{J}_2 - L\vec{J}_4 = 0 \quad \text{Eq. 162}$$

in terms of actual charge flows. The constraint on the fluxes, Eq. 161 or Eq. 162 implies that any net movement of ions on a sublattice must be neutralized by a reciprocal equivalent on the other sublattice. From this point of view, one may regard an ionic event on either sublattice as one on the molecular lattice in which electrically neutral quasi-molecules, $(\text{Mg}_{\text{Mg}}^{+2} \text{O}_{\text{O}}^{-2})^x$, or quasi-molecular vacancies, V_{MgO}^x , are involved.

Solving Eq. 162 for \vec{V}_ϕ with use of Eq.'s 157, 158 and 159 and Eq.'s 121, 122, 123 and 133, the thermal diffusion potential is obtained as;

$$\vec{V}_\phi = \frac{\vec{V}_T}{eT} \left[- \left(\frac{D_+ q_+^* - D_- q_-^*}{D_+ + D_-} \right) + \frac{h_s}{2} \left(1 + \frac{C_5}{C_4} \right) \left(\frac{D_+ - D_-}{D_+ + D_-} \right) \right], \quad \text{Eq. 163}$$

where the anion diffusion coefficient, D_- has replaced D_-^*/f_- . For an MgO-like stoichiometric solid with a high value of Schottky defect formation energy, an intrinsic value of the vacancy concentration is usually negligibly small compared to the concentration of ions,^{6,6} i.e., Eq. 155. A numerical estimation of the vacancy concentration is put at $C_5/C_4 \sim 10^{-6}$ for a pure MgO even at its melting point (3120 K) when we take

$h_s = 7.5 \text{ eV}^{76}$ (see Part I) and take the entropy-related term of Eq. 134 as unity. Due to Eq. 155, Eq. 163 may be rewritten as

$$\vec{\nabla}\phi = \frac{\vec{\nabla}T}{eT} \left[- \left(\frac{D_+ q_+^* - D_- q_-^*}{D_+ + D_-} \right) + \frac{h_s}{2} \left(\frac{D_+ - D_-}{D_+ + D_-} \right) \right]. \quad \text{Eq. 164}$$

Similar expressions have been obtained by many authors in their treatments of the thermoelectric power of ionic solids.⁵⁷⁻⁶¹

Substitution of the thermal diffusion potential, Eq. 164, reduces the phenomenological equations, Eq. 157, Eq. 158 and Eq. 159 to the following equations:

$$L_1 \vec{J}_1 = - D_-^* \vec{\nabla} C_1 - C_1 \frac{D_- D_+}{D_- + D_+} \frac{q_-^* + q_+^* - h_s}{kT^2} \vec{\nabla} T \quad \text{Eq. 165}$$

$$L_2 \vec{J}_2 = - D_-^* \vec{\nabla} C_2 - C_2 \frac{D_- D_+}{D_- + D_+} \frac{q_-^* + q_+^* - h_s}{kT^2} \vec{\nabla} T \quad \text{Eq. 166}$$

$$L_4 \vec{J}_4 = - C_+ \frac{D_- D_+}{D_- + D_+} \frac{q_-^* + q_+^* - h_s}{kT} \vec{\nabla} T \quad \text{Eq. 167}$$

In the derivation of Eq. 167, use has been made of $\vec{\nabla} C_4 \approx 0$ due to Eq. 156.

The salient feature of the present system is that there are net vacancy fluxes (or equivalently net mass fluxes) on both sublattices solely due to the applied temperature gradient in view of Eq.'s 124, 165 and 166 or Eq.'s 125 and 167, namely,

$$L_3 \vec{J}_3 = L_5 \vec{J}_5 = C \cdot \left(\frac{D_- \cdot D_+}{D_- + D_+} \right) \cdot \frac{(q_-^* + q_+^* - h_s)}{kT} \cdot \vec{\nabla} T \quad \text{Eq. 168}$$

where the approximation, $\vec{\nabla}(C_1+C_2) \approx 0$, has been employed in view of Eq. 156. They are strongly coupled (${}_L\vec{J}_3 = {}_L\vec{J}_5$) through the thermal diffusion potential so that one may regard the synchronous vacancy flows on both sublattices as a net flow of electrically neutral quasi-molecular vacancies, V_{MgO}^x , on the molecular lattice. A net flux of V_{MgO}^x , which is equal to ${}_L\vec{J}_3$ in Eq. 168, renders local lattice movement at a velocity, \vec{u}_L , relative to the Fick or the volume-fixed frame of reference for the preservation of the local defect equilibrium. The Fick frame of reference coincides with the laboratory frame in the present case, i.e., $\vec{u}_F = 0$, since no volume change may be assumed upon isotope-intermixing even in a temperature gradient. The relative velocity is thus given in Eq. 68 in Chapter 2;

$$\vec{u}_L = \frac{1}{C} {}_L\vec{J}_3 \quad \text{Eq. 169}$$

or, due to Eq. 168,

$$\vec{u}_L = \frac{D_- \cdot D_+ \cdot (q_-^* + q_+^* - h_s)}{D_- + D_+} \cdot \frac{1}{kT^2} \cdot \vec{\nabla} T. \quad \text{Eq. 170}$$

This relative velocity, \vec{u}_L , again very much reflects molecular characteristics. The combination of the self-diffusion coefficients, $(D_- D_+ / D_- + D_+)$ and the combination of the reduced heats of transfer, $(q_-^* + q_+^*)$ are the corresponding quantities of a quasi-molecule, $(Mg_{Mg}^{+2} O_O^{-2})^x$. The enthalpy of the Schottky defect formation, h_s , also corresponds to the formation enthalpy of a molecular vacancy, V_{MgO}^x . As would be

expected, thus, the relative velocity, Eq. 170, or the net vacancy flux, Eq. 168 is readily reduced to that for an elementary metal either by replacing the molecular quantities with the corresponding atomic quantities of the metal, i.e.,

$$\frac{D_- \cdot D_+}{D_- + D_+} = D \quad (\text{self-diffusion coefficient of the metal})$$

$$q_-^* + q_+^* = q^* \quad (\text{reduced heat of transfer of the metal})$$

$$h_s = h_v \quad (\text{vacancy-formation enthalpy of the metal})$$

or by setting

$$D_- = D_+ = D$$

$$q_-^* = q_+^* = q^*$$

$$h_s/2 = h_v.$$

A net vacancy flux induced by a temperature gradient in an elemental crystal has been given⁹ as

$$L \vec{J}_v = \frac{C_v D_v}{kT^2} (q^* - h_v) \vec{\nabla} T \quad \text{Eq. 171}$$

where C_v is the local equilibrium vacancy concentration and D_v is the diffusion coefficient of the metal vacancy.

Due to this relative motion of the local crystalline

lattice, the fluxes in the moving frame, Eq. 165, Eq. 166 and Eq. 167, are not accessible to an observer sitting in the Fick frame of reference. What is accessible experimentally and meaningful in the mathematics of diffusion is a flux (e.g. $F_1^{\vec{J}}$) which has been transformed to the Fick frame according to Eq. 66, or

$$F_1^{\vec{J}} = L_1^{\vec{J}} + C_1 \cdot \vec{u}_L. \quad \text{Eq. 172}$$

Substituting Eq.'s 165, 166 and 167 into Eq. 172, we obtain as the observable fluxes (or operable phenomenological laws):

$$F_1^{\vec{J}} = -D^* \vec{\nabla} C_1 \quad \text{Eq. 173}$$

$$F_2^{\vec{J}} = -D^* \vec{\nabla} C_2 \quad \text{Eq. 174}$$

$$F_4^{\vec{J}} = 0 \quad \text{Eq. 175}$$

It is necessarily true that, due to Eq. 156 or $\vec{\nabla} C_1 + \vec{\nabla} C_2 \approx 0$,

$$F_1^{\vec{J}} + F_2^{\vec{J}} = 0. \quad \text{Eq. 176}$$

One may note that the interference of the temperature gradient with the mass flow has disappeared completely in the Fick frame of reference (Eq. 175 and Eq. 176) and that the mixing of anion isotopes, ^{18}O and ^{16}O in the present case, has nothing to do with the cross effect (Eq. 173 and Eq. 174).

Therefore, no information about the cross effect or the heat of transfer can be extracted from the nonisothermal self-diffusion profile, $C_1(z,t)$, which is provided by the solution of the continuity equation,

$$\frac{\partial C_1}{\partial t} = -\text{div}_F \vec{J}_1 \quad \text{Eq. 177}$$

or, due to Eq. 173,

$$\frac{\partial C_1}{\partial t} = \vec{\nabla} \cdot (D_-^* \vec{\nabla} C_1). \quad \text{Eq. 178}$$

Time-dependent approximate solutions to Eq. 178 will be provided in the following section.

4.2. TIME-DEPENDENT SOLUTIONS

In the local defect equilibrium which has been assumed in the present analyses, the self-diffusion coefficient is a well-defined single-valued function of temperature alone;

$$D_-^* = D_{O-} \exp(-T_m/T). \quad \text{Eq. 179}$$

Inserting Eq. 179 into Eq. 178, we have

$$\frac{\partial C_1}{\partial t} = D_-^* \frac{\partial^2 C_1}{\partial z^2} + D_-^* \frac{T_m}{T^2} \cdot \frac{\partial C_1}{\partial z} \cdot \frac{dT}{dz} \quad \text{Eq. 180}$$

for a planar diffusion along the z-direction. It is very interesting to compare Eq. 180 with the time-dependent

differential equation for interstitials, Eq. 92, Chapter 3.

When $T_1^* = 0$, Eq. 92 becomes exactly Eq. 180.

In a thin intermixing zone, δ , such that

$$\frac{\delta}{L} \sim \epsilon^2 \quad ; \quad \epsilon^2 \ll 1,$$

where

$$T = T_0 + a \cdot z$$

and

$$\frac{a\delta}{T_0} \sim \epsilon^2 \quad ; \quad \frac{T_m}{T_0} \sim \frac{1}{\epsilon},$$

an approximate analytic solution to Eq. 180 can be obtained in exactly the same manner as the interstitial thermomigration as shown in Appendix 1. By putting $T_1^* = 0$ in the solutions for the interstitial thermomigration, Eq. 100, Eq. 103 and Eq. 106, we obtain:

For the initial and boundary conditions,

$$\left. \begin{aligned} C_1(z < 0; t = 0) &= C_s \text{ (artificial abundance of } {}^{18}\text{O)} \\ C_1(z > 0; t = 0) &= C_0 \text{ (natural abundance of } {}^{18}\text{O)} \end{aligned} \right\},$$

Eq. 181

the solution $C_1(z, t)$ is

$$\begin{aligned} \frac{C_1 - C_0}{C_s - C_0} &= \frac{1}{2} \operatorname{erfc}\left(\frac{z}{2\sqrt{\Delta_0 t}}\right) - \frac{1}{4\sqrt{\pi}} \left(\frac{a}{T_0}\right) \left(\frac{T_m}{T_0}\right) \sqrt{\Delta_0 t} \exp\left(-\frac{z^2}{4\Delta_0 t}\right) \\ &+ \frac{1}{8\sqrt{\pi}} \left(\frac{a}{T_0}\right) \left(\frac{T_m}{T_0}\right) \frac{z^2}{\sqrt{\Delta_0 t}} \exp\left(-\frac{z^2}{4\Delta_0 t}\right) + O(\epsilon^2) \quad \text{Eq. 182 a} \end{aligned}$$

or

$$\frac{C_1 - C_0}{C_s - C_0} = \frac{1}{2} \operatorname{erfc}(\eta) + \frac{1}{8\sqrt{\pi}} \left(\frac{a}{T_0}\right) \left(\frac{T_m}{T_0}\right) \xi (2\eta^2 - 1) \exp(-\eta^2) + O(\varepsilon^2)$$

Eq. 182 b

where

$$\Delta_0 \equiv D_0 \exp(-T_m/T_0),$$

$$\xi \equiv 2\sqrt{\Delta_0 t},$$

$$\eta \equiv z/\xi$$

and $O(\varepsilon^2)$ represents terms on the order of ε^2 or less. The leading term of $O(\varepsilon^2)$ is shown in Appendix 1 to be

$$- \frac{1}{8\sqrt{2\pi}} \left(\frac{a}{T_0}\right)^2 \left(\frac{T_m}{T_0}\right) \left(\frac{T_m}{T_0} - 2\right) \xi^2 \eta \exp(-\eta^2).$$

Eq. 183

For the initial and boundary conditions,

$$C_1(z=0; t=0) = \infty$$

$$C_1(|z| > 0; t=0) = C_0 \text{ (natural abundance of } ^{18}\text{O)}$$

Eq. 184

the solution $C_1(z, t)$ is

$$\begin{aligned} \frac{\sqrt{\pi}}{M} (C_1 - C_0) &= \frac{1}{2\sqrt{\Delta_0 t}} \cdot \exp\left(-\frac{z^2}{4\Delta_0 t}\right) - \frac{1}{8} \frac{aT_m}{T_0^2} \cdot \frac{z}{\sqrt{\Delta_0 t}} \cdot \exp\left(-\frac{z^2}{4\Delta_0 t}\right) \\ &+ \frac{1}{16} \frac{aT_m}{T_0^2} \frac{z^3}{(\Delta_0 t)^{3/2}} \cdot \exp\left(-\frac{z^2}{4\Delta_0 t}\right) + O(\varepsilon^2) \end{aligned}$$

Eq. 185 a

or

$$\frac{\sqrt{\pi}}{M}(C_1 - C_0) = \frac{1}{\xi} \exp(-\eta^2) + \frac{1}{4} \left(\frac{a}{T_0}\right) \left(\frac{T_m}{T_0}\right) (2\eta^2 - 1) \eta \exp(-\eta^2) + O(\varepsilon^2).$$

Eq. 185 b

M is again the total amount of ^{18}O or

$$M \equiv \int_{-\infty}^{\infty} (C_1 - C_0) \xi d\eta$$

and the leading term of $O(\varepsilon^2)$ (see Appendix 1) is

$$- \frac{1}{8} \left(\frac{a}{T_0}\right)^2 \left(\frac{T_m}{T_0}\right) \left(\frac{T_m}{T_0} - 2\right) (2\eta^2 + 1) \xi \exp(-\eta^2).$$

Eq. 186

For a finite source (or thick-film) initial and boundary conditions,

$$\begin{aligned} C_1(|z| < h; t=0) &= C_s \text{ (artificial abundance of } ^{18}\text{O)} \\ C_1(|z| > h; t=0) &= C_0 \text{ (natural abundance of } ^{18}\text{O)} \end{aligned} \quad \},$$

Eq. 187

the solution is given as;

$$\begin{aligned} \frac{C_1 - C_0}{C_s - C_0} &= \frac{1}{2} \left[\operatorname{erf}\left(\frac{h+z}{2\sqrt{\Delta_0 t}}\right) + \operatorname{erf}\left(\frac{h-z}{2\sqrt{\Delta_0 t}}\right) \right] \\ &+ \frac{1}{4\sqrt{\pi}} \frac{aT_m}{T_0^2} \sqrt{\Delta_0 t} \left\{ \exp\left[-\left(\frac{h+z}{2\sqrt{\Delta_0 t}}\right)^2\right] - \exp\left[-\left(\frac{h-z}{2\sqrt{\Delta_0 t}}\right)^2\right] \right\} \\ &+ \frac{1}{8\sqrt{\pi}} \frac{aT_m}{T_0^2} \frac{h^2 - z^2}{\sqrt{\Delta_0 t}} \left\{ \exp\left[-\left(\frac{h+z}{2\sqrt{\Delta_0 t}}\right)^2\right] - \exp\left[-\left(\frac{h-z}{2\sqrt{\Delta_0 t}}\right)^2\right] \right\} \end{aligned}$$

$$+ O(\epsilon^2) \quad \text{Eq. 188 a}$$

or

$$\begin{aligned} \frac{C_1 - C_0}{C_s - C_0} &= \frac{1}{2} \left[\operatorname{erf} \left(\frac{1+\rho}{\zeta} \right) + \operatorname{erf} \left(\frac{1-\rho}{\zeta} \right) \right] \\ &+ \frac{1}{8\sqrt{\pi}} \left(\frac{a}{T_0} \right) \left(\frac{T_m}{T_0} \right) h \zeta \left[1 + \frac{2(1-\rho^2)}{\zeta^2} \right] \left\{ \exp \left[- \left(\frac{1+\rho}{\zeta} \right)^2 \right] \right. \\ &\left. - \exp \left[- \left(\frac{1-\rho}{\zeta} \right)^2 \right] \right\} + O(\epsilon^2), \quad \text{Eq. 188 b} \end{aligned}$$

where

$$\zeta \equiv 2\sqrt{\Delta_0 t}/h \quad ; \quad \rho \equiv z/h.$$

The nonisothermal intermixing profiles expected from the semi-infinite source (Eq. 182 b), from the thin-film source (Eq. 185 b) and from the finite source (Eq. 188 b) will be the same as those for the interstitial thermomigration with $q_1^* = 0$ corresponding to the respective source conditions (see Eq. 100 b, Eq. 103 b and Eq. 106 b, Chapter 3). One may get the profiles by deleting the curve (b) respectively from Fig. 1, from Fig. 2 and from Fig. 3. It is observed that the location of reference concentration, i.e., $(C_1/C_0)/(C_s/C_0) = 1/2$ for the semi-infinite source or concentration maximum for the thin-film source, shifts from $z=0$, the location where that would be if isothermal. Its shift velocity is readily obtained from Eq. 113 either by deleting T_1^* or by setting $T_1^* = 0$ as

$$\dot{z}_0(z_0 \rightarrow 0) \equiv \lim_{z_0 \rightarrow 0} \left(\frac{\dot{z}_0}{t} \right) = - \frac{1}{2} \Delta_{OT} \frac{aT_m}{T_0^2} . \quad \text{Eq. 189}$$

It is noted that the locations of the reference concentrations, i.e., $(C_1 - C_0)/(C_s - C_0) = 1/2$ for the semi-infinite source and the concentration maximum for the thin-film source, shift always *down* the temperature gradient even without the thermomigration contribution. It is, as has been pointed out by Mock,^{7,2} because the source is stolen faster towards hotter side of the specimen which, in turn, erodes away the profile from the higher temperature side.

At this stage, one of our time-dependent solutions, Eq. 185 may be compared in its accuracy with the approximate solution that was used by Mock^{7,2} in his analysis of the non-isothermal self-diffusion profile developed from a thin-film of ^{195}Au embedded in ^{197}Au matrix. For a stationary temperature gradient, $dT/dz (= a)$, the approximate solution for the instantaneous planar source was

$$C(z, t) = \frac{M}{2\sqrt{\pi D^* t}} \exp\left[-\frac{(z + vt - z')^2}{4D^* t}\right], \quad \text{Eq. 190}$$

where M is the total amount of the source, D^* is the tracer diffusivity of Au, z' is the initial position of the planar source on the z -axis, and v corresponds to \dot{z}_0 in our notation, i.e., the shift velocity of the concentration maximum.

Concentration profiles of this kind, Eq. 190, have been encountered both in the Chemla experiment^{9,74} and in the

experiment of electromigration,^{7,7} in which a stationary electrical potential gradient is applied as a driving force for diffusion in addition to the relevant concentration gradient itself. Since both experiments are performed under an isothermal condition, not only D^* but also v is constant and hence Eq. 190 can become the exact solution for a diffusion profile drifted as a whole by the electrical potential gradient.

In a nonisothermal self-diffusion in which a stationary temperature gradient corresponds to the electrical potential gradient in electromigration, Mock^{7,2} employed Eq. 190 as a solution to Eq. 180 under the assumption that both D^* and D^*T_m/T^2 were constant in a relatively thin diffusion-zone. Then, the choice of a constant shift velocity,

$$v = D^*(T_m/T^2) (dT/dz) \quad \text{Eq. 191}$$

made Eq. 190 exact as the solution.

However, neither D^* nor v can be constant even in a thin diffusion zone due to their exponential dependence on temperature. Considering their temperature dependences, Eq. 190 leaves a residue between the right-hand-side (RHS) and the left-hand-side (LHS) of Eq. 180. The leading term of the residue is calculated to be

$$\left| \frac{(\text{RHS}) - (\text{LHS})}{(\text{LHS})} \right| \sim \left(\frac{\alpha \delta}{T} \right)^2 \left(\frac{T_m}{T} \right)^2 \quad \text{Eq. 192}$$

in our notation, where δ replaced $2\sqrt{D^*t}$ or equivalents. The accuracy of our solution, Eq. 185 and the others, Eq. 100, Eq. 103, Eq. 106, Eq. 182, and Eq. 188 has been shown to be the same as Eq. 192, (see Appendix 1 or Eq. 183 and Eq. 186). Thus, it can be concluded that our solution, Eq. 185 is as accurate as Eq. 190 along with Eq. 191 as a solution to Eq. 180.

In this connection, one may notice that the shift velocity, Eq. 191, obtained from Eq. 190 looks different from ours, Eq. 189 by a numerical factor 1/2 even at $z_0=0$. But it will be demonstrated by using Mock's thermomigration data in the following section that, as $z_0 \rightarrow 0$, v approaches $\dot{z}_0(z_0 \rightarrow 0)$ given in Eq. 189 presumably due to its position dependence.

4.3. MEASUREMENT OF SELF-THERMOMIGRATION IN MgO

Intuitively, we had expected that the cross effect in the temperature gradient will affect somehow the development of the nonisothermal anion self-diffusion profile, $C_1(z,t)$, from which the heat of transfer may be extracted. We have found, however, that it does not bear any information about the thermomigration in an MgO-like stoichiometric oxide, unlike the case of interstitial impurities (see Chapter 3). According to the rigorous treatment of the phenomenon in the light of irreversible thermodynamics, the isotopic flux with respect to our laboratory frame of reference is driven only by the isotopic concentration gradient or Eq. 173

$$F_1^J = - D_-^* \frac{\partial C_1}{\partial z}$$

and consequently, the local concentration must only satisfy Eq. 178,

$$\frac{\partial C_1}{\partial t} = \frac{\partial}{\partial z} \left(D_-^* \frac{\partial C_1}{\partial z} \right).$$

Why is that? It may be attributed to the diffusion mechanism – the vacancy mechanism itself. In the local lattice frame of reference, the isotopic ^{18}O ions perform not only random walks in the isotopic concentration gradient (ordinary self-diffusion), but also directional walks against the net vacancy flow \vec{J}_3 induced by the temperature gradient (thermo-migration). The former is confined only on the anionic sublattice. The latter is, however, of a molecular-like character. It has been already pointed out that, in a stoichiometric ionic solid, any net ionic or vacancy flux on one sublattice is coupled strongly to the reciprocal equivalent on the other sublattice via the charge neutrality condition so that one may regard them as a flux of electrically-neutral quasi-molecules $(\text{MgO})^x$ or quasi-molecular vacancy $(V_{\text{MgO}})^x$, respectively. In this sense, an MgO-like stoichiometric ionic solid can be treated in exactly the same way as an elementary metal with the vacancy diffusion mechanism. Such a concept may facilitate the atomistic interpretation of the Kirkendall

effect in an ionic system such as, for example, NaCl-KCl^{6,7} Likewise in the Kirkendall effect,^{6,8} the net flux of molecular vacancies, V_{MgO} , renders the local molecular lattice mobile in the same direction of $\vec{J}_{V_{\text{MgO}}}$ ($=\vec{J}_3=\vec{J}_5$) for the preservation of the local internal equilibrium for Schottky defect (or molecular vacancy) formation. This relative movement of the local lattice frame itself cancels out exactly the directional walk and, hence, the profile $C_1(z,t)$ observed in the Fick frame bears no information at all about the directional walk in the temperature gradient. The cancellation of the effect by the movement of the local lattice reference frame is the salient feature of the vacancy mechanism compared with the interstitial mechanism for diffusion.

How can the heat of transfer of oxygen ion then be determined experimentally in an MgO-like stoichiometric ionic solid? It should be noted that the response of the ionic lattice in an applied temperature gradient is of a molecular-like nature and that the molecular response is quite similar to the atomic response in elementary metals. In an elementary crystal where the vacancy mechanism is well-established, a local crystalline lattice plane is shown to move in a temperature gradient at the velocity, \vec{u}_L , given as⁹;

$$\vec{u}_L = D \cdot \frac{q^* - h_v}{kT} \cdot \frac{dT}{dz}, \quad \text{Eq. 193}$$

where $D(=D^*/f)$ is the self-diffusion coefficient, q^* the reduced heat of transfer, and h_v the vacancy formation enthalpy.

Thus, by measuring the moving velocity of a specific local lattice plane in a given temperature gradient, one can determine the reduced heat of transfer with the help of the presumably known self-diffusion coefficient. To apply this method, it is necessary to label a specific lattice plane in order to measure its speed. Two kinds of markers have been used for this purpose in studies of self-thermomigration in pure metal systems. The first kind is a surface indentation or scratch made, for example, by a Knoop indenter.^{6,9} The second consists of a thin filament of an inert material embedded in the crystal perpendicular to the temperature gradient^{7,0} as in the Kirkendall experiment.^{7,1} Quite recently, as a variation of the second type, Mock^{7,2} has used an inert radioactive marker. He inserted a thin layer of $^{181}\text{HfO}_2$ in a gold rod to measure the moving velocity of a local crystalline lattice in a temperature gradient of ~ 300 K/cm.

A similar technique may be applied to the MgO-like ionic solid on the basis of Eq. 170 or

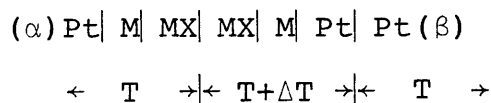
$$u_L = \frac{D_- \cdot D_+}{D_- + D_+} \cdot \frac{q_-^* + q_+^* - h_s}{kT^2} \cdot \frac{dT}{dz} \quad \text{Eq. 194}$$

in a temperature gradient along the z-direction. As stated earlier, the diffusion coefficient $(D_+ \cdot D_- / D_+ + D_-)$, reduced heat of transport, $(q_+^* + q_-^*)$, and the vacancy-formation enthalpy, h_s , for a quasi-molecule $(\text{Mg}_{\text{Mg}}^{+2} \text{O}_{\text{O}}^{-2})^x$ correspond to the atomic quantities, D , q^* , and h_v , respectively. Especially for an MgO crystal and similar oxides, the molecular

diffusion is governed by the anion diffusion coefficient since $D_- \ll D_+$ (see Part I). The relative velocity, u_L in Eq. 194, is thus well-represented by the approximation,

$$u_L \approx D_- \cdot \frac{q_-^* + q_+^* - h_s}{kT^2} \cdot \frac{dT}{dz}. \quad \text{Eq. 195}$$

We need one more independent piece of information to be able to separate the heat of transport of the anion, q_-^* , from the molecular quantity, $q_-^* + q_+^*$, which one can determine with, for example, a marker method. This information may be provided by a measurement of the thermoelectric power of the ionic system. There are various conditions on the kind of electrode-material and on the arrangement of electrodes in the measurement of the thermoelectric power of ionic compounds involving ionic and electronic conduction as elegantly reviewed by C. Wagner.^{6,1} For a compound with prevailing cationic conduction, many authors^{5,73,74,75} employed a thermocell with the uniform metal activity, $a_M=1$, throughout the MX sample enforced by placing foils of metal M between the Pt leads and compound MX;



The thermoelectric power, ϵ , of the thermocell shown above has been defined as;

$$\epsilon \equiv \lim_{\Delta T \rightarrow 0} \frac{\Delta \phi}{\Delta T} \quad \text{Eq. 196}$$

where $\Delta \phi$ represents a potential difference between Pt-electrodes α and β . According to Wagner,^{6,1} ϵ of the present thermocell is expressed in the Hittorf frame of reference (anion-fixed frame) as;

$$\epsilon = \frac{1}{e} (S_M^O - \bar{S}_+ - \frac{q_+^*}{T}) - \epsilon^{(Pt)} \quad \text{Eq. 197}$$

where S_M^O and \bar{S}_+ are the partial entropies of metal M and cation M^{+e} , respectively, and $\epsilon^{(Pt)}$ is the thermoelectric power of the Pt lead wire. On the basis of the two independent pieces of information, Eq. 193 and Eq. 197, q_+^* and q_-^* can be determined separately, in principle.

But, an experimental measurement of the local lattice velocity, u_L , is rather hopeless especially for an MgO crystal and similar oxides as the rate controlling anion diffusion is almost negligibly slow. For this reason, in fact, the anionic sublattice is often used as the appropriate coordinate system of reference for the description of transport phenomena in an ionic system.^{2,0} Let us now estimate the order of magnitude of the marker motion predicted for MgO by Eq. 195. On the basis of experience with elementary metals,^{1,8,48,77} the order of magnitude of the molecular heat of transfer, $q_-^* + q_+^*$, is at most the activation energy for molecular diffusion, $(h_{m-} + \frac{1}{2}h_s) + (h_{m+} + \frac{1}{2}h_s)$, where h_{m-} and h_{m+} are migration enthalpies of the

anion and cation vacancy, respectively. The theoretical estimates⁷⁶ for an MgO crystal are $h_{m-}=2.38$ eV, $h_{m+}=2.16$ eV, and $h_s=7.5$ eV (see also Part I). In Eq. 195, $q_-^*+q_+^*-h_s$ is thus 5 eV at most. A local temperature $T_o=2100$ K ($\sim 1800^\circ\text{C}$) may be taken as a practical maximum for an experiment, a limitation imposed by high vapor pressure of MgO above 1850°C . The diffusion coefficient of oxygen at 2100 K is estimated to be only 3.0×10^{-14} cm²/sec according to our measurements described in Part I. Let a temperature gradient, $dT/dz=2100$ K/cm be assumed to be realizable experimentally for prolonged periods of time. Under these conditions it will take 1.3×10^8 sec or around 4 years at least to produce a shift of only 1 μm (we must have recourse to optical means to measure the displacement of surface marks and the wavelength of visible light is on the order of 0.5 μm). Eq. 194 or Eq. 195 is presumed to be valid for an extrinsic MgO with defect structure controlled by cation impurities since the molecular diffusion is in any case governed by the anion diffusion coefficient. Even for a system in which the local defect equilibrium is violated, Eq. 194 or Eq. 195 provides an asymptotic limit of the local lattice velocity, u_L . A treatment of the latter system is given in Appendix 2 for an elementary metal system.

In closing this chapter, we will analyze the Au-thermo-migration data produced by Mock⁷² in view of one of our time-dependent solutions, Eq. 195 in order to demonstrate the workability of the present results including those for interstitial impurities. Eq. 195 has yielded a shift velocity of

the concentration maximum, Eq. 189;

$$\dot{z}_O(z_O \rightarrow 0) = -\frac{1}{2}\Delta_O a T_m / T_O^2$$

The local lattice velocity, u_L , is given by Eq. 193 for an elemental crystal with vacancies as the predominant defect, or

$$u_L(z_O \rightarrow 0) = \Delta_O a (q^* - h_V) / f k T_O^2.$$

Thus, a velocity of the concentration maximum relative to the local lattice plane represented by an inert marker is given by;

$$\lim_{z_O \rightarrow 0} (\Delta z / t) = - \Delta_O \frac{a}{k T_O^2} \left(\frac{Q}{2} + \frac{q^* - h_V}{f} \right), \quad \text{Eq. 198}$$

where $\Delta z \equiv (\dot{z}_O - u_L)t$ is a separation distance from the inert marker to the concentration maximum, and T_m has been replaced by Q/k , the activation energy for isothermal self-diffusion divided by the Boltzmann constant. Eq. 198 is supposed to become more accurate as the shift distance z_O approaches 0. This implicitly requires an extrapolation of a series of measurements of $(\dot{z}_O - u_L)$ to $z_O = 0$.

On the other hand, Eq. 190 produces the corresponding equation as;

$$\frac{\Delta z}{t} = - \Delta_O \frac{a}{k T_O^2} \left(Q + \frac{q^* - h_V}{f} \right) \quad \text{Eq. 199}$$

which has been used by Mock⁷² to analyze his Au-thermomigration data:

	t ($\times 10^5$ sec)	Δ_o ($\times 10^{-10}$ cm ² /sec)	T_o (°C)	a (K/cm)	Δz (μ m)	$\Delta z/t$ ($\times 10^{-9}$ cm/sec)
(i)	7.52	4.98 \pm 0.13	834 \pm 2	315 \pm 12	-16 \pm 3	2.1 \pm 0.4
(ii)	8.50	8.47 \pm 0.44	867 \pm 3	309 \pm 12	-35 \pm 3	4.1 \pm 0.4

The two runs, (i) and (ii), look quite similar in their experimental conditions. The magnitudes of $\Delta_o a/T_o^2$ for the two runs are respectively (i) $(1.5 \pm 0.1) \times 10^{-13}$ cm/sec K and (ii) $(2.0 \pm 0.2) \times 10^{-13}$ cm/sec K. Therefore, we may regard the two data as having been produced in the same experimental conditions except for annealing time, t . Although the number of data is limited to only two, we might expect to have $\Delta z/t \sim 1.0 \times 10^{-9}$ cm/sec as a limiting value as Δz approaches 0. Then, the quantity in the parenthesis of Eq. 198 turns out to be 0.53 eV, or

$$q_{Au}^* \approx 0.7 \text{ eV}$$

with help of the values⁷² $Q=1.83$ eV, $h_v=0.98$ eV and $f=0.78$ for Au and with help of the averaged values, $T_o=850^\circ\text{C}$, $\Delta_o=6.7 \times 10^{-10}$ cm²/sec, and $a=310$ K/cm for experimental conditions.

In his extraction of q_{Au}^* on the basis of Eq. 199, Mock

took an average of the two values for q_{Au}^* , 0.64 eV and 0.96 eV calculated from run (i) and run (ii), respectively. That is,

$$q_{\text{Au}}^* = 0.8 \text{ eV.}$$

The other reported values of q_{Au}^* were put at 0.8 eV⁷⁰, 0.6 eV⁷⁸, and 0.98 eV⁷⁹.

This example of a successful application of Eq. 198 is believed to assure the workability of our analyses. Eq. 198 may be a better machine for a unambiguous determination of the reduced heat of transport with a self-thermomigration experiment involving the measurements of $\Delta z/t$.

5. SUMMARY

The intermixing of two kinds of anion isotopes, ^{18}O and ^{16}O , in a temperature gradient is not influenced by the cross-effect, thermomigration, in an MgO-like ionic system, in which a relative shift of the anion and the cation center-of-masses is prohibited by the constraint that stoichiometry be preserved. In contrast, the distribution of interstitials is affected as the center-of-mass of interstitials is allowed to shift relative to the immobile host lattice. Consequently, no information about thermomigration via a vacancy mechanism can be extracted from the time and position dependence of a nonisothermal isotopic gradient. The conclusion is a consequence of the molecular-like nature of the response of a stoichiometric ionic system to an applied temperature gradient.

Approximate but explicit and highly accurate solutions for the isotope-intermixing via a vacancy mechanism in a stationary temperature gradient have been obtained for thin film, thick film and semi-infinite source boundary conditions. Those for the distribution of solute via an interstitial mechanism have also been obtained for the three kinds of source boundary conditions. The solutions obtained for the interstitial impurities suggest a new method for the measurement of the heat of transport, based on following a specific concentration as a function of position or time which is capable of producing reliable data in an order-of-magnitude

less time than conventional methods.

The molecular heat of transfer for a vacancy mechanism may be determined by measurement of the shift of an appropriately labeled local crystalline lattice plane with time as has been done in elementary metal systems. In the specific case of MgO, however, the extremely sluggish diffusion rate of the anion, as determined in the present and certain other works, causes the annealing time required to produce measurable shift of a local crystalline lattice plane to be unrealistically long, even for the optimum temperatures and temperature gradients which might be employed under practical laboratory conditions.

6. SUGGESTIONS FOR FUTURE WORK

At this point, we feel certain that a byproduct of the present work – the time-dependent solutions to the thermomigration of interstitials – has provided a valuable suggestion of experimental methods which are readily realizable as well as very economic in the determination of a heat of transport. The uncertainty of the methods based on the present solutions is no greater than ε^2 ($\varepsilon^2 \ll 1$) provided that $|a\delta/T_0| \sim \varepsilon^2$, $T_m/T_0 \sim 1/\varepsilon$ and $|T^*/T_0| \sim 1/\varepsilon$ (see, for detail, Section 3.2 or Appendix 1). These sufficient conditions may be reformulated as

$$|a\delta/T_m| \sim \varepsilon^3 \quad ; \quad T_0 \sim \varepsilon T_m$$

since $T^* \leq T_m$ on the basis of experimental and theoretical evidence accumulated so far. One may thus have two degrees of freedom (for example, ε and T_0) in the selection of a , δ , T_0 , and ε for an appropriate experiment. Here the following suggestions are offered for future work:

i) It is suggested that the present time-dependent solutions be tested and verified with a well-defined system in which the isothermal diffusivity of the interstitial is precisely known. The self-diffusion rate of the solvent atoms should be negligible compared with the solute diffusivity and, in order to have a standard with respect to which the

present procedure may be compared, the heat of transfer of the solute has to be available with a high precision. One of the possible choices for the system might be α -iron with C as the interstitial solute. For this system, the isothermal diffusion coefficients for both the solute and the solvent have been rather exhaustively studied. The ratio of the diffusivity of the solvent to the solute is on the order of magnitude of 10^{-5} at temperatures of 700°C to 900°C. Thus, the host lattice of α -iron may be taken as a reference coordinate system relative to which the solute flux is measured in a temperature gradient. A reliable value for the heat of transport of carbon has also been obtained by Shewmon³¹ with the stationary state technique.

ii) The present time-dependent solutions are supposed to be valid provided that the coupling of a temperature gradient to the diffusion flow under consideration persists in the Fick frame of reference, viz., $\vec{J}_i = -D_i \vec{\nabla} C_i - D_i C_i q_i^* \vec{\nabla} T / kT^2$, that the relevant diffusion coefficient, D_i , is a single-valued function of T alone or $D_i = D_i(T)$ and that the reduced heat of transport q_i^* or equivalent is a constant. Thus, the present solutions may presumably, with minor modifications, be applied to thermomigration in an MgO-like ionic crystal which is alloyed with substitutional cation impurities of the same valence as the solvent cations. An example might be $(\text{Na}_{1-x}\text{K}_x)\text{Cl}$ in a temperature gradient. The fluxes of the host cations and the solute cations are described in this case with respect to the relatively immobile anion sublattice which is

approximately congruent with the Fick frame of reference. It is thus suggested as a future work that the present solutions be modified to describe a time-dependent profile of thermomigration in such a system and hence to extract from the profile the corresponding heat of transport. The heat of transport in such an experiment might be expected to be a combination of the heats of transport of solvent and solute cations.

iii) We have phenomenologically demonstrated that, in a stoichiometric ionic solid MX in which a diffusion proceeds via a Schottky vacancy mechanism, a flux of quasi-molecular vacancies V_{MX}^x (i.e., synchronized fluxes of anion and cation vacancies) is induced by an applied temperature gradient. This vacancy flux, in turn, renders the local crystalline lattice mobile and, by measuring the velocity of a specific lattice plane \vec{u}_L , one may thus determine the molecular heat of transport, $q_+^* + q_-^*$. The velocity has been shown to be $\vec{u}_L = (D_- D_+ / (D_- + D_+)) (q_+^* + q_-^* - h_s) \vec{\nabla}T / kT^2$ (see Eq. 170 in the text). It is suggested that this velocity be experimentally tested with an appropriate system of MX by employing a technique which has been used for pure metal systems. The system MX is required to be ionic, to have a very narrow range of stoichiometry, and to be less sluggish in its self-diffusion on both sublattices so that a measurable shift could be produced in a reasonable time.

APPENDIX 1. SOLUTION OF THE DIFFERENTIAL EQUATION

1.1. DIFFERENTIAL EQUATION

The nonlinear partial differential equation, Eq. 88 in the text,

$$\frac{\partial C_i}{\partial t} = \frac{\partial}{\partial Z} \left(D_i \frac{\partial C_i}{\partial Z} \right) - T_i^* \frac{\partial}{\partial Z} \left[D_i C_i \frac{\partial}{\partial Z} \left(\frac{1}{T} \right) \right] \quad \text{Eq. 1-1}$$

is rewritten as

$$\begin{aligned} \frac{\partial C}{\partial t} = & D \frac{\partial^2 C}{\partial Z^2} + \left(\frac{\partial D}{\partial Z} \right) \left(\frac{\partial C}{\partial Z} \right) + D \frac{T^*}{T^2} \left(\frac{\partial C}{\partial Z} \right) \left(\frac{\partial T}{\partial Z} \right) + \frac{T^*}{T^2} \left(\frac{\partial D}{\partial Z} \right) \left(\frac{\partial T}{\partial Z} \right) C \\ & - 2D \frac{T^*}{T^3} \left(\frac{\partial T}{\partial Z} \right)^2 C + D \frac{T^*}{T^2} \left(\frac{\partial^2 T}{\partial Z^2} \right) C, \end{aligned} \quad \text{Eq. 1-2}$$

where the subscript "i" has been dropped for the sake of simplicity.

An approximate solution to Eq. 1-2 may be obtained by the perturbation method^{45, 46} as follows:

With respect to the temperature, we may assume that its temporal variation is stationary and its spatial variation linear;

$$\left. \frac{\partial T}{\partial t} \right|_Z = 0 \quad ; \quad \left. \frac{\partial T}{\partial Z} \right|_t = a \quad \text{Eq. 1-3}$$

The diffusion coefficient is supposed to be a single-valued function of the temperature alone in local thermodynamic equilibrium;

$$D = D_0 \exp(-T_m/T) \quad \text{Eq. 1-4}$$

and hence, due to the chain rule, $\partial D/\partial Z = (\partial D/\partial T) \cdot (dT/dZ)$,

$$\frac{\partial D}{\partial Z} = D \frac{aT_m}{T^2} . \quad \text{Eq. 1-5}$$

Substitution of Eq.'s 1-5 and 1-3 reduces Eq. 1-2

to

$$\frac{\partial C}{\partial t} = D \left[\left(\frac{\partial^2 C}{\partial Z^2} \right) + \frac{\alpha}{T^2} \left(\frac{\partial C}{\partial Z} \right) - \frac{\beta}{T^3} C + \frac{\gamma}{T^4} C \right], \quad \text{Eq. 1-6}$$

where

$$\alpha \equiv a(T_m + T^*), \quad \text{Eq. 1-7}$$

$$\beta \equiv 2a^2 T^* \quad \text{Eq. 1-8}$$

$$\text{and } \gamma \equiv a^2 T_m T^*. \quad \text{Eq. 1-9}$$

Any short time solution to the diffusion problem such as Eq. 1-6 is valid only for an infinite medium. In other words, if we let δ be an extent of diffusion and L be an overall dimension of the given system along the diffusion direction,

$$\delta \sim \sqrt{Dt} \ll L \quad \text{Eq. 1-10}$$

or

$$\frac{\delta}{L} \sim \epsilon^2 \quad ; \quad \epsilon^2 \ll 1 . \quad \text{Eq. 1-11}$$

Over such a thin diffusion zone δ about $Z=0$ where $T=T_0$, it is sufficiently accurate to assume a linear spatial variation of

temperature or

$$T = T_0 \left(1 + \frac{aZ}{T_0} \right) . \quad \text{Eq. 1-12}$$

The relative variation of temperature will be very small as well, or

$$\left| \frac{aZ}{T_0} \right| \ll \left| \frac{a\delta}{T_0} \right| \sim \epsilon^2 . \quad \text{Eq. 1-13}$$

Eq. 1-13 implies in association with Eq. 1-11 that a temperature gradient a is

$$|a| \sim \frac{T_0}{L} . \quad \text{Eq. 1-14}$$

If we take, for a numerical example,

$$\delta \sim 10\mu \quad \text{and} \quad L \sim 1 \text{ cm}$$

or

$$a \sim 10^3 \text{ K/cm} \quad \text{and} \quad T_0 \sim 10^3 \text{ K},$$

then

$$\epsilon^2 \sim 10^{-3} .$$

In addition, we may set

$$\frac{T_m}{T_0} \sim \frac{1}{\epsilon} \quad \text{Eq. 1-15}$$

and

$$\frac{T^*}{T_0} \sim \frac{1}{\epsilon} \quad \text{Eq. 1-16}$$

on the basis of experience:^{18,47,48} The typical value of activation energies and of reduced heats of transfer of interstitials are order of magnitude of 1 eV or less. Thus, $T_m \sim 10^4$ K and $T^* \sim 10^4$ K.

Due to Eq. 1-12 and Eq. 1-13, an approximation

$$T^n \cong T_0^n \left(1 + n \frac{aZ}{T_0}\right) \quad \text{Eq. 1-17}$$

is accurate within ϵ^4 and the diffusion coefficient D of Eq. 1-4 is well represented within accuracy ϵ^2 , due to Eq. 1-13 and Eq. 1-15, as

$$D \cong \Delta_0 + \Delta_1 Z \quad \text{Eq. 1-18}$$

where

$$\Delta_0 \equiv D(Z=0) = D_0 \exp(-T_m/T_0) \quad \text{Eq. 1-19}$$

and

$$\Delta_1 \equiv (\partial D / \partial Z)_{Z=0} = a T_m \Delta_0 / T_0. \quad \text{Eq. 1-20}$$

Substituting Eq. 1-17 and Eq. 1-18, Eq. 1-6 is reduced to:

$$\begin{aligned} \frac{\partial C}{\partial t} = & \Delta_0 \frac{\partial^2 C}{\partial Z^2} + \Delta_1 Z \frac{\partial^2 C}{\partial Z^2} + \Delta_0 \frac{\alpha}{T_0^2} \frac{\partial C}{\partial Z} + \Delta_1 \frac{\alpha Z}{T_0^2} \frac{\partial C}{\partial Z} - 2 \Delta_0 \frac{a \alpha Z}{T_0^3} \frac{\partial C}{\partial Z} \\ & - 2 \Delta_1 \frac{a \alpha Z^2}{T_0^3} \frac{\partial C}{\partial Z} - \Delta_0 \frac{\beta}{T_0^3} C - \Delta_1 \frac{\beta Z}{T_0^3} C + 3 \Delta_0 \frac{a \beta Z}{T_0^4} C \\ & + 3 \Delta_1 \frac{a \beta Z^2}{T_0^4} C + \Delta_0 \frac{\gamma}{T_0^4} C + \Delta_1 \frac{\gamma Z}{T_0^4} C - 4 \Delta_0 \frac{a \gamma Z}{T_0^5} C - 4 \Delta_1 \frac{a \gamma Z^2}{T_0^5} C. \end{aligned}$$

$$\text{Eq. 1-21}$$

Labeling the terms on the right-hand-side of Eq. 1-21 as 1, 2, 3,14 in the order of appearance, we may compare the magnitude of each term to that of the first term, on the basis of either Eq. 1-11 or Eq. 1-13 and both Eq. 1-15 and Eq. 1-16, as:

$$\begin{aligned} \frac{1}{1} &= 1 \\ \frac{2}{1} &\sim \left(\frac{a\delta}{T_0}\right) \left(\frac{T_m}{T_0}\right) \sim \epsilon \\ \frac{3}{1} &\sim \left(\frac{a\delta}{T_0}\right) \left(\frac{T_m+T^*}{T_0}\right) \sim \epsilon \\ \frac{4}{1} &\sim \left(\frac{a\delta}{T_0}\right)^2 \left(\frac{T_m}{T_0}\right) \left(\frac{T_m+T^*}{T_0}\right) \sim \epsilon^2 \\ &\dots\dots \\ \frac{14}{1} &\sim \left(\frac{a\delta}{T_0}\right)^4 \left(\frac{T_m}{T_0}\right)^2 \left(\frac{T^*}{T_0}\right) \sim \epsilon^5 \end{aligned}$$

where we have employed the approximations,

$$\frac{(\partial C/\partial Z)}{(\partial^2 C/\partial Z^2)} \sim \delta \quad ; \quad \frac{C}{\partial^2 C/\partial Z^2} \sim \delta^2.$$

If we take terms in Eq. 1-21 only upto the order of magnitude of ϵ , we obtain finally a differential equation;

$$\frac{\partial C}{\partial t} = \Delta_0 \frac{\partial^2 C}{\partial Z^2} + \Delta_1 Z \frac{\partial^2 C}{\partial Z^2} + \Delta_0 \frac{\alpha}{T_0^2} \frac{\partial C}{\partial Z} \quad \text{Eq. 1-22}$$

The subsequent perturbation in Eq. 1-22 is only of order of magnitude, ϵ^2 or smaller. Thus, the accuracy of Eq. 1-22 will be on the order of ϵ^2 .

If we let

$$C = C_0 + \sum_{k=0}^{\infty} C_k \quad \text{Eq. 1-23}$$

in which C_0 and C_k are such that

$$\frac{\partial C_0}{\partial t} - \Delta_0 \frac{\partial^2 C_0}{\partial Z^2} = 0 \quad \text{Eq. 1-24}$$

and using Eq. 1-7,

$$\frac{\partial C_k}{\partial t} - \Delta_0 \frac{\partial^2 C_k}{\partial Z^2} = \Delta_1 Z \frac{\partial^2 C_{k-1}}{\partial Z^2} + \Delta_0 \frac{a(T_m + T^*)}{T_0^2} \frac{\partial C_{k-1}}{\partial Z}. \quad \text{Eq. 1-25}$$

Then it is sufficiently accurate to solve for only C_0 and C_1 since the subsequent correction is again negligible due to Eq. 1-13, Eq. 1-15 and Eq. 1-16. We may choose $C_0(Z, t)$ to satisfy the initial and boundary conditions imposed and hence

$$C_k(Z, t = 0) = 0 \quad (k \geq 1). \quad \text{Eq. 1-26}$$

1.2. SOLUTION FOR A SEMI-INFINITE SOURCE

For the initial and boundary conditions

$$\left. \begin{aligned} C(Z < 0; t = 0) &= C_s \\ C(Z > 0; t = 0) &= 0 \\ C(Z = -\infty; t > 0) &= C_s \end{aligned} \right\} \quad \text{Eq. 1-27}$$

$$C(Z=\infty; t>0) = 0, \quad \text{Eq. 1-27}$$

The solution for $C_0(Z,t)$, Eq. 1-24 will be given, due to Eq. 1-26, as;

$$C_0(Z,t) = \frac{C_s}{2} \operatorname{erfc}\left(\frac{Z}{2\sqrt{\Delta_0 t}}\right), \quad \text{Eq. 1-28}$$

which corresponds to an isothermal diffusion profile at $T=T_0$.

Substituting from Eq. 1-28 into Eq. 1-25, the differential equation for $C_1(Z,t)$ will be

$$\frac{\partial C_1}{\partial t} - \Delta_0 \frac{\partial^2 C_1}{\partial Z^2} = -A \frac{1}{\sqrt{t}} e^{-Z^2/4\Delta_0 t} + B \frac{Z^2}{t\sqrt{t}} e^{-Z^2/4\Delta_0 t} \quad \text{Eq. 1-29}$$

where

$$A \equiv \frac{C_s}{2\sqrt{\pi}} \frac{a(T_m + T^*)}{T_0^2} \sqrt{\Delta_0} \quad \text{Eq. 1-30}$$

and

$$B \equiv \frac{C_s}{4\sqrt{\pi}} \frac{aT_m}{T_0^2} \frac{1}{\sqrt{\Delta_0}}. \quad \text{Eq. 1-31}$$

Let $C_1 = C_1^{(1)} + C_1^{(2)}$ such that

$$\frac{\partial C_1^{(1)}}{\partial t} - \Delta_0 \frac{\partial^2 C_1^{(1)}}{\partial Z^2} = -A \frac{1}{\sqrt{t}} e^{-Z^2/4\Delta_0 t} \quad \text{Eq. 1-32}$$

and

$$\frac{\partial C_1^{(2)}}{\partial t} - \Delta_0 \frac{\partial^2 C_1^{(2)}}{\partial Z^2} = B \frac{Z^2}{t\sqrt{t}} e^{-Z^2/4\Delta_0 t}. \quad \text{Eq. 1-33}$$

The differential equations, Eq. 1-32, and Eq. 1-33, are easily solved by using the Fourier transformation method.

Letting $Y^{(1)}(k,t)$ be the Fourier transform of $C_1^{(1)}(z,t)$

or

$$Y^{(1)}(k, t) [\equiv F[C_1^{(1)}(z, t)]] \equiv \frac{1}{\sqrt{2\pi}} \int_{-\infty}^{\infty} C_1^{(1)}(z, t) e^{ikz} dz, \quad \text{Eq. 1-34}$$

Eq. 1-32 is Fourier-transformed as

$$\frac{\partial}{\partial t} Y^{(1)} + \Delta_0 k^2 Y^{(1)} = -A\sqrt{2\Delta_0} e^{-k^2 \Delta_0 t} \quad \text{Eq. 1-35}$$

since

$$F[e^{-z^2/4\Delta_0 t}] = \sqrt{2\Delta_0 t} e^{-k^2 \Delta_0 t}.$$

The solution of the Fourier-transformed differential equation, Eq. 1-35, is a sum of the particular solution, $Y_p^{(1)}$, and the homogeneous solution, $Y_h^{(1)}$. $Y_h^{(1)}$ is, however, zero since we have chosen C_0 and C_1 such that the initial condition is met by C_0 alone and $C_1(z, 0) = 0$, Eq. 1-26. Therefore

$$Y^{(1)} = Y_p^{(1)}. \quad \text{Eq. 1-36}$$

Multiplying on both sides of Eq. 1-35 by $e^{k^2 \Delta_0 t}$ and rearranging, we obtain

$$\frac{\partial}{\partial t} (e^{k^2 \Delta_0 t} Y_p^{(1)}) = -A\sqrt{2\Delta_0}, \quad \text{Eq. 1-37}$$

which is integrated with respect to t as

$$Y_p^{(1)}(k, t) = -A\sqrt{2\Delta_0} t e^{-k^2 \Delta_0 t} \quad \text{Eq. 1-38}$$

since, in view of Eq. 1-26,

$$Y_p^{(1)}(k, 0) = 0. \quad \text{Eq. 1-39}$$

Taking the inverse transform on both sides of Eq. 1-38, we obtain $C_1^{(1)}(Z, t)$ as

$$C_1^{(1)}(Z, t) = -A\sqrt{t} e^{-Z^2/4\Delta_0 t}. \quad \text{Eq. 1-40}$$

On the other hand, Eq. 1-33 is Fourier-transformed as follows. By letting $\omega \equiv 1/4\Delta_0$, we rewrite Eq. 1-33 as

$$\frac{\partial C_1^{(2)}}{\partial t} - \Delta_0 \frac{\partial^2 C_1^{(2)}}{\partial Z^2} = -B \frac{1}{\sqrt{t}} \frac{\partial}{\partial \omega} e^{-\omega Z^2/t}, \quad \text{Eq. 1-41}$$

which is now turned quite similar to Eq. 1-32. The Fourier-transform of Eq. 1-41 is then

$$\frac{\partial}{\partial t} Y_p^{(2)} + \Delta_0 k^2 Y_p^{(2)} = 2\sqrt{2} B \Delta_0^{3/2} (1 - 2\Delta_0 k^2 t) e^{-\Delta_0 k^2 t} \quad \text{Eq. 1-42}$$

with use of the relation,

$$F\left[\frac{\partial}{\partial \omega} e^{-\omega Z^2/t}\right] = \frac{\partial}{\partial \omega} F[e^{-\omega Z^2/t}]. \quad \text{Eq. 1-43}$$

The homogeneous part of the solution, $Y_h^{(2)}$ has been again set to be zero for the same reason as $Y_h^{(1)} = 0$.

Multiplying both sides of Eq. 1-42 by $e^{\Delta_0 k^2 t}$, we have

$$\frac{\partial}{\partial t} (e^{k^2 \Delta_0 t} Y_p^{(2)}) = 2\sqrt{2} B \Delta_0^{3/2} (1 - 2\Delta_0 k^2 t) \quad \text{Eq. 1-44}$$

which is easily integrated as

$$Y_p^{(2)} = 2\sqrt{2} B \Delta_0^{3/2} (t - \Delta_0 k^2 t^2) e^{-\Delta_0 k^2 t}. \quad \text{Eq. 1-45}$$

The inverse-transformation of Eq. 1-45 yields $C_1^{(2)}$ as

$$C_1^{(2)}(Z, t) = B(\Delta_0 \sqrt{t} + \frac{Z^2}{2\sqrt{t}}) e^{-Z^2/4\Delta_0 t}. \quad \text{Eq. 1-46}$$

An approximate solution to Eq. 1-22 is then the linear combination of Eq. 1-28, Eq. 1-40 and Eq. 1-46 along with Eq.'s 1-30 and 1-31;

$$\begin{aligned} \frac{C(Z, t)}{C_s} = & \frac{1}{2} \operatorname{erfc}\left(\frac{Z}{2\sqrt{\Delta_0 t}}\right) - \frac{1}{4\sqrt{\pi}} \left(\frac{a}{T_0}\right) \left(\frac{T_m + 2T^*}{T_0}\right) \sqrt{\Delta_0 t} e^{-Z^2/4\Delta_0 t} \\ & + \frac{1}{8\sqrt{\pi}} \left(\frac{a}{T_0}\right) \left(\frac{T_m}{T_0}\right) \frac{Z^2}{\sqrt{\Delta_0 t}} e^{-Z^2/4\Delta_0 t}. \quad \text{Eq. 1-47} \end{aligned}$$

The solution, Eq. 1-47, is supposed to be accurate within ϵ^2 once the conditions, Eq. 1-13, Eq. 1-15 and Eq. 1-16 are satisfied. It is noted that the leading term of the solution, Eq. 1-47, is an odd function and the following terms of perturbation (or correction) are even functions. Thus the law of mass conservation is automatically satisfied, namely,

$$\int_0^C C(Z, t) dc = 0. \quad \text{Eq. 1-48}$$

1.3. SOLUTION FOR A THIN-FILM SOURCE

Now suppose that we have an instantaneous planar source. The initial and boundary conditions will then be

$$\left. \begin{aligned} C(z=0; t=0) &= \infty \\ C(|z|>0; t=0) &= 0 \end{aligned} \right\} \quad \text{Eq. 1-49}$$

and

$$\int_{-\infty}^{\infty} C(z,t) dz \equiv M, \quad \text{Eq. 1-50}$$

where M is the total amount of source. The solution is proceeded in a very much similar way to the previous case, the semi-infinite source initial and boundary conditions. The differential equation, Eq. 1-24, is readily solved along with Eq. 1-26 and the solution $C_o(z,t)$ is given by

$$C_o(z,t) = \frac{M}{2\sqrt{\pi\Delta_o t}} \exp\left(-\frac{z^2}{4\Delta_o t}\right). \quad \text{Eq. 1-51}$$

Substituting Eq. 1-51 into Eq. 1-25, we obtain a differential equation for $C_1(z,t)$ as

$$\frac{\partial C_1}{\partial t} - \Delta_o \frac{\partial^2 C_1}{\partial z^2} = -G \frac{z}{t\sqrt{t}} e^{-z^2/4\Delta_o t} + H \frac{z^3}{t^2\sqrt{t}} e^{-z^2/4\Delta_o t} \quad \text{Eq. 1-52}$$

where

$$G \equiv \frac{M}{4\sqrt{\pi\Delta_o}} \left(\frac{a}{T_o}\right) \left(\frac{2T_m + T^*}{T_o}\right) \quad \text{Eq. 1-53}$$

and

$$H \equiv \frac{M}{8\Delta_o\sqrt{\pi\Delta_o}} \left(\frac{a}{T_o}\right) \left(\frac{T_m}{T_o}\right). \quad \text{Eq. 1-54}$$

By letting $C_1 = C_1^{(1)} + C_1^{(2)}$, we may break Eq. 1-52 into the two differential equations for $C_1^{(1)}$ and $C_1^{(2)}$ as:

$$\frac{\partial C_1^{(1)}}{\partial t} - \Delta_0 \frac{\partial^2 C_1^{(1)}}{\partial Z^2} = -G \frac{Z}{t\sqrt{t}} e^{-Z^2/4\Delta_0 t} \quad \text{Eq. 1-55}$$

$$\frac{\partial C_1^{(2)}}{\partial t} - \Delta_0 \frac{\partial^2 C_1^{(2)}}{\partial Z^2} = H \frac{Z^3}{t^2\sqrt{t}} e^{-Z^2/4\Delta_0 t} \quad \text{Eq. 1-56}$$

which correspond to Eq. 1-32 and Eq. 1-33 for the semi-infinite source, respectively. These are easily solved again by the Fourier transformation method.

With the help of the relation,

$$F[Z e^{-Z^2/4\Delta_0 t}] = -i \frac{d}{dk} F[e^{-Z^2/4\Delta_0 t}] \quad \text{Eq. 1-57}$$

Eq. 1-55 is Fourier-transformed as

$$\frac{\partial}{\partial t} Y_p^{(1)} + k^2 \Delta_0 Y_p^{(1)} = -2\sqrt{2} G \Delta_0^{3/2} (ik) e^{-k^2 \Delta_0 t}. \quad \text{Eq. 1-58}$$

Eq. 1-58, multiplied by $e^{k^2 \Delta_0 t}$, is, in turn, integrated with respect to t to yield

$$Y_p^{(1)}(k, t) = -2\sqrt{2} G \Delta_0^{3/2} t(ik) e^{-k^2 \Delta_0 t}, \quad \text{Eq. 1-59}$$

the inverse transform of which gives the solution $C_1^{(1)}(Z, t)$;

$$C_1^{(1)}(Z, t) = -G \frac{Z}{\sqrt{t}} e^{-Z^2/4\Delta_0 t}. \quad \text{Eq. 1-60}$$

With use of the relation

$$F[Z^3 e^{-Z^2/4\Delta_0 t}] = i \frac{\partial^3}{\partial k^3} F[e^{-Z^2/4\Delta_0 t}], \quad \text{Eq. 1-61}$$

Eq. 1-56 is Fourier-transformed as

$$\frac{\partial}{\partial t} Y_p^{(2)} + k^2 \Delta_0 Y_p^{(2)} = 4\sqrt{2}H(3-2k^2\Delta_0 t)\Delta_0^{5/2} (ik)e^{-k^2\Delta_0 t}. \quad \text{Eq. 1-62}$$

Multiplying both sides of Eq. 1-62 by $e^{k^2\Delta_0 t}$ and integrating with respect to t , we obtain the solution $Y_p^{(2)}(k, t)$;

$$Y_p^{(2)}(k, t) = 4\sqrt{2}H\Delta_0^{5/2} t(3-k^2\Delta_0 t)(ik)e^{-k^2\Delta_0 t}, \quad \text{Eq. 1-63}$$

which is inverse-transformed to produce $C_1^{(2)}(Z, t)$;

$$C_1^{(2)}(Z, t) = H \frac{Z}{\sqrt{t}} (3\Delta_0 + \frac{Z^2}{2t}) e^{-Z^2/4\Delta_0 t}. \quad \text{Eq. 1-64}$$

Combining Eq. 1-51, Eq. 1-60 and Eq. 1-64, we obtain an approximate solution to Eq. 1-1 for a thin-film source;

$$\begin{aligned} \frac{1}{M}C(Z, t) &= \frac{1}{2\sqrt{\pi\Delta_0 t}} e^{-Z^2/4\Delta_0 t} - \frac{1}{8\sqrt{\pi}} \left(\frac{a}{T_0}\right) \left(\frac{T_m + T^*}{T_0}\right) \frac{Z}{\sqrt{\Delta_0 t}} e^{-Z^2/4\Delta_0 t} \\ &+ \frac{1}{16\sqrt{\pi}} \left(\frac{a}{T_0}\right) \left(\frac{T_m}{T_0}\right) \frac{Z^3}{(\Delta_0 t)^{3/2}} e^{-Z^2/4\Delta_0 t}. \quad \text{Eq. 1-65} \end{aligned}$$

This solution is also supposed to be accurate within ϵ^2 under the conditions, Eq. 1-13, Eq. 1-15, and Eq. 1-16.

Eq. 1-65 does not violate the law of mass conservation since

the leading term of an even function is modified by the two odd functions, and hence

$$\int_{-\infty}^{\infty} C(Z,t) dz = M \quad \text{Eq. 1-66}$$

1.4. SOLUTION FOR A THICK-FILM SOURCE

For the finite-source initial and boundary conditions,

$$\left. \begin{aligned} C(|Z| < h \quad ; \quad t = 0) &= C_s \\ C(|Z| > h \quad ; \quad t = 0) &= 0 \end{aligned} \right\} \quad \text{Eq. 1-67}$$

where $2h$ is the thickness of the finite planar source, the solution of Eq. 1-24, $C_o(Z,t)$, is the simple isothermal diffusion profile,

$$C_o(Z,t) = \frac{1}{2} C_s \left[\operatorname{erf}\left(\frac{h-Z}{2\sqrt{\Delta_o t}}\right) + \operatorname{erf}\left(\frac{h+Z}{2\sqrt{\Delta_o t}}\right) \right]. \quad \text{Eq. 1-68}$$

Substitution of Eq. 1-68 reduces Eq. 1-25 for $k=1$ to;

$$\begin{aligned} \frac{\partial C_1^{(1)}}{\partial t} - \Delta_o \frac{\partial^2 C_1^{(1)}}{\partial Z^2} &= K \frac{Z}{t\sqrt{t}} \left[(h+Z) e^{-(h+Z)^2/4\Delta_o t} \right. \\ &\quad \left. + (h-Z) e^{-(h-Z)^2/4\Delta_o t} \right] \end{aligned} \quad \text{Eq. 1-69}$$

$$\frac{\partial C_1^{(2)}}{\partial t} - \Delta_o \frac{\partial^2 C_1^{(2)}}{\partial Z^2} = L \frac{1}{\sqrt{t}} \left[e^{-(h+Z)^2/4\Delta_o t} - e^{-(h-Z)^2/4\Delta_o t} \right] \quad \text{Eq. 1-70}$$

where

$$K \equiv - \frac{C_s}{4\sqrt{\pi}} \left(\frac{a}{T_0}\right) \left(\frac{T_m}{T_0}\right) \frac{1}{\sqrt{\Delta_0}} \quad \text{Eq. 1-71}$$

$$L = \frac{C}{2\sqrt{\pi}} \left(\frac{a}{T_0}\right) \left(\frac{T_m + T^*}{T_0}\right) \sqrt{\Delta_0} \quad \text{Eq. 1-72}$$

These are corresponding to Eq. 1-32 and Eq. 1-33 for the semi-infinite source, respectively. Again using the Fourier transformation method, the differential equations, Eq. 1-69 and Eq. 1-70 are easily solved. The Fourier transform of Eq. 1-69 turns out to be

$$\frac{\partial}{\partial t} (Y_p^{(1)} e^{\Delta_0 k^2 t}) = 2\sqrt{2} K \Delta_0^{3/2} [(1 - i k h - 2\Delta_0 k^2 t) e^{-ikh} - (1 + i k h - 2\Delta_0 k^2 t) e^{ikh}], \quad \text{Eq. 1-73}$$

which is integrated with respect to t and then inverse-transformed to;

$$C_1^{(1)}(z, t) = \frac{K}{\sqrt{t}} \left[\Delta_0 t + \frac{1}{2}(z^2 - h^2) \right] [e^{-(z+h)^2/4\Delta_0 t} - e^{-(z-h)^2/4\Delta_0 t}]. \quad \text{Eq. 1-74}$$

The Fourier transform of Eq. 1-70 is

$$\frac{\partial}{\partial t} (Y_p^{(2)} e^{\Delta_0 k^2 t}) = \sqrt{2} L \Delta_0^{1/2} (e^{-ikh} - e^{ikh}), \quad \text{Eq. 1-75}$$

from which $Y_p^{(2)}$ is solved and inverse-transformed to;

$$C_1^{(2)}(z, t) = L\sqrt{t} [e^{-(z+h)^2/4\Delta_0 t} - e^{-(z-h)^2/4\Delta_0 t}] \quad \text{Eq. 1-76}$$

An approximate solution of Eq. 1-1 for a thick-film source is then the linear combination of Eq. 1-68, Eq. 1-74, and Eq. 1-76;

$$\begin{aligned} \frac{C}{C_s} = & \left[\operatorname{erf}\left(\frac{h-Z}{2\sqrt{\Delta_0 t}}\right) + \operatorname{erf}\left(\frac{h+Z}{2\sqrt{\Delta_0 t}}\right) \right] \\ & + \frac{1}{4\sqrt{\pi}} \left(\frac{a}{T_0}\right) \left(\frac{T_m+2T^*}{T_0}\right) \sqrt{\Delta_0 t} \left[e^{-(Z+h)^2/4\Delta_0 t} - e^{-(Z-h)^2/4\Delta_0 t} \right] \\ & - \frac{1}{4\sqrt{\pi}} \left(\frac{a}{T_0}\right) \left(\frac{T_m}{T_0}\right) \sqrt{\Delta_0 t} \left(\frac{Z^2-h^2}{2\Delta_0 t}\right) \left[e^{-(Z+h)^2/4\Delta_0 t} \right. \\ & \left. - e^{-(Z-h)^2/4\Delta_0 t} \right] \quad \text{Eq. 1-77} \end{aligned}$$

This solution is accurate also within ε^2 under the conditions Eq. 1-13, Eq. 1-15, and Eq. 1-16.

1.5. ACCURACY OF THE SOLUTIONS

It has been stated that Eq. 1-47, Eq. 1-65, and Eq. 1-77 are accurate within ε^2 as the approximate solutions to the differential equation, Eq. 1-6 or

$$\frac{\partial C}{\partial t} = D \left[\frac{\partial^2 C}{\partial Z^2} + \frac{a(T_m+T^*)}{T^2} \frac{\partial C}{\partial Z} + \frac{a^2 T^* (T_m - 2T)}{T^4} C \right] \quad \text{Eq. 1-78}$$

for the semi-infinite source, the thin-film source, and the thick-film source, respectively, provided that Eq. 1-13, Eq. 1-15, and Eq. 1-16 are satisfied, namely,

$$\left| \frac{a\delta}{T_0} \right| \sim \varepsilon^2 \quad ; \quad \frac{T_m}{T_0} \sim \frac{1}{\varepsilon} \quad ; \quad \left| \frac{T^*}{T_0} \right| \sim \frac{1}{\varepsilon} \quad \text{Eq. 1-79}$$

where $\varepsilon^2 \ll 1$. The sufficiency of this statement, Eq. 1-79, can be proved by substituting each solution into Eq. 1-78 and then by comparing the magnitudes of the both sides in view of Eq. 1-79. We will prove here the sufficiency only for the thin-film solution, Eq. 1-65, as the relevant algebra is the simplest to show. The result, however, remains the same for the other two solutions, Eq. 1-47 and Eq. 1-77.

We may define the accuracy of a solution as the difference between the values of both sides of Eq. 1-78, $|(RHS)-(LHS)|$, evaluated by substituting the solution, Eq. 1-65 in the present case, into Eq. 1-78, divided by either of the two values, for example, $|(LHS)|$,

$$(\text{Accuracy}) = \frac{|(RHS)-(LHS)|}{|(LHS)|} . \quad \text{Eq. 1-80}$$

Partial differentiation of Eq. 1-65 with respect to t (time) yields (LHS) as

$$\begin{aligned} \frac{\sqrt{\pi}}{M}(\text{LHS}) = & \left[-\frac{1}{4\sqrt{\Delta_0}} \frac{1}{t} + \frac{1}{16\sqrt{\Delta_0}} \left(\frac{a}{T_0}\right) \left(\frac{T_m+2T^*}{T_0}\right) \frac{Z}{t} + \frac{1}{8\Delta_0\sqrt{\Delta_0}} \frac{Z^2}{t^2} \right. \\ & \left. - \frac{1}{16\Delta_0\sqrt{\Delta_0}} \left(\frac{a}{T_0}\right) \left(\frac{T_m+T^*}{T_0}\right) \frac{Z^3}{t^2} + \frac{1}{64\Delta_0^2\sqrt{\Delta_0}} \left(\frac{a}{T_0}\right) \left(\frac{T_m}{T_0}\right) \frac{Z^5}{t^3} \right] \cdot \\ & \frac{1}{\sqrt{t}} \exp\left(-\frac{Z^2}{4\Delta_0 t}\right). \quad \text{Eq. 1-81} \end{aligned}$$

The 2nd and the following terms in the square bracket on the right-hand-side of Eq. 1-81 are on the order of magnitude ε

relative to the leading term, $1/4\sqrt{\Delta_0}t$, due to Eq. 1-79. Thus the denominator in Eq. 1-80 may be replaced by this leading term for an accuracy estimation, or

$$\left| \frac{(\text{RHS}) - (\text{LHS})}{(\text{LHS})} \right| \sim \frac{4\sqrt{\pi\Delta_0}t}{M} |(\text{RHS}) - (\text{LHS})| \quad \text{Eq. 1-82}$$

After some algebra, Eq. 1-82 turns out to be;

$$\begin{aligned} \left| \frac{(\text{RHS}) - (\text{LHS})}{(\text{LHS})} \right| \sim & \left| \frac{1}{8}(\lambda^2\xi^2)(\mu^2+2\nu^2-\mu\nu+8\nu) \right. \\ & + \frac{1}{2}(\lambda^2Z^2)(9\mu^2+8\mu\nu+2\nu^2) \\ & - \frac{3}{2}(\lambda^2Z^4\xi^{-2})\mu(3\mu+\nu) + (\lambda^2Z^6\xi^{-4})\mu^2 \\ & + \frac{1}{8}(\lambda^3Z\xi^2)\nu(\mu-2)(3\mu-2\nu) \\ & + \frac{1}{4}(\lambda^3Z^3)\mu(4\mu^2+2\nu^2+7\mu\nu-2\nu) \\ & - \frac{1}{2}(\lambda^3Z^5\xi^{-2})\mu^2(\mu+\nu) \\ & - \frac{1}{4}(\lambda^4Z^2\xi^2)\mu\nu(\mu+2\nu)(\mu-2) \\ & \left. + \frac{1}{4}(\lambda^4Z^4)\mu^2\nu(\mu-2) \right| \quad \text{Eq. 1-83} \end{aligned}$$

where

$$\lambda \equiv a/T_0,$$

$$\mu \equiv T_m/T_0,$$

$$\nu \equiv T^*/T_0$$

$$\text{and } \xi \equiv 2\sqrt{\Delta_0}t.$$

In this derivation of Eq. 1-83, we have disregarded, in the polynomial representations of D and T^n , the higher order terms of ε^2 or less being again based on the conditions, Eq. 1-79, or

$$D = \Delta_0(1 + \lambda\mu Z) \quad ; \quad T^n = T_0^n.$$

The use of these approximations affects by no means the final result showing the overall accuracy to be ϵ^2 because, otherwise, it would have produced additional terms the magnitudes of which are smaller than any term in Eq. 1-83. One may notice that, in Eq. 1-83,

$$\left. \begin{aligned} |\lambda \xi| &\leq |\lambda \delta| \\ |\lambda z| &\leq |\lambda \delta| \\ \text{and } |\lambda^{m-n} z^m \xi^{-n}| &\leq |(\lambda \delta)^{m-n}| \end{aligned} \right\} \text{Eq. 1-84}$$

In view of Eq. 1-84 and Eq. 1-79, thus, the accuracy, Eq. 1-83, may be written as

$$\frac{|(\text{RHS}) - (\text{LHS})|}{(\text{LHS})} \leq \left(\frac{a\xi}{T_0}\right)^2 \left(\frac{T_m}{T_0}\right)^2 \quad \text{Eq. 1-85 a}$$

or

$$\frac{|(\text{RHS}) - (\text{LHS})|}{(\text{LHS})} \leq \epsilon^2, \quad \text{Eq. 1-85 b}$$

in which the Schwarz inequality has been used.

Therefore, Eq. 1-79 is proved to be the sufficiency for the accuracy ϵ^2 of Eq. 1-65 as a solution to the differential equation, Eq. 1-78.

APPENDIX 2. SELF-THERMOMIGRATION
WITH LOCAL DEFECT EQUILIBRIUM VIOLATED

2.1. INTRODUCTION

It has been shown that, in a self-thermomigration system, the applied temperature gradient induces a net vacancy flux which causes the local crystalline lattice to move down or up the gradient depending on the sign of the heat of transfer for the preservation of local defect equilibrium.^{9,18,63,79} The formulation of the phenomenon in terms of irreversible thermodynamics is based on the postulate that the local thermodynamic equilibrium for the vacancy formation prevails in the system. It is, however, often violated in real systems⁸⁰ since the annihilation or creation of vacancies is a sluggish diffusion process, in general, to or from repeatable growth sites such as dislocations, grain boundaries and external or internal surfaces. The vacancy concentration is a function of not only temperature but also position and time. It may be supersaturated or undersaturated, though the vacancy concentration may be not much different from its local equilibrium one, $C_v^{eq}(T)$, in the proximity of a repeatable growth site. As a consequence, the velocity of the local lattice is obviously position dependent and the Fick frame of reference moves as well due to the incorporation of excess (or deficit) vacancies. It may cause a serious error in an experimental determination of the reduced heat of transfer by measurement of

the local lattice velocity. But a more fundamental question to be asked is whether the local formulation of the Gibbs equation remains valid for a system in which local defect equilibrium is violated. The applicability of irreversible thermodynamics in the linear regime should be justified. This will be done in what follows and thermal self-diffusion will then be reformulated in a more general way.

2.2. IRREVERSIBLE THERMODYNAMICS

The irreversible thermodynamics has been based upon the fundamental assumption that the Gibbs equation holds piecewise even in a continuous system in which the thermodynamic variable change continuously with space (\vec{r}) and time (t),²⁻⁶

$$ds = \frac{1}{T}du + \frac{P}{T}dv - \sum_k \frac{\mu_k}{T}dC_k, \quad \text{Eq. 2-1}$$

where s , u and v are respectively specific entropy, specific internal energy and specific volume. This is equivalent to the definition of the local thermodynamic potentials as surfaces in the space of local thermodynamic variables, for example,

$$s(\vec{r}, t) = s[u(\vec{r}, t), v(\vec{r}, t), C_k(\vec{r}, t)] \quad \text{Eq. 2-2}$$

$$G(\vec{r}, t) = G[T(\vec{r}, t), P(\vec{r}, t), C_k(\vec{r}, t)] \quad \text{Eq. 2-3}$$

which is the necessary condition for the applicability of the irreversible thermodynamics in the linear regime⁶

Now consider an elementary metal system subject to a stationary temperature gradient, in which vacancies are the predominant defect type. Such a system may be regarded as a collection of an infinite number of infinitesimal discontinuous systems, each of which is in the thermal equilibrium with a heat reservoir at the local temperature, $T(\vec{r})$. An isothermal subsystem may be or may be not in internal thermodynamic equilibrium with respect to the vacancy concentration. The Gibbs potential per unit volume, G , however, can be represented as an analytic function of the temperature, T , and the vacancy concentration, C_v , in the isobaric condition, irrespective of the local defect equilibrium. If one considers the subsystem a binary ideal solution of the vacancy solute and the metal solvent in the neighborhood of the solubility limit, $C_v^{eq}(T)$, such as

$$C_v^{eq}(T) \ll C, \quad \text{Eq. 2-4}$$

the Gibbs potential, G , may be written according to the statistical mechanics^{9, 74} as

$$G = G^{\circ} + C_v g_v + kT[C_v \ln(C_v/C) + (C - C_v) \ln(C - C_v)/C], \quad \text{Eq. 2-5}$$

where G° denotes the specific free energy of an ideal crystal and C is the concentration of lattice points. The chemical potential of a vacancy is then defined as

$$\mu_V \equiv \left(\frac{\partial G}{\partial C_V} \right)_T = g_V + kT \ln (C_V/C). \quad \text{Eq. 2-6}$$

The internal defect equilibrium corresponds to the condition,

$$\left(\frac{\partial G}{\partial C_V} \right)_T = 0 \quad \text{Eq. 2-7}$$

in which vacancies are in their solubility limit, $C_V^{\text{eq}}(T)$, and the chemical potential of the metal is determined uniquely in the sense of the exact thermodynamics.^{2,1} Due to Eq.'s 2-6 and 2-7,

$$\mu_V = kT \ln(C_V/C_V^{\text{eq}}) \quad \text{Eq. 2-8}$$

and

$$C_V^{\text{eq}} = C \exp(-g_V/kT). \quad \text{Eq. 2-9}$$

In view of Eq. 2-5, irreversible thermodynamics can be applied equally well to a system in which the local defect equilibrium is violated, but in which the deviation is not so far as to cripple the validity of Eq. 2-5. The evolution of the system is, now, less restrictive. If local defect equilibrium were to be imposed as a limiting condition, states for the system would be confined to a line of minima in G , i.e., $\mu_V=0$, on the G -surface. The evolution of the present system, in contrast, is allowed on the whole G -surface as shown in Fig. 2-1. This implies a presence of another evolutionary phenomenon associated with vacancies. If the

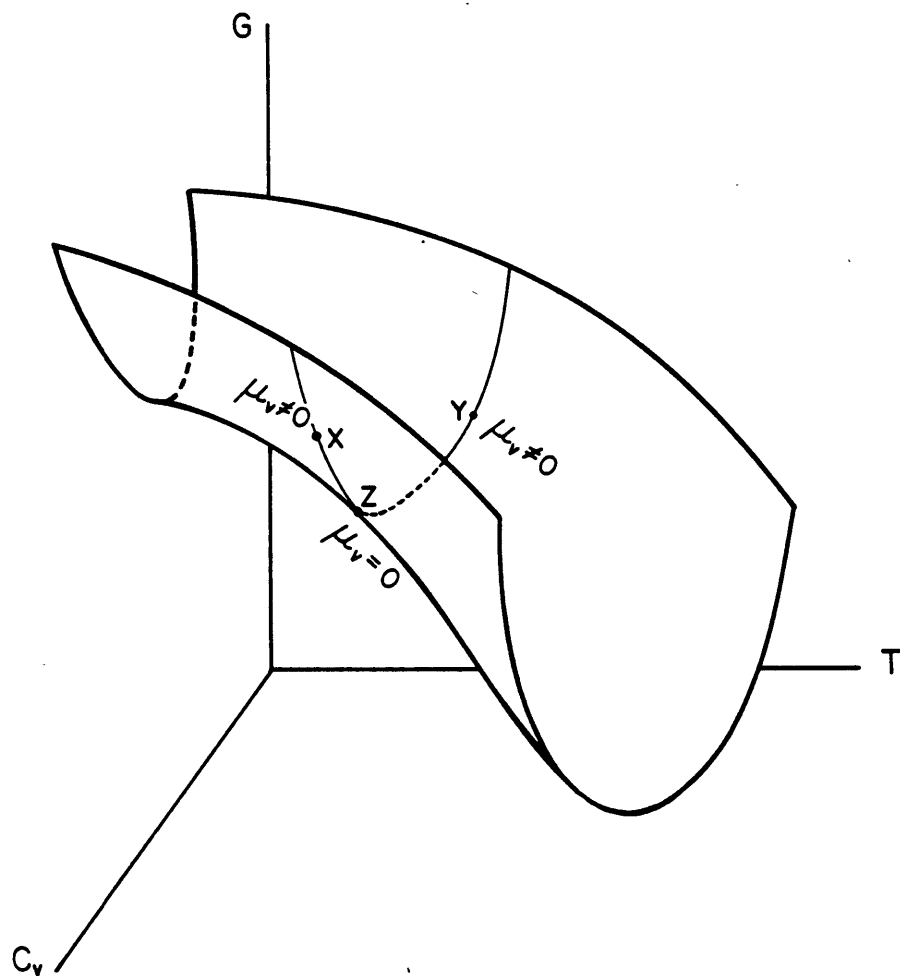
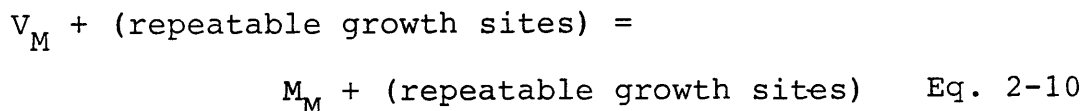


Fig. 2-1. G-surface of a system of the metal solvent and the vacancy solute.

system is off the line of minima on the G-surface, the vacancies are created or annihilated to lower the system energy, which requires them to diffuse from or to the repeatable growth sites. Though the process itself is of a vectorial character, the annihilation (or creation) of vacancies may be treated as a quasi-chemical reaction,^{6,4}



by analogy to a chemical reaction between conserved chemical species. The affinity for the reaction, A , is proportional to how far the system is off the line of minima, or

$$A \equiv -\left(\frac{\partial G}{\partial \xi}\right)_{\vec{r}} = \mu_V, \quad \text{Eq. 2-11}$$

where ξ denotes the degree of advancement of the reaction. If we let r be the reaction rate of Eq. 2-10, defined as the vacancy annihilation rate in a unit volume;

$$r \equiv -\left(\frac{\partial C_V}{\partial t}\right)_{\vec{r}}, \quad \text{Eq. 2-12}$$

the rate of entropy creation due to the chemical reaction, σ_{chem} , will be

$$\sigma_{\text{chem}} = r \cdot (A/T). \quad \text{Eq. 2-13}$$

When the vacancies are supersaturated (point X in Fig. 2-1), vacancies are annihilated and vice versa (point Y in Fig. 2-1);

$$\sigma_{\text{chem}} > 0 \text{ definite.} \quad \text{Eq. 2-14}$$

Equation 2-11 may be rewritten, in view of Eq. 2-8, as

$$A = kT \ln(1+S), \quad \text{Eq. 2-15}$$

where S is the supersaturation of vacancies⁴⁴ defined as

$$S \equiv (C_v - C_v^{\text{eq}}) / C_v^{\text{eq}}. \quad \text{Eq. 2-16}$$

For a small deviation from the local defect equilibrium, i.e.,

$$S \ll 1, \quad \text{Eq. 2-17}$$

Eq. 2-15 is approximated as

$$A = kTS \quad \text{Eq. 2-18}$$

In such a case, it is justified⁴ that the linear phenomenological law for the reaction is valid;

$$r = L A \quad \text{Eq. 2-19}$$

or, due to Eq. 2-16 and Eq. 2-18,

$$r = \frac{kTL}{C_v^{eq}} (C_v - C_v^{eq}). \quad \text{Eq. 2-20}$$

The phenomenological coefficient (reaction constant), L , contains information on the kinetics of the vacancy annihilation. By introducing the relaxation time or the lifetime of the vacancy, τ , one may replace

$$1/\tau = kTL/C_v^{eq} \quad \text{Eq. 2-21}$$

to obtain

$$r = (C_v - C_v^{eq})/\tau. \quad \text{Eq. 2-22}$$

Equation 2-22 is what Adda et al.,^{7,9} Balluffi,^{8,1} and Fara and Balluffi^{8,2} employed.

2.3. FORMULATION

In a thermal self-diffusion system which is off the line of the minima, $\mu_v=0$, on the G-surface in Fig. 2-1, there may arise two kinds of irreversible phenomena; the heat flux (thermal conduction) and mass flux (thermomigration) are induced by the temperature gradient, and the system itself evolves towards the state of the local defect equilibrium (point Z in Fig. 2-1) by creating or annihilating the vacancies when undersaturated (point Y in Fig. 2-1) or supersaturated (point X in Fig. 2-1), respectively. It is noted that, while the former (heat and mass flux) are of vectorial character,

the rate of change of vacancy concentration intrinsically is of scalar character no matter what the mechanism of the vacancy creation or annihilation is. We may treat it as a quasi-chemical reaction, Eq. 2-10. Due to Curie's Principle⁴, the vectorial phenomena (the heat and mass fluxes) do not interfere with the scalar phenomenon (the vacancy annihilation).

From irreversible thermodynamics, the rate of entropy creation of the system, σ , for the present system will be

$$T\sigma = \vec{J}_V \cdot (\vec{X}_V - \vec{X}_M) + \vec{J}_q \cdot \vec{X}_q + r \cdot A \quad \text{Eq. 2-23}$$

as Adda et al.^{7,9} have derived, and the phenomenological equations are written as:

$$L \vec{J}_V = L_{VV} (\vec{X}_V - \vec{X}_M + q_V^* \vec{X}_q) \quad \text{Eq. 2-24}$$

$$r = L A, \quad \text{Eq. 2-19}$$

in which the local lattice conservation,

$$L \vec{J}_V + L \vec{J}_M = 0, \quad \text{Eq. 2-25}$$

has been used. Instead of the reduced heat of transport of the metal atom, q^* , the corresponding quantity of the vacancy, q_V^* , is introduced in the Eq. 2-24, which can be shown to be

$$q_V^* = - q^* \quad \text{Eq. 2-26}$$

with use of Eq. 2-25.

With respect to the temperature, we again assume a stationary temperature gradient,

$$\left(\frac{\partial T}{\partial t}\right)_{\vec{r}} = 0 \quad \text{Eq. 2-27}$$

and hence the heat flux, \vec{J}_q , has been omitted in the phenomenological equations.

Due to Prigogine's theorem, Eq. 70 and Eq.'s 33 and 10 for the thermodynamic forces, X, Eq. 2-24 is rewritten as

$$L_V \vec{J}_V = -D_V \left(\vec{\nabla} C_V - \frac{C_V q^*}{kT^2} \vec{\nabla} T \right) \quad \text{Eq. 2-28}$$

in which the assumption, $C_V \ll C_M \approx C$, has been used and the diffusion coefficient of the vacancy, D_V , defined as kTL_{VV}/C_V .

The local vacancy concentration, $C_V(\vec{r}, t)$, is changing with the vacancy flux induced by the applied temperature gradient and with its creation or annihilation. For a system of n-components, in general, in which no chemical reaction takes place between the components, the law of mass conservation reads

$$\frac{\partial}{\partial t} \left(\sum_{k=1}^n C_k \right) = -\vec{\nabla} \cdot \left(\sum_{k=1}^n C_k \vec{u}_k \right) \quad \text{Eq. 2-29}$$

or

$$\frac{\partial}{\partial t} \left(\sum_{k=1}^n C_k \right) = -\vec{\nabla} \cdot \sum_{k=1}^n L_k \vec{J}_k - \vec{\nabla} \cdot \left(\sum_{k=1}^n C_k \right) \vec{u}_L \quad \text{Eq. 2-30}$$

due to Eq. 64,

$$\vec{J}_k = C_k (\vec{u}_k - \vec{u}_L).$$

In the crystalline lattice with vacancies as predominant defects,

$$C_V + \sum_{k=1}^n C_k = C \quad \text{Eq. 2-31}$$

and, since the local crystalline lattice is conserved,

$$\vec{J}_V + \sum_{k=1}^n \vec{J}_k = 0. \quad \text{Eq. 2-32}$$

Substitution of Eq.'s 2-31 and 2-32 into Eq. 2-30 results in

$$\left(\frac{\partial C_V}{\partial t} \right)_{\vec{r}} = -\vec{\nabla} \cdot \vec{J}_V + \vec{\nabla} \cdot (C \vec{u}_L), \quad \text{Eq. 2-33}$$

in which use has been again made of the approximation,

$$C_V \ll C \quad \text{or} \quad \sum_{k=1}^n C_k \cong C.$$

It should be noted that the 2nd term on the r.h.s. of Eq. 2-33 corresponds to the creation or annihilation of vacancies and that it is equated with Eq. 2-19 or Eq. 2-22;

$$\vec{\nabla} \cdot (C \vec{u}_L) = -r = \frac{C_V^{\text{eq}} - C_V}{\tau}. \quad \text{Eq. 2-34}$$

By substituting Eq.'s 2-34 and 2-28 into Eq. 2-33, we obtain

a differential equation,

$$\left(\frac{\partial C_v}{\partial t}\right)_{\vec{r}} = \vec{\nabla} D_v (\vec{\nabla} C_v - \frac{C_v q^*}{kT^2} \vec{\nabla} T) + \frac{C_v^{eq} - C_v}{\tau} . \quad \text{Eq. 2-35}$$

For the appropriate initial and boundary conditions, Eq. 2-35 can be solved, in principle, to give the local concentration of vacancies as a function of position, \vec{r} , and time, t ;

$$C_v = C_v(\vec{r}, t) . \quad \text{Eq. 2-36}$$

The relaxation time or the life time of vacancies, τ , is assumed to be known as a function of the vacancy diffusion coefficient or the temperature and the geometry of vacancy sinks.^{6,4} The net vacancy flux is, then, recalculated, by putting back Eq. 2-36 into Eq. 2-28, as

$$\vec{J}_v(\vec{r}, t) = -D_v(\vec{r}) \cdot (\vec{\nabla} C_v(\vec{r}, t) - \frac{C_v(\vec{r}, t) \cdot q^*}{kT(\vec{r})^2} \vec{\nabla} T) . \quad \text{Eq. 2-37}$$

The supersaturation (or undersaturation) of vacancies causes the Fick reference frame to move with a velocity \vec{u}_F relative to the laboratory frame due to the volume expansion (or contraction) accompanying the incorporation of the non-equilibrium vacancies. The l.h.s. of Eq. 2-33 is, thus, equated with the divergence of \vec{u}_F , or

$$\vec{\nabla} \cdot (C \vec{u}_F) = \left(\frac{\partial C_v}{\partial t}\right)_{\vec{r}} . \quad \text{Eq. 2-38 a}$$

This expression looks more self-explanatory if C is replaced by $1/\Omega$ where Ω is an atomic volume,

$$\frac{1}{\Omega} \vec{\nabla} \cdot \vec{u}_F = \left(\frac{\partial C_V}{\partial t} \right)_{\vec{r}}. \quad \text{Eq. 2-38 b}$$

From Eq. 2-33 and Eq. 2-38 a, the relative velocity of the two reference frames is given by

$$\vec{u}_L - \vec{u}_F = {}_L \vec{J}_V / C \quad \text{Eq. 2-39}$$

or, due to Eq. 2-37,

$$\vec{u}_L - \vec{u}_F = -D_V \cdot \left(\vec{\nabla} N_V - \frac{N_V q^*}{kT^2} \vec{\nabla} T \right), \quad \text{Eq. 2-40}$$

a result which is congruent with Eq. 67 in Chapter 2, that has been derived from the definitions of reference velocities.

Here $N_V \equiv C_V / C$.

For local defect equilibrium, represented by the line of minima on the G -surface of Fig. 2-1, the vacancy concentration would be determined by the local temperature alone, i.e., Eq. 2-9. As consequences, the Fick frame coincides with the laboratory frame,

$$\vec{u}_F = 0, \quad \text{Eq. 2-41}$$

and the lattice reference frame moves with its limiting velocity,

$$\vec{u}_L = D \frac{q^* - h_v}{kT^2} \vec{\nabla} T, \quad \text{Eq. 2-42}$$

where D is the self-diffusion coefficient, $D = D_v N_v$.

The relative velocity, Eq. 2-39 or Eq. 2-40 is what we measure in thermal self-diffusion with the help of Darken's chips²⁵ or inert markers embedded. It is obvious that the reduced heat of transport, q^* , may be subject to a serious error when determined from the experimental measurement of the relative velocity, $\vec{u}_L - \vec{u}_F$, and by using Eq. 2-42, instead.

If the life time of the vacancy, τ , is very short or consequently,

$$\left(\frac{\partial C_v}{\partial t} \right)_{\vec{r}} \sim 0 \quad ; \quad S \sim 0. \quad \text{Eq. 2-43}$$

Then, Eq. 2-42 will be a good approximation of Eq. 2-40 in view of Eq. 2-33. For such a case, its first order correction can be easily made. If we rewrite Eq. 2-16,

$$C_v = C_v^{\text{eq}} (1 + S) \quad \text{Eq. 2-44}$$

where $S \ll 1$. The supersaturation of vacancies, S , is assumed to be a function of the local temperature alone in a given sample geometry (grain size, etc.). From Eq.'s 2-9 and 2-44,

$$\frac{\vec{\nabla} C_v}{C_v} = \left[\frac{h_v}{kT^2} + \frac{1}{1+S} \left(\frac{dS}{dT} \right) \right] \cdot \vec{\nabla} T \quad \text{Eq. 2-45}$$

Substituting Eq. 2-45 into Eq. 2-40, we obtain

$$\vec{u}_L - \vec{u}_F \cong D_V C_V^{eq} (1 + S) \cdot \left(\frac{q^* - h_V}{kT^2} - \frac{1}{1 + S} \frac{dS}{dT} \right) \cdot \vec{\nabla} T$$

or, due to Eq. 2-43,

$$\vec{u}_L - \vec{u}_F \cong D \cdot \frac{1}{kT^2} \cdot (q^* - h_V - \frac{dS}{dT}) \cdot \vec{\nabla} T. \quad \text{Eq. 2-46}$$

What is determined experimentally is, thus, the quantity in the parentheses which may be called the "effective heat of transport", q_{eff}^* ;

$$q_{eff}^* = q^* - h_V - dS/dT \quad \text{Eq. 2-47}$$

The temperature dependence of the vacancy supersaturation is presumably determined mainly by the temperature dependence of the vacancy lifetime in the condition of Eq. 2-43. From Eq.'s 2-16 and 2-34,

$$S = \frac{\tau}{C_V^{eq}} (-\vec{\nabla} \cdot C_V \vec{u}_L) \quad \text{Eq. 2-49}$$

from which

$$\frac{dS}{dT} \propto \frac{d\tau}{dT} \quad \text{Eq. 2-50}$$

for a given sample geometry. According to Schmalzried^{6,4} the relaxation time for the equilibration of vacancies on the

dislocation network in metals is given by

$$\tau = \frac{f(\rho_d, \alpha)}{\pi \rho_d D_v}, \quad \text{Eq. 2-51}$$

where ρ_d is the dislocation density, α is the radius of dislocation core, and $f(\rho_d, \alpha)$ is a function of ρ_d and α . For the special case of a whisker crystal of radius, r_o ,

$$\tau = \frac{r_o^2}{5.76 D_v}. \quad \text{Eq. 2-52}$$

In this case, only the surface can serve as a sink or source for vacancies. From Eq. 2-52, we may conclude that

$$\frac{dS}{dT} \propto \frac{d\tau}{dT} < 0 \quad \text{Eq. 2-53}$$

Therefore, from Eq. 2-47,

$$q_{\text{eff}}^* > q^* - h_v \quad \text{Eq. 2-54}$$

or a heat of transport determined from a self-thermomigration experiment, q_{eff}^* , is likely to be greater than what it would be if local defect equilibrium were established in an elementary metal system.

REFERENCES

1. K. G. Denbigh, *The Thermodynamics of the Steady State*, Methuen & Co., Ltd., London, 1950
2. S. R. de Groot, *Thermodynamics of Irreversible Processes*, North Holland Publishing Co., Amsterdam, 1951
3. S.R. de Groot and P. Mazur, *Non-Equilibrium Thermodynamics*, North Holland Publishing Co., Amsterdam, 1962
4. I. Prigogine, *Introduction to Thermodynamics of Irreversible Processes*, John Wiley & Sons, Inc., New York, 1967
5. R. Haase, *Thermodynamics of Irreversible Processes*, Addison-Wesley Publishing Co., Reading, Mass, 1969
6. G. Nicolis, *Rep. Prog. Phys.*, 42, 225, 1979
7. L. Onsager, *Phys. Rev.*, 37, 405, 1931; *Phys. Rev.*, 38, 2265, 1931
8. I. Prigogine, *Physica* 15, 272, 1949
9. R. E. Howard and A. B. Lidiard, *Rep. Prog. Phys.*, 27, 161, 1964
10. E. A. Guggenheim, *J. Phys. Chem.*, 33, 842, 1929; 34, 1540, 1930
11. H. B. Casimir, *Rev. Mod. Phys.*, 17, 343, 1945
12. G. J. Hooyman and S. R. de Groot, *Physica* 21, 73, 1955
13. P. Mazur and I. Prigogine, *J. Phys. radium.* 12, 616, 1951,
14. J. Meixner, *Ann. Physik.*, (5)43, 244, 1943
15. B. D. Coleman and T. Truesdell, *J. Chem. Phys.*, 33, 28, 1960

16. E. D. Eastman, J. Am. Chem. Soc., 48, 1482, 1926; 50, 283, 1928
17. C. Wagner, Ann. Physik., (5)3, 629, 1929
18. A. R. Allnatt and A. V. Chadwick, Chem. Rev., 67, 681, 1967
19. M. J. Gillan, J. Phys. C: Solid State Phys., 10, 1641, 1977
20. C. Wagner, Progr. Sol. State Chem., 10(part 1), 3, 1975
21. C. Wagner, Ber. Bunsenges. Physik. Chem., 78, 611, 1974
22. J. G. Kirkwood, R. L. Baldwin, P. J. Dunlop, L. J. Gosting and G. Kegeles, J. Chem. Phys., 33, 1505, 1960
23. A. D. LeClaire, Progr. Metal. Phys., 4, 265, 1953
24. G. Matano, Jap. J. Phys., 8, 109, 1933
25. L. S. Darken, Trans. AIME, 174, 184, 1948
26. J. E. Lane and J. S. Kirkaldy, Can. J. Phys., 42, 1643, 1964
27. G. J. Yurek and H. Schmalzried, Ber. Bunsenges. Physik. Chem., 78, 1379, 1974
28. A. T. Fromhold, Jr., S. R. Coriell and J. Kruger, J. Phys. Soc. Jap., 34, 1452, 1973
29. A. Katchalsky and P. F. Curran, *Nonequilibrium Thermodynamics in Biophysics*, Harvard University Press, Cambridge, Mass., 1967
30. L. S. Darken and R. A. Oriani, Acta Met., 2, 841, 1954
31. P. G. Shewmon, Acta Met., 8, 605, 1960
32. O. D. Gonzales and R. A. Oriani, Trans. Met., Soc., AIME, 233, 1873, 1965

33. A. Sawatzky, *J. Nucl. Mater.*, 2, 321, 1960
34. J. W. Droege, Atomic Energy Commission, Report BMI-1502, 1961; *Chem. Abstr.*, 55, 17139b (1961)
35. R. P. Marshall, *Trans. Met. Soc. AIME*, 233, 1449, 1965
36. A. W. Sommer and W. F. Dennison, U. S. Atomic Energy Commission, Report NAA-SR-5066, 1960; *Chem. Abstr.*, 55, 4084f (1961)
37. G. D. Rieck and H. A. C. M. Bruning, *Nature*, 190, 1181, 1960
38. G. D. Rieck and D. L. Vogel, *Acta Met.*, 14, 1703, 1966
39. A. Kirchheim and E. Fromm, *Acta Met.*, 22, 1543, 1974
40. S. R. de Groot, *Physica*, 9, 699, 1942
41. C. C. Tanner, *Trans. Faraday Soc.*, 49, 611, 1953
42. A. Sawatzky and E. Vogt., *Trans. Met. Soc. AIME*, 227, 917, 1963
43. R. Kirchheim, *Phys. Stat. Sol. (b)*, 91, 123, 1979
44. P. G. Shewmon, *Diffusion in Solids*, McGraw-Hill Book Co., New York, 1963
45. W. F. Ames, *Nonlinear Partial Differential Equations in Engineering*, Vol. 18, Academic Press, New York, 1965
46. G. F. Carrier and C. E. Pearson, *Partial Differential Equations, Theory and Technique*, Academic Press, New York, 1976
47. J. Askill, *Tracer Diffusion Data for Metals, Alloys, and Simple Oxides*, IFI/Plenum Data Corp., New York, 1970
48. R. A. Oriani, *J. Phys. Chem. Solids*, 30, 339, 1969
49. R. E. Howard, *J. Chem. Phys.*, 27, 1377, 1957

50. A. R. Allnatt and A. V. Chadwick, *Trans. Faraday Soc.*, 62, 1726, 1966
51. A. R. Allnatt and A. V. Chadwick, *Trans. Faraday Soc.*, 63, 1929, 1967
52. A. R. Allnatt and P. Pantelís, *Trans. Faraday Soc.*, 64, 2100, 1968
53. S. J. C. Rushbrook Williams and A. R. Allnatt, *J. Chem. Phys.*, 66, 2272, 1977
54. S. J. C. Rushbrook Williams and A. R. Allnatt, *Trans. Faraday Soc.*, 73, 1093, 1977
55. J. L. Crolet, *These Orsay*, 1971, quoted from Ref. 56
56. J. Dupuy, in *Physics of Electrolytes*, Vol. 2, edited by J. Hladik, Academic Press, New York, 1972, pp 699-745
57. R. E. Howard and A. B. Lidiard, *Disc. Faraday Soc.*, 23, 113, 1957
58. R. E. Howard, *Phil. Mag.*, 2, 1462, 1957
59. E. Haga, *Jap. J. Phys. Soc.*, 13, 1090, 1958; 14, 992, 1959; 14, 1176, 1959
60. A. R. Allnatt and P. W. M. Jacobs, *Proc. Roy. Soc. A.* 260, 350, 1961
61. C. Wagner, *Progr. Sol. State Chem.*, 7, 1, 1972
62. F. A. Kröger and V. J. Vink, in *Solid State Physics*, Vol. 3, edited by F. Seitz and D. Turnbull, Academic Press, Inc., New York, 1956, pp 307-435
63. A. B. Lidiard, in *Thermodynamics*, Proceedings of the Symposium on Thermodynamics with Emphasis on Nuclear Materials and Atomic Transport in Solids, Vienna, 1965,

- Vol. II, International Atomic Energy Agency, Vienna, 1966, pp 3-22
64. H. Schmalzried, *Solid State Reactions*, 2nd edition, Verlag Chemie GmbH, Weinheim, West Germany, 1981
65. J. O'M. Bockris and A. K. N. Reddy, *Modern Electrochemistry*, Plenum Publishing Co., New York, 1970
66. W. D. Kingery, H. K. Bowen and D. R. Uhlmann, *Introduction to Ceramics*, 2nd edition, John Wiley & Sons, Inc., New York, 1976
67. L. Bonpunt, N. B. Chanh and Y. Haget, *J. de Physique*, C6, 289, 1980
68. J. Bardeen and C. Herring, in *Imperfections in Nearly Perfect Crystals*, John Wiley & Sons, Inc., New York, 1952, pp 261-288
69. P. G. Shewmon, *J. Chem. Phys.*, 29, 1032, 1958
70. C. J. Meechan and G. W. Lehman, *J. Appl. Phys.*, 33, 634, 1962
71. L. C. Correa da Silva and R. F. Mehl., *Trans. Met. Soc. AIME*, 191, 155, 1951
72. W. Mock, Jr., *Phys. Rev.* 179, 663, 1969
73. J. N. Agar, in *Advances in Electrochemistry and Electrochemical Engineering*, Vol. 3, edited by P. Delahay, Interscience Publishers, New York, 1963, pp 31-121
74. A. B. Lidiard, in *Encyclopedia of Physics*, Vol. 20, Springer-Verlag, Berlin, 1957, pp 246-349
75. K. S. Pitzer, *J. Chem. Phys.*, 65, 147, 1961
76. W. C. Mackrodt and R. F. Stewart, *J. Phys. C: Solid State*

- Phys., 12, 5015, 1979
77. H. B. Huntington, in *Diffusion*, American Society for Metals, 1973, pp 155-184
 78. D. Jaffe and P. G. Shewmon, *Acta Met.*, 12, 515, 1964
 79. Y. Adda, G. Brebec, N. V. Doan, M. Gerl and J. Philibert, in *Thermodynamics*, Proceedings of the Symposium on Thermodynamics with Emphasis on Nuclear Materials and Atomic Transport in Solids, Vienna, 1965, Vol. II, International Atomic Energy Agency, Vienna, 1966, pp 255-295
 80. R. A. McKee and J. P. Stark, *Phys. Rev. B*, 11, 1374, 1975
 81. R. W. Balluffi, *Acta Met.*, 2, 194, 1954
 82. H. Fara and R. W. Balluffi, *J. Appl. Phys.*, 30, 325, 1959

BIOGRAPHICAL NOTE

The author, Han-Ill Yoo was born in Korea on October 20, 1951 a year after the Korean War broke out. He dropped out of senior high school after a brief attendance and then went through the following three years looking for something which, since then, has been neither spoken nor written about but only buried deep in his heart. Through the qualification examination for college entrance, the author resumed, in 1970, his education at the Department of Materials Science of Seoul National University. After his graduation with a B.S. in 1974, he attended the then newly-established graduate school, the Korea Advanced Institute of Science, for the next two years. In this graduate school, he met his mentor, Dr. Kee Soon Kim, as his M.S. thesis supervisor. The seed of the author's interest in materials science was sown by him who had been a former disciple of the author's thesis supervisor, Prof. B. J. Wuensch and who has now passed away for nearly 5 years. As soon as he had finished his M.S. in 1976, the author joined as a research scientist the then just one-month old Korea Standards Research Institute. He devoted the next three and a half years to the establishment of the new organization. Between December of 1976 and March of 1977, he briefly visited the National Bureau of Standards in Gaithersburg, Maryland, where he met Dr. R. S. Roth as the supervisor of his visiting scholarship. Dr. Roth, a close friend of Prof. B. J. Wuensch, introduced the author to M.I.T. and fertilized the author's interest in materials science. The author resigned from the Korea Standards Research Institute in August, 1979, and crossed the Pacific to enter the Department of Materials Science and Engineering of M.I.T. as a graduate student for his advanced degree. He has been married since 1978. He is now a father of a five-year-old daughter and a six-month-old son.

As he winds up a four-and-a-half-year long studentship abroad the author has a feeling that he begins to touch the other one of Janus' faces and to appreciate the beauty of the "pebbles on the seashore."